Kern- und Teilchenphysik

In-trap decay spectroscopy on highly-charged radioactive ions towards measurements on intermediate nuclei in $\beta\beta$ decay

Inaugural-Dissertation
zur Erlangung des Doktorgrades
der Naturwissenschaften im Fachbereich Physik
der Mathematisch-Naturwissenschaftlichen Fakultät
der Westfälischen Wilhelms-Universität Münster

vorgelegt von

Annika Lennarz

aus Münster

Juni 2015

Kern- und Teilchenphysik

In-trap decay spectroscopy on highly-charged radioactive ions towards measurements on intermediate nuclei in $\beta\beta$ decay

Dekan: Prof. Dr. Christian Weinheimer

Erster Gutachter: Prof. Dr. Dieter Frekers

Zweiter Gutachter: Prof. Dr. Jens Dilling

Tag der mündlichen Prüfung: 13.07.2015

Tag der Promotion: 13.07.2015

Für Oma.

CURRICULUM VITAE

ABSTRACT

This thesis presents the development and commissioning of a novel experimental setup to perform in-trap decay spectroscopy on highly-charged radioactive ions. The primary objective for such a device is the measurement of the weak ($\geq 10^{-5}$) electron-capture branching ratios of the odd-odd intermediate nuclei in double-beta ($\beta\beta$) decay. Those branching ratios will provide experimental input to benchmark theoretical shell-model calculations for the nuclear matrix elements in $\beta\beta$ decay.

The spectroscopy setup is part of the TITAN (TRIUMF's Ion Trap for Atomic and Nuclear science) facility at TRIUMF in Vancouver, Canada. The apparatus employs an open-access electron-beam ion trap (EBIT) to provide a low-background environment as well as backing-free ion storage, and is surrounded radially by seven low-energy planar silicon-lithium drifted (Si(Li)) photon detectors. While charged particles are guided out of the trap center by the strong (up to 6 T) magnetic field, the photons from the decay inside the EBIT are detected by the Si(Li) detector array. This feature provides a high suppression of β-decay induced background, which is an important advantage towards conventional methods, as the electron-capture branch is usually suppressed by several orders of magnitude relative to its β^- counterpart, which is usually the main decay part of the odd-odd intermediate nuclei decay.

Employing the electron beam of the EBIT for charge breeding optimizes the ion-cloud confinement due to the deeper trapping potential for highly-charged ions and increases the ion holding time in the trap, thereby allowing half-life measurements up to minutes or even beyond.

The successful application of the spectroscopy apparatus during two commissioning experiments on ^{124}Cs and ^{116}In as well as a detailed data analysis including the investigation of atomic structure effects as a consequence of charge breeding is outlined in this work. The experiment on ^{124}Cs has already been published: A. Lennarz et. al., Phys. Rev. Lett. 113, 082502 (2014). A first test measurement towards future applications of this setup is also described, followed by a brief introduction to further proposed measurements for the investigation of the decay properties of highly-charged ions and the impact on nuclear astrophysics.

ZUSAMMENFASSUNG

Gegenstand der hier vorliegenden Arbeit ist die Entwicklung und Inbetriebnahme einer neuen Zerfallsspektroskopieanlage mit dem Ziel die schwachen Elektroneneinfangs-Verzweigungsverhältnisse der uu-Zwischenkerne im doppelten Betazerfall zu bestimmen. Die experimentell gewonnenen Daten sind von besonderer Bedeutung für theoretische Schalenmodellrechnungen, welche sich mit der Bestimmung der Kernmatrixelemente des doppelten Betazerfalls befassen.

Hauptbestandteil der neuartigen Anlage ist eine Elektronenstrahl-Ionenfalle (EBIT) des TITAN (*TRIUMF's Ion Trap for Atomic and Nuclear science*) Experiments am TRIUMF in Vancouver, Kanada, mit welcher radioaktive Ionen allein durch eine Kombination aus elektrischen und magnetischen Felder und ohne Implantierung auf einem Trägermaterial gespeichert werden können. Dadurch werden zum einen der Untergrund, z.B. verursacht durch Bremsstrahlungsprozesse von konkurierenden β Zerfällen, stark reduziert und zum anderen eine Absorption der in der Falle emittierten Röntgenstrahlung verhindert. Die Ionenfalle besitzt sieben Zugangs-Ports in radialsymmetrischer Orientierung, an welchen jeweils ein Siliziumdriftdetektor (Si(Li)) angebracht ist. Durch das starke Magnetfeld (bis zu 6 T) werden innerhalb der Falle emittierte β-Teilchen (e^-, e^+) entlang der Feldlinien aus der Falle heraus geleitet, während Röntgen- und Gammaquanten ungehindert die Si(Li) Detektoren erreichen. Die räumliche Trennung der Photonen und β-Teilchen trägt maßgeblich zur Reduzierung des Untergrunds bei, womit der Aufbau um mehrere Größenordnungen sensitiver auf Elektroneneinfangsprozesse ist als herkömmliche Methoden, bei welchen ein radioaktiver Strahl auf einer beweglichen *tape station* implantiert wird.

Neben der effektiven Reduzierung des Untergrunds, bietet die Verwendung der EBIT den Vorteil einer nahezu verlustfreien Speicherung von hochgeladenen Ionen. Die Verwendung

des Elektronenstrahls sorgt auf Grund der Raumladung für eine Minimierung der räumlichen Ausdehnung der Ionenwolke innerhalb der Falle. Gleichzeitig wird die Dauer der Ionenspeicherung durch die hohen Ladungszustände der Ionen und das dadurch resultierende tiefere Potential vergrößert, wodurch eine präzise Messung von Halbwertszeiten in der Größenordnung von Minuten und länger ermöglicht wird.

In dieser Arbeit werden zwei Testexperimente an den Kernen ^{124}Cs and ^{116}In beschrieben, welche die erfolgreiche Inbetriebnahme der Spektroskopiefalle demonstrieren, wobei die Messung an ^{124}Cs bereits publiziert worden ist: A. Lennarz et. al., Phys. Rev. Lett. 113, 082502 (2014). Eine detailierte Analyse der Zerfallsspektren inklusive einer Untersuchung atomarer Effekte, welche durch die Erhöhung der Ladungszustände verursacht werden, ist Basis für weitere Applikationen dieser neuartigen Spektroskopiemethode. Erste Testmessungen bezüglich neuer Anwendungsgebiete sowie eine Einführung in die Zerfallseigenschaften von hochgeladenen Ionen, welche z.B. Einfluss auf nukleare astrophysikalische Prozesse haben, werden am Ende dieser Arbeit vorgestellt.

ACKNOWLEDGEMENTS

At this point I would like to thank all the people who helped and supported me over the last years. First of all, I would like to thank my supervisor Dieter Frekers for giving me the unique opportunity to work on the TITAN-EC project at the TRIUMF facility and the constructive feedback to my thesis. I enjoyed working on this project and appreciate the countless important experiences I made during that time. Further, my thanks goes to Jens Dilling for welcoming me in the TITAN group, for his support and good advice. I would also like to thank all my amazing colleagues I had the privilege to work with and who became good friends of mine during my time at TRIUMF. I appreciated the warm and joyful working atmosphere, which is so rare to find and which I will miss dearly.

Very special thanks to Alex Grossheim for his guidance, friendship, constant support and for the valuable corrections to my thesis. I am genuinely grateful I had the opportunity to work with and learn from him, and will keep our time at TITAN-EC in good memory.

Next I would like to thank Kyle Leach for constantly encouraging me over the last 2 1/2 years, for being a great colleague and an amazing friend and always having good advice for me. Thank you so much for your thorough reading, I am glad I had you around. I would also like to thank Thomas Brunner, especially for helping me out during my first weeks at TRIUMF and introducing me to the house I called home for the last four years. I will never forget the wonderful people and friends I found during this time. Thank you.

Last but not least I want to thank my parents, siblings and friends in Germany for believing in me and encouraging my decision to move to Vancouver. Thank you for supporting me even in those times, I should have been home with you. Special thanks to Sonja Lennarz and Melanie Liedtke for making home feel less far away. Very special thanks to Christoph Schilling for always encouraging and supporting me. Thank you for believing in me, caring for me and keeping me motivated by making sure that I would spend at least a few hours outside to clear my head. I am lucky I met you.

Contents

List of Figures

List of Tables

Introduction

In the late 1990s, neutrino-oscillation experiments provided the first direct evidence for a non-zero neutrino mass. The determination of the absolute neutrino mass, however, currently remains one of the most important unresolved questions in physics as its determination is of paramount importance to gain insight into the evolution of the universe as well as the physics beyond the Standard Model.

Studies which are devoted to probe the neutrino mass are therefore extensive, and are a current focus of experimental physics. One of the most promising venues is the neutrinoless mode (0ν) of double-beta decay ($\beta\beta$). The observation of the $0\nu\beta\beta$ decay will have profound implications on modern physics as it would signal a Majorana character of the neutrino and further allow extracting the effective Majorana neutrino mass. In order to extract the mass from the $0\nu\beta\beta$-decay rate, a precise knowledge of the nuclear matrix elements (NME) of the decay is required. As the matrix elements depend on detailed nuclear structure characteristics, precise and accurate experimental measurements can provide insight into these systems.

Characterizing radioactive decay via the measurement of photon detection is one of the most commonly employed experimental techniques in nuclear physics. The advent of rare-isotope beam (RIB) facilities has provided access to increasingly exotic nuclei, and allows for studies on the decay of the odd-odd intermediate nuclei in $\beta\beta$ decay. To observe subtle nuclear structure effects, low-background decay environments are required.

In this work, the development and commissioning of a novel in-trap decay spectroscopy apparatus for measurements of the electron-capture branching ratios of the odd-odd intermediate nuclei in $\beta\beta$ decay is presented.

Chapter I

THEORETICAL BACKGROUND

1.1 Double-beta decay

Double-beta decay is a rare transition between two nuclei with the same mass number A, whereby the atomic number Z changes by two units (N-2, Z+2). The $\beta\beta$ decay occurs only in even-even nuclei, when the single β decay (n$\longrightarrow$p or p$\longrightarrow$n) to an odd-odd isobar is energetically forbidden or severely suppressed by the angular momentum, whereas the second order decay into the (Z+2) daughter nucleus is still energetically allowed [1]. The second order $\beta\beta$-decay process connects the ground-state spins and parities via a $0^+ \longrightarrow 0^+$ transition. The process is depicted via the mass parabolas shown in Fig. 1.1.

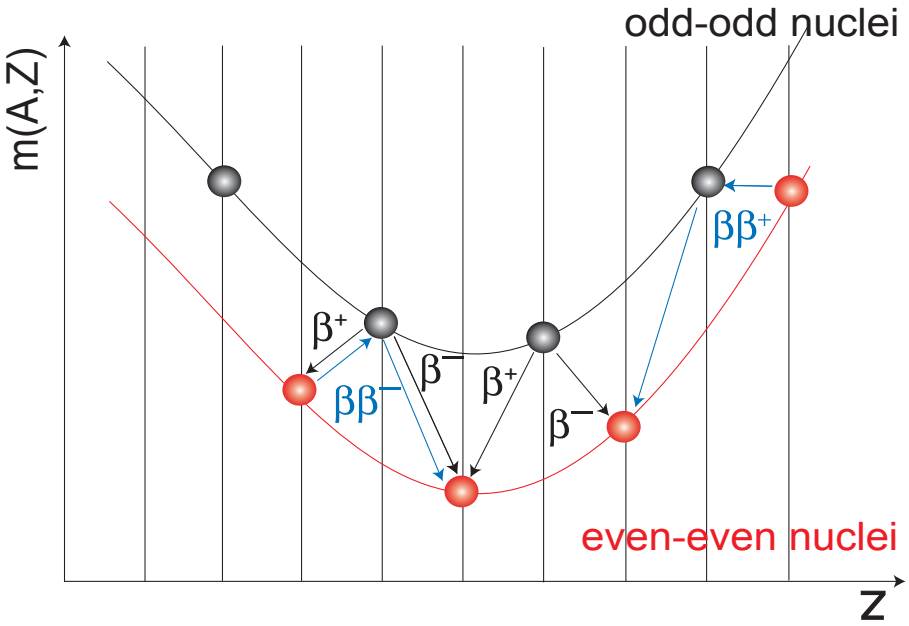

Figure 1.1: The mass parabolas illustrate the energy levels of possible $\beta\beta$ emitters. Odd-odd nuclei are positioned on the upper parabola at higher masses. Due to the pairing energy, the ground states of the even-even nuclei are located energetically lower than their neighboring odd-odd nuclei. These nuclei only decay via the emission of two electrons and neutrinos into a stable isotope [2].

The $\beta\beta$ decay is believed to occur via two different decay modes, the two-neutrino double-beta decay ($2\nu\beta\beta$) and the neutrinoless double-beta decay ($0\nu\beta\beta$). Fig. 1.2 shows the diagrams for both decay modes.

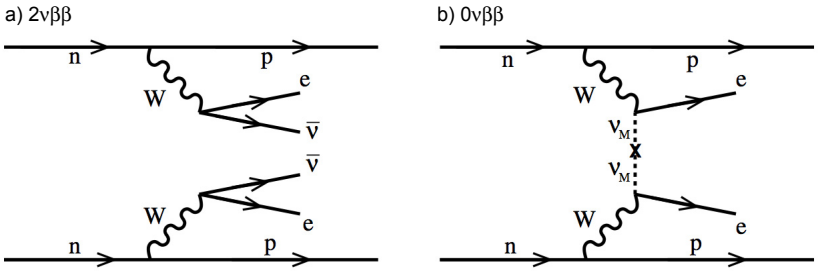

Figure 1.2: Diagrams for a) the $2\nu\beta\beta$ decay and b) the $0\nu\beta\beta$ process. Figure taken from Ref. [3].

1.1.1 The $2\nu\beta^-\beta^-$ -decay process

The $2\nu\beta^-\beta^-$ decay can be described as two single beta decays occurring simultaneously where two electron anti-neutrinos ($\bar{\nu_e}$) and two electrons are emitted [2]:

$$(Z, A) \xrightarrow{\beta^-\beta^-} (Z + 2, A) + 2e^- + 2\bar{\nu}_e. \tag{1.1}$$

The $2\nu\beta\beta$ decay is understood as a second-order weak process within the Standard Model (SM) and is proportional to G_F^4, where G_F is the Fermi constant. This dependence results in long half-lives relative to the single beta-decay process. Thus, $2\nu\beta\beta$ decays occur with half-lives of the order of 10^{18} to 10^{24} years [4]. There are 35 isotopes, which can decay via $2\nu\beta\beta$ decay [5] and the decay has already been measured for a variety of nuclei: ^{48}Ca, ^{76}Ge, ^{82}Se, ^{96}Zr, ^{100}Mo, ^{116}Cd, ^{128}Te, ^{130}Te, ^{130}Ba, ^{150}Nd and ^{238}U and more recently ^{136}Xe [4, 6, 7]. Tab. 1.1 lists the $2\nu\beta\beta$-decay half-lives for several isotopes.

The $2\nu\beta^-\beta^-$ decay rate is given by [9]:

$$\begin{aligned} \Gamma^{2\nu}_{(\beta^-\beta^-)} &= \frac{C}{8\pi^7}\left(\frac{G_F}{\sqrt{2}}\cos(\Theta_C)\right)^4 g_A^4\, \mathcal{F}^2_{(-)} \left|M^{(2\nu)}_{\mathrm{DGT}}\right|^2 f(Q) \\ &= G^{2\nu}(Q, Z, g_A^4)\left|M^{(2\nu)}_{\mathrm{DGT}}\right|^2, \end{aligned}$$

Isotope	$T^{2\nu}_{1/2}$ [y]
^{48}Ca	$\left(4.4^{+0.6}_{-0.5}\right) \times 10^{19}$
^{76}Ge	$(1.926 \pm 0.095) \times 10^{21}$
^{82}Se	$(0.92 \pm 0.07) \times 10^{20}$
^{96}Zr	$(2.3 \pm 0.2) \times 10^{19}$
^{100}Mo	$(7.1 \pm 0.4) \times 10^{18}$
^{116}Cd	$(2.80 \pm 0.05(stat.) \pm 0.4(syst.)) \times 10^{19}$
^{128}Te	$(2.0 \pm 0.3) \times 10^{24}$
^{130}Te	$(7.0 \pm 0.9(stat.) \pm 1.1(syst.)) \times 10^{20}$
^{136}Xe	$(2.11 \pm 0.04(stat.) \pm 0.21(syst.)) \times 10^{21}$
^{150}Nd	$(8.2 \pm 0.9) \times 10^{18}$
^{238}U	$(2.0 \pm 0.6) \times 10^{21}$

Table 1.1: Measured $2\nu\beta^-\beta^-$ -decay half-lives for several isotopes [8]. The value for ^{76}Ge is taken from Ref. [7] and the one for ^{136}Xe is quoted in Ref. [6].

where $G^{2\nu}\left(Q, Z, g_A^4\right)$ is the phase-space factor, which depends on the Q-value of the reaction and the Z number of the decaying nucleus and g_A is the axial-coupling constant of the weak interaction. The Q-dependence is expressed in terms of an 11^{th} order polynomial to leading order. Further, Θ_C is the Cabibbo angle, α the fine-structure constant, and Z the proton number of the daughter nucleus. The factor C is a relativistic correction factor for the $\beta^-\beta^-$ decay, which increases as a function of Z, and is ~ 1 for Z = 20 and $\sim$5 for Z = 50. For the Coulomb factor $\mathcal{F}_{(-)}$ of the β^- decay one gets:

$$\mathcal{F}_{(-)} = \frac{2\pi\alpha Z}{1 - \exp(-2\pi\alpha Z)}. \tag{1.2}$$

Tab. 1.2 shows an overview of the $2\nu\beta^-\beta^-$ phase-space factors for several isotopes. The values for the phase-space factors are model dependent, and depend on the calculated nuclear-charge radii.

The Gamow-Teller matrix element of the double-beta decay ($M^{(2\nu)}_{\mathrm{DGT}}$) includes the nuclear-structure dependence and can be derived from a combination of the GT^+ and GT^- strengths. Since the $2\nu\beta\beta$ decay is accompanied by the emission of two neutrinos, the contributing intermediate states will be of $J^\pi = 1^+$ type. Fermi-type contributions are negligible, since the initial and final states belong to different isospin multiplets.

The $2\nu\beta^-\beta^-$ process is allowed within the SM and neither violates charge conservation nor lepton-number conservation, independent of the character of the neutrino, i.e., whether it

	$G^{2\nu}\left(Q, Z, g_A^4\right) \ln 2 \ \left[y^{-1}\right]$
^{48}Ca	1.05×10^{-17}
^{76}Ge	2.98×10^{-20}
^{82}Se	1.00×10^{-18}
^{96}Zr	4.03×10^{-18}
^{100}Mo	1.97×10^{-18}
^{110}Pd	8.14×10^{-20}
^{116}Cd	1.75×10^{-18}
^{128}Te	1.72×10^{-22}
^{130}Te	9.90×10^{-19}
^{136}Xe	9.29×10^{-19}
^{150}Nd	2.32×10^{-17}
^{238}U	7.80×10^{-20}

Table 1.2: Overview of the phase-space factors in the $2\nu\beta^-\beta^-$ decay for several nuclei. The given values refer to the $G^{2\nu}$ for transitions to the ground state and are given in y^{-1}. The factors were calculated based on the values of Ref. [10], however, with the matrix elements in units of MeV^{-1} and including g_A=1.2694(28) [11]. The calculations in Ref. [10] take into account the exact Dirac wave functions with finite nuclear size and electron screening and use a Coulomb potential derived from a realistic proton density distribution in the daughter nucleus. See also Ref. [12].

is of Majorana or Dirac type.

In addition to the $2\nu\beta^-\beta^-$ decay, also $2\nu\beta^+\beta^+$ decay can occur, for which one has to differentiate between three decay scenarios. Processes like positron emission as well as electron capture (EC) and double-electron capture (ECEC) are possible:

$$(Z, A) \overset{\beta^+\beta^+}{\longrightarrow} (Z-2, A) + 2e^+ + 2\nu_e + 4m_e c^2, \tag{1.3}$$

$$e^- + (Z, A) \overset{EC,\beta^+}{\longrightarrow} (Z-2, A) + e^+ + 2\nu_e + 2m_e c^2 \tag{1.4}$$

and

$$e^- + e^- + (Z, A) \overset{EC,EC}{\longrightarrow} (Z-2, A) + 2\nu_e. \tag{1.5}$$

On the $\beta^+\beta^+$ side the single-particle transitions are strongly hindered since protons cannot decay into neutron states, which belong to the same major shell. This effect is referred to as Pauli-blocking [13]. During the $\beta^+\beta^+$ decay two positrons are emitted and the decay rate is severely suppressed by the available decay energy. This results in a small phase space and long decay half-lives for β^+/EC processes. The latter are on the order of $\sim10^{27}$ y for $\beta^+\beta^+$ processes, $\sim10^{22}$ y for β^+/EC processes with a reduction of the Q-value by a factor

$2m_e c^2$ and $\sim 10^{21}$ y for ECEC processes [14]. Consequently, these decays are difficult to access experimentally.

1.1.2 The $0\nu\beta^-\beta^-$ -decay process

The $0\nu\beta^-\beta^-$ -process occurs without the emission of neutrinos, as its mechanism is based on the emission of an electron antineutrino at the first decay vertex, which is absorbed at the second vertex [13]:

$$(Z, A) \longrightarrow (Z + 2, A) + 2e^-. \tag{1.6}$$

This process violates lepton-number conservation by two units, and is thus forbidden in the Standard Model. In contrast to the $2\nu\beta^-\beta^-$ process, the neutrinoless process has a more complex structure, as the neutrino enters the description as a virtual particle. As a result, the angular momentum forbiddenness is lifted and not only the 1^+-states but also other intermediate states have to be included into the description of the nuclear matrix element. As a consequence of the helicity matching condition, where the neutrino has to be absorbed in the second vertex with the "wrong" handedness, the decay rate depends on the effective neutrino mass $\langle m_{\nu_e} \rangle$ and is given via the following relation [13]:

$$\Gamma^{0\nu}_{(\beta^-\beta^-)} = G^{0\nu}(Q, Z)\, g_A^4 \left| M^{(0\nu)}_{\mathrm{DGT}} - \frac{g_V^2}{g_A^2} M^{(0\nu)}_{DF} \right|^2 \langle m_{\nu_e} \rangle^2, \tag{1.7}$$

where g_V is the vector weak coupling constant. The phase-space factor $G^{0\nu}(Q, Z)$ (compare Eq. 1.7) only depends to 5^{th} order on the Q-value since less particles than in the 2ν process are emitted. The generalized 0ν GT and Fermi matrix elements $M^{(0\nu)}_{\mathrm{DGT}}$ and $M^{(0\nu)}_{DF}$ of the $0\nu\beta^-\beta^-$ process can be written as [13, 15, 16, 17, 18]:

$$M^{(0\nu)}_{\mathrm{DGT}} = \langle f | \sum_{lk} \sigma_l \sigma_k \tau_l^- \tau_k^- H_{\mathrm{GT}}(r_{lk}, E_\alpha) | i \rangle \tag{1.8}$$

$$M^{(0\nu)}_{DF} = \langle f | \sum_{lk} \tau_l^- \tau_k^- H_F(r_{lk}, E_\alpha) | i \rangle. \tag{1.9}$$

Here $H_{\mathrm{GT}}(r_{lk}, E_\alpha)$ and $H_{\mathrm{F}}(r_{lk}, E_\alpha)$ describe a phenomenological neutrino potential [5, 13] and r_{lk} is the distance of a proton and a neutron in the nucleus. E_α stands for an energy parameter, which is connected to the excitation energy, while σ_k is the Pauli spin-operator

of the kth nucleon. The ladder operator τ_k^- decreases the isospin during a (p,n)-reaction and the sum $\sum_{lk}$ runs over all pairs of neutrons or protons [19].

The Schechter-Valle or black-box theorem [20] connects the decay operator of the $0\nu\beta^-\beta^-$ decay, which is defined as a black box, to the effective Majorana mass of the electron neutrino [21] (compare Fig. 1.3).

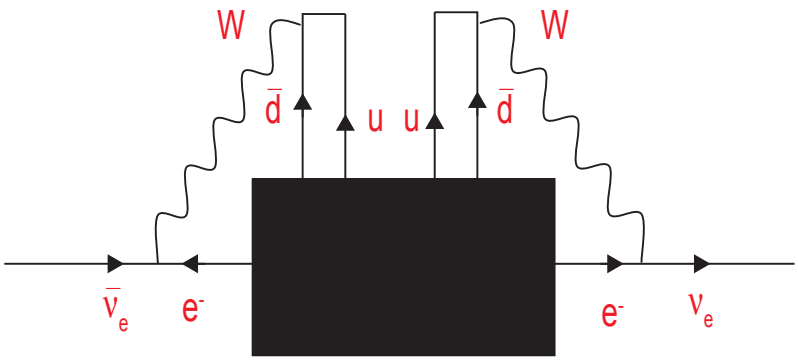

Figure 1.3: Schematic illustration of the $0\nu\beta^-\beta^-$ decay according to the Schechter-Valle theorem. The effective operator of the $0\nu\beta^-\beta^-$ decay is represented by a black box. Figure is adapted from Ref. [20].

Assuming a left-handed effective interaction ($(\bar{\nu}_{eL}\gamma_\mu e_L + \bar{u}_L\gamma_\mu d_L)\, W^\mu$), and given that the u- and d-quarks, which are involved in the process have finite mass, the interaction is facilitated by the production of two neutrinos of the same type on both vertices [20, 21]. In the standard interpretation, the $0\nu\beta\beta$ process is mediated by light and massive Majorana neutrinos, whereas all other mechanisms, which potentially lead to the $0\nu\beta\beta$ process have a negligible or no contribution [22].

Since the amplitude of the neutrinoless decay mode is small as a result of the small neutrino mass, it has not been possible to observe the $0\nu\beta^-\beta^-$ decay experimentally. Consequently, the determination of the matrix elements depends entirely on theoretical models. However, experiments like GERDA [23, 24], MAJORANA [25], MOON [26, 27, 28], NEMO 3 [29], SNO+, CUORE [30, 31], COBRA [32], CANDLES [33], TGV [34] or EXO [35]

and KamLAND-Zen [36] are currently aimed at proving the existence of the neutrinoless process, which would prove the neutrino to be a Majorana particle. Since the process is proportional to the effective neutrino mass square, its observation would further offer the possibility to calculate the neutrino mass, provided the nuclear matrix elements associated with the decay process are known. The present status of the NMEs is discussed in Sec. 1.2.

1.1.3 Neutrino oscillations and the neutrino-mass hierarchy

Even though the absolute neutrino mass has not been determined yet, the fact that neutrinos do have a non-zero mass has already been proven by neutrino-oscillation experiments (Super-Kamiokande [37], SNO [38], KamLAND [39], CHOOZ [40]). These experiments allow determining the difference of the masses squared, whereas the absolute mass cannot be extracted [19].

In a simplified two-neutrino system, the oscillation probability for an electron neutrino with the traveling distance L and the kinetic energy E is given by [11]:

$$P\left(\nu_e \longrightarrow \nu_\mu\right) = \sin^2 2\theta \sin^2 \frac{\Delta m^2 L}{4E}, \tag{1.10}$$

where θ is the mixing angle. In a system with three neutrino flavors, however, the mixing becomes more complicated. Neutrino oscillation implies a superposition of the mass eigenstates of the weak lepton-eigenstates $|\nu_\alpha\rangle$ (with $\alpha = e, \mu, \tau$), which are created via the interaction of charged currents [41], with the mass-eigenstates $|m_i\rangle$ ($i = 1, 2, 3$) of the neutrinos [42, 43]. A unitary transformation connects the $|\nu_\alpha\rangle$- and $|m_i\rangle$-states [41]:

$$|\nu_\alpha\rangle = U_{\alpha i} \, |m_i\rangle \, , \tag{1.11}$$

where $U_{\alpha i}$ are the elements of the mixing matrix. In the case of neutrinos being Dirac-particles, the matrix can be parameterized in the standard CKM form (Cabibbo-Kobayashi-Maskawa) [44, 45]:

$$U_{\alpha i} = \begin{pmatrix} U_{e1} & U_{e2} & U_{e3} \\ U_{\mu 1} & U_{\mu 2} & U_{\mu 3} \\ U_{\tau 1} & U_{\tau 2} & U_{\tau 3} \end{pmatrix} = \begin{pmatrix} c_{12}c_{13} & c_{13}s_{12} & s_{13}e^{-i\delta} \\ -c_{23}s_{12} - c_{12}s_{13}s_{23}e^{-i\delta} & c_{12}c_{23} - s_{12}s_{13}s_{23}e^{-i\delta} & c_{13}s_{23} \\ s_{12}s_{23} - c_{13}c_{23}s_{13}e^{-i\delta} & -c_{12}s_{23} - c_{23}s_{12}s_{13}e^{-i\delta} & c_{13}c_{23} \end{pmatrix} \tag{1.12}$$

The matrix includes three mixing angles θ_{12}, θ_{13}, θ_{23}, which appear as $c_{ij} = \cos\theta_{ij}$ and $s_{ij} = \sin\theta_{ij}$ ($i = 1, 2$ and $j = 2, 3$). θ_{12} and θ_{23} are the dominant angles for solar and atmospheric oscillations, respectively [46].

Experiments like GALLEX/GNO [47, 48] and SAGE [49, 50] were aimed at measuring solar-neutrino oscillations. Super-Kamiokande [51] (atmospheric neutrinos), Daya Bay [52], the KamLAND reactor experiment [53, 54, 55] and CHOOZ [40, 56] (reactor neutrinos) are presently increasing the precision of the current values for the mixing angles.

The parity violating phase δ [57], which accompanies the oscillations only "survives" in the matrix elements U_{e3} and $U_{\tau 1}$ because its effect becomes negligible in the elements $U_{\mu 1}$, $U_{\mu 2}$ and $U_{\tau 2}$. This is due to the quadratic dependence of these elements on the sine of the mixing angles.

If neutrinos are Majorana-particles, two Majorana-phases (ϕ_1 and $\phi_2 \in [0, 2\pi]$ [57]) are created by the absence of right-handed fermion fields and the mixing matrix is written in form of the so called Pontecorvo-Maki-Nakagawa-Sakata (PMNS) version of the neutrino-mixing matrix version [58, 59, 60]:

$$U_{\alpha i} = \begin{pmatrix} c_{12}c_{13} & c_{13}s_{12} & s_{13}e^{-i\delta} \\ -c_{23}s_{12} - c_{12}s_{13}s_{23}e^{-i\delta} & c_{12}c_{23} - s_{12}s_{13}s_{23}e^{-i\delta} & c_{13}s_{23} \\ s_{12}s_{23} - c_{13}c_{23}s_{13}e^{-i\delta} & -c_{12}s_{23} - c_{23}s_{12}s_{13}e^{-i\delta} & c_{13}c_{23} \end{pmatrix} \begin{pmatrix} 1 & & \\ & e^{i\Phi_1} & \\ & & e^{i\Phi_2} \end{pmatrix} \quad (1.13)$$

Processes, where the Majorana mass contributes linearly to the amplitude, i.e., the $0\nu\beta\beta$ decay, are sensitive to these two extra phases, which affect the interference between mass eigenstates in the effective neutrino mass [46]. Because of the helicity-matching requirement the decay rate Γ of that process is proportional to the square of the effective neutrino mass:

$$\Gamma \propto \left|M^{0\nu}\right|^2 \cdot |m_{\nu_e}|^2 . \quad (1.14)$$

Here, $\left|M^{0\nu}\right|^2$ represents the square of the nuclear matrix element and $|m_{\nu_e}|^2$ is given by:

$$|m_{\nu_e}|^2 = \left|\sum_{i=1}^{3} U_{ei}^2 m_i\right|^2 . \quad (1.15)$$

A three-flavor neutrino-oscillation analysis reported in Ref. [61] combines the results from SNO with results of other solar neutrino and reactor neutrino experiments, which results

in the following values for the squares of the mass differences [53, 62]:

$$\Delta m^2_{sol} = m^2_2 - m^2_1 = \left(7.46^{(+0.20)}_{(-0.19)}\right) \cdot 10^{-5}\ \mathrm{eV}^2$$
$$\tan^2\theta_{12} = 0.443^{(+0.030)}_{(-0.025)}, \tag{1.16}$$

and the best fit values for Δm^2_{atm} quoted by the T2K collaboration are [63]:

$$\Delta m^2_{atm} = m^2_3 - m^2_1 = (2.51 \pm 0.10) \cdot 10^{-3}\ \mathrm{eV}^2,$$
$$\sin^2\theta_{23} = 0.514^{(+0.055)}_{(-0.056)}. \tag{1.17}$$

The values given above correspond to the maximal possible disappearance probability for the three-flavor formula. By using the Daya Bay value for $\theta_{13} = 0.11$ [52] and the approximations $\theta_{23} \approx \frac{\pi}{4}$ and $\theta_{12} \approx \frac{\pi}{6}$ one can constrain $|m_{\nu_e}|^2$:

$$\begin{aligned} |m_{\nu_e}|^2 &= \left|\sum_{i=1}^{3} U^2_{ei} m_i\right|^2 \\ &\simeq \left|c^2_{12}c^2_{13}e^{-2i\phi_{12}}m_1 + c^2_{13}s^2_{12}e^{-2i\phi_{23}}m_2 + s^2_{13}e^{-2i\delta}m_3\right|^2. \qquad (1.18) \\ &\backsimeq \left|\frac{3}{4}e^{-2i\phi_{12}}m_1 + \frac{1}{4}e^{-2i\phi_{23}}m_2 + \frac{1}{66}e^{-2i\delta}m_3\right|^2. \qquad (1.19) \end{aligned}$$

This demonstrates the dependence of the $0\nu\beta\beta$-decay rate on the mixing angles, neutrino masses as well as the Majorana phases. Currently, the uncertainty on the NMEs limits the precision for the extraction of these quantities.

For the neutrino masses m_i $(i = 1, 2, 3)$ one has the following constraints: $m^2_1 < m^2_2$ and $0 < m^2_{12} \equiv m^2_2 - m^2_1 < \left|\Delta m^2_{31}\right|$, with $m^2_{31} \equiv m^2_3 - m^2_1$ [64]. The crucial factor for the neutrino mixing matrix and the effective neutrino mass is the mass hierarchy for which the order is presently unknown. There are two scenarios for the neutrino mass hierarchy that satisfy the current oscillation data, the normal ($\Delta m^2_{31} > 0$ and $m^2_3 > m^2_2$) hierarchy and the inverted hierarchy with $\Delta m^2_{31} < 0$ and $m^2_3 < m^2_2$:

- **normal** : $\mathrm{m_3 > m_2 > m_1}$ with $\mathrm{m_2 = \sqrt{m^2_1 + \Delta m^2_{sol}}};\ \mathrm{m_3 = \sqrt{m^2_1 + \Delta m^2_{atm}}}$
- **inverted** : $\mathrm{m_2 > m_1 > m_3}$ with $\mathrm{m_2 = \sqrt{m^2_3 + \Delta m^2_{sol} + \Delta m^2_{atm}}};\ \mathrm{m_1 = \sqrt{m^2_3 + \Delta m^2_{atm}}}$.

Solving the problem of the neutrino-mass hierarchy will further answer the question whether the isolated m^2_3 part is heavier or lighter than the other two neutrino masses (m^2_1, m^2_2) [64], which lie closer together. The situation is illustrated in Fig. 1.4.

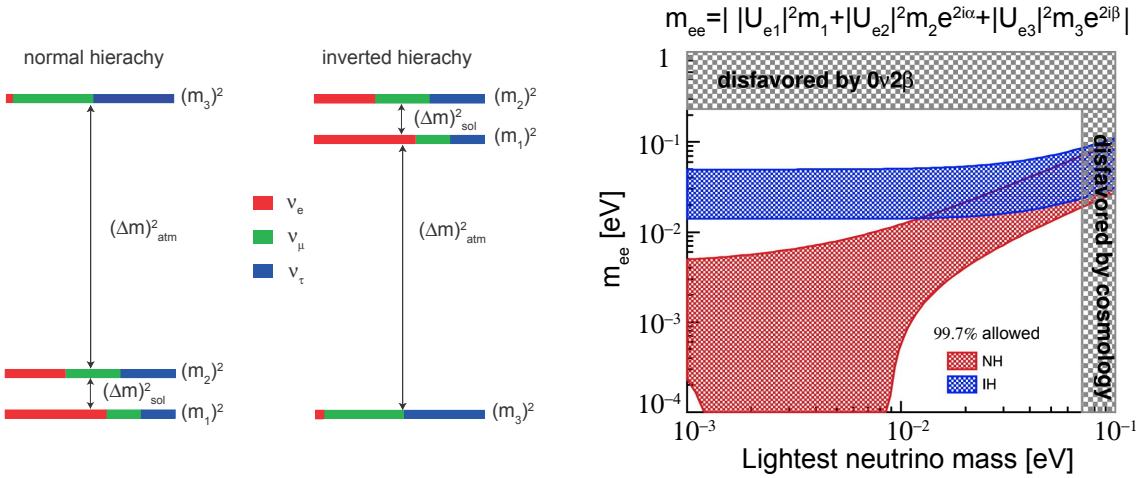

Figure 1.4: Left: Shown are the two possible hierarchy scenarios of the neutrino masses, which correspond to the current neutrino data and fixed mixing angles and squares of the mass differences. Each color is assigned to a $|U_{\alpha i}|^2$-part of the corresponding neutrino-flavors ν_α (α=e, μ, τ) in the mass eigenstate ν_i ($i = 1, 2, 3$). Figure adapted from Ref. [41]. Right: Effective neutrino mass probed in experiments searching for the $0\nu\beta\beta$ decay as a function of the lightest neutrino mass. The blue band corresponds to the inverse ordering and the red one to the normal hierarchy. Figure from Ref. [65].

1.2 Nuclear matrix elements

Presently, the extraction of the effective Majorana neutrino mass from $0\nu\beta\beta$-decay half-lives is limited by poor knowledge of the nuclear matrix elements. The matrix elements of the $2\nu\beta\beta$ decay can be determined experimentally via isospin-changing nuclear charge-exchange reactions (CER) [66, 67], i.e., (^{3}He, t), (d, ^{2}He) [68, 69, 70, 71, 72, 73]. This can be done selectively for the β^+ as well as for the β^- direction by extracting the $B(\mathrm{GT}^\pm)$ value:

$$B(\mathrm{GT}^\pm) = \frac{1}{2\mathrm{J_i}+1}\left|\mathrm{M}^{\mathrm{GT}^\pm}\right|^2. \tag{1.20}$$

These matrix elements can already set the grounds for the theoretical nuclear-structure calculations, even though they are not complete.

The matrix element, which is the sum of two consecutive single β decay GT matrix elements between the initial and an intermediate state and between the same intermediate state and

the final state, can be described by the following formula [13, 74]:

$$\begin{aligned} M_{\mathrm{DGT}}^{(2\nu)} &= \sum_m \frac{\left\langle 0_{g.s.}^{f} \right| \sum_k \sigma_k \tau_k^- \left| 1_m^+ \right\rangle \left\langle 1_m^+ \right| \sum_k \sigma_k \tau_k^- \left| 0_{g.s.}^{i} \right\rangle}{\frac{1}{2} Q_{\beta\beta}(0_{g.s.}^{(f)}) + E(1_m^+) - E_0} \\ &= \sum_m \frac{M_m^{\mathrm{GT}^+} \cdot M_m^{\mathrm{GT}^-}}{\frac{1}{2} Q_{\beta\beta}(0_{g.s.}^{(f)}) + E(1_m^+) - E_0}. \end{aligned} \tag{1.21}$$

Here, $E(1_m^+) - E_0$ describes the energy difference between the m^{th} intermediate 1^+-state and the ground state of the mother nucleus. The sum $\sum_k$ runs over all neutrons of the decaying nucleus. $\left\langle 0_{g.s.}^{f} \right|$ and $\left| 0_{g.s.}^{i} \right\rangle$ are the 0^+-ground states of the final and the initial nucleus, while $|1_m^+\rangle$ and $\langle 1_m^+|$ are the 1^+-states of the intermediate odd-odd nuclei with energies E_m. The transition operators $\sigma_k \tau_k^-$ are the Gamow-Teller operators of the β^- decay, which have no spatial dependence. As a result, the matrix element describes a $0^+ \longrightarrow 0^+$ transition via a $0^+ \longrightarrow 1^+ \longrightarrow 0^+$ decay path. The Fermi part, however, is not relevant, which is due to the fact that the initial and final states are not members of the same isospin-multiplet. The factor $\frac{1}{2}$ in front of the $Q_{\beta\beta}$-value has to be included since the decay process is accompanied by the emission of two neutrinos as well as the emission of two electrons, which share the released energy.

The nuclear matrix elements for the transition to the intermediate nucleus can also be probed through measurements of the electron-capture branching ratios (ECBRs) of the ground-state transitions of the intermediate odd-odd nuclei, which are sensitive to the ground-state nuclear-wave function [75]. The development of an experimental approach to measure these ECBRs is described in this thesis. For illustration purposes, the decay scheme for the intermediate nucleus ^{100}Tc is depicted in Fig. 1.5.

The key to the determination of the neutrino mass, however, is a precise knowledge of the matrix elements of the neutrinoless process. To improve the input parameters for the calculations extensive experimental effort is presently ongoing and does not only include charge-exchange reactions but also nucleon transfer reactions [76] and muon capture [77]. Furthermore, Penning traps are employed for measuring the relevant Q-values to sub-keV

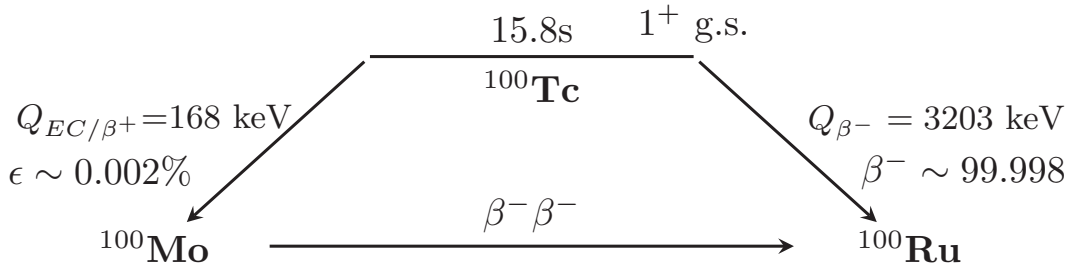

Figure 1.5: Partial decay scheme for the decay of ^{100}Tc, the intermediate nucleus in the double-beta decay of ^{100}Mo to ^{100}Ru.

precision [78, 79, 80]. The present situation of the NME calculations is described in Ref. [81], where the theoretical quantities for a variety of new systems derived from various model calculations, which currently constitute the only means for evaluating the NMEs are presented. The most widely used models are: the Quasi-Particle Random Phase Approximation (QRPA) [82, 83, 84, 85, 86], the Shell Model (SM) [87, 88, 89, 90, 91], the angular momentum Projected-Hartree-Fock-Bogoliubov method (PHFB) [92, 93] and the Interacting Boson Model (IBM-2) [94]. The results still display large variations for the different models (compare Fig. 1.6). The structure for the $0\nu\beta\beta$ NMEs is significantly more complex than the 2ν decay mode as a result of the high momentum transfer of up to $\sim$ 100 MeV/c at the two neutrino vertices. The intermediate state coupling for both, the $2\nu\beta\beta$ and the $0\nu\beta\beta$ process is illustrated in Fig. 1.7 for ^{116}Cd. In order to constrain the theoretical models more information about electron-capture branching ratios is essential.

1.3 Electron-capture branching ratios (ECBRs)

Determining the single β-decay rates of the odd-odd intermediate nuclei in $\beta\beta$ decay provides input for the NMEs calculations. In particular those calculations, which make predictions about the single β decay and the EC decay.

However, in most cases, the EC branches are suppressed by several orders of magnitude relative to their β^- counterparts, which is a result of the lower decay energies [75]. The signature of an EC process is the subsequent emission of an X-ray following the de-excitation of the atomic electrons after the K-shell capture. In the presence of a dominating β-particle

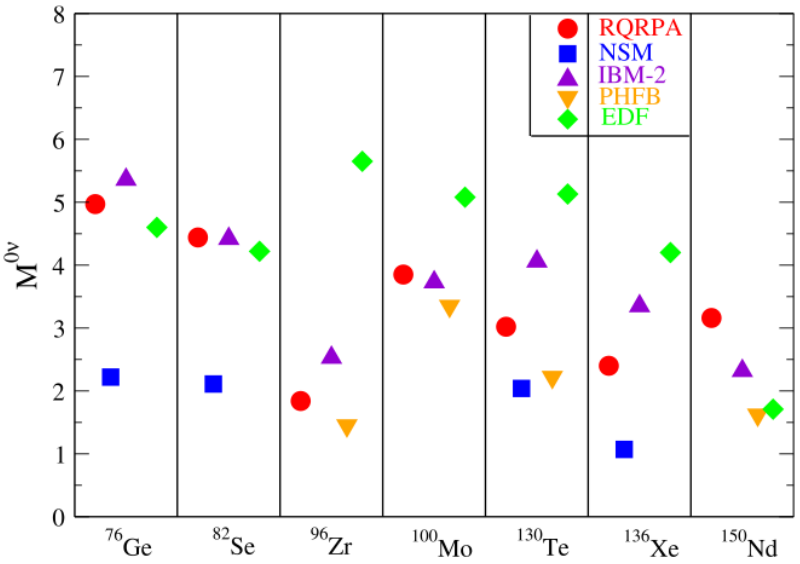

Figure 1.6: Comparison of calculated $M^{0\nu}$ for a selection of nuclei derived with different theoretical models. (R)QRPA: Average $\langle M^{0\nu} \rangle$ calculated within the renormalized QRPA for different treatments of the short-range correlations and averaging over different parameter sets. Nuclear Shell Model (NSM): NME calculated within the Shell Model. IBM-2: $M^{0\nu}$ calculated in the Interacting Boson Model. PHFB: $M^{0\nu}$ calculation within the Projected-Hartree-Fock-Bogoliubov method. Furthermore, the values for the energy density functional (EDF) method are presented. Figure from Ref. [81].

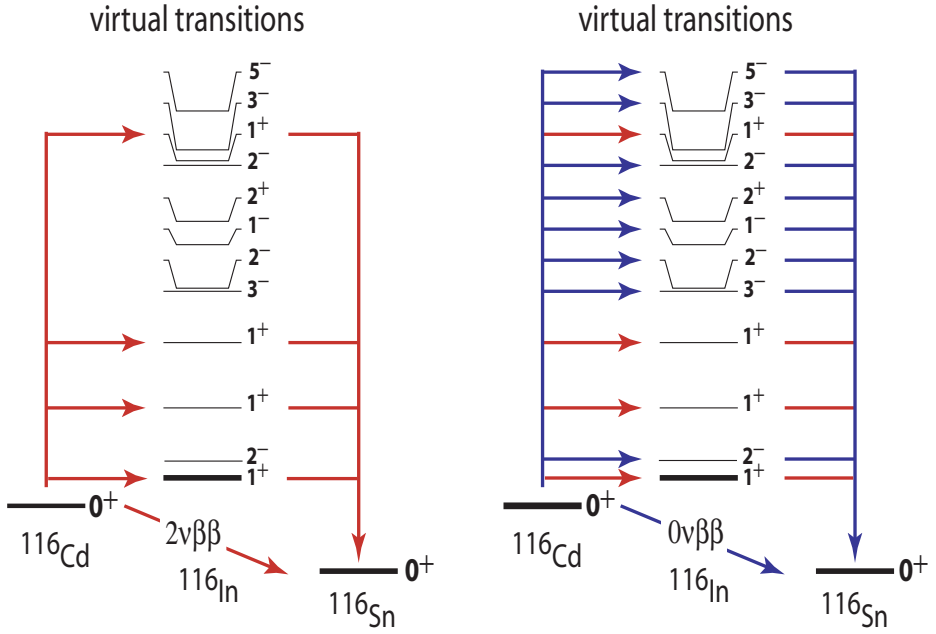

Figure 1.7: Schematic illustration of the excited states for the two $\beta\beta$ decay modes for the nucleus ^{116}Cd. The red arrows mark the excited 1^+ states of the intermediate nucleus ^{116}In. Figure adapted from Ref. [75].

background, the detection of these EC X-rays is extremely difficult and has been impossible in some cases. The traditional experimental approach to measure the EC rates is carried out via irradiation of a movable tape station to measure the K-shell X-rays. This method suffers from a relatively high background, which limits the sensitivity.

Tab. 1.3 gives an overview of seven odd-odd intermediate nuclei relevant for $\beta\beta$ decay which are planned to be investigated with the novel spectroscopy setup.

mother nucleus	transition	daughter nucleus	$K_{\alpha_{1,2}}$ [keV]	$T_{1/2}$
^{100}Tc	$1^+ \longrightarrow 1^+$	^{100}Mo	17.5	15.8 s
^{110}Ag	$1^+ \longrightarrow 1^+$	^{110}Pd	21.2	24.6 s
^{114}In	$1^+ \longrightarrow 1^+$	^{114}Cd	25.3	71.9 s
^{116}In	$1^+ \longrightarrow 1^+$	^{116}Cd	21.7	14.1 s
^{82m}Br	$2^- \longrightarrow 1^+$	^{82}Se	11.2	6.1 min
^{128}I	$1^+ \longrightarrow 1^+$	^{128}Te	27.5	25.0 min
^{76}As	$2^- \longrightarrow 1^+$	^{76}Ge	9.9	26.2 h

Table 1.3: Half-lives and $K_{\alpha_{1,2}}$-shell X-ray energies for the electron-capture decays of the intermediate odd-odd nuclei in $\beta\beta$ decay [75].

As pointed out in Ref. [95] there is an ongoing discussion whether the present theoretical models (QRPA) actually describe the single decay rates (β^-, as well as EC rates) correctly. Part of the description of the above mentioned QRPA is the adjustable particle-particle parameter part g_{pp} of the proton-neutron two-body interaction. Here g_{pp} enters into the description of the nuclear many-body Hamiltonian, and is thus used for single and double-beta decay calculations.

The g_{pp} parameter is traditionally adjusted to reproduce the experimental $2\nu\beta^-\beta^-$ decay half-life. By using this value of g_{pp}, one derives the $0\nu\beta\beta$ NMEs. However, these NMEs appear to be less sensitive to the g_{pp} parameter than the $2\nu\beta\beta$ elements, except for the 1^+ transition matrix elements [75]. The decomposition of the $0\nu\beta\beta$-decay matrix elements for the case of ^{76}Ge $\longrightarrow$ ^{76}Se into multipole components for various values of g_{pp} parameters is presented in Fig. 1.8.

Even though, this model seems to be capable of an adequate description of the $0\nu\beta\beta$-decay matrix elements, one argues whether the fact that the theoretical model agrees with the experimentally derived $2\nu\beta^-\beta^-$ rates is due to a too high EC rate and a too low β^- rate.

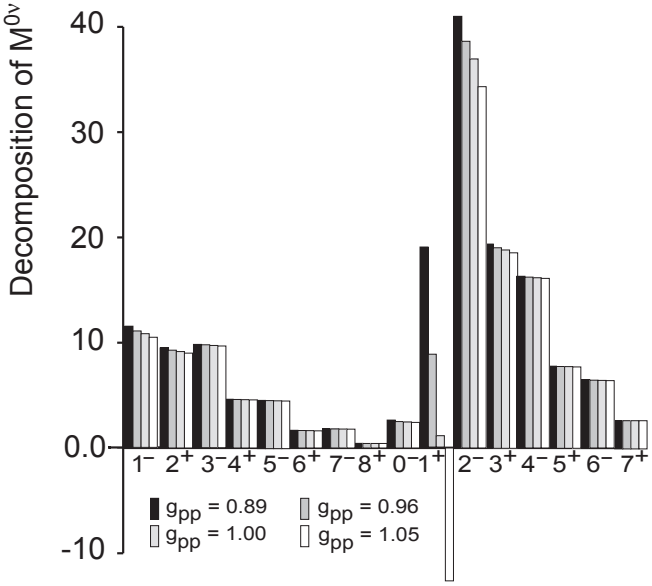

Figure 1.8: Decomposition of the $0\nu\beta\beta$-decay matrix elements (^{76}Ge $\longrightarrow$ ^{76}Se) into multipole components for various values of g_{pp} parameters. The components are separated into natural and unnatural parity parts. Figure adapted from Ref. [96].

These two assumptions would compensate each other and mistakenly lead to an agreement between theory and experiment, thus highlighting an underlying problem with the employed theoretical method. Due to the lack of precise experimental data on ECBRs, there may be discrepancies on the order of up to two magnitudes for the EC matrix elements [75].

For $2\nu\beta^-\beta^-$ transitions where the ground state of the intermediate nucleus is a 1^+ state, one makes the assumption that the corresponding transition matrix element is governed by two virtual transitions. One transition goes from the initial ground state to the 1^+ ground state of the intermediate nucleus, while the second transition goes from that 1^+ state to the ground state of the final nucleus [97]. This property is described as a single-state dominance (SSD) [98] and the nuclear matrix element can be written in a simplified form:

$$M_{tot}^{(2\nu)} \approx \frac{M_{EC} M_{\beta^-}}{\frac{1}{2} Q_{\beta\beta}(0_{g.s.}^{(f)}) + E_{g.s.}(1^+) - E_0}, \tag{1.22}$$

where M_{EC} stands for the matrix element of the electron-capture branch and M_{β^-} describes the one for the single β^- branch. Hence, a measurement of the single decay branches allows for the experimental determination of the total matrix element. Since g_{pp} also enters into

the theoretical calculations of the single β^- decay, those calculations can be benchmarked directly via a comparison to the experimental data.

1.4 Electron-capture subshell ratios

After outlining the nuclear physics background, which motivates the studies carried out in this work, a brief review of the relevant atomic physics background, will be recalled in the following sections based on the descriptions in Ref. [99], Ref. [100] and Ref. [101].

In the case a nucleus with the atomic mass number Z and mass number A surrounded by Z electrons, which fill the lowest electronic states, is unstable against positron emission but does not have a high enough decay energy for positron creation, the decay proceeds via orbital electron capture (EC) with the emission of a neutrino:

$$p + e^- \longrightarrow n + \nu. \tag{1.23}$$

The total energy release for that process is given by:

$$Q_{EC} = \left[M\left(Z, A; Z\right) - M\left(Z-1, A; Z-1\right)\right] c^2. \tag{1.24}$$

Here the energy has to be shared between the emitted neutrino, atomic excitation of the daughter system, recoil energy and a potential nuclear excitation of the daughter system. The observed electromagnetic radiations are the characteristic X-rays of the daughter nucleus, depending on the subshell of the captured electron.

Due to the short range of the weak interaction, the EC decay rate depends on the electron density in the subshells around the nucleus. Since the electron density in the s-shell is larger than for electrons of higher orbital angular momentum, the s-electron capture is the dominant process. However, the mere dependence of the subshell ratios (K to L capture or L to M capture) on the electron density for allowed and first-forbidden transitions is only given when the decay energy is significantly larger than the binding energy in the various subshells [102]. When the decay energy is on the order of the binding energy in the K-shell, the L to K capture ratio depends on the decay energy, whereby the emission of a high-energy neutrino is more favorable.

The total EC transition probability is given by:

$$\lambda = \frac{g^2}{2\pi^3} \sum_x n_x C_x F_x, \tag{1.25}$$

where g is the fundamental weak interaction coupling constant, n_x is the occupation probability of an orbital x in the initial atomic state (n_x=1 for closed shells), C_x is the EC shape factor, which contains the nuclear matrix element and the sum runs over all atomic subshells x. F_x complies to the Fermi function of the β decay:

$$F_x = \frac{\pi}{2} q_x^2 \beta_x^2 B_x. \tag{1.26}$$

Here, $q_x = W_0 + W_x$ is the neutrino energy, which depends on the EC transition energy (W_0) and the energy of the bound electron in the parent atom (W_x). β_x is the wavefunction amplitude of an electron in an orbital x, and B_x is an exchange and overlap correction factor.

For allowed transitions the EC subshell ratio can then be derived from Eq. 1.25 and Eq. 1.26. For the L_1/K ratio one gets:

$$\frac{\lambda_{L1}}{\lambda_K} = \left(\frac{n_{L1} C_{L1}}{n_K C_K} \right) \frac{q_{L1}^2 \beta_{L1}^2 B_{L1}}{q_K^2 \beta_K^2 B_K}. \tag{1.27}$$

The capture ratios for L_2/K, M_1/K, L_2/L_1 or M_1/L_1 are derived in a similar way.

1.5 Internal conversion

Internal conversion (IT) is another example for a decay mode of an excited state in a nucleus, which depends on the atomic environment and leads to the emission of characteristic X-rays [99]. In the IT process, the excitation energy of the nucleus is transferred to an electron bound in one of the innermost atomic shells. Consequently, the electron is ejected from the atom with an energy E_e:

$$E_e = E^* - E_B, \tag{1.28}$$

where E^* is the excitation energy of the nucleus and E_B the electron-binding energy. The ejected electron leaves a vacancy, which is filled by an electron with a higher orbital angular momentum, which is accompanied by the emission of characteristic X-rays.

The IT process is in direct competition with γ-ray emission. The ratio of the number of emitted conversion electrons N_e to the number of γ-rays N_γ is defined as the internal-conversion coefficient:

$$\alpha_C = \frac{N_e}{N_\gamma}. \tag{1.29}$$

Since the increase of α_C is proportional to Z^3, while it decreases with higher E^*, internal conversion predominantly occurs in heavy nuclei with low-lying excited states [99].

1.6 Fluorescence yield

The collision of an atom with an incoming projectile, i e., a photon, may cause the ejection of an inner atomic-shell electron, which leads to a vacancy in that particular subshell. The atom is assumed to return to its ground state by filling that vacancy via two possible modes [103].

One possibility for de-excitation is the emission of a fluorescence (characteristic) X-ray with a photon energy that is defined as the energy difference of the energy of the inner shell featuring the vacancy and the energy of the outer shell from which an electron is used to fill the vacancy. The second possibility is the radiationless ejection of an outer-shell electron (Auger or Coster-Kroning transition) using the excess energy, which results in a vacancy in higher atomic shells.

The probability for filling a vacancy in the atomic shell, caused by radiative processes, is defined as the fluorescence yield $\omega_i(Z)$ (ω_K, ω_{L1}, ...) and is needed for the calculation of X-ray or Auger-electron intensities [104]:

$$\omega_i(Z) = \frac{f_i(Z)}{\nu_i(Z)}. \tag{1.30}$$

Here, $f_i(Z)$ denotes the average number of fluorescence X-rays following the creation of vacancies $\nu_i(Z)$ in the i^{th} subshell. For example, f'_{12} and f'_{13} ($f'_{12} \ll f'_{13}$) are the intrashell radiative yields and are defined as the probabilities for X-ray emission per vacancy in the L_1 subshell, subsequently resulting in an L_2 or respectively L_3 subshell vacancy.

The probabilities for electron emission per vacancy in an L shell are the so called Coster-Kroning yields (f_{12}, f_{13}, f_{23}), which result in a vacancy in one of the higher L subshells.

Under the assumption, that the different decay modes are independent, the total decay rate S is the sum of the three partial rates (fluorescence (S_F), Auger (S_A), Coster-Kroning (S_C)) [105]:

$$S = S_F + S_A + S_C. \tag{1.31}$$

The probabilities for electron emission per vacancy in atomic shells can be calculated for any shell i and are described as Auger yields a:

$$a_i = 1 - \omega_i + f_i, \tag{1.32}$$

with $f_1 = f_{12} + f_{13}$ and $f_2 \equiv f_{23}$ [100, 104].

1.7 Atomic-structure effects in highly-charged ions

Ionizing an atom by the removal of the outer-shell electrons affects the X-ray energies from inner-shell transitions [106]. As a consequence, the electrons of the inner shells are bound stronger to the nucleus than in a neutral atom, which results in an increased binding energy with increasing degree of ionization.

The energy of a characteristic X-ray is defined as the difference between the binding energy of the electron of an inner-shell vacancy and the higher-shell electron subsequently filling that vacancy. The ionization of the outer shells influences the energy levels of all lower lying shells, which results in a change of the characteristic energies, an effect known as ionization-energy shift [106].

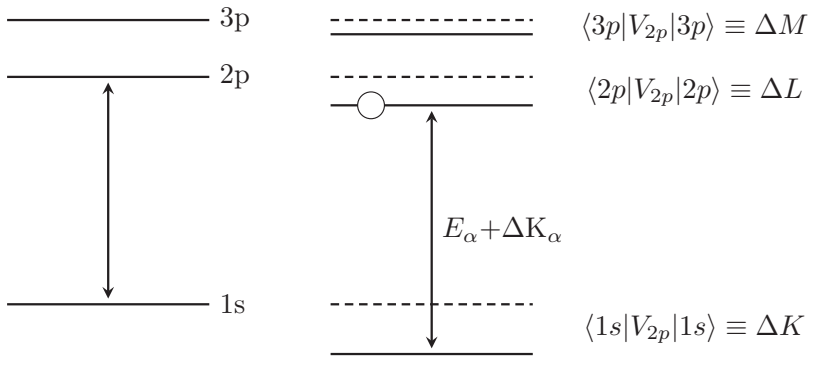

Figure 1.9: Binding-energy level diagram illustrating the removal of a 2p electron and the resulting increase in binding energy for each level. The unshifted and shifted K_α X-ray energies are indicated, where no distinction between $K_{\alpha 1}$ and $K_{\alpha 2}$ was made here. Figure adapted from Ref. [107].

The situation for the removal of a 2p electron is illustrated in Fig. 1.9. By using the approximation that the transition energies are defined as the differences between the binding energies, one gets for the transition-energy shifts of the X-rays:

$$\Delta K_\alpha = \Delta K - \Delta L, \tag{1.33}$$

$$\Delta K_\beta = \Delta K - \Delta M, \tag{1.34}$$

with the binding-energy shifts [107]:

$$\Delta K = \langle 1s|V_{2p}|1s\rangle, \tag{1.35}$$

$$\Delta L = \langle 2p|V_{2p}|2p\rangle \tag{1.36}$$

and

$$\Delta M = \langle 3p|V_{2p}|3p\rangle. \tag{1.37}$$

The pertubation potential V_{2p} caused by the vacancy in the 2p shell can be calculated according to the following relation:

$$V_{2p}(r) = \frac{1}{r} - \frac{4\pi}{r}\int_r^\infty \rho_{2p}(r')(r'^2 - rr')\,\mathrm{d}r', \tag{1.38}$$

where Ψ_{2p} is the hydrogenic wave function and $\rho_{2p}(r)$ the charge density of the 2p electrons at a distance r from the nucleus [107, 108].

Electron-electron correlation, relativistic and quantum electrodynamical effects strongly influence the electron-binding energy with increasing charge state. Hence, the atomic spectrum varies with the electronic configuration. Therefore, one has to account for any relativistic and quantum electrodynamic (QED) effects to provide a realistic description of X-ray spectra from highly-charged ions [109]. Due to its relevance for the data analysis in Ch. 5, the basic principles of the relativistic multiconfigurational Dirac-Fock code FAC (flexible atomic code) [110] configuration interaction program are described in the following. The FAC code computes the energy levels in an N-electron system by diagonalizing the effective Hamiltonian $\mathcal{H}$:

$$\mathcal{H} = \sum_{i=1}^{N}\mathcal{H}_D(i) + \sum_{i<j}^{N}\frac{1}{r_{ij}}, \tag{1.39}$$

with the single-electron Dirac operator $\mathcal{H}_D(i)$ for the ith electron in the potential field of the nucleus, assuming a pure Coulomb potential $-2Z/r_i$. In atomic units $\mathcal{H}_D(i)$ can be written as:

$$\mathcal{H}_D(i) = \alpha \cdot p_i + (\beta - 1) + V_{nuc}(r_i), \tag{1.40}$$

with the 4×4 Dirac matrices α and β, the electron momentum p_i and the nuclear potential $V_{nuc}(r_i)$ [106].

The configuration state functions (CSF) or, respectively, basis states ϕ_ν are the anti-symmetric sums of the product of N one-electron Dirac spinors $\varphi_{n\kappa m}$:

$$\varphi_{n\kappa m} = \frac{1}{r} \begin{pmatrix} P_{n\kappa}(r)\chi_{\kappa m}(\theta, \phi, \sigma) \\ iQ_{n\kappa}(r)\chi_{-\kappa m}(\theta, \phi, \sigma) \end{pmatrix}, \tag{1.41}$$

whereby the spinors $\varphi_{n\kappa m}$ are solutions of the Dirac equation for the central potential $V(r)$. $P_{n\kappa}(r)$ and $Q_{n\kappa}(r)$ represent the large or, respectively, the small components of the radial function, $\chi_{\kappa m}$ are the spin-angular functions:

$$\chi_{\kappa m}(\theta, \phi, \sigma) = \sum_{m_l, m_s} C\left(l \frac{1}{2} m_l m_s; jm\right) \mathcal{Y}_{lm}(\theta, \phi)\, \delta(m_s \mid \sigma), \tag{1.42}$$

n is the principle quantum number and m denotes the z-component of the total angular momentum j and the relativistic angular quantum number κ, which is connected to the orbital (l) and the angular (j) momentum via:

$$\kappa = (l - j)(2j + 1). \tag{1.43}$$

The energy of the configuration is minimized with the atomic-state functions Ψ, which are linear combinations of the CSFs and can be approximated by mixing the basic states with the same symmetries:

$$\Psi = \sum_{\nu=1}^{N_{CSF}} b_\nu \Phi_\nu, \tag{1.44}$$

where b_ν represent the configuration mixing coefficients derived from the diagonalization of the total Hamiltonian in Eq. 1.40 by adding and subtracting the electron-electron electrostatic contributions $V^{ee}(r_i)$ to the central potentials $V(r_i)$. To cope with challenges like core-hole excitation, the usual approach is to build up the wave function stepwise starting from the configuration state only and subsequently adding more orbitals [111].

Chapter II

EXPERIMENTAL SETUP

2.1 The TRIUMF-ISAC facility

The Isotope Separator and Accelerator (ISAC) [112, 113] facility at TRIUMF in Vancouver, BC, Canada produces intense beams of exotic nuclei, which are produced via proton spallation reactions on thick, stable targets [114] capable of withstanding the high-power and high-intensity (up to 100 μA) proton beam at an energy of up to 480 MeV. To purify the Rare Isotope Beams (RIBs) and to make them accessible for various experiments at TRIUMF, the isotope separation on-line (ISOL) technique is applied [115, 116].

The proton beam is generated and accelerated in a sector-focused H^- cyclotron, which has the potential to deliver a total of four separate proton beams at energies between 70 to 520 MeV [117], which is possible due to the acceleration of H^- ions. The electrons of the H^- ions are stripped off at extraction via 11 μm thick pyrolytic graphite foils leaving an H^+ beam. As a consequence of the polarity switch, the direction of the protons changes due to the magnetic field of the cyclotron. Thus, the protons are guided out of the cyclotron and extracted with high efficiency.

The caveat of accelerating H^- ions is their fragility, which limits the maximal usable magnetic-field strength to 0.58 T in order to prevent the ions from being dissociated. This limitations is compensated by larger orbits, which makes TRIUMF's cyclotron (diameter of $\sim$ 18 m) the largest cyclotron in the world [117].

For rare isotope beams, the production targets commonly used are UC_x, Ta, Nb, SiC and Zr [118]. The production targets are operated at high temperatures of up to 2300 °C to increase the diffusion of nuclei out of the production target [119]. Via a hot transfer tube, the isotopes are guided to the various ion source systems, where either a surface ionization source, a resonant laser ionization source (TRILIS) [120], an ion guide laser ion source (IGLIS) [121] or a Force Electron Beam Ion Arc Discharge (FEBIAD) source [122] are used

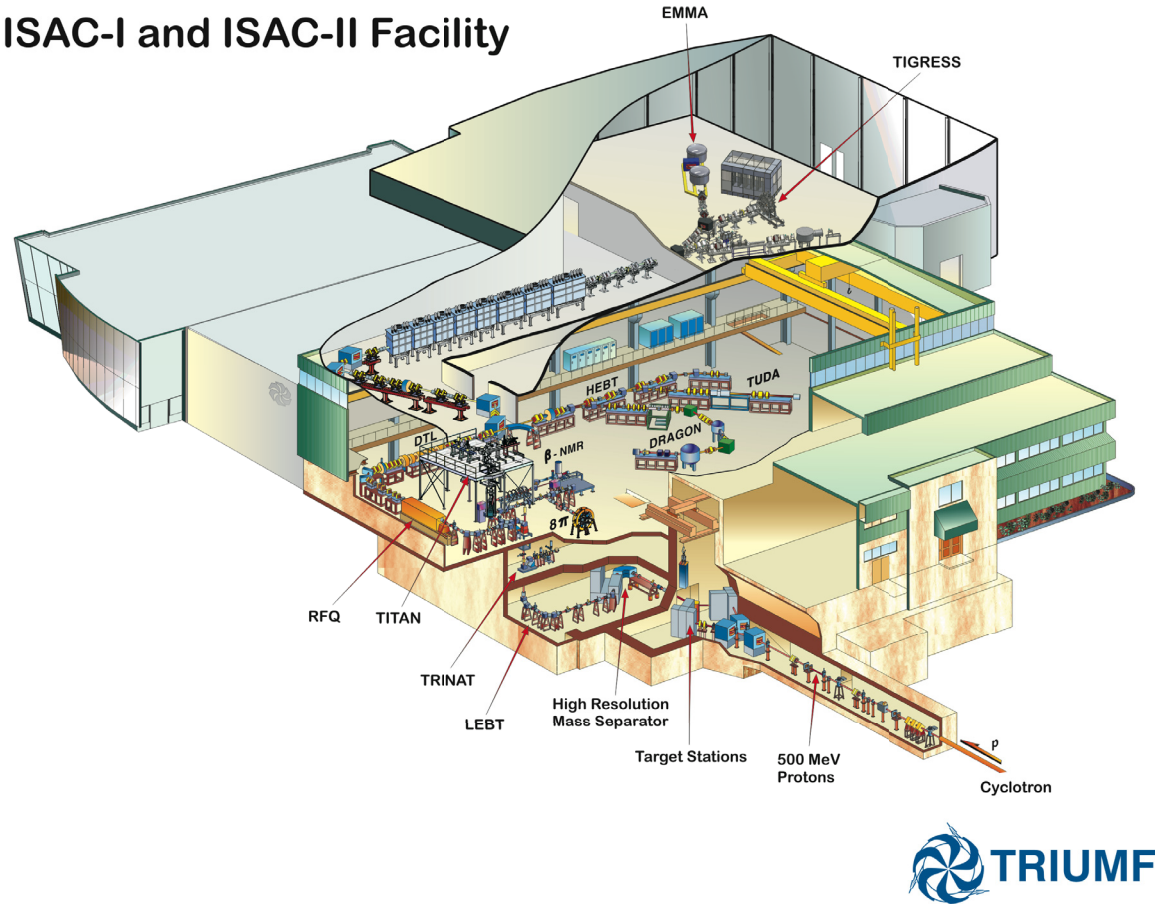

Figure 2.1: Schematic view of the ISAC facility at TRIUMF [124].

for ionization. The singly-charged radioactive ions are mass separated and then delivered to the experimental facilities at energies below 60 keV via an electrostatic beam transport system [123]. A schematic view of the ISAC facility is presented in Fig. 2.1.

2.2 The TITAN facility

TRIUMF's Ion Trap for Atomic and Nuclear science (TITAN) [125] is located in the low-energy region of the ISAC-I experimental hall. Currently the system consists of three ion traps, a buffer-gas filled radio-frequency-quadrupole (RFQ) [126] cooler and buncher, a high-precision mass measurement Penning trap (MPET) [127] featuring a 3.7 T magnet, and an electron-beam ion trap (EBIT) [128] for providing highly-charged ions (HCIs). In addition, the EBIT is used to store and to charge-breed ions for decay-spectroscopy experiments [129, 130]. Fig. 2.2 presents a schematic view of the TITAN system.

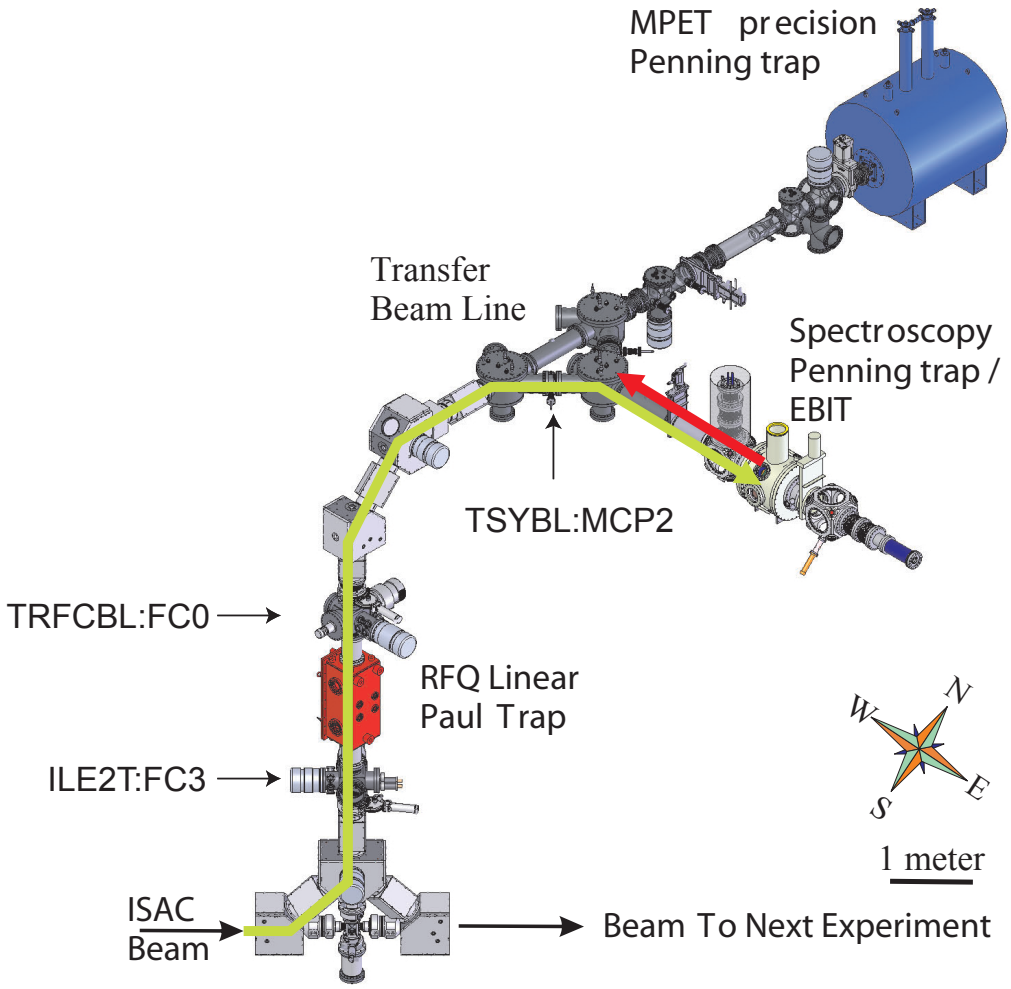

Figure 2.2: Schematic view of the TITAN facility. The cooled ion bunches from the RFQ are either send directly as singly-charged ions to MPET or first to the EBIT for charge breeding or decay-spectroscopy experiments. Figure adapted from Ref. [126].

The limited resolving power of the ISAC dipole magnet is insufficient for providing isobarically pure radioactive ion beams, which can make mass measurements as well as decay-spectroscopy experiments at TITAN extremely challenging.

The continuous beam produced at ISAC is delivered to the TITAN RFQ at ≈ 20 keV via the Low Energy Beam Transport (LEBT) system [123]. The RFQ high-voltage is matched to the energy of the radioactive ion beam, which is then decelerated and trapped transversely via a square-wave radio frequency that is applied to a total of four half-circular rods [126]. Collisions with an inert He-buffer gas at 2×10^2 mbar inside of the RFQ [126, 131] causes the ion beam to cool down to thermal energies. The bunched beam is then extracted from the pulse-drift tube at an energy of ≤ 2 keV and delivered either to MPET for a mass measurement or to the EBIT for charge-breeding or decay spectroscopy.

2.2.1 Measurement Penning trap (MPET)

The TITAN facility is primarily dedicated to the performance of high-precision mass measurements. The experimental data provided by the facility is used as input to various physics fields, such as nuclear structure [132] (shell closures [133, 134], island of inversion [134], shape coexistence, halo nuclei [135], etc.), astrophysics (abundance of stable elements, r-process, etc.) and particle physics (Standard Model, unitarity of the CKM matrix [136], Q-values in context with ν physics [79, 137, 138], $\beta\beta$ decay [79, 129], etc.).

TITAN is the "fastest" Penning trap system in the world, with the ability to measure isotopes with lifetimes of less than 10 ms [139], by applying the ion-cyclotron resonance time-of-flight (TOF-ICR) method [140, 141].

A 3.7 T superconducting solenoid magnet houses the hyperbolic Penning trap, where ions are confined by a combination of an electrostatic-quadrupole field and a magnetic field (compare Fig. 2.3 (left)). As a result of the Lorentz force, ions are forced on a circular orbit through which they are confined radially. The electric quadrupole field created by a DC voltage U_0 applied between the ring electrode and the two end caps provides axial confinement [109, 142, 143]. The ion motion inside of the trap is a superposition of three

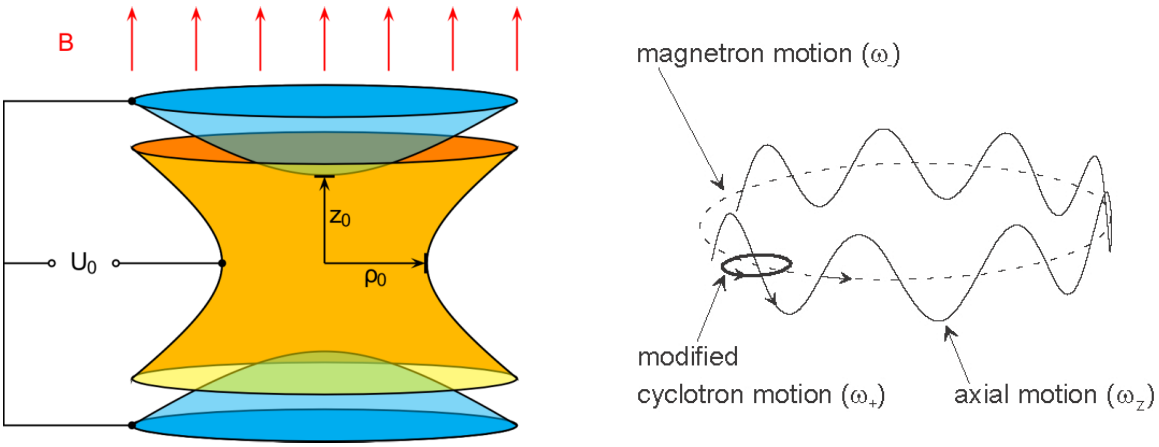

Figure 2.3: Left: Schematic view of a basic electrode configuration in a Penning trap. Ions are confined radially by the homogenous magnetic field, while axial confinement is realized by an electrical quadrupole field. Right: Schematic illustration of the three eigenmotions in a Penning trap. Figures adapted from Ref. [144].

harmonic eigenmotions characterized by their angular frequencies:

$$\nu_+ \gg \nu_z \gg \nu_-, \tag{2.1}$$

as indicated in Fig. 2.3 (right). Parallel to the magnetic field lines, the ions oscillate with the frequency ν_z:

$$\nu_z = \left(\frac{qeU_0}{m_i d^2}\right)^{1/2}, \tag{2.2}$$

where $d^2 = z_0^2/2 + \rho_0^2/4$ is the characteristic trap dimension. The cyclotron frequency ν_c is the sum of the magnetron motion ν_- and the reduced cyclotron motion (azimuthal drift) ν_+:

$$\nu_c = \nu_+ + \nu_-, \tag{2.3}$$

with

$$\nu_\pm = \frac{1}{2}\left[\nu_c \pm \left(\nu_c^2 - 2\nu_z^2\right)^{1/2}\right]. \tag{2.4}$$

By measuring the ions cyclotron frequency ν_c,

$$\nu_c = \frac{1}{2\pi} \cdot \frac{q}{m} \cdot B, \tag{2.5}$$

the mass of the ion can be extracted by performing a resonance scan with a varying RF-excitation frequency where the associated TOF is measured. The minimum of the TOF-resonance corresponds to the cyclotron frequency.

To eliminate the uncertainty of the magnetic field, the mass of a well known reference ion is measured before and after the mass of the radioactive ion of interest and linearly interpolated to the measurement time of the radioactive ion. For the cyclotron-frequency ratio one gets:

$$R = \frac{\nu_{ref}}{\nu_c} = \frac{m}{m_{ref}} \times \frac{q_{ref}}{q}, \tag{2.6}$$

where $\nu_{c(ref)}$ stands for the cyclotron frequency, $m_{(ref)}$ for the mass and $q_{(ref)}$ for the charge state of the (reference) ion. After including the electron-binding energies, the atomic mass can be determined from the ratio. The relative precision of the mass measurement is proportional to the charge state of the ion and can be approximated by the following formula:

$$\frac{\delta m}{m} \propto \frac{1}{q \cdot B \cdot T_{RF} \cdot \sqrt{N}}, \tag{2.7}$$

where T_{RF} stands for the excitation time in the magnetic field B, and N represents the number of measurements. The achieved precision $\delta m/m$ is typically around 10^{-7}-10^{-9}.

2.2.2 The Electron-Beam Ion Trap (EBIT)

The main purpose of the electron-beam ion trap is to create highly-charged ions (HCIs) via electron-impact ionization utilizing an intense electron beam. Since the precision of a mass measurement in a Penning trap is proportional to the charge state q (compare Eq. 2.7), the former can be increased by performing a mass measurement on HCIs.

The EBIT is essentially composed of three parts: a 500 mA electron gun, a cold drift-tube assembly, which is thermally coupled to a superconducting magnet, and an electron collector. A two-stage Gifford-McMahon helium cryo-cooler is used to cool the superconducting magnet down to temperatures <6 K via a compressor unit, which delivers high-pressure helium gas to the cold-head and recompresses the returned gas [128]. Fig. 2.4 shows a technical illustration of the EBIT, where the trajectories of the injected and extracted ion-bunches are indicated.

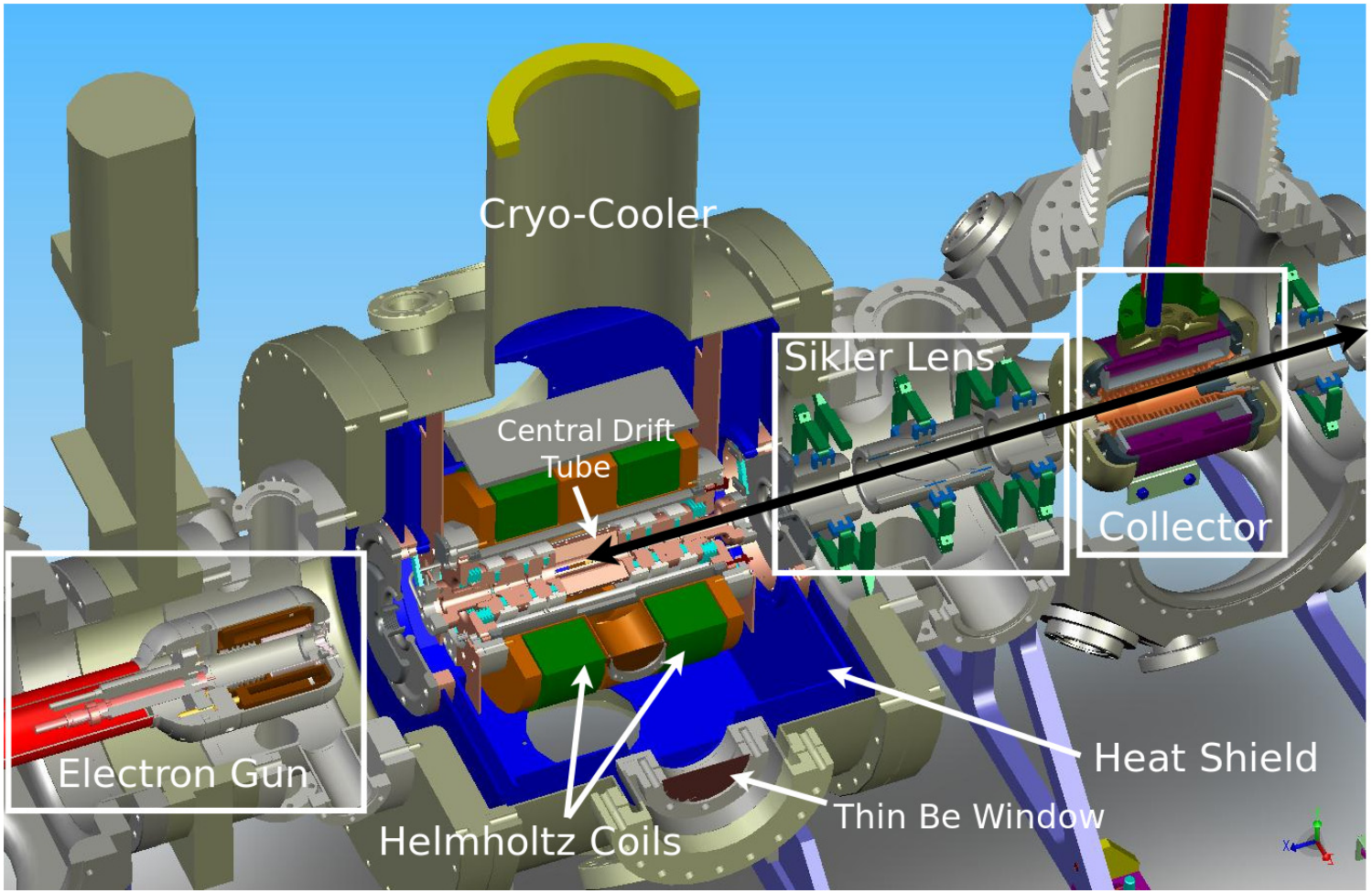

Figure 2.4: Illustration of the TITAN electron-beam ion-trap (EBIT). The black double-arrow indicates the trajectories of the ion-bunches for extraction and injection. Figure taken from Ref. [130].

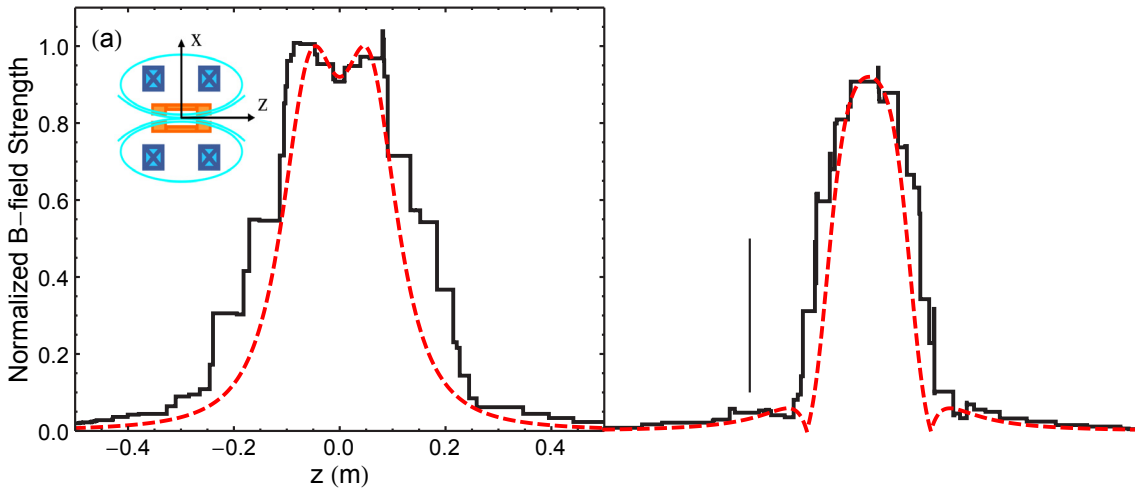
(a)
x
z
Normalized B−field Strength
1.0
0.8
0.6
0.4
0.2
0.0
−0.4
−0.2
0.0
0.2
0.4
z (m)

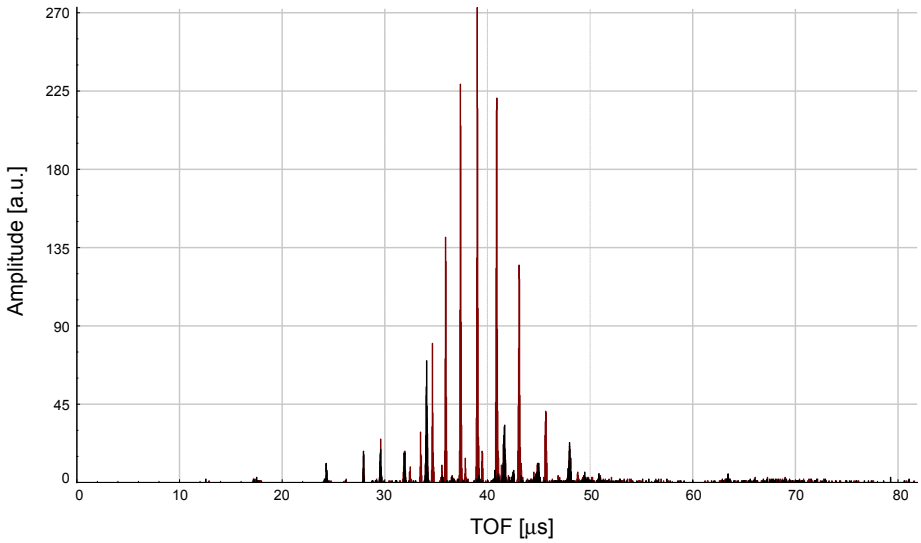

Figure 2.6: Arbitrary charge-state distribution presented as a function of the TOF.

Via electron-impact ionization, the injected singly charged ions are ionized to higher atomic charge states until an equilibrium with ion loss processes, i.e., electron capture, is reached, or until the ions are extracted from the trap [109]. Ionization times depend on the electron-beam current density and the charge state and are of the order of a few 100 ms in the TITAN EBIT. The average time $\tau_i(q)$ for creating a charged ion with the charge state q starting from the neutral atom by stripping of the electrons is given by [109]:

$$\tau_i(q) = \sum_{q'=0}^{q-1} \langle n_e v_e \sigma^I_{q',q'+1} \rangle^{-1}, \tag{2.8}$$

with the electron density n_e and the cross section $\sigma^I_{q',q'+1}$ for single ionization.

In general, the EBIT does not produce a single atomic charge state but rather a charge-state distribution. By threshold-charge breeding the ions, which can be applied whenever there is a large difference in the ionization energies of two charge states, the EBIT parameters can be set accordingly to primarily populate the threshold charge state. This technique is usually applied for ions at closed atomic shells (K- and L-shell).

The charge-state equilibrium distribution depends on the electron-beam energy, its current density, as well as on the ionization time and the vacuum conditions. For monitoring purposes, the ions are send to a micro-channel plate (MCP) located downstream of the

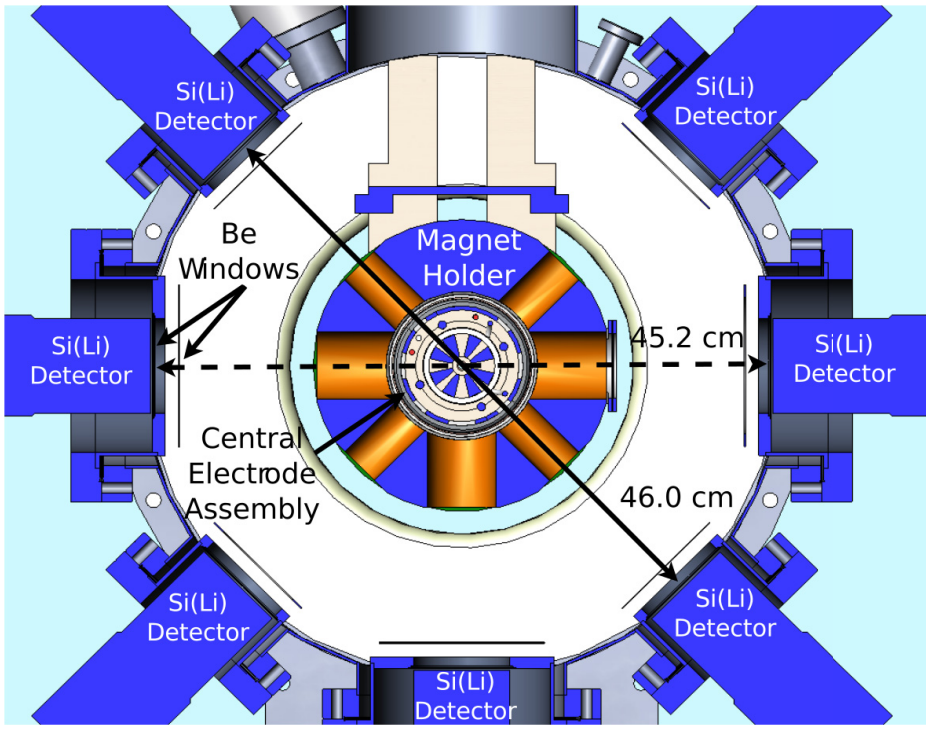

Figure 2.7: Cross-sectional view of the EBIT. The outer housing features seven access ports for the Si(Li) detectors. The trap center consists of the central electrode and the magnet-coil holder inside the vacuum vessel [130].

RFQ and detected after each trapping cycle. For illustration purposes, a measured charge-state distribution for ^{116}Cd upon extraction from the EBIT is presented in Fig. 2.6.

2.3 The TITAN-EC decay-spectroscopy setup

The present setup employs the EBIT as a spectroscopy Penning trap [149], which, apart from storing ions backing-free in a magnetic field of up to 6 T, offers the possibility to perform in-trap decay spectroscopy through seven open-access ports that are separated from each other by 45° with a 35.0 mm radius opening.

The use of a trap for ion storage instead of a target on a backing material minimizes the ambient background and the isobaric and isotopic contamination, which is a common problem limiting the sensitivity of tape-station techniques. Photon detectors can be mounted on the access ports in close geometry (226 mm or 230 mm) to the trap center (see Fig. 2.7), which results in a total geometrical acceptance of $\sim$ 2.1% for seven detectors compared to only 0.08% in the previous setup of Ref. [146, 150] with only one low-energy germanium

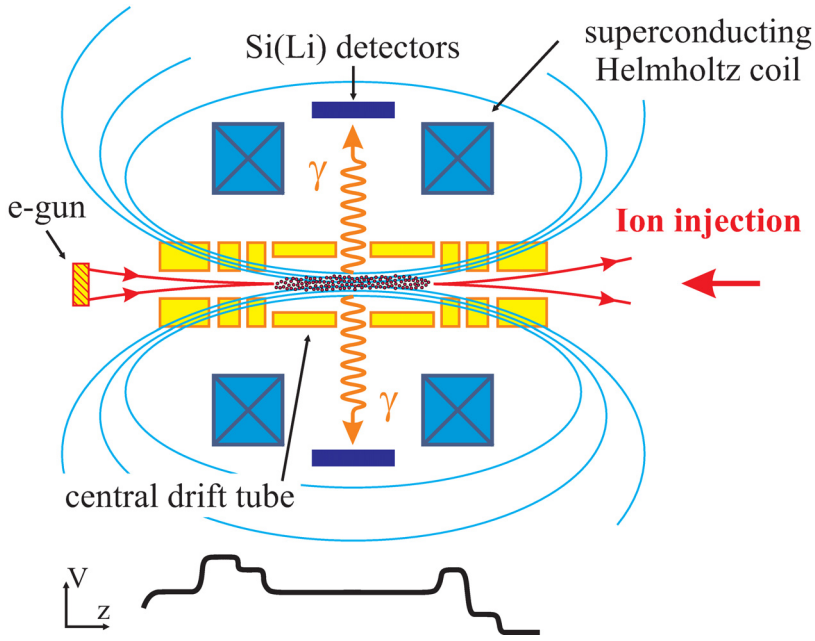

Figure 2.8: Schematic drawing of the EC branching-ratio measurement setup. X-rays following EC decays inside the trap are detected by the Si(Li) or HPGe detectors, while electrons are guided out of the trap along axis by the magnetic field. Figure has been modified from the version in Ref. [146].

detector. The presence of the magnetic field offers the additional advantage that electrons or positrons from the β^- or β^+ decays follow the magnetic field lines and are directed on axis out of the trap and away from the EBIT surrounding detectors as displayed in Fig. 2.8. This spatial separation of X-rays and β-decay induced particles reduces the background significantly and increases the sensitivity for measuring low-intensity X-rays and weak electron-capture branching ratios. The condition for β particles (β^+/β^-) originating from radioactive decay inside the trap to escape the trap volume is a larger emission angle than critical trapping angle. The latter depends on the ratio between the magnetic field at the origin of the electron path and the maximal $\vec{B}$-field [130]. A realistic simulation requires a relativistic approach. However, non-relativistic SIMION [151] simulations suggest that $\sim$ 77% of the decay electrons have an emission angle large enough to escape the trap center. Additionally, the cyclotron frequency for electrons in a high magnetic field is significantly increased ($\sim$ 10 - 100 GHz), which results in a higher scattering probability with the ion cloud [152]. Due to the high scattering probability, the β particles are slowed and cooled down. Therefore, the majority of the charged decay products do not possess a high enough

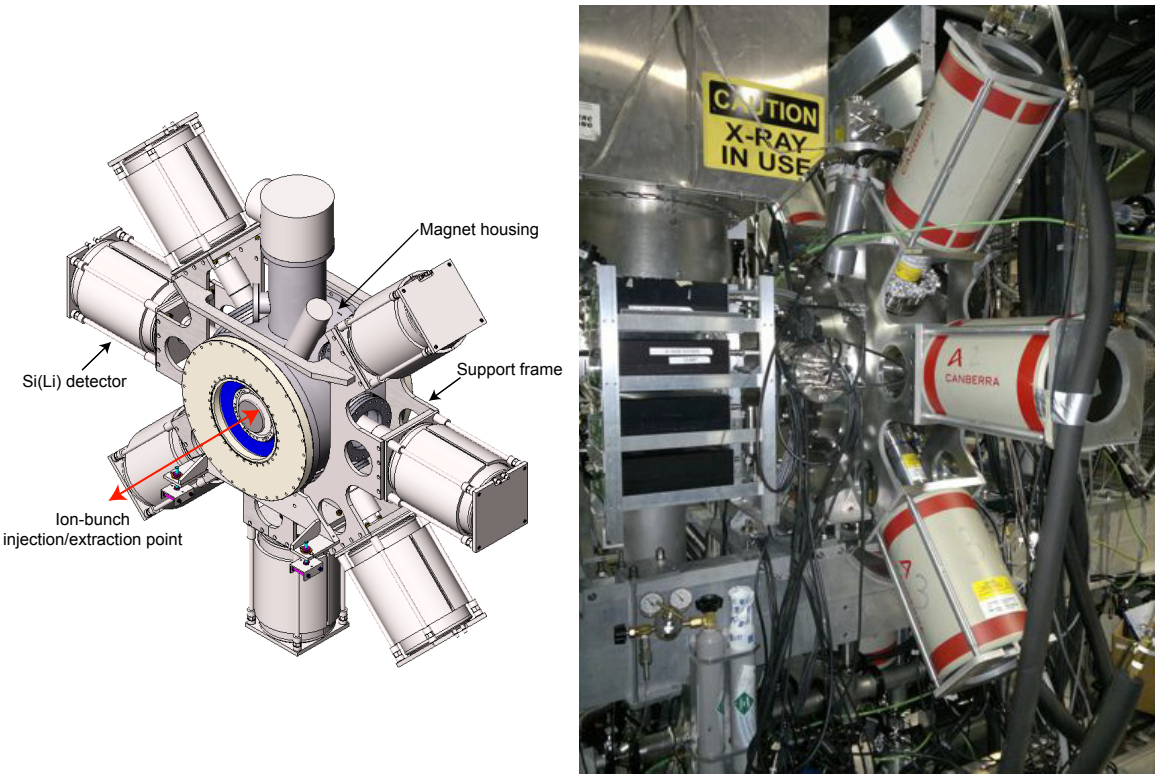

Figure 2.9: Left: Technical drawing of the decay-spectroscopy setup located around the EBIT. The seven Si(Li) detectors are mounted perpendicular to the beam axis [130]. Right: Photo of the TITAN-EC setup, showing Si(Li) detectors mounted around the EBIT.

energy to leave the trap center and are discharged from the trap. Consequently, the majority of the β decay products are guided on axis out of the trap volume, which leads to a suppression of 511 keV positron annihilation background from inside the trap. The efficient suppression was observed in the commissioning experiment described in Sec. 5.5.6.

Another advantage of the decay-spectroscopy setup at TITAN is the provision of rare and intense radioactive beams by ISAC. The location of the setup in combination with the low-background environment provides a unique opportunity to perform decay spectroscopy.
The present setup features six Si(Li) detectors for X-ray detection and one HPGe detector for γ-ray detection, which are described in detail in Ch. 3, and are mounted perpendicular to the beam axis around the trap center. The Si(Li) detectors occupy the 45°, 90°, 135°, 180° (bottom of the trap), 270° and 315° ports as presented in Fig. 2.9.
To minimize the X-ray absorption on their way towards the detectors, ultra-thin (0.25 mm

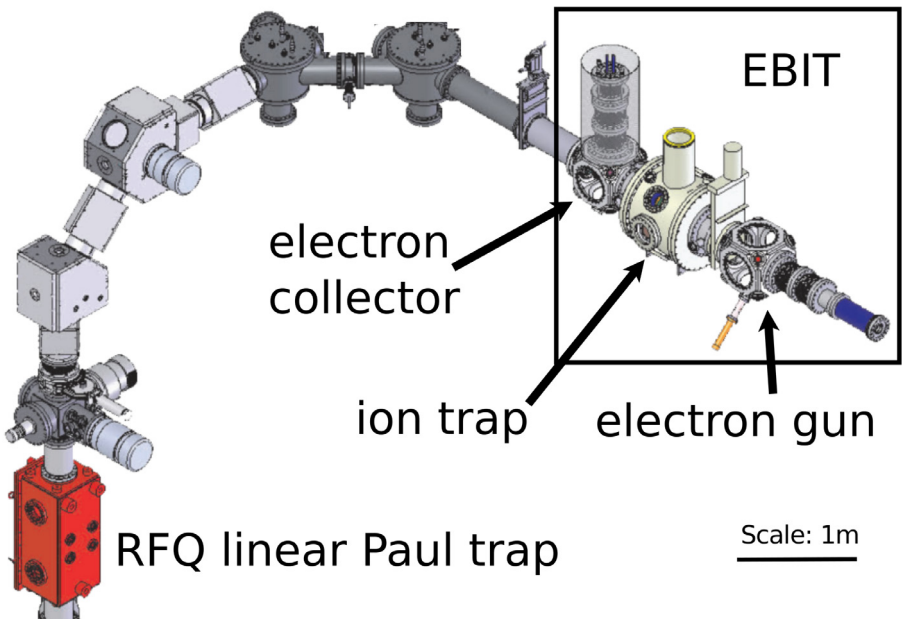

Figure 2.10: The beam-line and the two ion traps, which are operated during an in-trap decay spectroscopy experiment. After ion-bunch extraction from the RFQ, the singly charged ions are injected into the EBIT, where they are charge-bred and stored for decay spectroscopy. Figure is taken from Ref. [153].

thickness), high-purity ($\leq 99\%$) and pinhole-free Be-windows have been installed as vacuum barriers and heat shields. A second Be-window of 0.08 mm thickness is installed as internal heat shield of the trap for each port.

The 225°-port can be occupied by a HPGe detector of 40 mm thickness at a ~ 30 cm distance between the crystal and the outer Be-window. This detector can be used for monitoring purposes and for measuring γ-rays, which accompany the nuclear decays in the EBIT trap. Figure 2.9 shows a photo of the TITAN-EC Si(Li) detector array.

2.3.1 EBIT operation and ion storage

A decay-spectroscopy experiment requires the use of two ion traps of the TITAN system, the RFQ and the EBIT (Fig. 2.10). After extracting cooled ion bunches from the RFQ, the singly-charged ions are injected into the EBIT, where they are confined, charge-bred and trapped. Storage times of the order of minutes are possible [129] due to the efficient confinement provided by the use of the electron-beam.

Long trapping times, however, require controlling the thermal energy of the ions. Mechanisms like elastic electron-ion collisions, ionization heating initiated by the change of the charge state of the ion in the potential well or plasma instabilities cause the heating of heavy ions in the trap with the rate [109]:

$$\frac{dE_q}{dt} = \frac{0.442q^2 j_e \ln(\rho_{max}/\rho_{min}) n_q}{AE_e}\ eVs^{-1}cm^{-3}, \tag{2.9}$$

where n_q stands for the number density of the ions and A represents the atomic mass number. ρ_{max} and ρ_{min} are the maximum or respectively minimum impact parameters, where ρ_{max} is equal to the Debye length or the electron-beam diameter. $\frac{dE_q}{dt}$ can be on the order of a few keV per second for each ion, and the potential depth of the trap is less than 1 keV. Efficient cooling is therefore essential for long storage times at minimal ion losses and is realized by the evaporative cooling technique. These effects are described in detail in Ref. [109].

The ion-trapping capacity of the EBIT is determined by the compensation of the negative space charge of the electron beam by the highly positively charged ions [154]. In case of the TITAN EBIT, the maximum space charge in the central trap region is about 10^9 e for an electron beam with an intensity of typically 100 mA and an energy of 1.7 keV (used for the experiment on ^{116}In described in Ch. 4 and Ch. 5). For example, the maximum number of highly-charged ions in the trap for an average charge-state of $q \approx 25^+$ is roughly $\geq 10^7$ ions [145].

The main ion-loss mechanism is the so called "axial evaporation", which can be regulated by applying voltage to the central drift tubes [109]. As the cathode emits materials like barium or tungsten, those materials are always present in the trap, which leads to higher evaporative losses for elements lighter than Z=50 [109].

The programmable pulse-generator (PPG) of the EBIT allows controlling the cycles via logic signals, which regulate the drift-tube electrodes of the EBIT. During a decay-spectroscopy experiment, the EBIT cycle is divided into four parts: ion injection, storage/trapping and extraction followed by an empty-trap background measurement. Each event detected in the

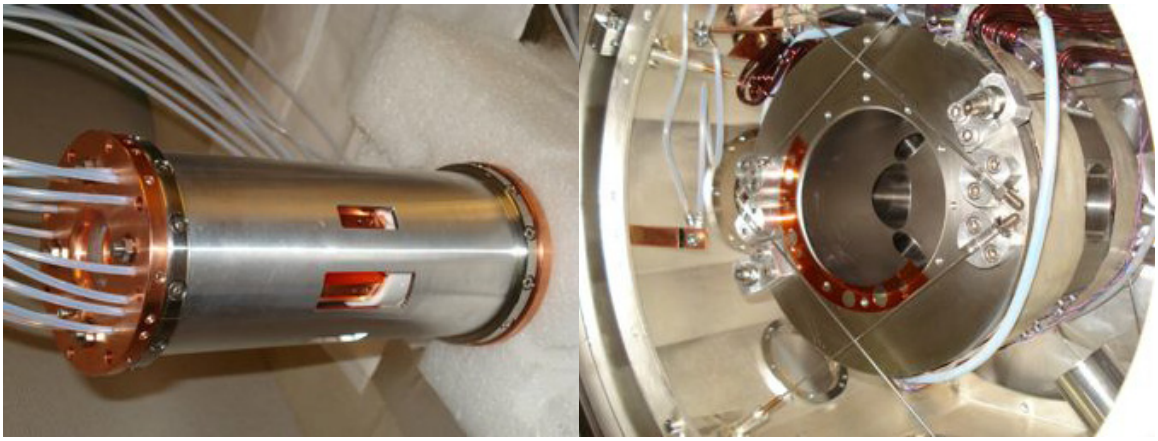

Figure 2.11: Left: Photo of the opening slits in the EBIT central drift tube housing also operating as heat shield. As can be observed, the slits for the small acceptance ports are smaller than for the large acceptance ports, resulting in a decrease of acceptance for the former. Right: Coil holder [155].

Si(Li)s is time-stamped (see Sec. 3.4), which can be accomplished via a correlation of the EBIT PPG and the ADC clock of the DAQ. Depending on the half-life of the investigated ion species, the EBIT trapping cycles can be adjusted. Typical storage times vary from tens of seconds up to minutes.

2.3.2 Geometric acceptance

During the ^{124}Cs commissioning experiment (see Ch. 4.1) a decrease of geometric acceptance of roughly a factor of 2 for the detectors that were mounted on the small acceptance ports compared to the ones on the larger acceptance ports was noticed, which manifested itself in a smaller absolute detection efficiency. Re-examining the geometry revealed that two components effectively limit the acceptance:

1. the size of the slits in the housing cylinder of the central drift tube of the EBIT shown on the left in Fig. 2.11, and

2. the magnetic-coil holder as displayed in the photo on the right in Fig. 2.11.

In order to perform in-trap decay spectroscopy, the cylinder covering the electrode, which functions as a heat shield, has been designed with seven longitudinal slits parallel to the drift-tube along the axis. The slits for the small acceptance ports are smaller than for the large acceptance ports, in horizontal as well as in vertical direction, which limits the

acceptance.

In order to understand the relation between acceptance and trap geometry in dependence of the source distribution, eight sets of simulations [156] with three different ^{133}Ba-source distributions:

- an ideal point-like source in the trap center,
- a realistic source distribution on-axis spread 60 mm along the beam axis,
- and a 1 mm^3 cubic source in the trap center,

and three different geometries, i.e., varying combinations of coil-holder and cylinder:

- all volumes included,
- with the removal of either the coil holder or the cylinder,
- and all volumes removed,

in order to determine which parts of the geometry limit the acceptance the most, were generated. The results are presented in Fig. 2.12 and Fig. 2.13. Each figure shows four panels, each presenting an overlay of Monte-Carlo simulated ^{133}Ba spectra for a detector mounted on a small acceptance port (blue curve) and a large acceptance (black curve) port within an energy region of 25 keV to 50 keV to illustrate the X-ray region. The inset in each panel displays the energy region from 70 keV to 90 keV to show the 81 keV γ-transition.

For the point-like source (Fig. 2.12 top) as well as for the cubic source (Fig. 2.12 bottom), the acceptance for both types of ports is comparable independent of the geometry. For the realistic source distribution (Fig. 2.13) on the other hand, the acceptance is approximately a factor of 2 smaller for the small acceptance ports, independent of the energy, when both components are included in the geometry. By removing both, the cylinder and the coil holder one recovers most of the losses (see Fig. 2.13 bottom, left).

Even though the simulation shows that the large acceptance ports do not seem to experience any significant acceptance losses, one has to keep in mind that the real ion-cloud distribution might not be exactly on-axis, and up to 70 mm long, which is a limitation affecting

the smaller ports more than larger ports. Furthermore, the Monte-Carlo simulation does not account for possible misalignments, as all materials and electrodes are input exactly according to the design drawings.

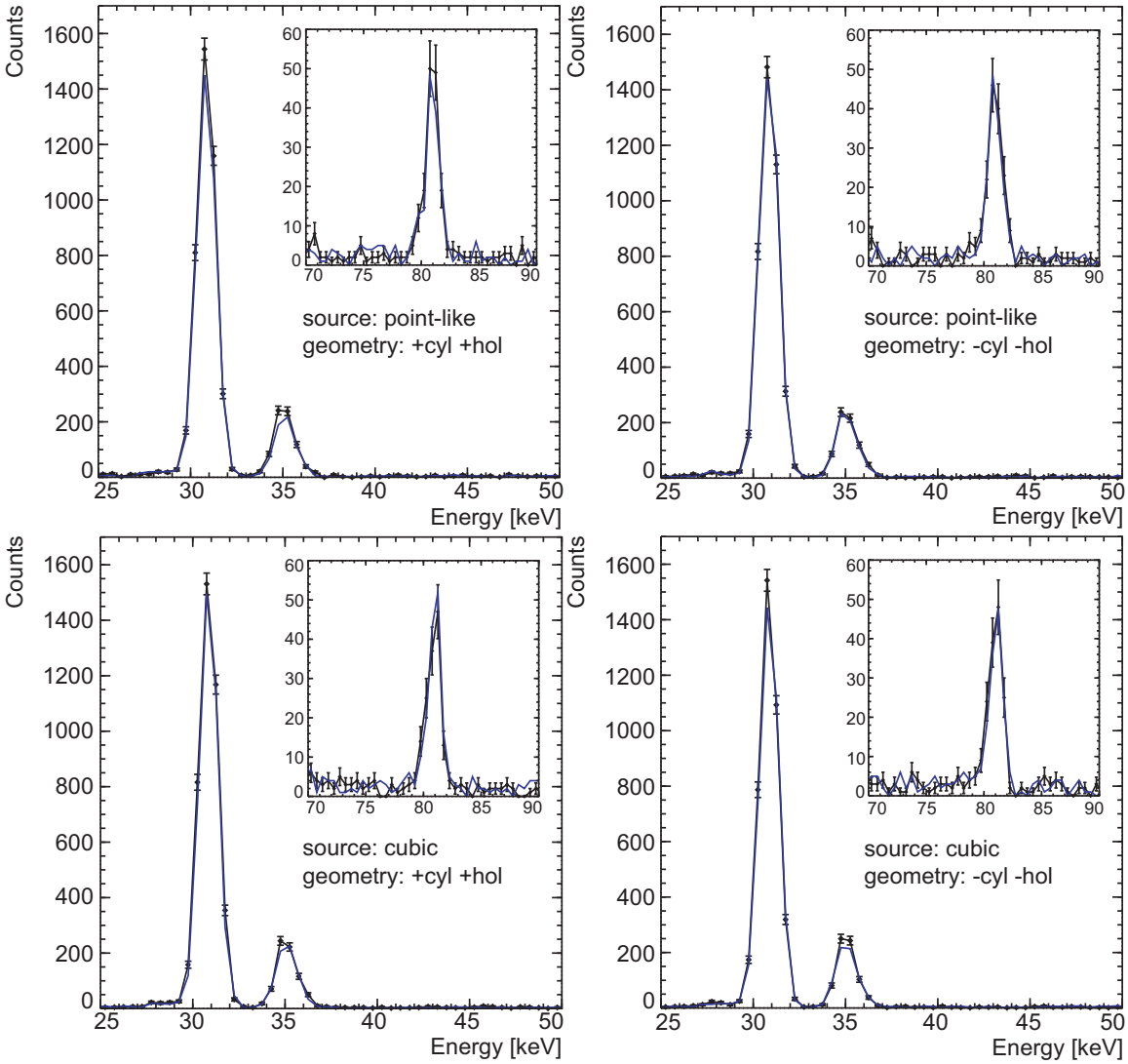

Figure 2.12: Simulations for a point-like ion source (top) as well as for the cubic source (bottom) with two different cylinder and coil-holder combinations. The black curve represents the detector on a large acceptance port and the simulation for a Si(Li) on a small acceptance port is shown in blue. All spectra were normalized to each other [156].

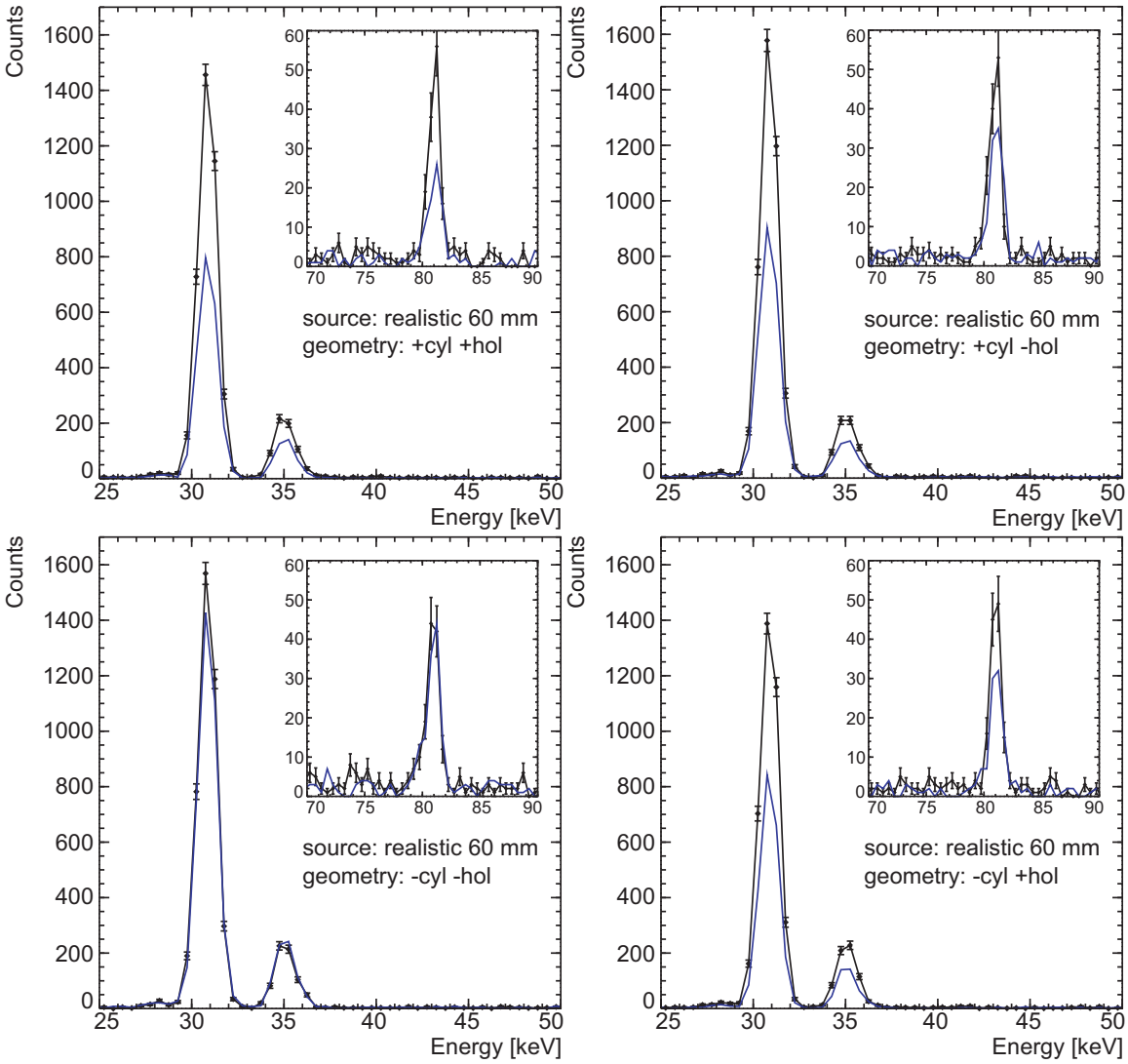

Figure 2.13: Shown are the simulations for the source distribution with a 60 mm ion-cloud length for four different coil-holder and cylinder combinations. The black curve represents the detector on a large acceptance port and the simulation for a Si(Li) on a small acceptance port is shown in blue. All spectra were normalized to each other [156].

Chapter III

LITHIUM-DRIFTED SILICON (SI(LI)) DETECTORS

In this chapter the performance tests and experiences with the previously introduced X-ray detectors and their specifications are described in detail, before the commissioning experiments as well as the data analysis are outlined in the following chapters.

Lithium-drifted silicon detectors (Si(Li) detectors) are p-i-n junction detectors formed by lithium compensation or by slowly drifting lithium into the silicon crystal lattice [157]. The depletion depth of pure silicon detectors is limited to only 1-2 mm, which is the reason for the use of lithium-drifted silicon detectors, where the crystal thickness is merely limited by the distance over which the lithium drifting can be applied [157]. The drift process is realized by applying a reverse bias to a p-n junction which consists of a lithium-diffused n-type region on top of p-type silicon. The bias causes the lithium ions to drift towards the negative side where the negative ions, fixed in the silicon crystal lattice, are compensated and a wide depletion layer can be generated. Typically, Si(Li) detectors are manufactured in a planar geometry, where the lithium is drifted from the flat surface of a silicon wafer. The large entrance surface provided by the planar configuration is beneficial for the detection of X-rays or electrons [157].

The drifting process for the detectors described in this chapter was performed at a temperature of 105 °C and a voltage of 400 V, which led to a drift velocity of $4{\times}10^{-10}$ m/s [158]. For photon energies below $\sim$ 30 keV, the detection efficiency for Si(Li) detectors is comparable to the efficiency of high-purity germanium (HPGe) detectors. For MeV-scale photon energies, however, the efficiency of HPGe is roughly three orders of magnitude higher, which is due to the higher atomic number of germanium (Z=32) compared to silicon (Z=14).

For low-energy γ- or X-rays, which are of primary interest for the experiments discussed in this thesis, the photoelectric-absorption cross section is relatively high, even for thin Si(Li) detectors of only a few millimeters thickness. At the same time, the Compton background

in the low-energy region is reduced significantly because of the lower Z [157]. In addition, the X-ray escape peaks for silicon are much reduced since the characteristic X-rays at 1.8 keV are less likely to escape the crystal volume than germanium X-rays between ∼10 and ∼11 keV. The ratio of full-energy peak to escape peak is therefore 2-3 orders of magnitude higher for Si(Li) detectors than for HPGe detectors. Further, the K_α X-ray energy for germanium is close to the X-ray region of interest for electron-capture branching-ratio measurements of the cases proposed in Ref. [75].

Therefore, Si(Li) detectors are a suitable tool for performing low-energy γ- or X-ray spectroscopy in a low-background environment and have thus been chosen for the detector array of the decay-spectroscopy apparatus at TITAN.

3.1 Specifications

The seven custom-made planar Si(Li) X-ray detectors used in the decay-spectroscopy array were designed and manufactured by Canberra, France [158]. Each detector features a 5 mm thick Si(Li) crystal with a $\lesssim 0.2$ μm thick dead-layer and an active surface area of 2000 mm^2. Figure 3.1 shows a schematic drawing of the typical cross-sectional view of the detector chamber. A carbon window of 0.6(1) mm thickness operates as a vacuum shield and is followed by a 3 mm wide vacuum zone, behind which the 5 mm thick Si(Li) crystal is located.

The detector-electronics housings mainly consists of aluminum, except for the polyoxymethylen (delrin) section that supports the polychlorotrifluoroethene (PTFCE) contact, between the cold finger and the crystal. The volumes around the crystal function as back-plate and support ring of the crystal and are made out of aluminum type 2017 [159], where the HV connection to the aluminum ring is also maintained with aluminum. The diode features a female aluminum connector, which is plugged into a copper cold finger, and the connection to the crystal is made by a spring which is constructed of beryllium coated with gold and connects to a plastic cover shield with a feed-through to connect to the junction gate field-effect transistor (JFET). The spring-load adjusts for thermal expansion and contraction. The spring is sensitive to high and medium frequency microphonia and any

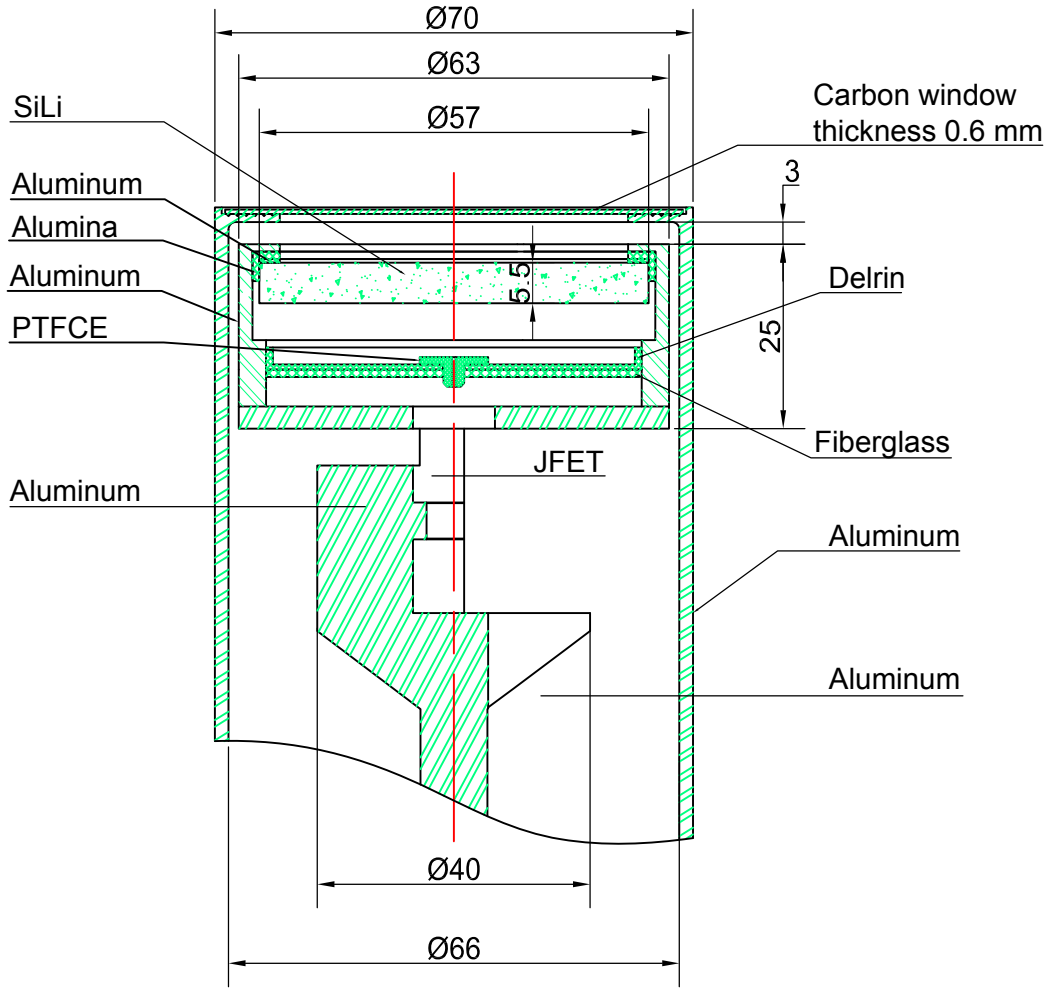

Figure 3.1: Cross section of a Si(Li) detector chamber. The dimensions are given in mm. Figure originally provided by Canberra, France [158].

disturbance leads to a change in the entrance capacitance directly influencing the signal. To overcome this, a thin layer of indium ($\sim$ 0.1 mm) is used for mechanical stability. In order to prevent a contamination of the spectra with fluorescent indium X-rays resulting from activated material next to the crystal, the indium was initially not implemented into the detectors with the serial numbers #431, #432, #438. However, since this caused significant microphonia in the detector output signals, and deteriorated the performance, the indium was implemented for those detector at a later stage as well.

The section where the JFET is located as well as the region around the cold finger are also fabricated of aluminum type 2017. The position of the FET close to the cold finger is prescribed, as good energy resolution at low energies requires noise reduction and consequently lowering the temperature of the JFET input stage of the preamplifier. The bottom part of the detector housing holds the cabling for all electronics, i.e., pulsed-reset preamplifier, JFET, alarm card (40×30×10 mm^3) and main card (60×40×10 mm^3) as presented in Fig. 3.2. A GEANT4 representation of the detector housing designed according to the above given information and the drawing in Fig. 3.1 is presented in Fig. 3.3. Detailed knowledge about the utilized materials is crucial to understand the sources of photon backscattering within the detector chamber.

3.2 Pulsed-reset preamplifier and output signals

Each Si(Li) detector features a transistor-reset preamplifier, which is a type of preamplifier that was originally developed to eliminate the noise contributions of the usually employed preamplifier feedback resistors, while improving the high count-rate capability [160, 161]. The feedback resistor is replaced by a feedback device, which is only switched on for the short time period ($\sim$ 1 μs) needed to reset the preamplifier output back to the baseline. A typical reset signal is presented in Fig. 3.4.

In resistive feedback amplifiers the charge accumulated at the feedback capacitor is removed between the detector events. As this function does not exist for transistor-reset amplifiers, each event, as well as the charge caused by the current leakage of the sensor material, causes an increase in the DC voltage of the preamplifier output. Thus, the accumulated charge

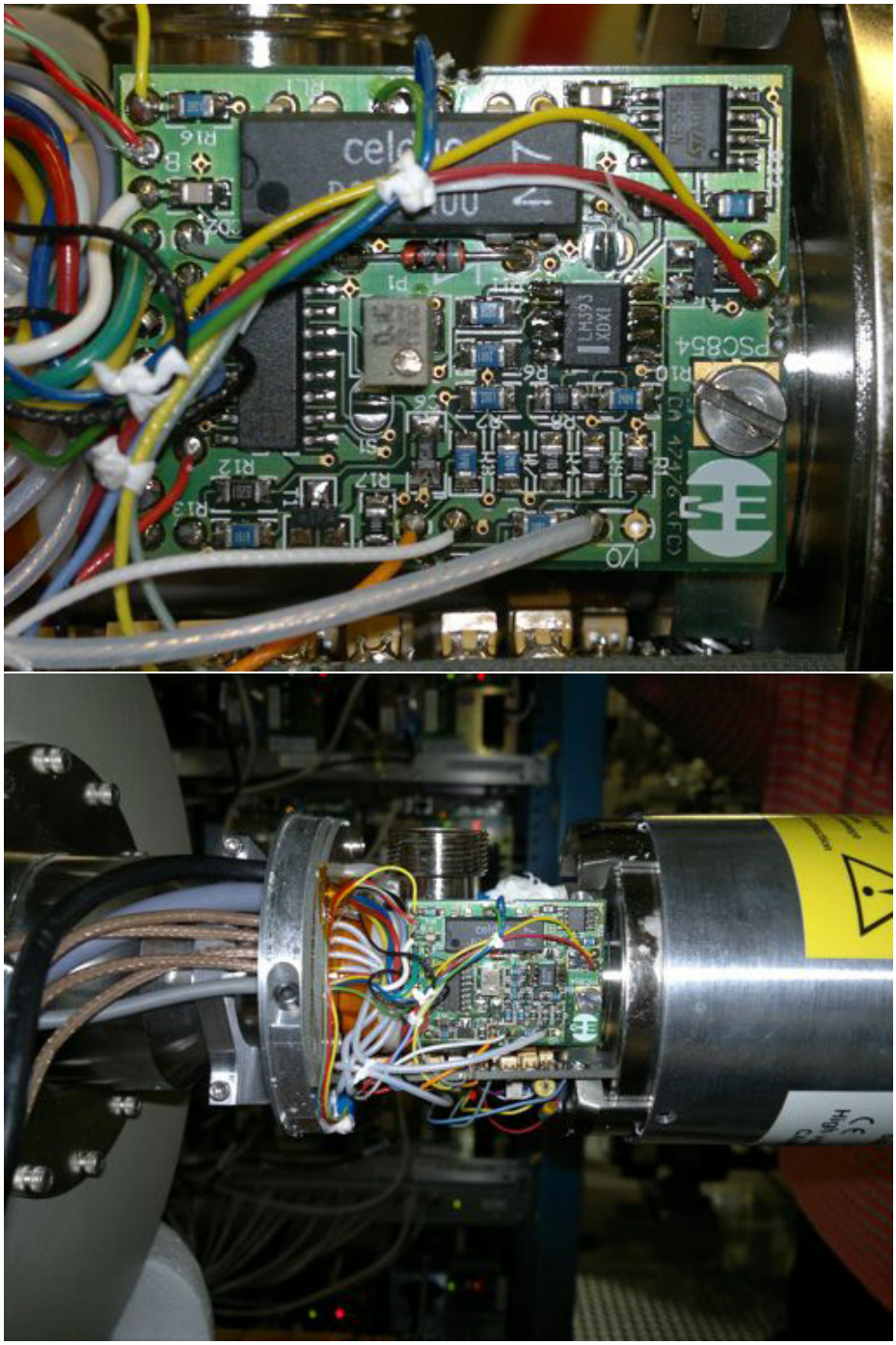

Figure 3.2: Top: Photo of the main card of the Si(Li)-detector electronics. Bottom: Photo of an open pre-amplifier electronics housing.

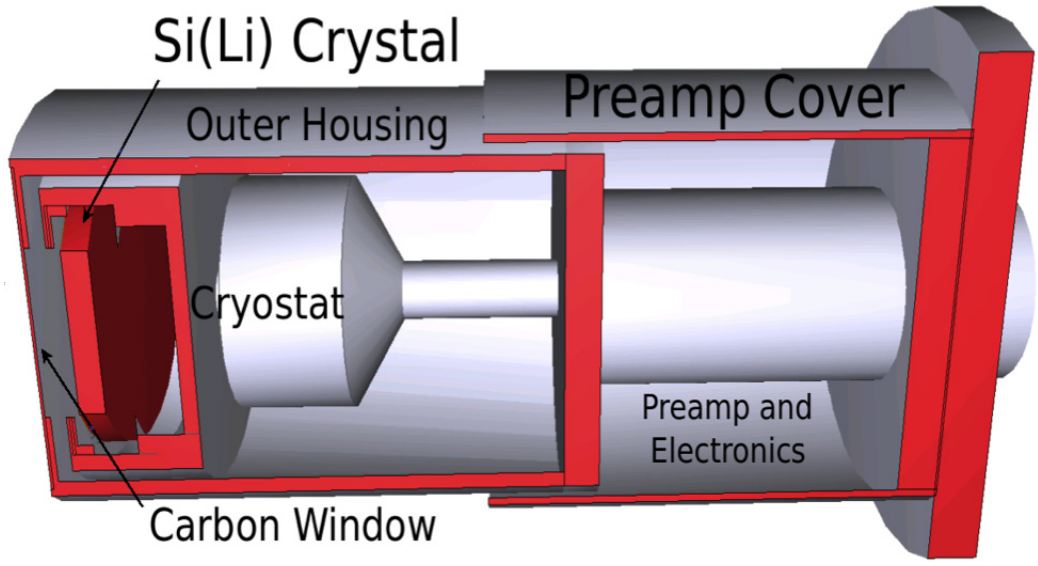

Figure 3.3: GEANT4 geometry of the detector and its housing [156].

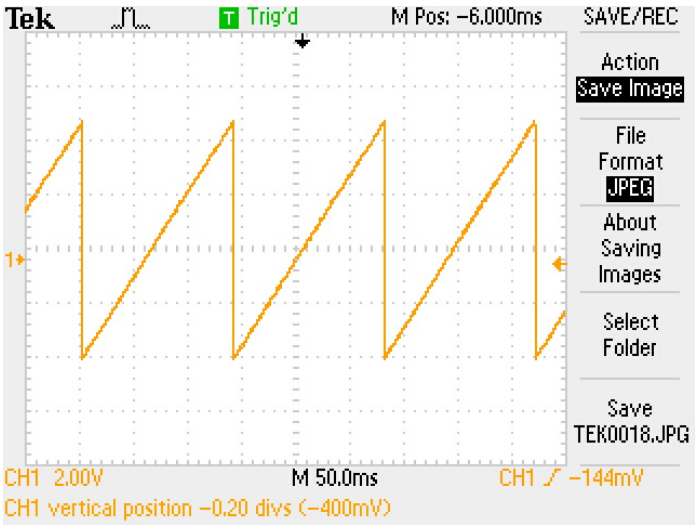

Figure 3.4: Direct transistor-reset signal. The steadily increasing voltage ramp caused by charge build-up due to the leakage current is superimposed by sharp steps originating from the charge created by photon events. Those steps are of the order of a few μV and not visible on this scale.

has to be periodically reset in order to prevent a saturation of the preamplifier. At a predetermined charge level, the voltage across the feedback capacitor is reset to the baseline by a voltage comparator. For the Si(Li) detectors discussed here, the reset occurs among a voltage drop of 4.5 V. This allows for linear operation of the preamplifier output even at high count rates, whereby the count-rate maximum and the rise time is defined by the percent dead time based on the reset. With increasing count rate, the reset rate has to increase as well, which eventually leads to a too high percentage of dead time.

For energy measurements, the energy signal output of the preamplifier has to be connected to the input of the ADC via a 50 Ω BNC-to-BNC cable (CL85 type). In order to get output pulses with positive polarity, the polarity of the amplifier signal input has to be set accordingly [162].

The preamplifier also features a TEST input, which can be used to apply electronic signals to the detector input stage. However, the use of this function should be minimized since baseline disturbances at the amplifier output can degrade the energy resolution. Therefore, it was never used over the course of the work presented in this thesis.

An inhibit output signal (positive-logic TTL signal) has specifically been integrated for the pulsed-reset amplifier in order to locate disturbances at the amplifier output corresponding to the reset rate of the preamplifier and to prevent data collection during the reset time and reset recovery. The signal width is adjustable, and can be set according to the time constant.

3.3 Cryogenic operation

The Si(Li) detectors are operated at LN_2 temperature, whereby temperature gradients or long storage at room temperature are to be avoided as the lithium might slowly redistribute at room temperature. Due to the continuous release of gaseous nitrogen through the vent tube (about 2 liters a day), the individual LN_2 dewar of each detector with a capacity of 7 liters has to be filled every three days, which is accomplished via a partially automated ISAC-EPICS [163] controlled filling system. This system was designed at TRIUMF and installed on the TITAN platform in 2012.

The LN_2 manifold features 7 channels to cover all detectors installed around the EBIT, and two additional channels for an extension to automatically fill the MPET and CPET magnets in the future. This functionality is already implemented into the EPICS system. The system will be completely automated with the installation of the LN_2-transfer line in the ISAC I experimental hall in 2016 to fully automate the filling process.

A temperature sensitive LED at the detector output of each dewar operates as fill-stop indicator, for which the LED voltage is read out via the EPICS system. Once a dewar is full, liquid nitrogen is released from the cryostat output and cools down the LED. As a result its voltage increases and the valve for that particular channel is closed. The threshold voltage can be altered and is usually set to 4.5 V.

All detectors are equipped with another indicator LED, which provides information about the cooling status of the detector crystal. A flashing red light signals that the detector is warm and ready to be cooled down, a solid red light on the other hand indicates that the detector is in the process of warming up and cannot be filled until the red light flashes again. The detector is cold when the red LED is off completely. That LED signal is read out by EPICS and directly connected to the high-voltage (HV) power supply. In the case a detector warms up while it is under high voltage, an interlock system ramps down the voltage to zero automatically in order to prevent damage to the crystal.

A green LED indicates the preamplifier-reset rate and remains off or flashes at a low frequency as long as the detectors remain unbiased. During the high-voltage ramp-up, the LED flashes at high frequencies of the order of kHz until the desired voltage is reached and the reset rate settles at around 20-40 Hz depending on the detector. At roughly -100 V, the feedback capacitor starts initiating the reset process. The preamplifier-reset frequency can be monitored via the INHIBIT output signal. A frequency of $\sim$100 Hz or more without a radioactive source indicates excessive reverse current.

3.4 Power Supplies and DAQ

To limit the fluctuations of the low-voltage power for the detector electronics and preamplifier to $\approx$ 1 mV, the power is regulated by a DC $\pm$28 V power supply. Passively cooled

linear voltage regulators provide voltages of DC ±12 and ±24 V individually for each detector [130], which run stable to ∼ 1 mV. The Si(Li) crystals are biased to a voltage of -600 V or, respectively, -550 V for Si(Li) #438 via an 8-channel *I*SEG EHS 8210x high-precision high-voltage (HV) power supply, which is software controlled through a CAN-interface, where voltage and current for each channel are controlled independently. In case of a detector warm-up, an auto-shutdown feature, which is connected to the HV control system, has been implemented. The embodied alarm card of the PSC 854 preamplifier induces an alarm, which initiates the high-voltage to ramp down via a global interlock signal.

All power supplies, including preamplifier, high-voltage and data acquisition (DAQ) are secured by a Tripp-Lite SU1000RTXLCD2U UPS back-up system, that provides power conditioning with a 1 kVA (900 W) on-line, double-conversion (pure sine wave) capability. This stability results in an output voltage regulation of ±2%.

After preamplification, the signals from each detector pass a custom-built signal-processing amplifier before they can be digitized by an ADC converter. The amplifier decouples the 4 V transistor-reset output signal from the detector and further filters the signal. The first stage is a high-pass filter, which allows the high-frequency, positive-step signal to pass through, while removing the low-frequency (∼ few Hz) noise from the EBIT cryo compressor underneath the experimental platform. This signal is then amplified to match the ADC impedance, and integrated by a low-pass filter before digitization.

Signal digitization is performed by a self-triggered, 8-channel SIS3302 FPGA-based sampling ADC, clocked at 100 MHz [164], capable of signal integration as well as of a complete pulse-shape readout. The latter function was not used for the analysis of the experimental data.

The trigger threshold can be adjusted individually for each channel, depending on the detector. For pulse integration, a trapezoidal energy filter is applied in the ADC hardware. The latter generates a moving-average window (MAW) with variable parameters like the peaking and gap time. Details are given in Ref. [164].

Each triggered event is recorded with a 48-bit time-stamp generated by the ADC clock, that is correlated to the programmable pulse-generator (PPG) signal provided by the EBIT, thus

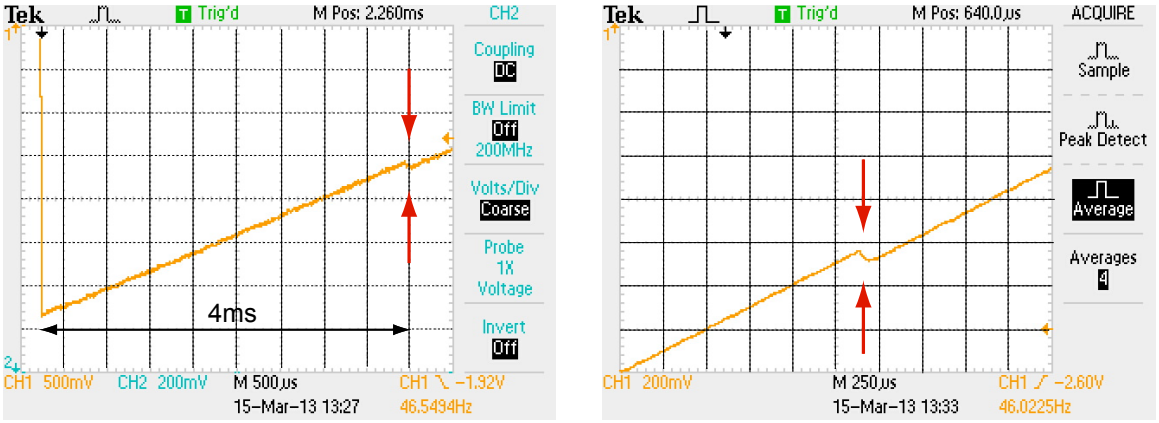

Figure 3.5: Analog Si(Li) output signals displaying the preamplifier reset. At 4 ms one observes an irregular feature on the ramp-up slope, which causes a low-energy ghost peak in the spectra.

providing the timing information for each event relative to the start of each measurement cycle as described in Sec. 2.3.1. Up to 65 k samples of the pulse shapes can be recorded per event and used for an off-line pulse-shape analysis (PSA) [130, 164]. A detailed PSA enables further suppression of invalid signals caused by noise and false triggers in order to reduce background events. Additionally, the altering and fitting of valid pulses has been shown to improve the spectral resolution. The implementation of this analysis feature into the general analysis has not been completed thus far.

3.4.1 Preamplifier non-linearity

Some of the detectors exhibited an irregular, "bump-like" feature in the output signal that is observed with a 4 ms delay after each reset (Fig. 3.5). The presented images show the direct output signals recorded in a vibration-free environment and without the presence of the EBIT $\vec{B}$-field.

Depending on the front-end electronics, this irregularity causes a low-energy "ghost peak" between 5 and 10 keV in the spectra, which is above pure electronics noise. It was confirmed that the peak always occurs at the same energy for a specific detector and is independent of the voltage level.

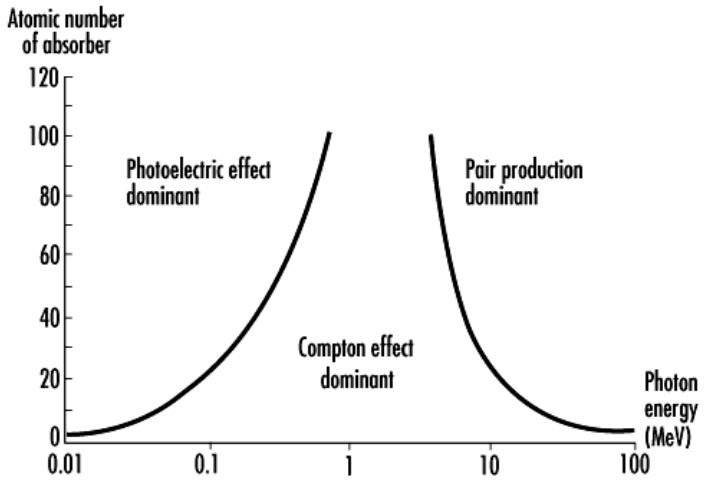

Figure 3.6: Dominant interaction processes as a function of the incident photon energy. The solid lines define the values of Z and hν for which the two neighboring effects are equally probable. Figure adapted from Ref. [157].

3.5 Performance

The planar Si(Li) detectors were specifically designed by Canberra, France for best energy resolution and photon detection efficiency at low energies, i.e., below 50 keV for improved X-ray detection. However, the detectors were not specifically constructed for optimal performance in a magnetic field, which is one of the key features of the decay-spectroscopy setup. Hence, the detection efficiency as well as the resolution of the Si(Li) detectors were studied in the trap environment at different magnetic-field strengths. In addition to the Si(Li) performance dependence on the magnetic field, the effect of the applied high-voltage on the energy resolution and detection efficiency was investigated prior to the online experiments.

3.5.1 Detection efficiency

Photoelectric absorption, Compton scattering and pair production are the three main interaction processes (c.f. Fig. 3.6) for photons in matter which are essential in radiation detection. In all of these processes, the photon energy is partially or completely transferred to electron energy and the photon is either scattered under a specific angle or disappears [157]. Which of the three processes is dominant depends on the photon energy, as well as on the atomic number of the nucleus. Since γ-rays and X-rays can travel long distances between interactions with the crystal, photon counters are usually less than 100% efficient. Thus, a

precise efficiency calibration becomes mandatory [157].

The detection efficiency is usually defined in two types, the intrinsic and the absolute efficiency. The intrinsic efficiency is defined as the ratio of the number of recorded pulses to the number of incident photons on the detector $N_{photons}(E)$:

$$\epsilon_{int} = \frac{N_{pulse}(E)}{N_{photons}(E)}, \tag{3.1}$$

and is independent of the solid angle. ϵ_{int} depends on the detector material, the radiation energy, as well as on the physical thickness of the detector crystal, its dead-layer and the thickness of its carbon or beryllium window in the direction of the incident radiation.

The absolute efficiency ϵ_{abs}, on the other hand, is defined as the ratio between the number of recorded pulses $N_{pulse}(E)$ and the number of photons $N_{source}(E)$ with the energy E emitted by the source:

$$\epsilon_{abs} = \frac{N_{pulse}(E)}{N_{source}(E)}. \tag{3.2}$$

ϵ_{abs} depends on the detector geometry, as well as on the counting geometry, i.e., the source-to-detector distance (d) and the solid angle Ω of the detector seen from the actual source position [157]:

$$\Omega = 2\pi \left(1 - \frac{d}{\sqrt{d^2 + r^2}}\right), \tag{3.3}$$

where r is the detector crystal radius. For isotropic sources the relation between ϵ_{abs} and ϵ_{int} is given by:

$$\epsilon_{abs} = \epsilon_{int} \cdot \frac{\Omega}{4\pi}. \tag{3.4}$$

More detailed information can be found in Ref. [157].

Since the absolute counting efficiency depends primarily on the surface area of the detector crystal, the low-energy Si(Li) detectors were fabricated in planar geometry to maximize the surface area. Towards higher energies, however the peak efficiency decreases, thereby following the trend of the photoelectric cross section in silicon.

The maximum intrinsic detection efficiency of the seven Si(Li) detectors lies between 4 keV and 20 keV, as illustrated in Fig. 3.7, where the intrinsic efficiency of the Si(Li) detectors

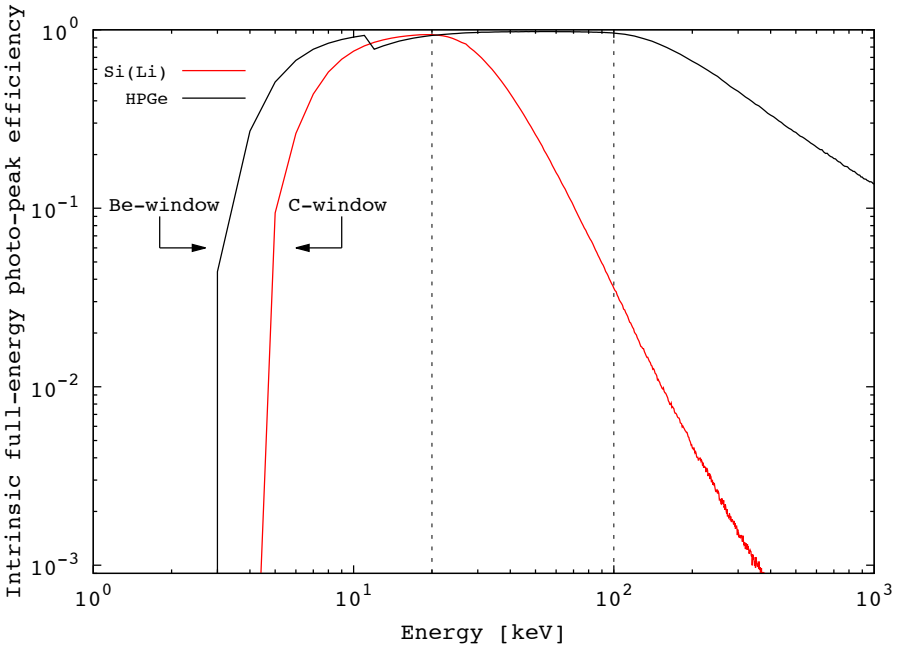

Figure 3.7: Simulated intrinsic efficiency curves for the Si(Li) detectors (red) and an 8π HPGe (black). The Si(Li) efficiency is highest between 4 keV and 20 keV, which is the typical energy region for the X-rays of interest for a TITAN-EC experiment. Figure adapted from Ref. [130].

is shown relative to the one for a typical HPGe detector. For energies below $\sim$ 20 keV the functions are comparable, while the HPGe is orders of magnitudes more efficient than the Si(Li) detectors at higher energies. At $\sim$ 11 keV one observes a drop in the efficiency of the HPGe detector due to the germanium absorption edge, which results from the escape peak at that energy.

The absolute photo-peak efficiency of the Si(Li) crystal was also reproduced by simulations. This was accomplished by adjusting the detector geometry in order to match the radioactive calibration source (^{241}Am, ^{152}Eu, ^{133}Ba) data. The source activities at the time of the measurements were 2.3 μC (^{133}Ba), 10.9 μCi (^{241}Am) and 0.7 μCi (^{152}Eu) based on the value determined in 1989 with an accuracy of 5%. The source-to-detector distance was 13.0(3) cm. Fig. 3.8 shows the simulated curve of the photopeak-detection efficiency in direct comparison with the absolute efficiency response gained from the three calibration sources. The uncertainties for the data points result from the statistical uncertainties as well as from the uncertainties induced by the geometry of the measurement setup and from the uncertainty of the source activities. The detection efficiency may alter over periods of

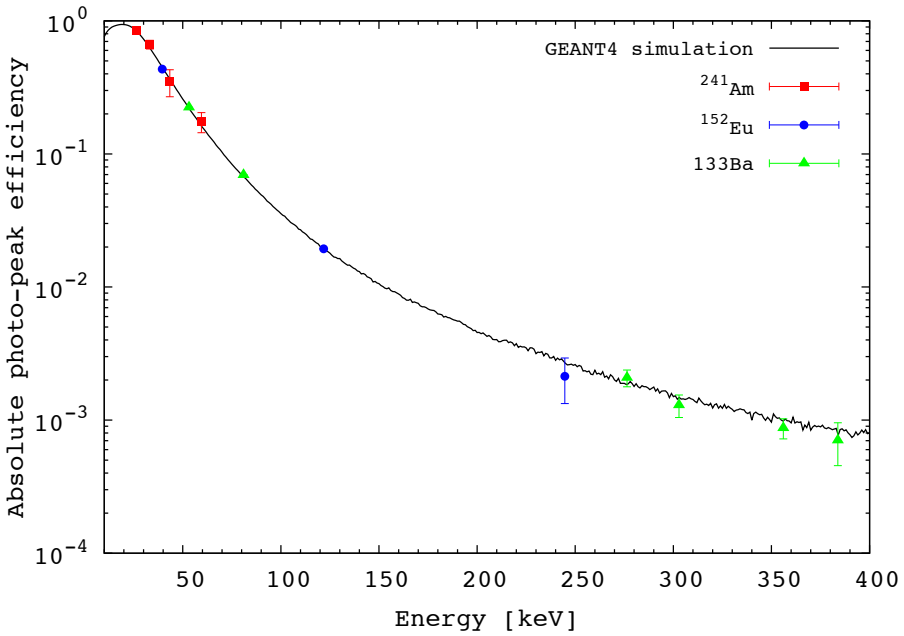

Figure 3.8: Direct comparison of the experimentally determined absolute efficiency response and the simulated efficiency function in dependence of the photon energy. The uncertainties result from the combination of the statistical uncertainty and the uncertainty of the geometry, i.e., source-to-detector distance, and are for some calibration points smaller than the point size.

months or years, as a result of variations in the charge-collection efficiency and alterations of the dead-layer thickness. Consequently, efficiency calibrations have to be performed on a regular basis.

The specified dimensions of the Si(Li) crystal as well as the C-window and dead-layer thicknesses are given in Sec. 3.1. However, since the reliability of the given uncertainties for the dimensions, especially for the dead-layer, remained unclear, the effect of variations in the crystal, dead-layer and window thicknesses on the detection efficiency was studied via simulations [155, 156]. A Penelope simulation was performed to estimate the contribution of the uncertainty in the efficiency to the overall systematic uncertainty. Fig. 3.9 presents a comparison of the efficiency function simulated according to the specified dimensions (5 mm crystal, 100 nm dead-layer (DL), 0.6 mm C-window) with a function simulated with a reduced crystal thickness of 2 mm and a thinner dead-layer of 100 pm, and one function simulated without the implementation of a carbon window.

Below 20 keV one observes an efficiency close to 100% for a 5 mm thick crystal without

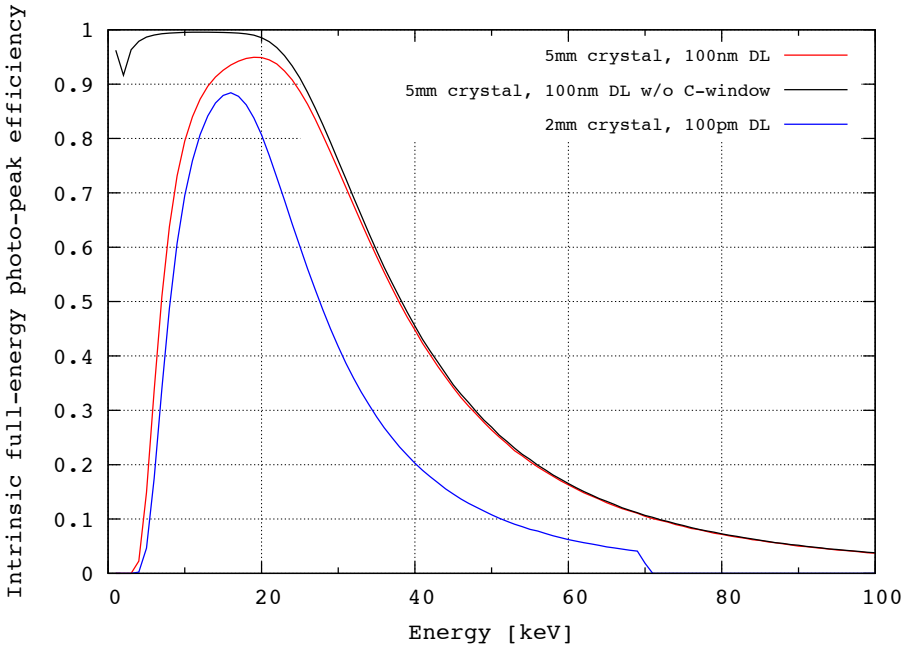

Figure 3.9: Simulated photo detection efficiency response of a Si(Li) detector as a function of energy. The red curve represents the nominal efficiency function, while the black line shows the response without the implementation of a C-window. The blue curve illustrates the loss in efficiency for a reduced crystal thickness [155].

including the carbon window (black curve) in the simulation, whereas the maximal efficiency for the nominal response function is reduced to $\sim 95\%$ at ~ 19 keV (red curve). For higher energies the effect of the C-window becomes negligible, which can be concluded from the fact that the two curves overlap for energies ≥ 50 keV. The reduction of the crystal volume (blue curve) reduces the efficiency over the complete energy region simulated here and a maximal efficiency of 88% at ~ 16 keV. Below ~ 15 keV the red and blue curves differ by 12% to 20%. Furthermore, one observes that the function, which was generated with a 5 mm crystal (red) has a wider (~ 10 keV) high-efficiency range than the blue function (~ 7 keV) and exhibits higher efficiencies at higher energies, which is a factor of ~ 2 on average from 30 to 60 keV. A noticeable effect from varying the dead-layer thickness from 100 nm to 100 pm was not observed.

Overall, a systematic uncertainty of $\lesssim 5\%$ is extracted from the above described study, assuming a maximal deviation of 15% for the carbon window and dead-layer from the specified values and a maximum deviation of 10% for the crystal thickness.

3.5.2 Energy resolution

The resolving power δE of a detector is defined as the width of the energy distribution (ΔE) divided by the peak energy (E) [157]:

$$\delta E = \frac{\Delta E}{E}, \tag{3.5}$$

where ΔE can be determined by the Full Width at Half Maximum (FWHM) of a Gaussian distribution. Drifts of the operating characteristics within the measurement time and noise sources within the detector electronics (preamplifier, amplifier, etc.) represent the noise contribution n which varies from detector to detector. The statistical noise represents the main contribution, and results from the fact that the charge generated by the incident radiation is defined by a discrete number of charge carriers.

Assuming only statistical fluctuations as a noise contribution, the response function would be described by a Gaussian function [157]:

$$G(x) = \frac{A}{\sigma\sqrt{2\pi}} \exp\left(-\frac{(x-x_0)^2}{\sigma^2}\right), \tag{3.6}$$

where the parameter σ defines the FWHM of the Gaussian via FWHM$= 2 \cdot \sqrt{2 \cdot \ln 2} \cdot \sigma$, x_0 defines the peak centroid and A is the peak area. Given a linear detector response, one derives the resolution limit R (Poisson limit) based on the statistical fluctuations in the number of charge carriers:

$$R_{limit} = \frac{2.35}{\sqrt{N}} \tag{3.7}$$

However, in reality, the total number of charge carriers cannot be described by simple Poisson statistics, but one observes a deviation from the predicted variance, which can be expressed by the Fano factor F [157]:

$$F = \frac{Observed\, variance\, in\, N}{Poisson\, predicted\, variance}. \tag{3.8}$$

As the variance is defined by σ^2, one gets for the resolution limit:

$$R_{limit} = 2 \cdot \sqrt{2 \cdot \ln 2} \cdot \sqrt{\frac{F}{N}}. \tag{3.9}$$

For a realistic estimation of the detector resolution, one now has to take into account the dependence on the incident photon energy $E_{h\nu}$ as well as the pair creation energy in silicon

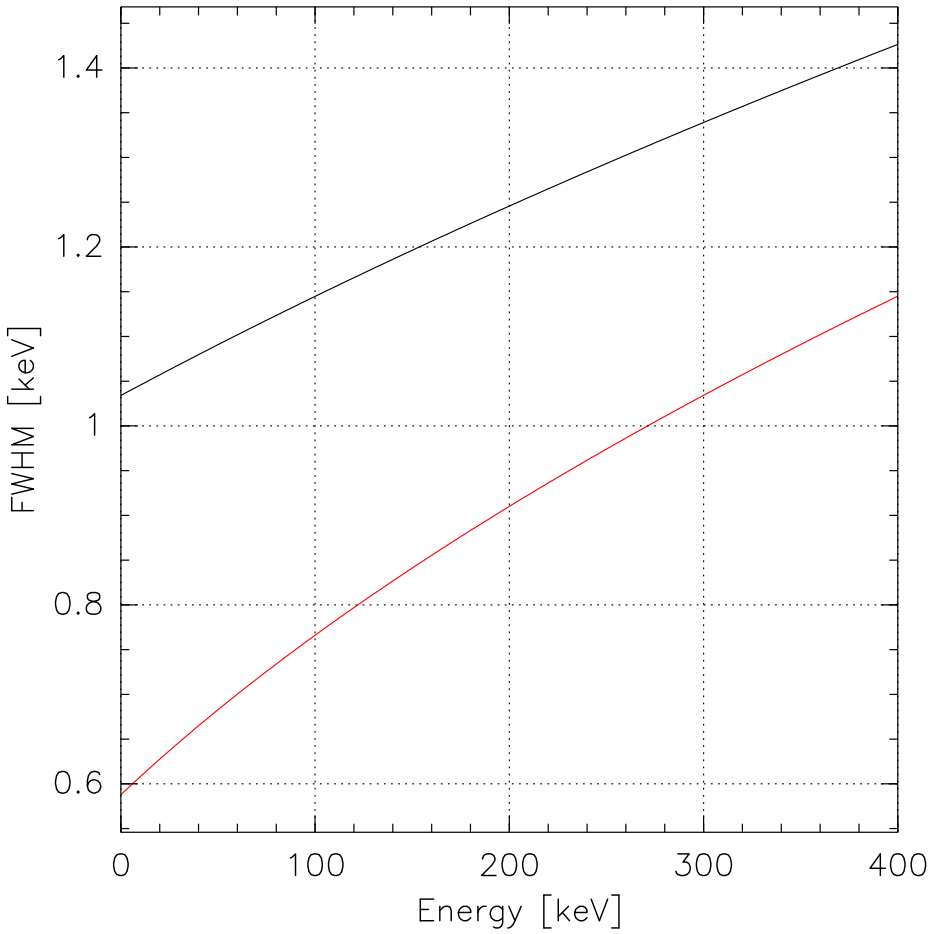

Figure 3.10: Comparison of the energy resolution (FWHM) specified by the manufacturer (red) and the function generated based on measured values during the commissioning experiment (black).

(E_{pair}=3.8 eV), the Fano factor ($F_{Si} = 0.115$) and the electronics noise contribution n, which leads to [157]:

$$FWHM = 2.35\sqrt{(F \times E_{h\nu} \times E_{pair}) + n^2}. \tag{3.10}$$

Fig. 3.10 shows a comparison of the expected energy resolution as a function of the photon energy as specified by the manufacturer with the function generated based on measured values during the commissioning experiment. Both curves are based on Eq. 3.10 and have a variable parameter for the electronics noise contribution n.

3.5.3 Peak shape

For energies below $\sim$ 30 keV, photoelectric absorption is the dominant process in silicon. Given a high enough electric field in the detector, the charge collection is complete and

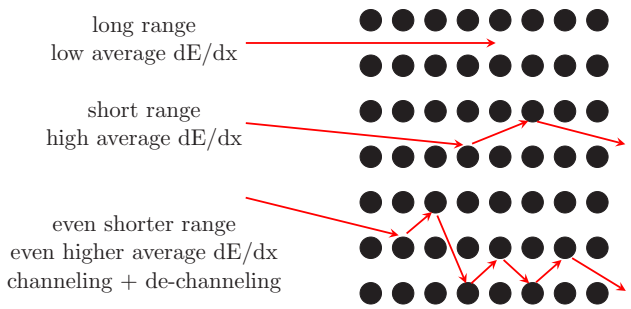

Figure 3.11: Illustration of the channeling effect in a crystal, where the rate of the energy loss of a charged particle depends on the orientation of the particle trajectory (red arrows) relative to the crystal. Various possible particle trajectories lead to different ranges and result in a decreased energy resolution.

the peak shape can be described by a Gaussian distribution [157]. However, impurities and defects in the crystal structure can hinder the transport of electrons and holes to the detector electrodes [165, 166]. As a result, the charge carriers are trapped in the energy levels between the silicon valence band and the conduction band. This reduces the collected charge as well as the detected energy, and the peak shape exhibits an asymmetric low-energy tail. A detailed study of this peak asymmetry in Si(Li) detectors can be found in Ref. [166]. Channeling effects, i.e., the steering of charged particles in open regions in the crystal lattice can also contribute to incomplete charge collection. Particles that travel parallel to the crystal planes are less affected by energy loss than those particles with arbitrary directions relative to the crystal planes [157]. Consequently, particles with a lower energy loss can penetrate farther through the crystal. Fig. 3.11 illustrates the effect for three different scenarios, i.e., an ideal particle trajectory parallel to the crystal plane, a particle, which is scattered multiple times within two planes and a multiply scattered particle travelling between different crystal planes, thereby causing a decrease in energy resolution [157]. Since channeling can affect the pulse height even in those cases when the particle is fully stopped in the crystal volume, attempts to minimize the effect by manipulating the crystal in such a way that the $\langle 111 \rangle$ orientation is perpendicular to the waver surface.

3.5.4 Magnetic-field studies

To investigate the influence of the EBIT's magnetic field on the detector performance, test measurements with a ^{133}Ba source were carried out at various magnetic-field strengths from 0 T to 2.5 T. The values for the $\vec{B}$-field strength given in the following refer to the strength in the trap center and not to the field at the position of the Si(Li) crystal, where the field is already about a factor of 40 lower as illustrated in Fig. 2.5. During the test measurements, the studied Si(Li) detector was mounted at the horizontal 90° port of the EBIT, without any shielding or vibration damping, while the source was located close to the crystal at the preamplifier-electronics housing. The detector-to-source distance as well as the DAQ setting were not modified between the different measurements. All studies very repeated multiple times yielding consistent results.

From studies with HPGe detectors in magnetic fields [167, 168] one knows that the deflection of the charge carriers in the magnetic field and the Penning effect in the vacuum surrounding the semiconductor crystal can substantially influence the operation of large volume semiconductor devices. Therefore, one can also expect the magnetic field to cause an increase of the signal rise time and a distortion of the generated Si(Li) signals, which affects the full-energy peaks in the spectra. The signal degradation can be quantified by the loss in the detection efficiency, a shift of the full-energy peak and a decrease in the energy resolution. In the following, the analysis of the effect of the $\vec{B}$-field alteration on the peak centroid, the intrinsic efficiency and energy resolution is presented.

3.5.4.1 Effect on the peak centroid

Analyzing the spectra revealed a shift of the peak centroid towards lower energies with increasing magnetic-field strength for all observed transitions in the ^{133}Ba spectra, where the effect is larger towards higher peak energies. Figure 3.12 shows an overlay of five ^{133}Ba spectra taken at different $\vec{B}$-field strengths illustrating the peak shift towards lower channels. Displayed is the X-ray region, the transition at 81 keV as well as the 356 keV transition. Especially at higher energies, a decrease in energy resolution with increasing magnetic-field strength can be observed in addition to the peak-center shift. That effect is investigated in

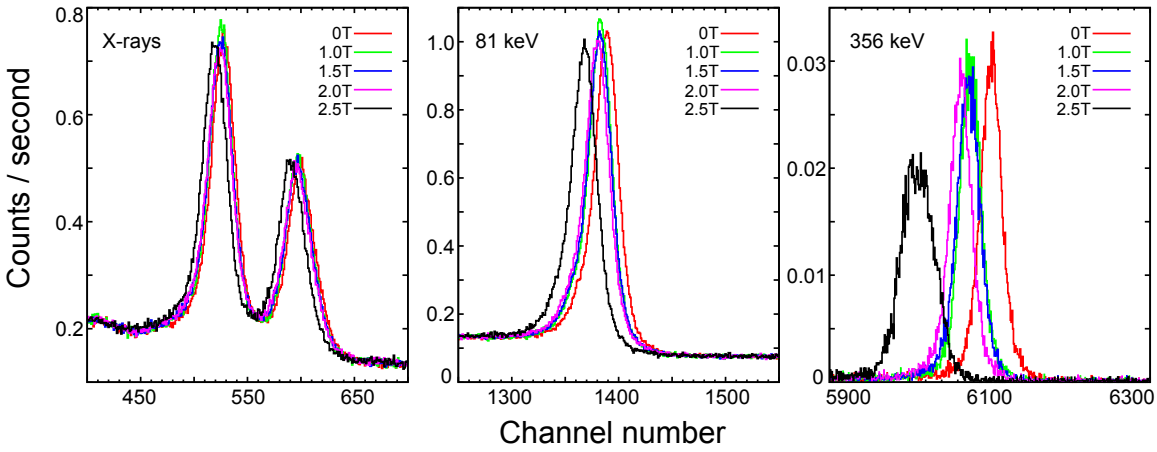

Figure 3.12: Shown are three energy regions (X-rays, 81 keV, 356 keV) of an overlay of five ^{133}Ba spectra taken with a Si(Li) detector at different $\vec{B}$-field strengths. With increasing $\vec{B}$-field, the peak center shifts to lower channel numbers. The effect is larger for higher energies. In addition, a decrease in energy resolution can be observed.

the following subsection 3.5.4.2.

The values for the channel numbers as a function of the magnetic field and energy are presented in Tab. 3.1. Further, the table contains the maximum difference in channel number (ΔCh) or, respectively, peak energy (ΔE) for the two extreme B-fields (B=0 T and B=2.5 T) as a function of the energy of the ^{133}Ba transitions. Plotting the difference in channel number between the peak center at 0 T and the one at 2.5 T for each energy (compare Tab. 3.1) reveals a linear trend, whereby the absolute difference (ΔCh) becomes larger with increasing energy as illustrated in the top panel of Fig. 3.13. For completeness, the linearity of the peak shift in units of keV is presented in the bottom panel of Fig. 3.13. The observed centroid shift is caused by incomplete signal integration by the main amplifier as a result of the increased charge collection time [167]. The linearity can be attributed to the linear response function of Si(Li) detectors. From the observation of the linear correlation between energy and centroid shift one can conclude that the FET was unaffected by the exposure to the magnetic field.

However, since the $\vec{B}$-field is kept at a constant value for all calibration measurements as well as during an experiment, this effect does not pose a problem for the physics measurements. Besides, the spectra taken during the experiments were calibrated by using known transitions in the respective spectra.

	Peak centroid [Ch]			
nominal $\vec{B}$-field [T]	K_α	K_β	53 keV	81 keV
0	527.9(1)	599.6(2)	908.7(2)	1387.4(2)
1	524.8(1)	597.3(2)	905.4(2)	1381.8(2)
1.5	524.5(1)	596.9(2)	904.6(2)	1381.1(2)
2	523.8(1)	595.8(2)	903.2(2)	1378.8(2)
2.5	519.2(1)	590.7(2)	895.2(2)	1366.7(2)
ΔCh [Ch]	7.9(2)	8.8(2)	13.5	20.8(2)
ΔE [keV]	0.4639(1)	0.5158(2)	0.7920(13)	1.2136(12)
	Peak centroid [Ch]			
nominal $\vec{B}$-field [T]	276 keV	303 keV	356 keV	383 keV
0	4737.7(4)	5190.5(3)	6101.4(2)	6578.0(4)
1	4718.3(5)	5168.9(3)	6075.7(2)	6550.6(4)
1.5	4715.6(4)	5166.8(3)	6073.2(2)	6547.7(4)
2	4708.5(5)	5158.1(3)	6063.4(2)	6537.8(4)
2.5	4666.3(8)	5113.8(5)	6010.2(3)	6480.6(6)
ΔCh [Ch]	71.4(9)	76.7(5)	91.2(3)	97.4(7)
ΔE [keV]	4.1660(28)	4.4772(15)	5.3227(23)	5.6831(36)

Table 3.1: Influence of the magnetic-field strength on the peak center given in channel numbers. The bottom of each column contains the values for the difference between the highest (B=0 T) and lowest (B=2.5 T) channel number (ΔCh) or, respectively, energy (ΔE) of the peak centers at different energies. The given energies for the transitions are taken from ref [169]. The errors for ΔCh and ΔE result from the analytical fit.

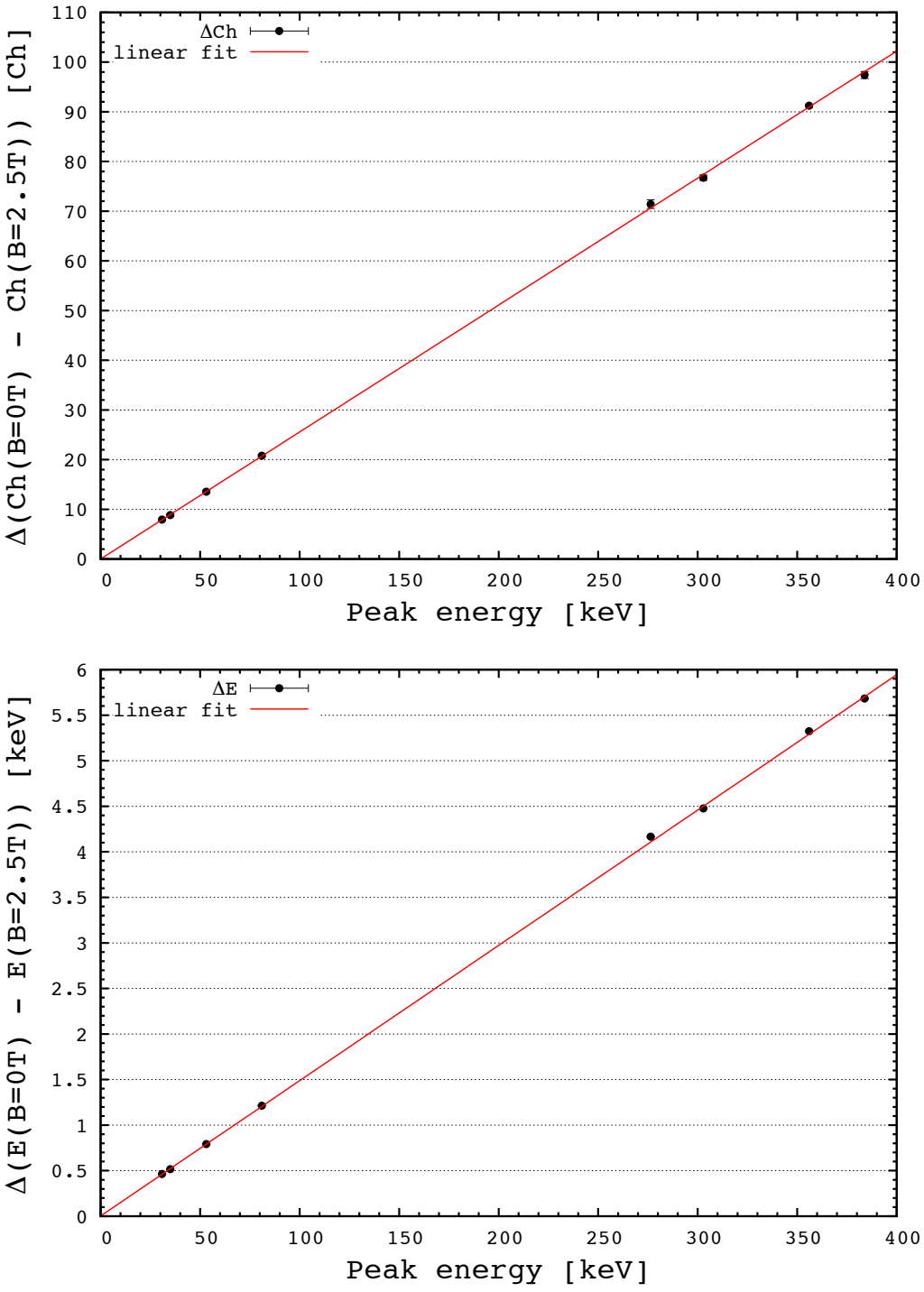

Figure 3.13: Top: Difference between the highest (B=0 T) and lowest (B=2.5 T) channel number of the peak center depending on the energy for the observed transitions in a ^{133}Ba spectrum. The red line represents a linear fit to the data. The slope m of the curve is m=0.256(1) Ch/keV. Bottom: Difference between the highest (B=0 T) and lowest (B=2.5 T) energy of the peak center depending on the energy for the observed transitions in a ^{133}Ba spectrum. The red line represents a linear fit to the data. The slope m of the linear fit is m=0.015(1) Ch/keV.

	Energy resolution [%]			
nominal $\vec{B}$-field [T]	K_α	K_β	53 keV	81 keV
0	1.78(2)	1.95(2)	1.64(3)	1.81(2)
1	1.75(9)	1.88(3)	1.60(3)	1.73(2)
1.5	1.81(2)	1.92(3)	1.66(3)	1.79(2)
2	1.86(2)	1.98(3)	1.73(3)	1.82(2)
2.5	1.86(2)	1.96(3)	1.66(3)	1.90(2)
ΔFWHM((2.5 T)-(1 T)) [%]	6.3(3)	4.3(1)	3.8(1)	9.8(2)
nominal $\vec{B}$-field [T]	276 keV	303 keV	356 keV	383 keV
0	1.77(6)	1.94(3)	2.05(2)	1.92(4)
1	1.73(7)	1.90(4)	2.01(2)	1.71(4)
1.5	1.83(6)	2.07(3)	2.17(2)	2.14(4)
2	1.96(6)	1.97(3)	2.11(2)	2.11(5)
2.5	2.33(10)	2.68(6)	2.90(3)	2.64(7)
ΔFWHM((2.5 T)-(1 T)) [%]	35(2)	41(1)	44(3)	54(6)

Table 3.2: Influence of the magnetic-field strength on the energy resolution. Column one lists the $\vec{B}$-field strength, while the other four columns show the energy resolution for each observed transition in the ^{133}Ba spectrum in %. The quantity ΔFWHM describes the loss in resolution from 1 T to 2.5 T.

3.5.4.2 Effect on the energy resolution

In addition to the effect on the peak center, the $\vec{B}$-field also affects the energy resolution. Between 0 T and 1 T the resolution increases slightly for all energies before it decreases again with increasing $\vec{B}$-field. Figure 3.14 shows the dependence of the energy resolution on the magnetic-field strength for different energies. While the resolution only worsens by $4-10\%$ between 1 T and 2.5 T for the transitions up to 81 keV, a decrease in resolution from 35(2)% up to 54(6)% with an increasing field strength can be observed in addition to the peak-center shift for the transitions between 200 keV and 400 keV (compare Tab. 3.2). The correlation of the degradation in the energy resolution to the magnetic field was observed in accordance to the observations in Ref. [167] and is correlated to the change in rise time.

3.5.4.3 Effect on the detection efficiency

Analyzing the effect of the $\vec{B}$-field on the intrinsic efficiency for different peak energies revealed only small count-rate alterations as a function of the magnetic-field strength, which were on the order of a few percent and, hence, within the statistical uncertainty. The alterations did not follow a clear trend as it is reflected in Tab. 3.3 as well as in Fig. 3.15

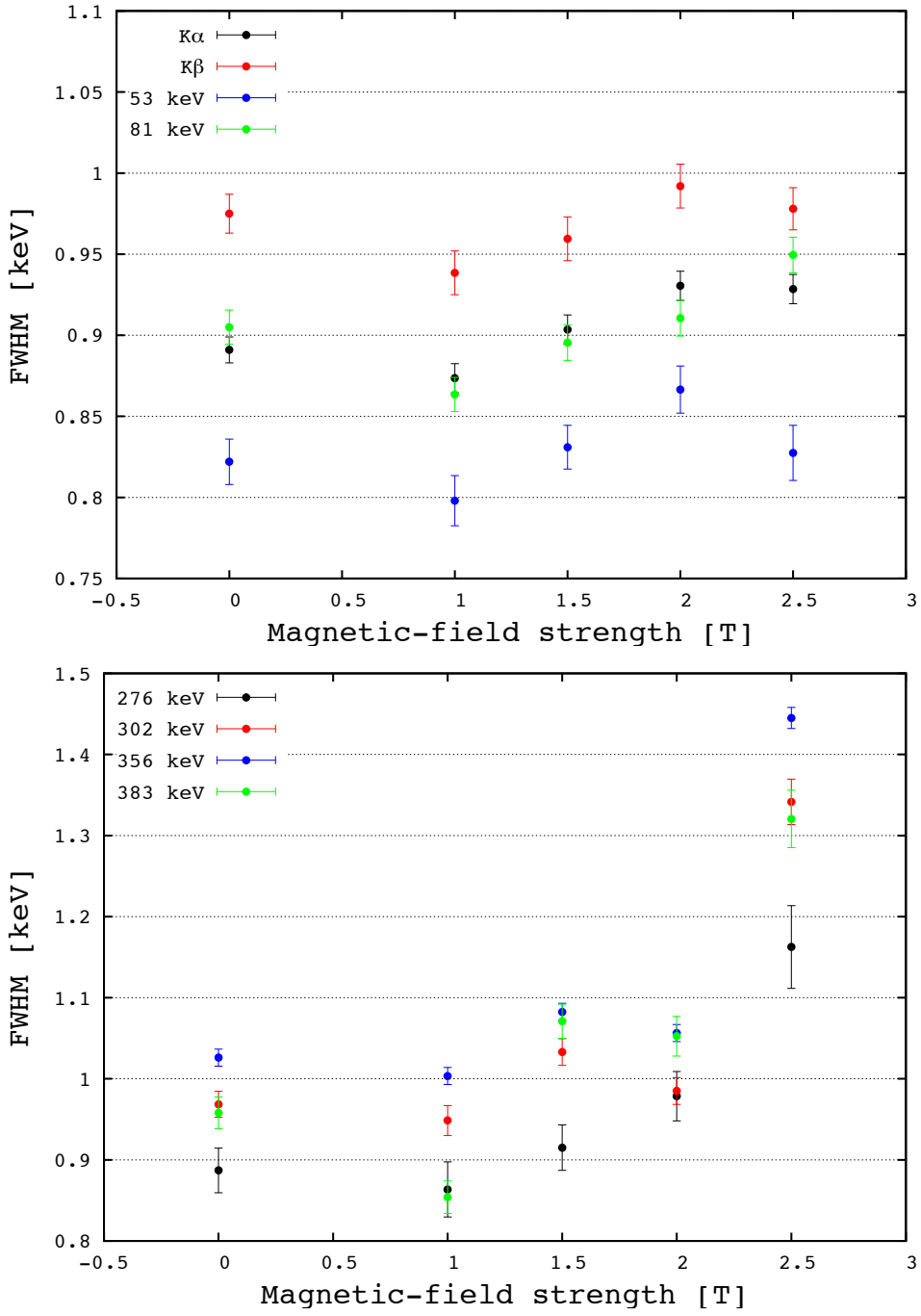

Figure 3.14: Shown is the energy-resolution (FWHM) as a function of the strength of the magnetic field for various energies between 30 keV and 383 keV. The displayed error bars represent the statistical uncertainty.

	Count rate [/s]			
nominal $\vec{B}$-field [T]	K_α	K_β	53 keV	81 keV
0	171.9(1)	115.8(1)	30.90(6)	275.5(2)
1	171.7(2)	115.4(1)	31.23(7)	271.4(2)
1.5	169.8(1)	113.1(1)	31.38(5)	270.3(2)
2	170.5(1)	114.2(1)	31.49(6)	267.0(2)
2.5	172.0(2)	116.9(1)	30.21(7)	273.2(2)
Δ_{max}	2.19(29)	3.83(24)	1.28(13)	8.5(33)
nominal $\vec{B}$-field [T]	276 keV	303 keV	356 keV	383 keV
0	2.17(1)	4.40(2)	10.22(3)	1.19(1)
1	2.12(2)	4.34(3)	9.92(4)	1.11(1)
1.5	2.12(1)	4.40(3)	10.19(3)	1.23(1)
2	2.26(1)	4.17(3)	9.79(3)	1.17(1)
2.5	2.33(2)	4.40(3)	10.39(4)	1.07(1)
Δ_{max}	0.21(4)	0.23(6)	0.60(7)	0.16(2)

Table 3.3: Influence of the magnetic-field strength on the count rate. The given errors are purely statistical.

and Fig. 3.16.

3.5.4.4 Preamplifier current

Exposing the Si(Li) detectors to the magnetic field further increased the current draw of the preamplifier-power supply. A testing scheme with three Si(Li) detectors was carried out, whereby the number of operated detectors was altered once with and once without the presence of the magnetic field (4.5 T at the trap center). Tab. 3.4 contains the corresponding values for the current needed for different detector combinations. While the current needed for biasing the preamplifier of one detector to +28 V is 0.12 A when it is operated without the magnetic field, the current increases by roughly a factor of 2 (0.26 A) for operation in the $\vec{B}$-field. Powering the preamplifiers of three detectors that were exposed to the $\vec{B}$-field simultaneously, increased the current up to 0.7 A, causing the power supply to warm up. Comparing that value to the value for the current used for preamplifying three detectors with the $\vec{B}$-field off (0.26 A) shows a difference of a factor of ~ 2.7.

The origin of the increased power consumption has not be identified unambiguously. One explanation is an increased leakage current under the influence of the $\vec{B}$-field, directly

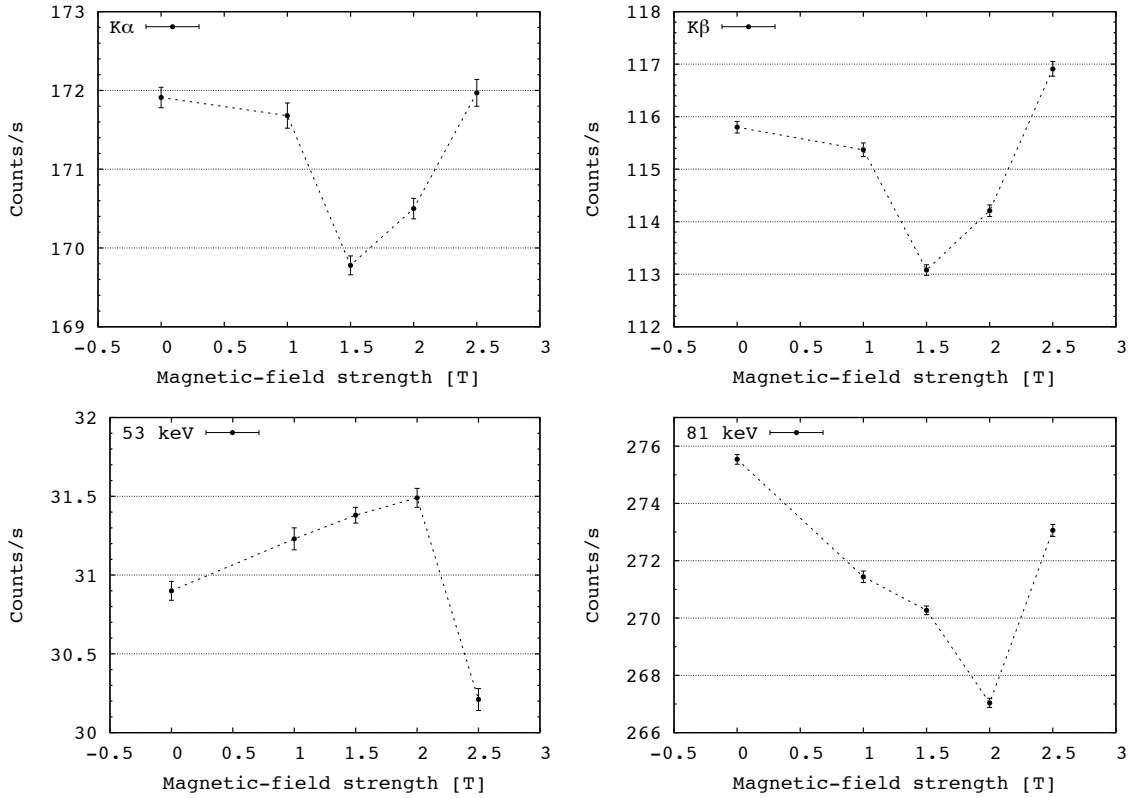

Figure 3.15: Shown is the count-rate dependence on the magnetic field for various energies between 30 keV and 81 keV. The errorbars represent the statistical uncertainty.

	SiLi2	SiLi4	SiLi6	Neg. Voltage [V]	Current [A]	Pos. Voltage [V]	Current [A]
$\vec{B}$-field on	X	X	X	-28	0.15	+28	0.70
		X	X	-28	0.08	+28	0.49
		X	X	-28	0.11	+28	0.48
	X		X	-28	0.11	+28	0.47
	X			-28	0.08	+28	0.26
		X		-28	0.08	+28	0.26
			X	-28	0.07	+28	0.27
$\vec{B}$-field off	X	X	X	-28	0.15	+28	0.27
	X	X		-28	0.11	+28	0.20
		X	X	-28	0.11	+28	0.19
	X		X	-28	0.11	+28	0.20
	X			-28	0.08	+28	0.14
		X		-28	0.08	+28	0.12
			X	-28	0.08	+28	0.12

Table 3.4: Influence of the magnetic field on the preamplifier current. The letter "X" indicates an operational detector for a specific test setting. The upper half of the table displays the values for the preamplifier voltage and current while the detectors were operated in the magnetic field. The lower half shows the results for the same 7 detector combinations without the influence of the $\vec{B}$-field.

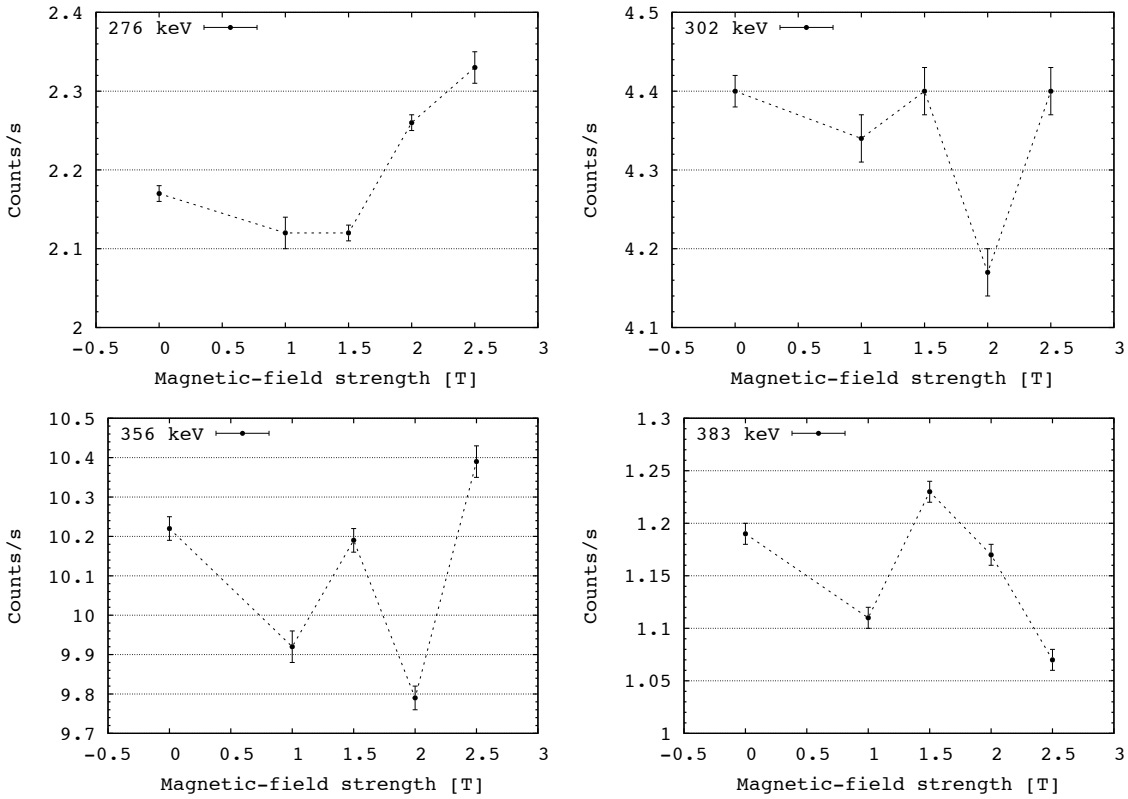

Figure 3.16: Shown is the count-rate dependence on the strength of the magnetic field for various energies between 276 keV and 383 keV. The errorbars represent the statistical uncertainty.

leading to a higher current draw. Another possibility is a magnetic relay in the detector circuitry which was originally implemented for initiating the HV-shutdown signal but was not functioning in the magnetic field. Though, according to the manufacturer, it is not powered as long as the detectors are cold.

The observation of the increased power consumption made a redesign of the power supplies necessary, i.e., the supplies were secured with the UPS back-up system (Sec. 3.4).

3.5.5 High-voltage studies

To test whether the applied high-voltage affects the energy resolution and efficiency of the Si(Li) detectors, the high-voltage was ramped from -450 V up to -850 V in 50 V steps after confirming with Canberra that biasing the detectors to voltages higher than -600 V would not damage the crystal or FET of the detectors. Radioactive source spectra with ^{133}Ba were taken for each high-voltage setting with one of the Si(Li) detectors, whereby the source-to-crystal distance was 13.0(3) cm. For those tests, the detector was not mounted on the EBIT and not exposed to the magnetic field.

3.5.5.1 Effect on the peak centroid

Similar to the effect of the magnetic field on the peak center, the high-voltage also affects the position of the peak center (see Tab. 3.5 and Tab. 3.6). An overlay of all ^{133}Ba spectra taken at different voltages is shown in Fig. 3.17, where three different energy regions (X-rays, 81 keV, 356 keV) are presented.

	Peak centroid [Ch]					
Voltage (V)	K_α	K_β	53 keV	81 keV	303 keV	356 keV
-450	456.38(2)	517.41(7)	786.80(14)	1201.07(7)	4490.69(61)	5278.61(35)
-500	456.72(1)	518.20(3)	787.86(15)	1202.28(7)	4496.31(55)	5284.73(29)
-550	457.23(3)	518.43(8)	788.25(15)	1203.34(7)	4498.81(58)	5288.69(28)
-600	457.65(2)	518.82(12)	788.96(15)	1204.30(7)	4502.44(69)	5294.24(30)
-650	456.29(2)	517.32(9)	786.78(15)	1200.97(7)	4491.87(44)	5278.05(32)
-750	455.92(2)	517.03(8)	786.14(15)	1200.04(8)	4487.21(41)	5274.22(31)
-800	455.78(2)	517.02(12)	785.61(16)	1199.69(8)	4485.38(41)	5273.16(29)
-850	455.92(1)	517.02(7)	786.17(11)	1200.16(8)	4487.52(40)	5274.96(27)

Table 3.5: Listed are the peak centroids for transitions in ^{133}Ba as a functions of the applied high voltage.

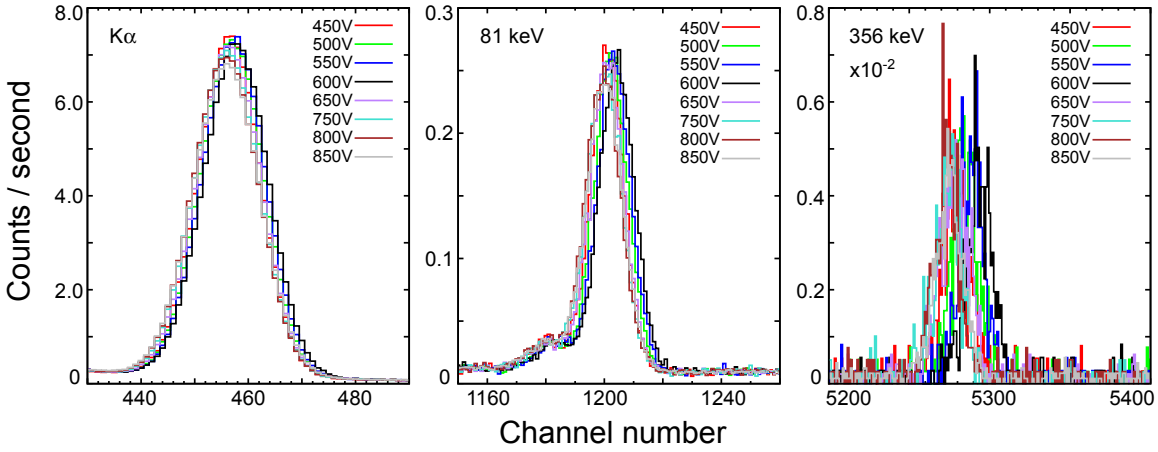

Figure 3.17: Shown are three energy regions (X-rays, 81 keV, 356 keV) of an overlay of eight ^{133}Ba spectra taken with a Si(Li) detector at different high voltages. At higher energies, a decrease in energy resolution can be observed in addition to the peak-centroid shift.

Peak energy [keV]	Δ(Ch(-600 V)-Ch(-450 V)) [Ch]	Δ(Ch(-600 V)-Ch(-800 V)) [Ch]
K_α	1.27(4)	1.87(4)
K_β	1.41(19)	1.80(24)
53	2.17(30)	3.36(31)
81	3.23(13)	4.62(15)
303	11.8(1.3)	17.1(1.1)
356	15.63(66)	21.08(59)
Peak energy [keV]	Δ(E(-600 V)-E(-450 V)) [keV]	Δ(E(-600 V)-E(-800 V)) [keV]
K_α	0.086(3)	0.127(3)
K_β	0.095(13)	0.122(16)
53	0.146(20)	0.227(21)
81	0.218(9)	0.312(9)
303	0.792(88)	1.152(75)
356	1.054(44)	1.423(40)

Table 3.6: The upper half of the table lists the difference in channel number between the measurements at -600 V and -450 V as well as the difference between the channel numbers measured at -600 V (Ch_{max}) and -800 V (Ch_{min}) depending on the peak energy. In the lower half, the same difference is expressed in units of keV.

As displayed in Fig. 3.18, the trend of the peak shift is similar for all peak energies, and shifts towards higher channels between -450 V and -600 V. Between -800 V and -850 V, the direction of the shift changes again, which potentially signals towards an oscillation pattern, and therefore channeling effects. This can only be confirmed by extending the study with even higher voltages which, however, may damage the crystal.

The value of the shift depends on the photon energy and the increase of the shift towards higher energies can be described by a linear function, which is illustrated in Fig. 3.20 and Fig. 3.19. While the upper two panels in Fig. 3.20 show the linearity of the peak-center shift from -450 V to -600 V, the lower two panels present the peak shift from -600 V to -800 V. The observed shift can be attributed to channeling effects of charged particles in a crystalline material as described in Sec. 3.5.3. Similar to the observed linearity in the effect of the $\vec{B}$-field on the peak center the linearity of the Si(Li) detector response function explains the linear increase of the peak shift towards higher peak energies.

3.5.5.2 Effect on the detection efficiency

The extracted count rates for the K_α and K_β X-rays as well as for the 53 keV, 81 keV, 303 keV and 356 keV transitions from ^{133}Ba are given for Si(Li) #404 in Tab. 3.7. Plotting the count rates for different energies as a function of the high-voltage (compare Fig. 3.21 and Fig. 3.22) proves that the highest efficiency at the energy of the K_α X-ray is measured at -600 V. Biasing the detector to -650 V resulted in an efficiency decrease of about 1.6% ($\sim$16 counts/s) at that energy. Increasing the voltage up to -850 V further decreased the efficiency by $\sim$ 2.5% relative to the maximum value at -600 V. Ramping the voltage down to values lower than -600 V also led to lower efficiencies, the loss, however, was not as large as for higher voltages as can be read out from Tab. 3.7.

The trend observed for X-rays around 30 keV was different from the trend observed at higher energies. While the trend for the 53 keV transition is relatively stable, the efficiency for the 81 keV γ-line increases significantly at -600 V by 3.1% relative to the rate at -550 V. A further voltage ramp-up on the other hand brings the efficiency down to an even lower value than at -550 V. Those variations are usually known to occur over larger time periods

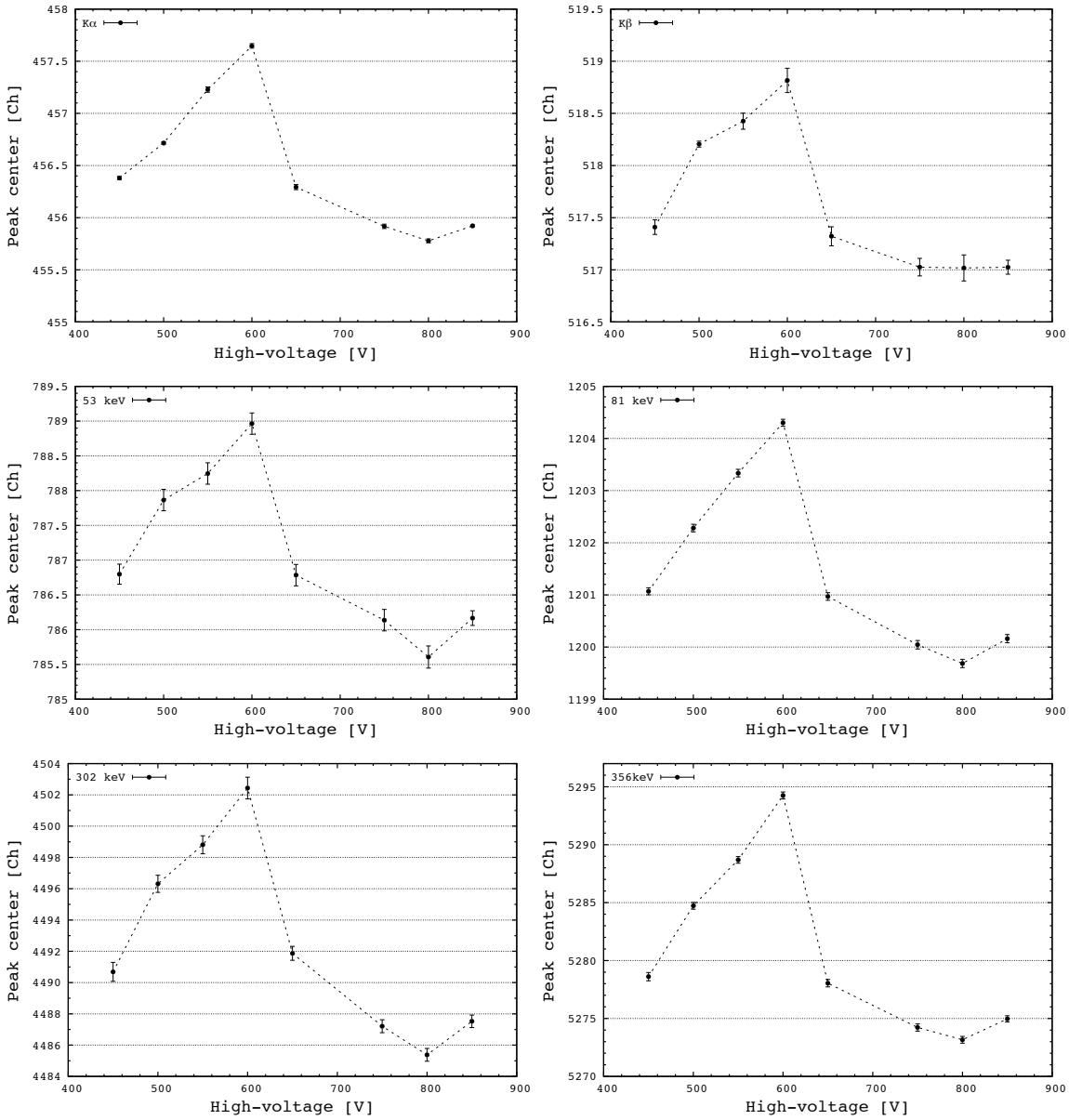

Figure 3.18: Peak centroids as a function of the applied high-voltage for various energies between 30 keV and 360 keV. Note that the polarity of the applied voltage is negative.

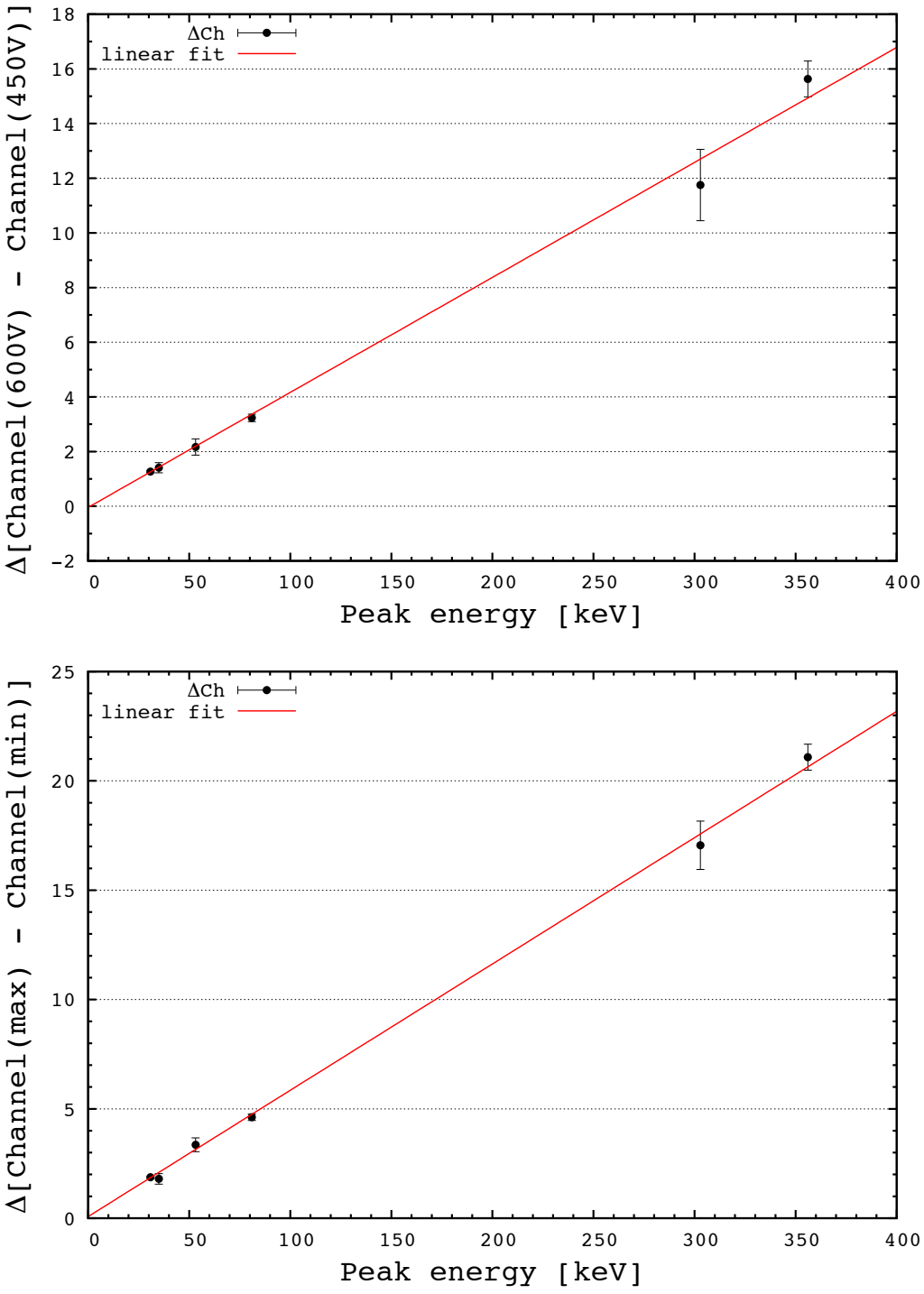

Figure 3.19: Top: Difference in channel number between the fitted peak center in a spectrum recorded at a voltage of -450 V and the peak center for a spectrum taken at -600 V as a function of the peak energy. The linear fit has a slope of m=0.042(1) ΔCh/keV. Bottom: Difference in channel number between the fitted peak center in a spectrum recorded at a voltage of -600 V (maximum channel number) and the peak center for a spectrum taken at -800 V (minimum channel number) as a function of the peak energy. The slope is m=0.058(1) ΔCh/keV.

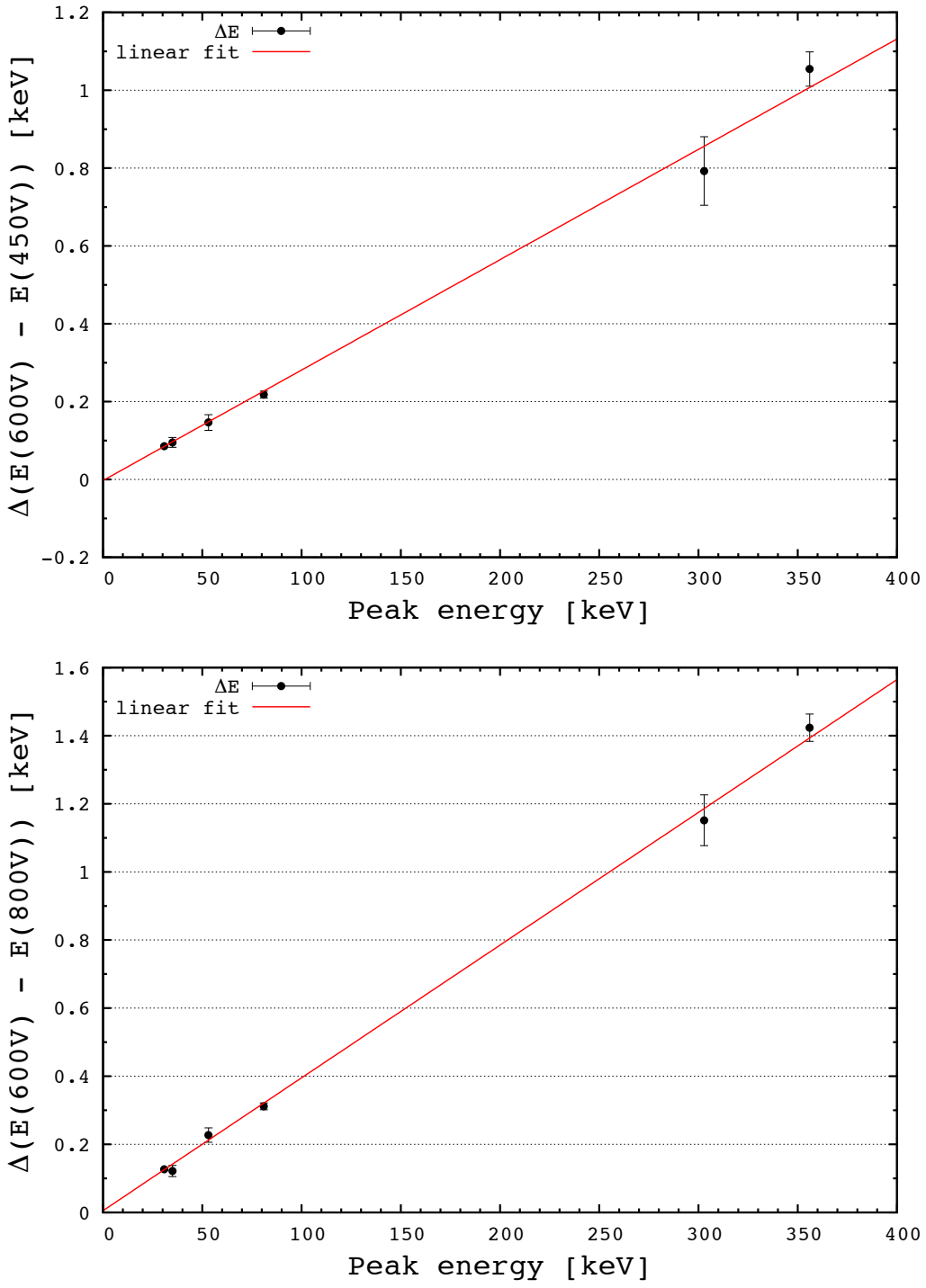

Figure 3.20: Top: Energy difference between the fitted peak center in a spectrum recorded at a voltage of -450 V and the peak center for a spectrum taken at -600 V as a function of the peak energy. The linear fit has a slope of m=0.003(1) ΔkeV/keV. Bottom: Energy difference between the fitted peak center in a spectrum recorded at a voltage of -600 V (maximum energy) and the peak center for a spectrum taken at -800 V (minimum energy) as a function of the peak energy. The slope is m=0.004(1) ΔkeV/keV.

of the order of months [157]. The analysis confirmed the optimal value for the operating voltage to be -600 V, as the detection efficiency at the X-ray energies turns out to have its maximum between -550 V and -600 V, which was the recommended value by Canberra.

	Counts/s					
Voltage (V)	K_α	K_β	53 keV	81 keV	303 keV	356 keV
-450	1040.993(53)	164.78(21)	7.43(4)	35.51(10)	0.33(1)	0.67(1)
-500	1052.50(54)	166.14(21)	7.68(4)	35.59(10)	0.35(1)	0.86(1)
-550	1060.60(54)	169.60(22)	7.58(5)	35.54(10)	0.24(1)	0.79(1)
-600	1062.04(54)	168.30(22)	7.40(5)	36.65(10)	0.31(1)	0.76(1)
-650	1045.13(47)	165.20(19)	7.68(4)	35.22(9)	0.35(1)	0.86(1)
-750	1041.41(51)	169.11(21)	7.41(4)	35.09(9)	0.39(1)	0.75(1)
-800	1036.96(51)	170.57(21)	7.47(4)	35.29(9)	0.38(1)	0.83(1)
-850	1036.34(34)	167.00(14)	7.38(3)	35.29(6)	0.36(1)	0.82(1)

Table 3.7: Dependence of the count rate on the high-voltage for different photon energies.

3.5.5.3 Effect on the energy resolution

The dependence of the energy resolution on the high-voltage is illustrated in Fig. 3.23, where it is plotted in units of % as well as in eV as a function of the voltage. For the X-rays, the resolution gradually decreases between -450 V and -600 V, before it increases slightly at -650 V and continues to decrease again between -650 V and -850 V (see also Tab. 3.8). The resolution at the energies of the 53 keV and 81 keV transitions shows a similar behavior, whereas no clear trend can be determined for the energies at 303 keV and 356 keV. Hence, the operating voltage of -600 V was a compromise between detection efficiency and energy resolution within the X-ray energy region. Similar to the count rate, the changes in charge collection resulting from channeling can cause the overall negative trend of the energy resolution.

3.5.6 Performance dependence on temperature fluctuations

The day-night temperature variations in the experimental hall can be relatively large and fluctuations within 5 °C and up to 10 °C are observed regularly. The maximum temperature measured around the EBIT and thus, around the Si(Li) crystals and preamplifier electronics was $\sim$ 35 °C in the summer. Thermocouple wires are installed around the EBIT as well as

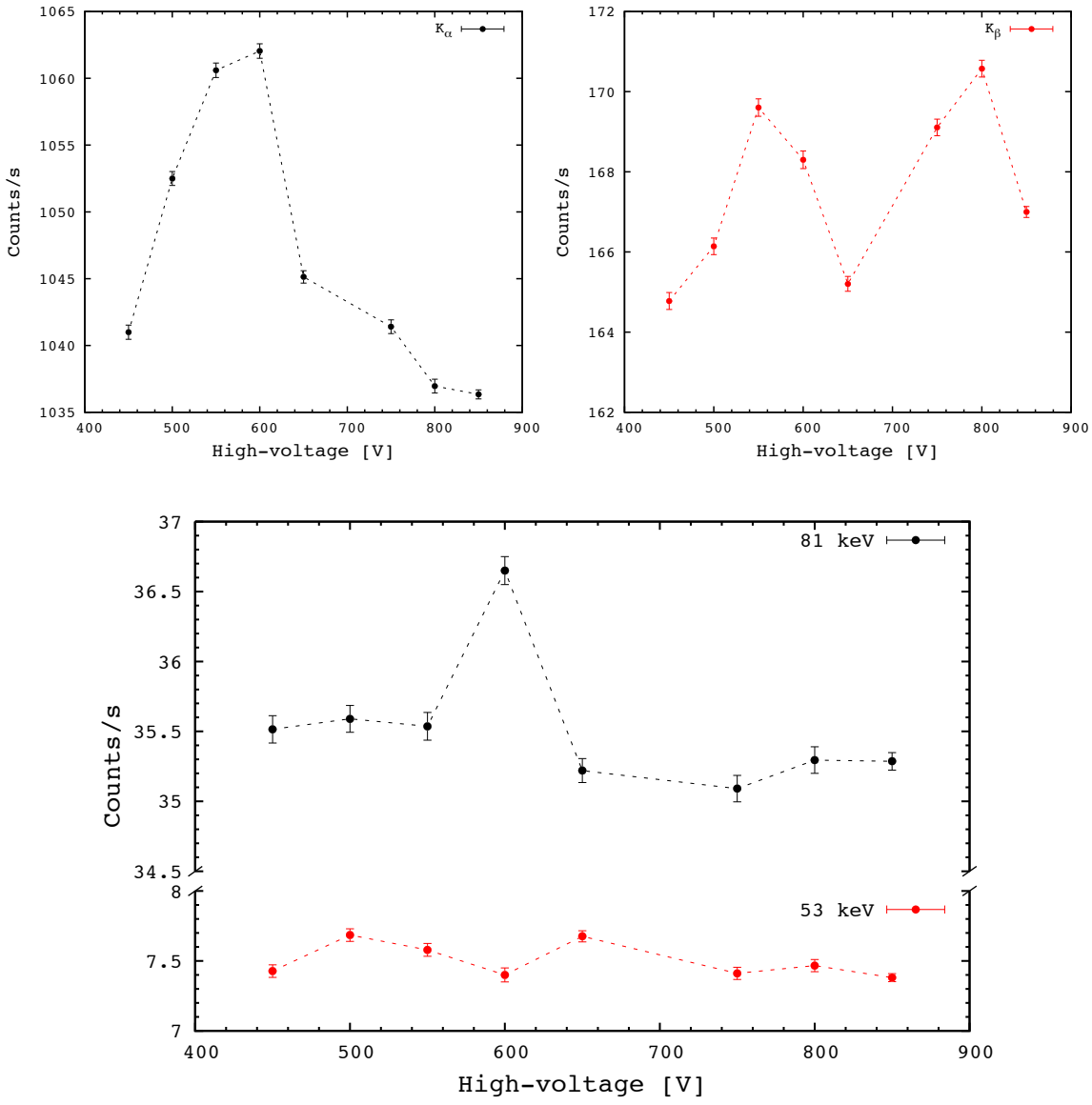

Figure 3.21: Count rate as a function of the applied high-voltage for various energies of ^{133}Ba transitions. Note that the polarity of the applied voltage is negative.

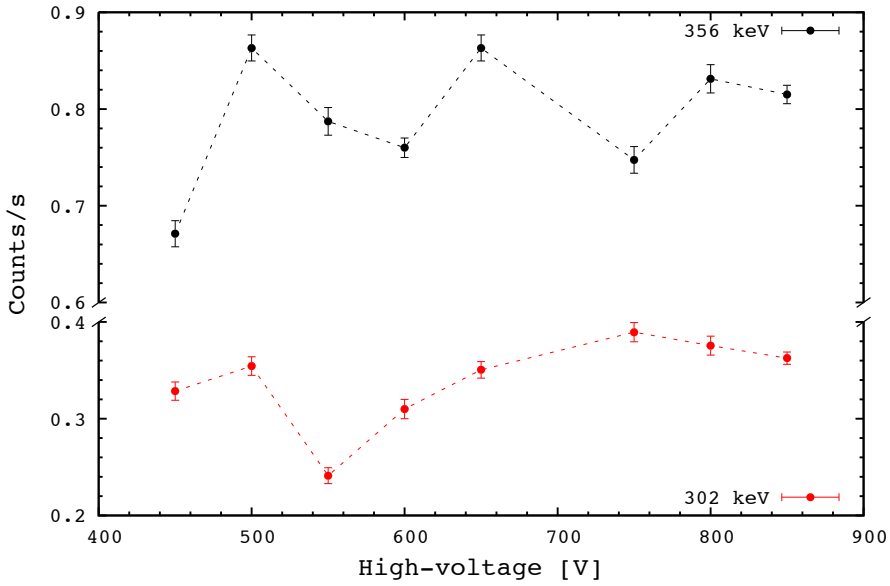

Figure 3.22: Count-rate dependence on the high-voltage for the ^{133}Ba transitions at 303 keV and 356 keV. Note that the polarity of the applied voltage is negative.

around the electronics crate and the read-out is integrated into the EPICS system, which allows for studying the temperature dependence of the detector response.

While the energy resolution and the detection efficiency do not change noticeably as a function of the temperature, the amplification is affected as illustrated in Fig. 3.24. This effect can be understood as a gain drift of the preamplifier electronics with changing temperature. Large variations can broaden the peaks and thus, worsen the signal-to-background ratio as well as the energy resolution for data taken over a long time period of the order of days. The data displayed in Fig. 3.24 were taken over a period of ∼37 h to monitor two day-night cycles. By slicing the data into 1 h time cuts one can fit the 53 keV line in the spectrum of each time cut and generate the trend of the amplification. The average fitted FWHM is ≈ 47 channels. As the correlation to the temperature fluctuations is relatively regular, one can correct the spectra for this gain-drift effect.

Not only are the temperatures around the EBIT monitored, but also the temperature around the ADC and the preamplifier power supply. Maximum temperatures of up to 40° were recorded, which means that the ADC is operated at temperatures well above its specifications of maximal 25°C. This might further influence the gain drift. In order to reduce

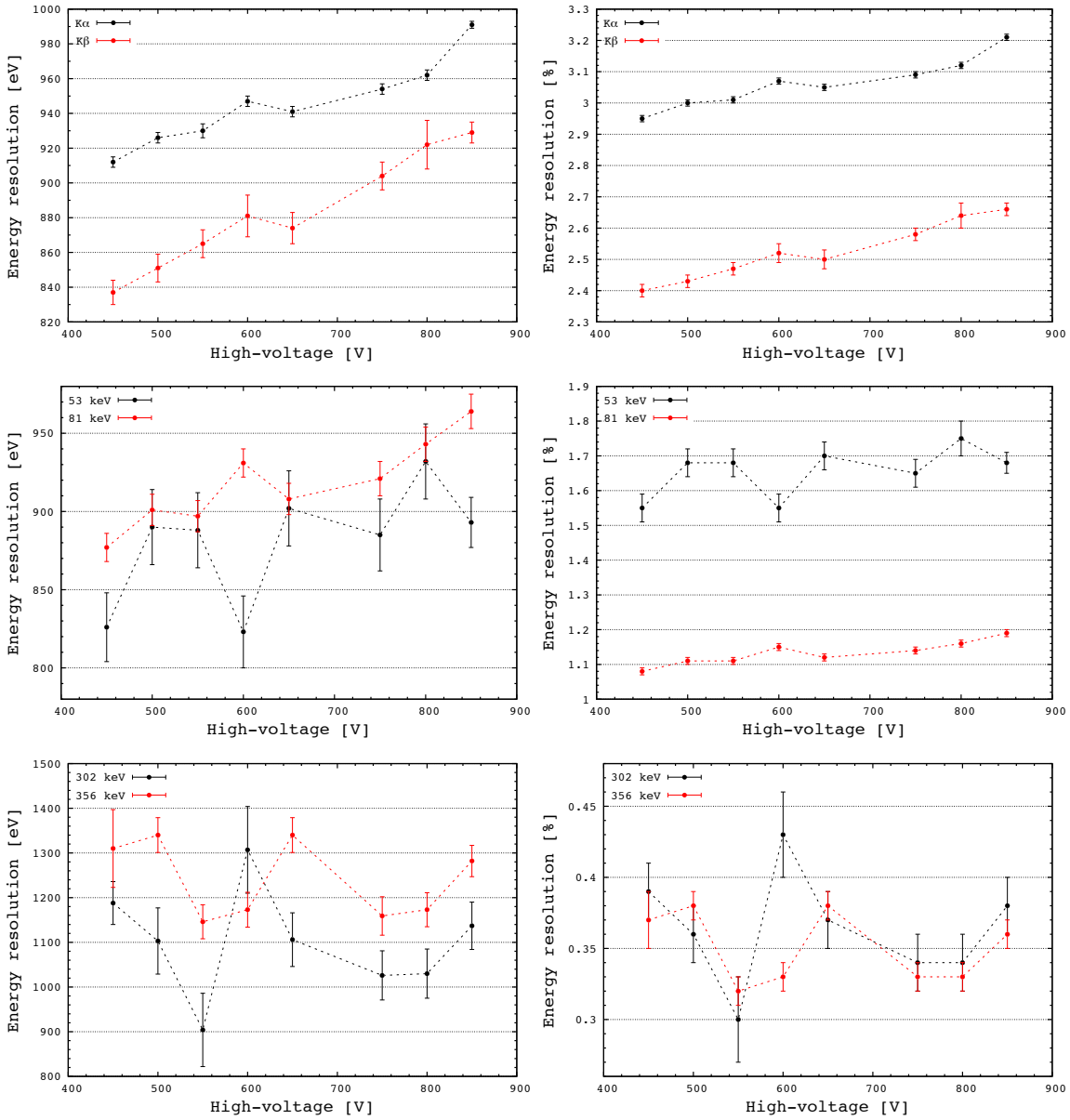

Figure 3.23: Energy resolution for various energies between 30 keV and 384 keV as a function of the applied high voltage. Note, that the polarity of the applied voltage is negative.

Voltage (V)	Energy resolution [%]					
	K_α	K_β	53.161 keV	80.99 keV	303 keV	356 keV
-450	2.95(1)	2.40(2)	1.55(4)	1.08(1)	0.39(2)	0.37(2)
-500	3.00(1)	2.43(2)	1.68(4)	1.11(1)	0.36(2)	0.38(1)
-550	3.01(1)	2.47(2)	1.68(4)	1.11(1)	0.30(3)	0.32(1)
-600	3.07(1)	2.52(3)	1.55(4)	1.15(1)	0.43(3)	0.33(1)
-650	3.05(1)	2.50(3)	1.70(4)	1.12(1)	0.37(2)	0.38(1)
-750	3.09(1)	2.58(2)	1.65(4)	1.14(1)	0.34(2)	0.33(1)
-800	3.12(1)	2.64(4)	1.75(5)	1.16(1)	0.34(2)	0.33(1)
-850	3.21(1)	2.66(2)	1.68(3)	1.19(1)	0.38(2)	0.36(1)
Voltage (V)	Energy resolution [eV]					
	K_α	K_β	53.161 keV	80.99 keV	303 keV	356 keV
-450	912(3)	837(7)	826(22)	877(9)	1188(48)	1310(87)
-500	926(3)	851(8)	890(24)	901(10)	1103(74)	1340(39)
-550	930(4)	865(8)	888(24)	897(10)	904(82)	1146(38)
-600	947(3)	881(12)	823(23)	931(9)	1307(97)	1173(39)
-650	941(3)	874(9)	902(24)	908(10)	1106(60)	1340(39)
-750	954(3)	904(8)	885(23)	921(11)	1026(55)	1159(43)
-800	962(3)	922(14)	932(24)	943(11)	1030(55)	1173(38)
-850	991(2)	929(6)	893(16)	964(11)	1137(53)	1282(35)

Table 3.8: Dependence of the energy resolution on the high-voltage and photon energy. The upper half of the table lists the resolution in %, while the lower half shows the values in units of eV.

possible systematic effects induced by the gain drift, the run time during an experiment is limited to 2 h, while the temperatures at various locations of the setup are monitored constantly.

3.5.7 Conclusion

Studying the performance of the low-energy Si(Li) detectors in the trap environment, i.e., exposed to the EBIT's magnetic field and under high voltage, revealed variations in energy resolution, peak centroid position and detection efficiency. All these properties showed an additional energy dependence. Although not all of the observed effects can be explained, channeling effects, which cause changes in the charge collection efficiency are a possibility. These effects can directly affect the path of charged particles in the crystal and depend on the magnetic field as well as the applied voltage as it has been observed in these studies. The peak centroid shift with varying $\vec{B}$-field strengths or high-voltages does not preclude the use of the Si(Li)s for measurements, since calibration data can be taken under the same

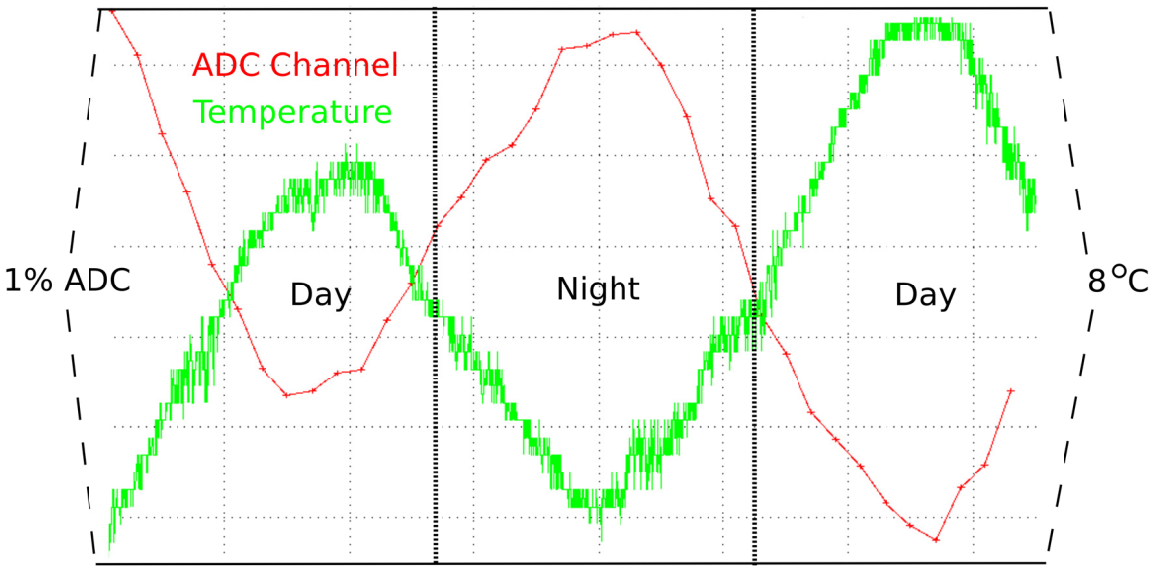

Figure 3.24: Overlay of the measured temperature of the detector environment and the fitted peak centroid (channels) for a particular peak (53 keV line of ^{133}Ba) over a time period of ∼37 h. The temperature scale on the right ordinate shows the interval from 26°C to 32°C, whereas the ordinate on the left presents the ADC channel from 3135 to 3170.

conditions as the online data. For the experiments described in this thesis, the energy calibration was performed using know transitions in the online-data spectra and was therefore not dependent on any source data taken prior to the experiment.

The deterioration of the energy resolution does not preclude the measurements described in this work. A permanent effect on the detector performance caused by the exposure to the magnetic field was not observed, which is consistent with studies performed on HPGe detectors [170].

The effect of the applied high-voltage on the efficiency did not affect the measurements either, since the voltage stayed constant at -600 V, as specified by the manufacturer Canberra. The existing functions for the efficiency are only applicable for correcting spectra taken at -600 V. The fact that the detection efficiency in the X-ray energy region is highest at -600 V had priority over the slight gain in resolution at lower voltages. While the resolution slightly decreases when the detectors are operated in the magnetic field, the efficiency changes are on the order of the analytical uncertainty.

In conclusion, the magnetic field around the EBIT is not favorable for the detector performance, especially the loss in energy resolution needs to be understood in order to optimize Si(Li) detectors for use in magnetic fields. Nevertheless, it is possible to operate the detectors at a suitable resolution in a magnetic field at a constant field strength. This condition is given for the online experiments, where slight $\vec{B}$-field drifts within three days of data taking time are negligible.

3.6 Vibration-induced noise

The Si(Li) detectors are mounted on a custom-built aluminum support structure, which is attached to the base of the EBIT magnet housing and surrounds the center of the EBIT. Vibrational noise at low frequencies around 1.2 Hz generated by the He-compression cylinder is transferred to the EBIT via its cold-head but does not affect the detector signals, as it is filtered out before digitization. However, the fact that additional high-frequency vibrations resonate in the support structure of the detectors is a major concern as they generate acoustic noise of up to a few hundred Hz [130] leading to microphonia noise problems in the detector signals. As a consequence, the detectors cannot reach the specified performance. Fig. 3.25 displays the pulse shape of a captured Si(Li) event featuring a microphonia induced vibration frequency on the order of MHz.

At $\sim$ 120 Hz and $\sim$ 380 Hz, the noise contribution is particularly high. The effect on the detector signal depends on the vibration sensitivity of each detector as well as on its position around the EBIT. As a result of the vibrational noise, which is only present when the compressor is running (compare Fig. 3.26), the energy resolution of the detectors is decreased by up to 20%. To find a solution for this problem, a detailed vibration-sensitivity study was carried out for all detectors.

3.6.1 Vibration diagnostics

For vibration diagnostics, a TinkerForge Inertial Measurement Unit (IMU) [171] that features a 3-axis accelerometer was used to record vibration data on several locations on and around the EBIT with two different detectors. Vibrations were recorded for three dimensions with a run duration of 20-40 s at a sampling rate of 1 kHz and a fraction of a milli-g

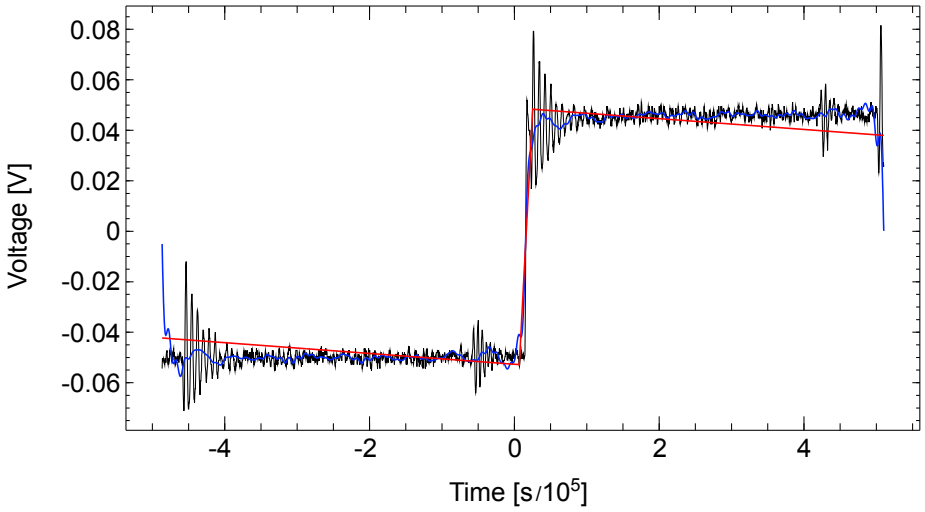

Figure 3.25: Captured Si(Li)-event superimposed by a noise frequency (∼MHz) caused by microphonia. The pulse was recorded at a 25 MHz sampling rate. The blue line shows the back-transformed function after noise filtering and the red line illustrates a rough step function to fit the filtered signal. The distribution of the noise pattern is random and not correlated with the particulars of the pulse shape [156].

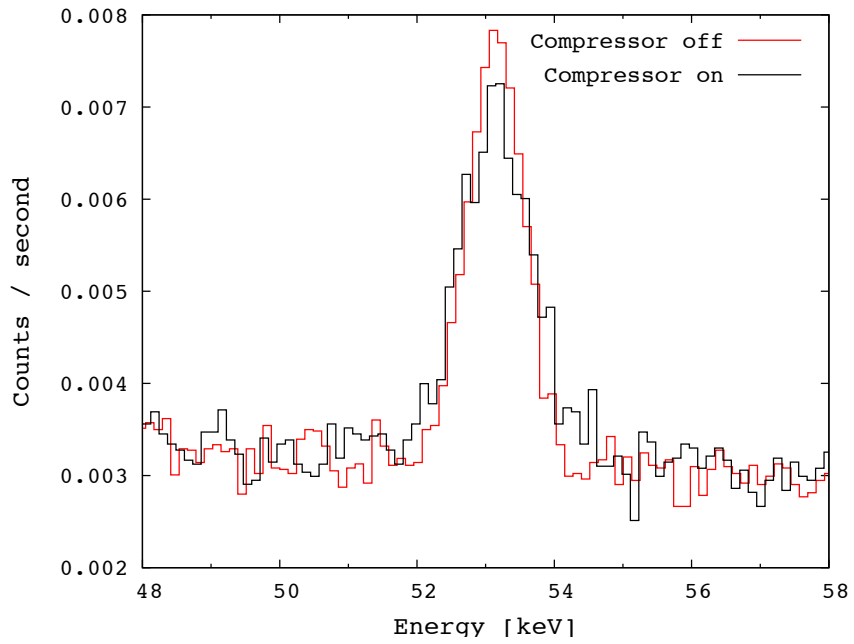

Figure 3.26: Dependence of the energy resolution on the EBIT compressor vibration. The induced mechanical vibrations worsen the resolution from 2.1% to 2.8%.

resolution.

For the tests carried out on-trap, the sensor was placed on the electronics housing of a Si(Li) detector mounted on the horizontal access port at 270°. The detector for the off-trap tests was resting on foam on the platform next to the EBIT, while the sensor was located on the electronics housing as well. Reference measurements were taken when the He-compressor was switched off and compared to the data recorded while the compressor was running. For each data set, the IMU unit records three spectra to cover three dimensions, i.e., north-south, east-west and the up-down movement. The vibration studies showed that the effect of the vibrations originating from the compressor on the detector located off-trap are minimal as long as it is resting on foam. The vibration spectra recorded with the compressor on and off did not display noticeable differences. Removing the foam on the other hand led to a decrease in the energy resolution from 1.6(1)% to 1.8(1)% at 53 keV for the case of the least vibration-sensitive detector of the array. The difference in performance varies from detector to detector and is described in detail in appendix C. Fig. 3.27 displays the vibration spectra recorded with a detector mounted on trap for both compressor settings, where the compressor-induced vibrations at $\sim$ 120 Hz and $\sim$ 380 Hz are visible for all three dimensions. The spectra were generated by performing a fast-Fourier-transform (FFT) on the IMU data. As the studies revealed a vibration reduction by insulating the detectors with foam, further tests with vibration-isolation materials for a modification of the support structure were carried out and are presented in detail in the following.

3.6.2 Vibration-damping materials

In order to reduce the effect of the vibrations on the detector signals, a new support structure design as shown in Fig. 3.28 was developed. In combination with an efficient damping material the structure will reduce the vibration-induced noise and will additionally improve the versatility of the detector array as it will simplify the interchangeability of different photon detector types with different geometries. Design drawings can be found in appendix B. A photograph of a detector mounted within the new support structure on the trap is presented in Fig. 3.28.

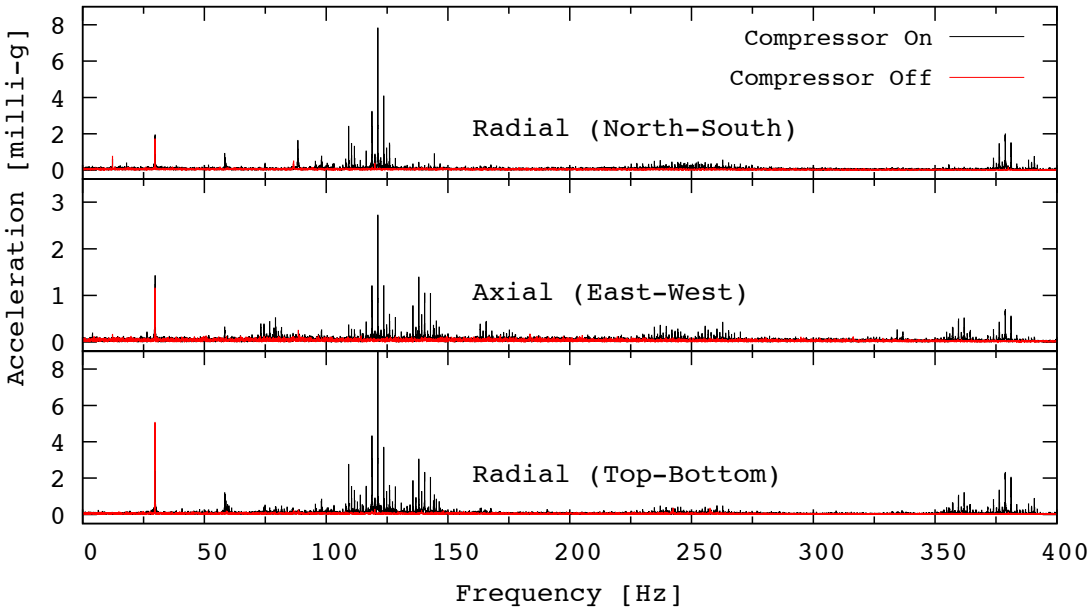

Figure 3.27: Vibration-frequency spectra for three dimensions within 10-400 Hz. The data was recorded with a Si(Li) detector mounted on the horizontal access port at 270° with the cryo-cooler switched on (black) and off (red).

Two materials were tested for vibration damping and isolation, *Polytech®high-density polyurethane foam-grade* 40 (PHU-40) [173], and *POLYFORM®high-density molded - non-skinned (PHDM-NS)* polyurethane foam [174]. The low-modulus PHU-40 material consists of an open cell polyurethane foam with low compressibility as well as low permeability. Additionally, it features a high impact resistance [173]. The PHDM-NS material is a more flexible but still a highly resilient foam with good tear strength and elongation properties. Both materials possess desirable properties for a long-term vibration isolation and their vibration-damping effect was tested via studying the energy resolution and signals for all Si(Li)s at four different settings or, respectively, damping environments:

- **Off-trap**: The detector was tested while resting on a test bench on the TITAN platform isolated from vibrations. The energy resolution achieved in this setup is considered a reference value for the damping-test measurements.

- **No damping**: The detector was tested while mounted on-trap on a horizontal port

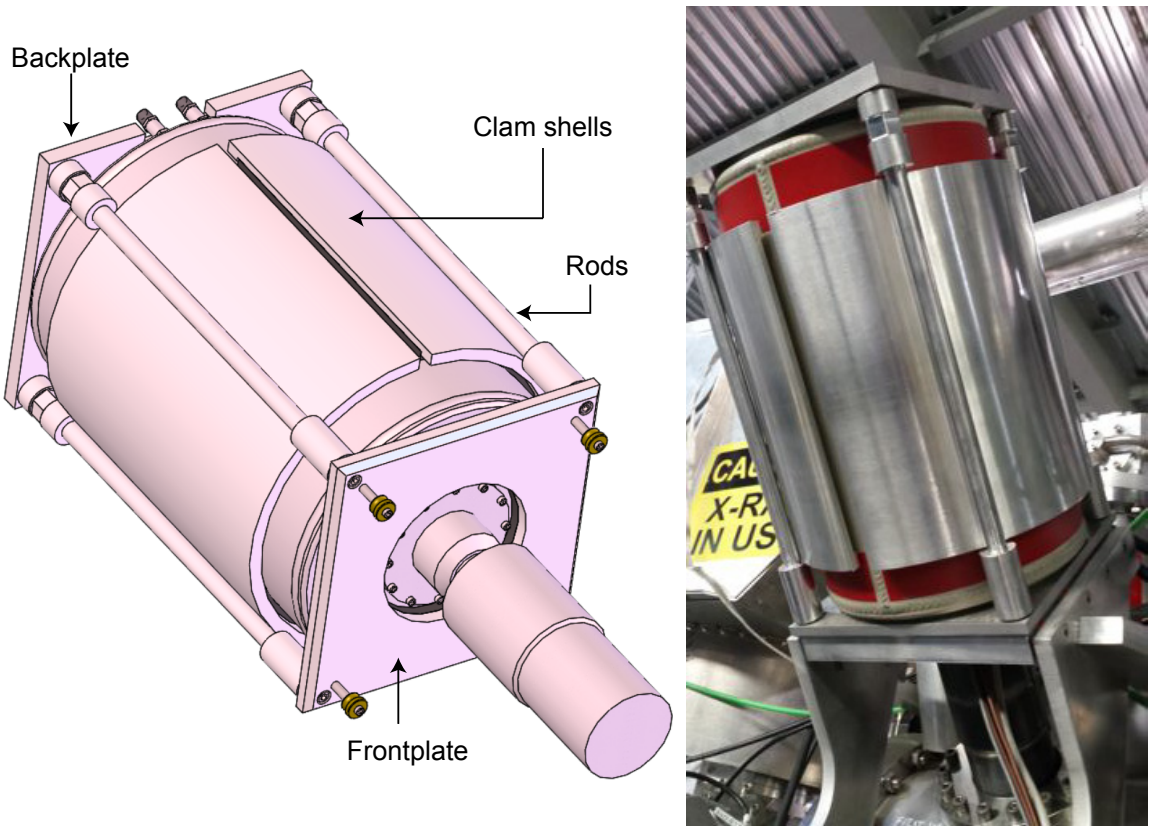

Figure 3.28: Left: Design drawing of a Si(Li) detector in its mounting structure with vibration-isolation material between each contact point (front- and back-plates and a "clam-shell" structure around the dewar) with the support structure [172]. Right: Photograph of a Si(Li) detector mounted in the structure prototype on the EBIT.

	Energy resolution [%]			
Det. #	Off-trap	No damping	PHU-40	PHDM-NS
427	2.0(1)	3.5(1)	2.4(1)	**2.1(1)**
438	1.9(1)	2.4(1)	2.4(1)	**2.2(1)**
404	1.6(1)	1.9(1)	1.7(1)	**1.6(1)**
432	2.1(1)	2.7(1)	2.2(1)	**2.0(1)**
431	2.0(1)	2.8(1)	2.7(1)	**2.0(1)**

Table 3.9: Overview of the achieved energy resolution for five tested Si(Li) detectors depending on the environment and damping material (c.f. Appendix C).

in its support structure. No vibration damping material was applied for those measurements, which was the same situation for the online experiments.

- **PHU-40**: The detector was tested while mounted on-trap with PHU-40 damping material placed between the support structure and the contact points.

- **PHDM-NS**: The detector was tested while mounted on-trap with PHDM-NS damping material placed between the support structure and the contact points.

The test measurements in the trap environment were taken with a collimated ^{133}Ba source facing the detector from the opposite port. Placing the calibration source inside the trap center itself is not possible.

3.6.3 Results of tests

Five out of seven detectors were tested with the two damping materials and the results were compared with the off-trap reference measurements, as well as with the "no damping" runs. The resulting energy resolutions at the 53 keV γ-line from the decay of ^{133}Ba for five out of seven detectors are presented in Tab. 3.9. The remaining two detectors are presently considered unusable for data taking due to technical defects. Details are described in appendix C.

For all tested detectors, the resolution achieved on-trap with the PHDM-NS damping was comparable to the nominal resolution measured off-trap. In general, the results with PHDM-NS were slightly better than for the PHU-40 material and custom-tailored segments to cover the front and back, as well as the dewar of all detectors (see Appendix B) are going to be

implemented permanently in the new support structure.

The above described tests were followed by further studies (February 2015) regarding the dependence of the resolution on the detector position. For detector # 431 an energy resolution of 1.9% was achieved on-trap on the port at 45°, where the detector is mounted in a downfacing position. Therefore, one can also expect a resolution gain for the other detectors of the array.

3.7 Background reduction

Prior to the online experiments, various background measurements were performed in order to study the possible sources of background:

1. general ambient background,
2. background correlated with the beam production and beam transport, and
3. background caused by the nuclear decay of radioactive ions inside the trap. This includes a time-correlated Compton background during the trapping part of the EBIT cycle (compare Sec. 5.4.1).

The ambient background originating from outside the trap is the major contribution to the background spectrum. Figure 3.29 shows the background spectrum recorded during an experiment while the EBIT was empty (compare Ch. 4). This is consistent with the nominal offline background and shows the background-reduction capability of the present experimental setup in combination with the applied EBIT-operation scheme.

3.7.1 Passive background shielding

To avoid contamination of the spectra by the ambient background the housings of all Si(Li) detectors were shielded by a combination of copper and low-activity lead cylinders (see photos in Fig. 3.30), which were designed at TRIUMF and manufactured at the University of Münster. The shields consist of an inner 1-2 mm thick copper shield and an outer 2 mm low-activity lead shield, which covers the entire crystal and preamplifier housing, from the

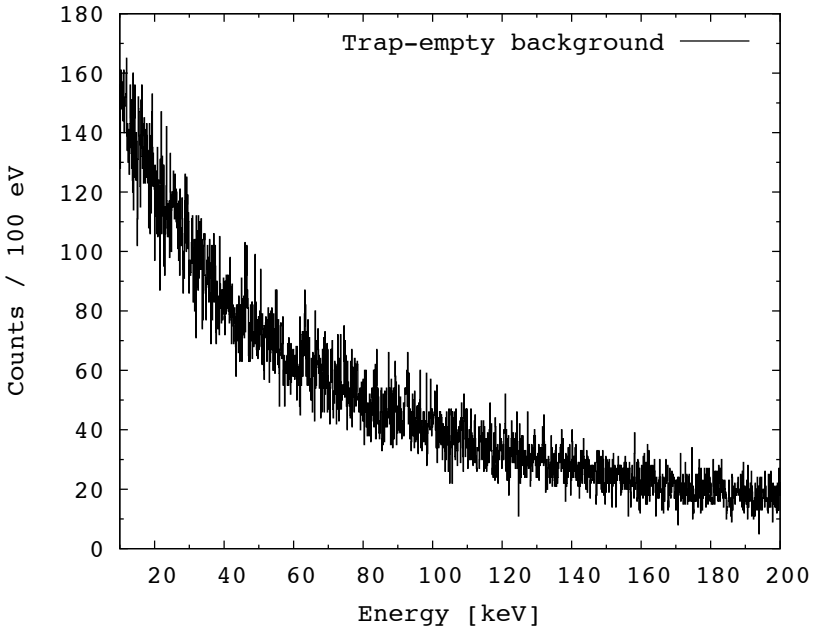

Figure 3.29: Spectrum of ambient photon background in the ISAC I experimental hall shown from 10 to 200 keV. Statistics were accumulated over a period of $\sim$ 10 h.

crystal to the dewar. The copper shield is 1 mm thinner for detectors that are mounted on the smaller access ports due to space limitations. While the lead shield prevents background caused by high energy photons, the copper is important for the Compton background suppression in the low-energy region and the Pb fluorescence X-rays.

A series of measurements with different CuPb-shield combinations (i.e., no shield, Cu shield only, thin and thick CuPb shields) were performed for detectors mounted on the trap, as well as off trap, for which high statistics runs with at least 24 h of data were taken. Fig. 3.31 shows the comparison of the energy-calibrated spectra taken with different types of shieldings normalized to counts per second and with the reference measurement taken off-trap without any shielding (green spectrum). The low-energy cut-off is determined by the ADC trigger threshold.

The EBIT (see black spectrum) acts as an efficient shield itself with a background reduction factor of $\sim$ 2.5 when a detector is mounted on trap without any shielding. The same reduction is provided by a thick as well as by a thin CuPb shield where small difference can be observed below 10 keV, where the thick CuPb shield is more efficient. Evidently,

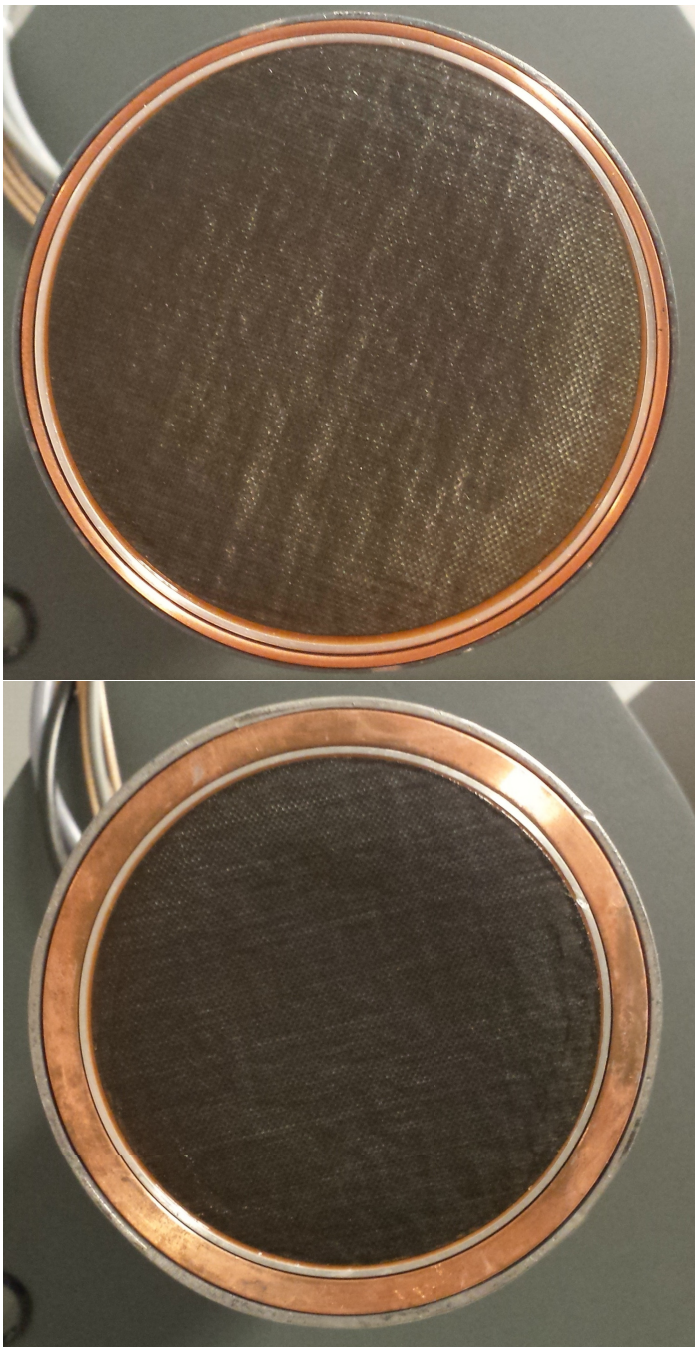

Figure 3.30: Photos of a CuPb cylinder pulled over a Si(Li) electronics housing. Top: Thin CuPb shielding. Bottom: Thick CuPb shielding.

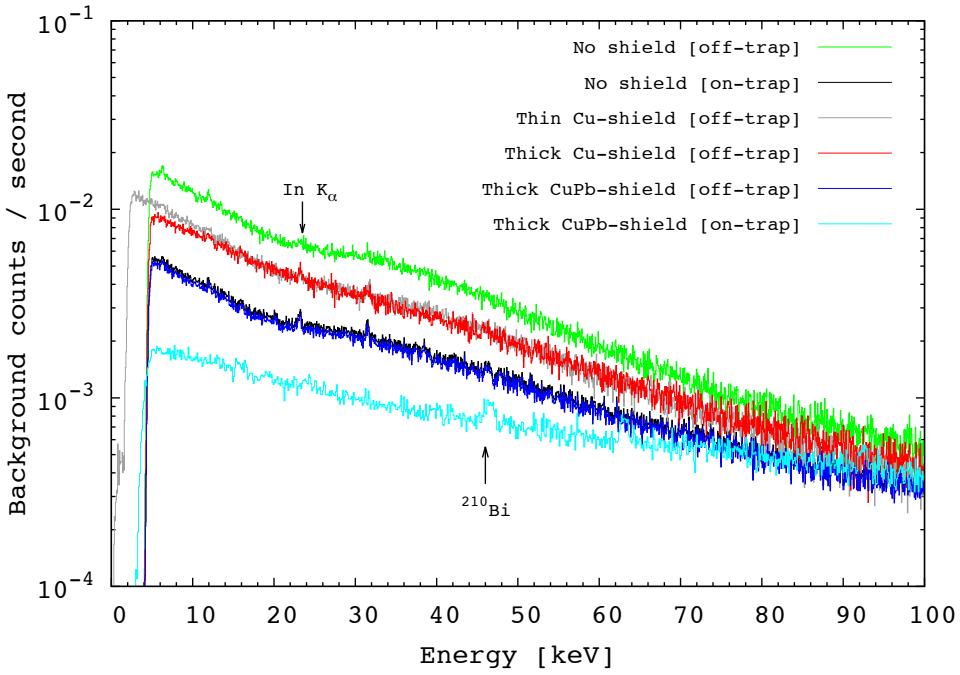

Figure 3.31: Background spectra taken with different CuPb shielding combinations on detectors located on and as well as off trap.

the same trend is visible when comparing the thick and thin copper shields without the lead cylinder. The thick CuPb shieldings in combination with the shielding provided by the EBIT itself allows for a passive reduction of the ambient background by a factor of ~ 5.6 (compare the cyan blue and green spectra in Fig. 3.31). The suppression factors are based on the energy region of interest for X-ray spectroscopy, i.e., at ~ 25 keV.

Some of the spectra in Fig. 3.31 exhibit the indium K-shell X-rays, resulting from the fluorescence of the indium used for mechanical stability. Further, the 46 keV line from the decay of excited states in ^{210}Bi populated by the β^- decay of ^{210}Pb ($T_{1/2} = 22.20(22)$ y, I_γ=4.25(4)%) can be identified in one of the spectra (Thick CuPb-shield, on-trap), which originates from a low percentage of Pb in the material used for soldering the connection point of the crystal and the pre-amplifier.

The trigger rate was monitored for all runs and stayed constant over the entire data-taking time, thus indicating no hardware or DAQ related issues causing the slight background alterations.

3.7.2 Active Compton background suppression

A major background contribution results from Compton scattering inside the detector crystal, when a photon does not deposit its complete energy, but rather exits the crystal volume after scattering off an electron in the lattice structure. The spectrum is characterized by a continuous, low-energy background. This background complicates the detection of low-energy (below ∼100 keV) photons and, hence, impedes the measurements of weak electron-capture branching ratios.

A possibility to increase the detection sensitivity is provided by active Compton suppression, where background events are removed from the data. That technique uses a mechanically robust and high-efficient scintillator, Bismuth Germanium Oxide (BGO)), which has a high Z and thus, a high photon-absorption cross section that surrounds the Si(Li) detector. The effective signal-to-background ratio is increased by vetoing the events with incomplete energy deposition in the Si(Li) crystal.

As the Si(Li) detectors are exposed to the magnetic fringe field of the EBIT (up to 0.15 T at the detector housings), it is no longer possible to use photo-multiplier tubes (PTMs) [157] for the BGO read-out. Instead, the coupling of the BGO crystals to silicon photo-multipliers (SiPMs) is currently being developed to improve the decay-spectroscopy setup [153].

A design concept for the BGO shield prototype is presented in Fig. 3.32. The 18 BGO segments will be located in the flange of the access ports a few mm in front of the Be-window, surrounding the detector radially. The SiPMs will be coupled individually to each crystal segment and will have to be cooled via a Peltier cooling element to reduce dark noise [153]. GEANT4 [175] simulations predict an achievable Compton background suppression by a factor of 4 relative to the reduction achieved with passive shielding in the low energy region of $\sim$ 30 keV. The comparison of A=124 decay spectra obtained with active and passive shielding as illustrated in fig. 3.33 demonstrates the power of active background suppression and the significant gain in sensitivity.

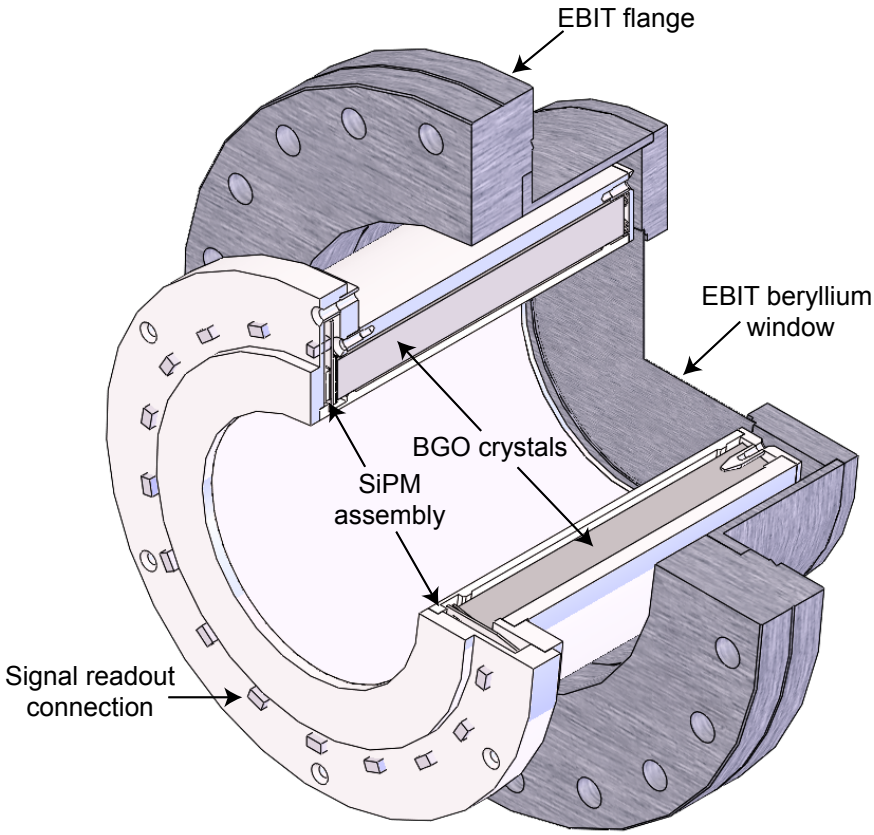

Figure 3.32: A conceptual design of an active Compton suppression shield consisting of 18 BGO crystal segments. The shields are located inside the flange on the outside of the EBIT access ports and surround the detector radially. Figure adapted from Ref. [153].

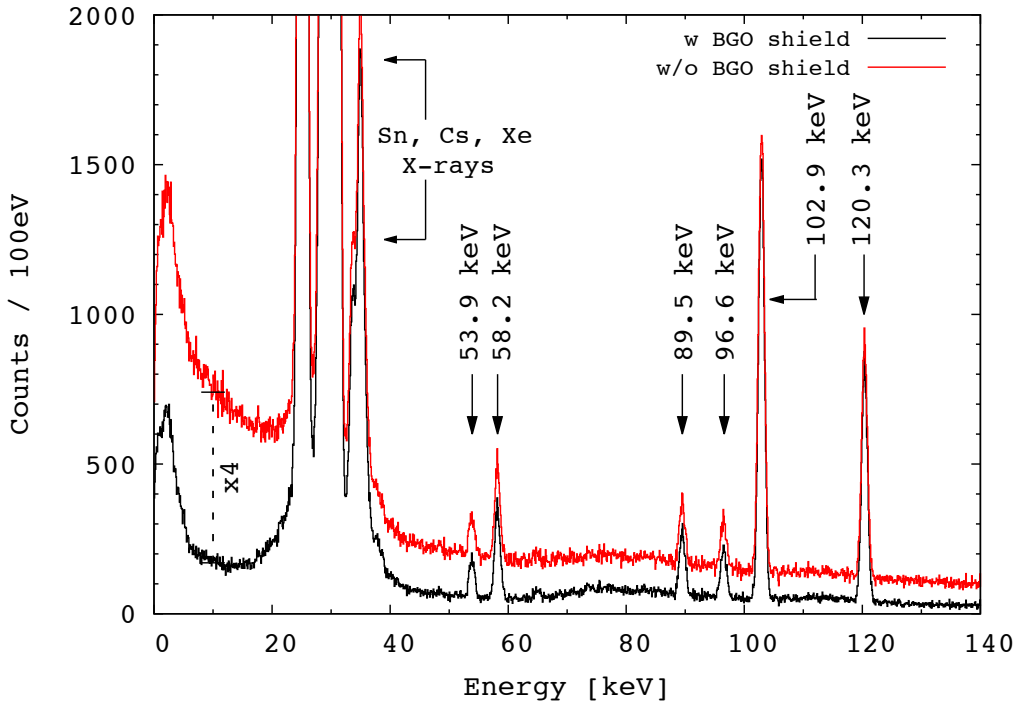

Figure 3.33: GEANT4 [175] simulation to demonstrate the power of active Compton suppression using BGO shields. To simulate the spectra, the same number of events to reproduce a spectrum from the ^{124}Cs experiment [129] taken with one detector was used. The black curve shows a Compton suppressed photon spectrum with 1 cm BGO around the detector. At 10 keV the suppression with BGO is a factor of four higher than for the passive CuPb shielding presented in red. Figure adapted from Ref. [153].

Chapter IV

COMMISSIONING EXPERIMENTS

After assembling the setup of the TITAN decay-spectroscopy apparatus, a radioactive ion beam delivered by ISAC was mandatory in order to test its performance. Presently, the EBIT design does not allow installing an easily removable radioactive source in the trap center for detector calibration with a more realistic source distribution. Furthermore, the TITAN off-line ion source produces stable ion beams only, leaving an online commissioning experiment with a radioactive ISAC beam as the only option to test the setup. Using radioactive beam further offered the possibility to test the ion-cloud confinement as well as the EBIT extraction efficiency via half-life measurements and background studies.
This chapter outlines technical details of the two commissioning experiments on ^{124}Cs and ^{116}In, which includes a description of the setup and beam properties as well as of the applied EBIT cycles necessary for analyzing the time-structure of the recorded data. Furthermore, the beam-tune stability as well as the experimental background are discussed before a more detailed analysis of the decay spectra is described in Ch. 5.

4.1 ^{124}Cs electron-capture decay

A performance test measurement with the decay-spectroscopy setup was performed on the radioactive isotope ^{124}Cs in November 2012 and is reported in a Phys. Rev. Lett. publication [129]. The objective was to demonstrate the successful separation of photons and charged particles in the EBIT for background reduction. Further, the goal of this experiment was to increase the ion-storage time by optimizing the ion-cloud confinement via charge-breeding, thereby providing the opportunity to study the decay of radio isotopes.

4.1.1 Setup and beam delivery

The decision to use ^{124}Cs was motivated by its relatively high electron-capture branching ratio of 7% [169], the favorable ground-state half-life of $T_{1/2}$=30.9(4) s [169], the possibility

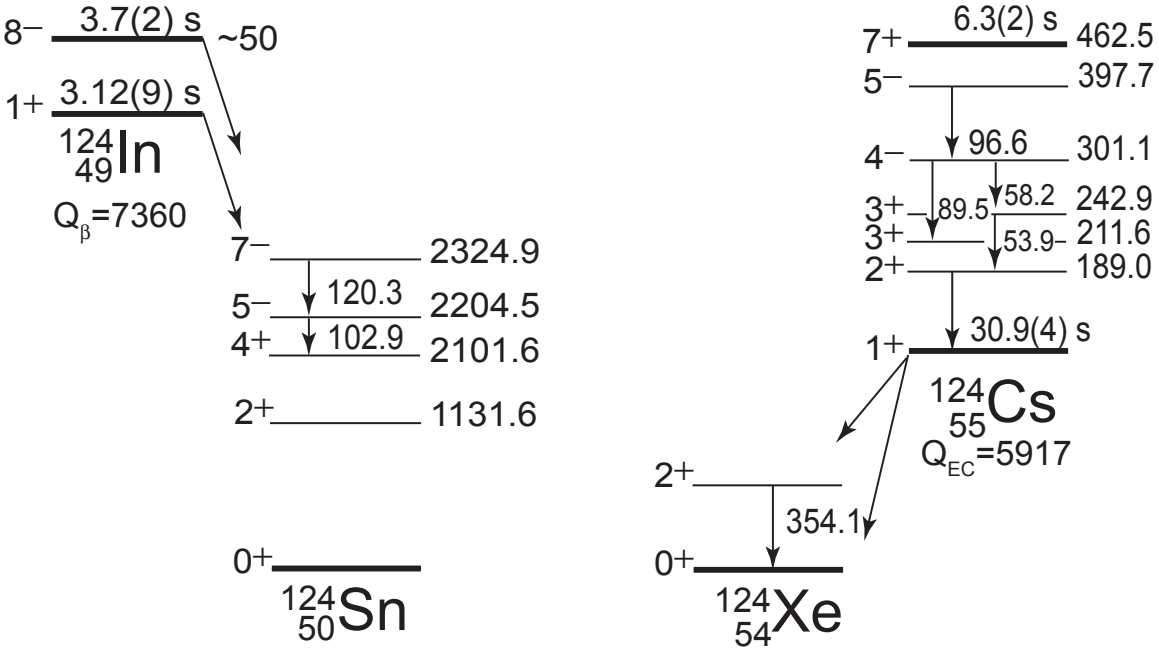

Figure 4.1: Decay schemes of the ^{124}In and ^{124}Cs decay. Transitions observed during the experiment are indicated by arrows [129].

to normalize the detector efficiencies, and the comparatively high yields expected from ISAC. The ISAC beam was composed of the ^{124}Cs, $J^\pi = 1^+$, ground state at an intensity of approximately 8×10^6 pps and of the $J^\pi = 7^+$, 462.5 keV isomer ($T_{1/2}$=6.3(2) s [169]) at approximately 3×10^5 pps according to the yield measurements. It was produced at the ISAC facility by bombarding a uranium-carbide (UC) production target with a 480 MeV, 9.8 μA proton beam in combination with a surface-ionization source. The beam also contained significant ^{124}In contamination, which appeared predominantly as the $J^\pi = 8^-$ isomer at $\approx$ 50 keV excitation energy [169]. A contribution from the $J^\pi = 1^+$ ground state was not observed, as it decays via β^- decay into the ground state of ^{124}Sn. Both components are short-lived and feature a half-life of the order of three seconds ($T_{1/2}(g.s.)$=3.12(9) s, $T_{1/2}(8^-)$=3.7(2) s [169]). The rather high level of ^{124}In contamination was due to the use of the UC-target, since in a former experiment [146, 150], which used a Ta-target, no detectable ^{124}In component was observed in the spectra. The relevant decay schemes of the two nuclei together with their isobars are shown in Fig. 4.1.

The beam was delivered to the TITAN-RFQ at an energy of ~20 keV and was injected

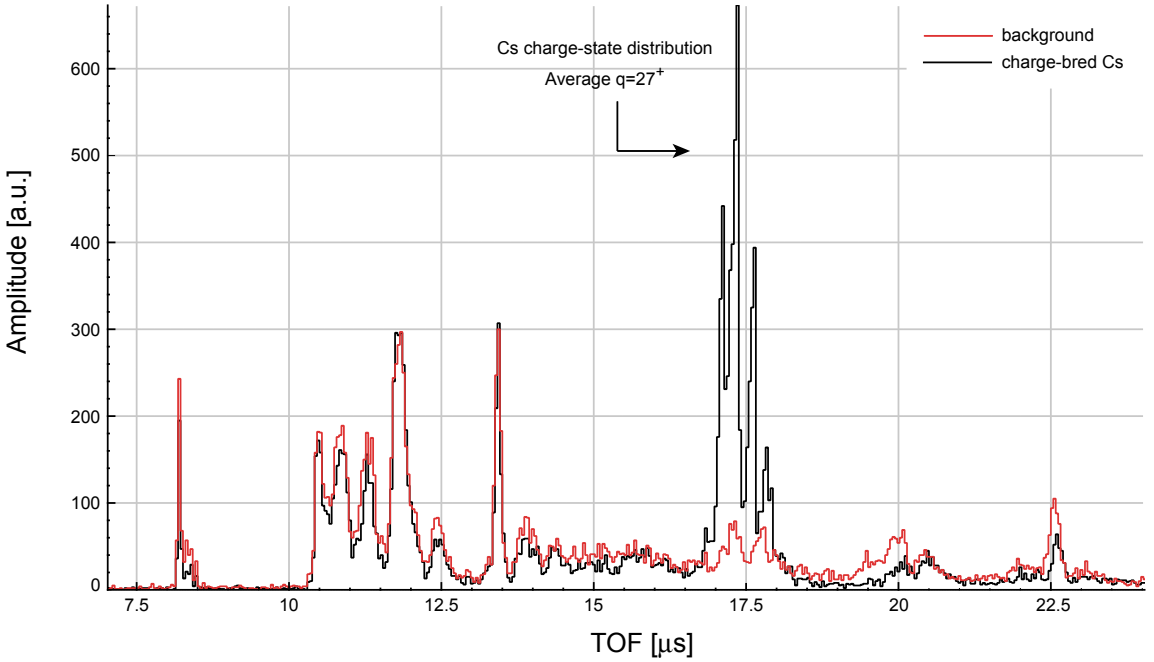

Figure 4.2: Charge-state distribution for ^{124}Cs. The red spectrum shows a charge-bred spectrum without A=124 beam injected into the EBIT. The black curve presents the charge-bred spectrum with A=124 beam inside the EBIT. The electron-beam energy was 1.5 keV.

into the EBIT using a transport voltage of 1 kV. Beforehand, a uranium pilot beam with a measured current of 17 nA on Faraday Cup 3 (FC_3) was tuned through the RFQ in DC and bunched mode, before the bunched mode was optimized on the ^{124}Cs beam.

In order to lengthen the trapping times, the trapping efficiency and ion-cloud confinement in the EBIT had to be optimized. Therefore, the ions were bombarded with a high-intensity electron beam of 85 mA across a voltage drop of an extra $U_{cath} = 500\ V$ resulting in an electron-beam energy of 1.5 keV. At these settings the ^{124}Cs-ions were charge-bred up to an average charge state of $q \approx 27^+$. A charge-state distribution is shown in Fig. 4.2.

In order to investigate systematic effects of charge breeding, the cathode voltage was increased from $U_{cath} = 500\ V$ to $U_{cath} = 1000\ V$ over the course of the experiment resulting in an electron-beam energy of 2 keV and an intensity of 100 mA. This increased the charge state for the Cs ions up to an average of $q \approx 32^+$. The electron configurations for Cs at those charge states correspond to a complete removal of the atomic N-shell as well as parts of the M-shell. The effects of charge breeding on the atomic structure are discussed in Sec. 5.5.7.

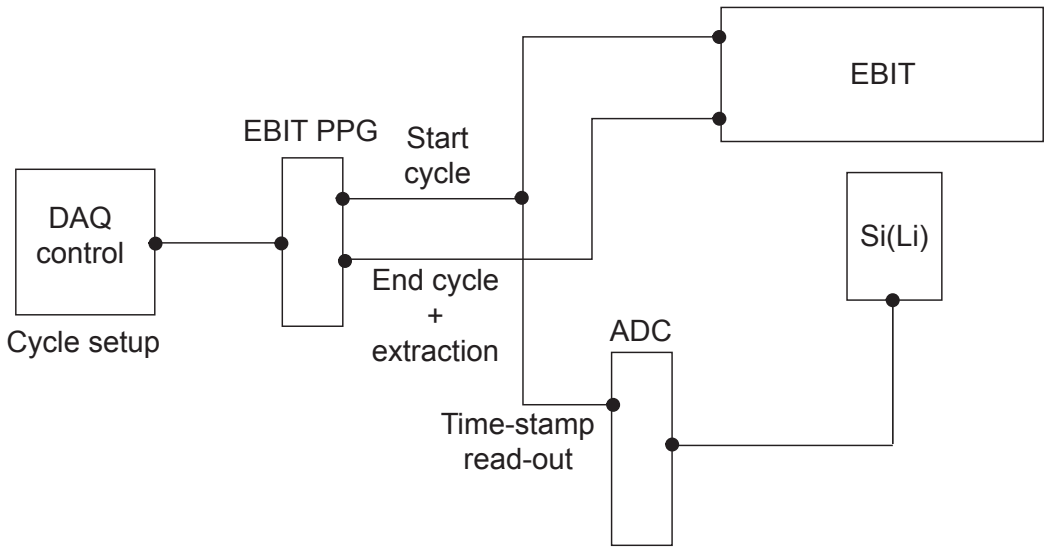

Figure 4.3: Schematic illustration of the time synchronization between ADC and EBIT PPG.

During this commissioning experiment, six Si(Li) detectors for X-ray detection were mounted at the 45°, 90°, 180°, 270° and the 315° access ports of the EBIT and shielded with the cylindric CuPb background shields as described in Sec. 3.7.1. The remaining port at 225° was occupied by an unshielded HPGe detector of ∼40 mm thickness at a distance of ∼30 cm to the Be-window. This detector was used for monitoring purposes and for detecting high-energy γ-rays accompanied with the nuclear decays in the EBIT.

Four out of six shifts of the experiment were used for data collection, while two shifts were required for RFQ and EBIT tuning as well as for optimizing the ADC settings for best achievable energy resolution with the Si(Li) detectors. A total of 18 physics runs equivalent to 172946 s (∼ 48 h) of data taking time are taken into account for the analysis.

4.1.2 Trapping cycle and time dependence

The ADC clock is synchronized to the EBIT PPG and allows recording time-stamped events and, thus time-dependent spectra, which enables half-life measurements. A schematic illustration of the time synchronization is presented in Fig. 4.3.

An EBIT trapping cycle of 30 s total, consisting of either 20 s or 25 s of trapping time and 10 s or 5 s of background-measurement time, respectively, was applied continuously over

run	T_{run} [± 1s]	$T_{trapping}$ [± 1s]	$T_{background}$ [± 1s]	# of cycles	e-beam energy [keV]
760	10872	9061	1811	362	
761	10892	9076	1815	363	
762	10815	9013	1805	361	
763	10950	9125	1825	365	
764	7343	4895	2450	245	
765	7245	4830	2420	242	1.5(1)
766	7564	5043	2520	252	
769	8145	5430	2720	272	
771	2447	1631	82	82	
772	645	430	215	22	
773	9016	6011	3005	301	
777	11997	7998	3999	400	
778	13901	9267	4634	463	
779	10824	9021	1805	361	
782	14466	12055	2411	482	2.0(1)
784	10814	9012	1800	360	
785	9923	8269	1655	331	
786	11854	9878	1975	395	

Table 4.1: Overview of the usable physics runs taken during the ^{124}Cs experiment for two different electron-beam energies. Trapping time and empty-trap background-measurement times of the EBIT cycle are listed individually.

the complete data-taking time. Prior to the start of the background-measurement cycle, the ions were expelled from the trap. Tab. 4.1 lists all runs that granted the data quality requirements and were used for the data analysis. Further, it gives an overview of trapping and background-measurement times.

In the upper part of Fig. 4.4, a decay spectrum summed over all runs and integrated over the full-trap time period from 0 to 20 s is shown for the energy range from 10 to 140 keV. Between 25 and 34 keV one observes the (partially overlapping) K_α and K_β X-ray peaks (shown in the lower part of Fig. 4.4) from the three isobars, i.e., Cs X-rays from the internal conversion (IC) decay of the ^{124}Cs $J^\pi=7^+$ isomer, Xe X-rays from the EC decay of the ^{124}Cs ground-state and Sn X-rays from the decay of excited states in ^{124}Sn populated by the decay of the ^{124m}In 8^- isomer (see Fig. 4.1). Further, γ-rays from the ^{124m}Cs isomer decay are visible in the spectrum at 53.9 keV, 58.2 keV, 89.5 keV and 96.6 keV. The transition at 120.3 keV results from the decay of the 7^- state in ^{124}Sn into the 5^- state, where the 7^- is populated by the decay of the ^{124m}In isomer with a half-life of $T_{1/2} = 3.7 \pm 0.2$ s [169].

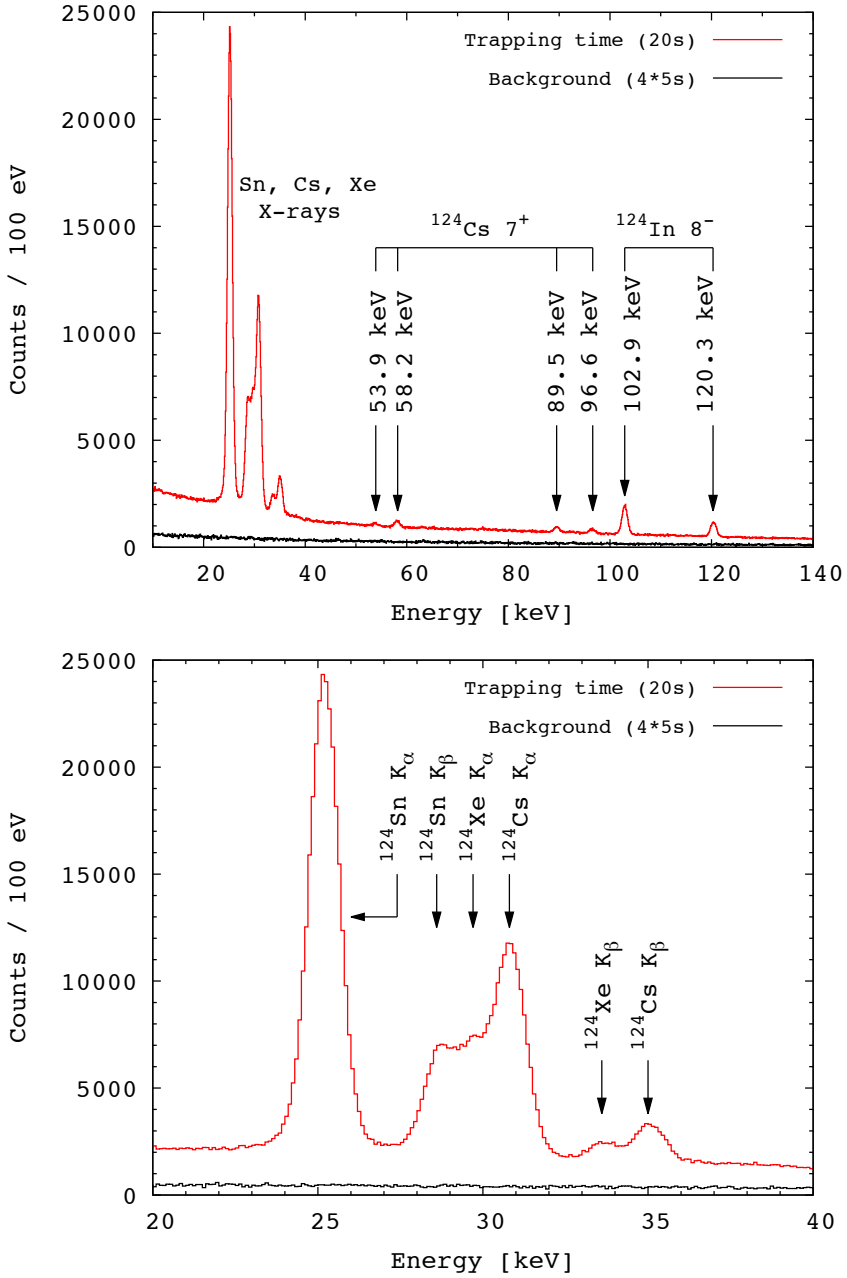

Figure 4.4: Top: Time-integrated γ- and X-ray spectra of the ^{124}Cs and ^{124}In decays. The 7^+ ^{124}Cs isomer produces transitions at 53.9 keV, 58.2 keV, 89.5 keV and 96.6 keV and the 8^- ^{124}In isomer features transitions at 102.9 keV and 120.3 keV. The black spectrum displays the 5 s background measurement scaled by a factor of four for a direct comparison to the 20 s full-trap spectrum. Bottom: Enlargement of the X-ray energy region between 20 keV and 40 keV. The K_α and K_β X-rays from three isobars (^{124}Cs, ^{124}Sn and ^{124}Xe) are visible in the spectrum.

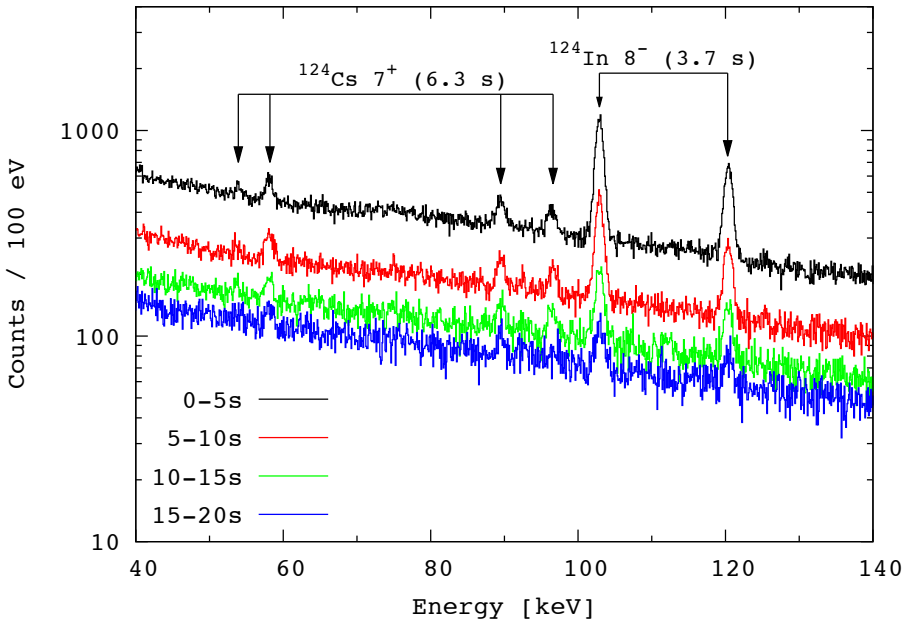

Figure 4.5: Displayed are four time-sliced spectra [0 s-5 s], [5 s-10 s], [10 s-15 s] and [15 s-20 s] within an energy region of 40 to 140 keV to illustrate the time-dependent structure of the data. The background in the first time slice is enhanced by roughly factor of 4.5 relative to the background in the last five seconds. Note the disappearance of the transitions following the decay of the ^{124m}In (8^{-}) and ^{124}Cs (7^{+}) isomers at longer trapping times as a result of the shorter half-lives relative to the ^{124}Cs ground state.

The γ-line at 102.9 keV is assigned to the decay of the 5^{-} state in ^{124}Sn into the 4^{+} state. The ^{124}Cs ground-state decay also populates the first excited $J^{\pi}=2^{+}$ state in ^{124}Xe at 354.01(6) keV, which further decays into the ^{124}Xe ground state under the emission of a 354 keV γ-ray with a relative intensity of 47% [169].

In Fig. 4.5, a comparison of four time-sliced γ-ray spectra for the time intervals [0 s-5 s], [5 s-10 s], [10 s-15 s] and [15 s-20 s] is presented showing the disappearance of the short-lived ^{124}Sn (K_{α} at $\sim$25.2 keV and K_{β} at $\sim$28.4 keV) and ^{124}Cs (K_{α} at $\sim$30.9 keV and K_{β} at $\sim$34.9 keV) X-rays as well as the disappearance of the γ-ray lines at 53.9 keV, 58.2 keV, 89.5 keV and 96.6 keV from the decay of the 6.3 s ^{124m}Cs isomer and of the 102.9 keV and 120.3 keV γ-rays following the ^{124}In(8^{-}) $\longrightarrow$ ^{124}Sn decay. At the same time one observes the enhanced signature of the longer-lived ^{124}Xe X-rays (K_{α} at $\sim$29.6 keV and K_{β} at $\sim$34.5 keV) from the ^{124}Cs ground-state decay as illustrated in Fig. 4.6. Here, the X-ray region between 20 keV and 40 keV for the same four time slices is presented in four separate panels in order to show the dominance of the ^{124}Xe X-rays at longer trapping times.

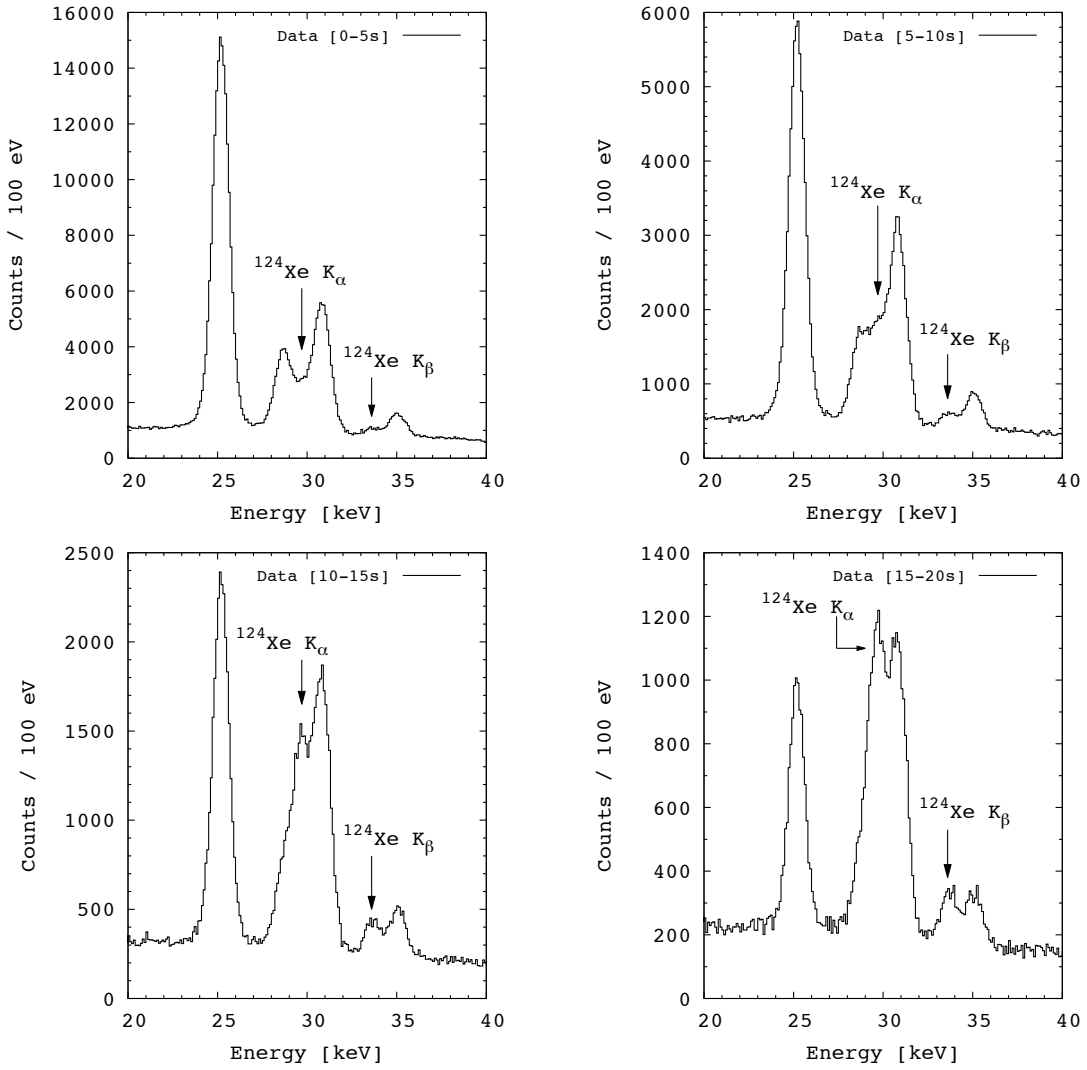

Figure 4.6: Time-sliced X-ray spectra ([0 s-5 s], [5 s-10 s], [10 s-15 s] and [15 s-20 s]) illustrating the time dependence of the data. As a result of the relatively long half-life of the ^{124}Cs ground state, the ^{124}Xe X-rays increase over the 20 s of trapping time where the Xe K$_\alpha$ X-ray becomes the dominant component of the spectrum.

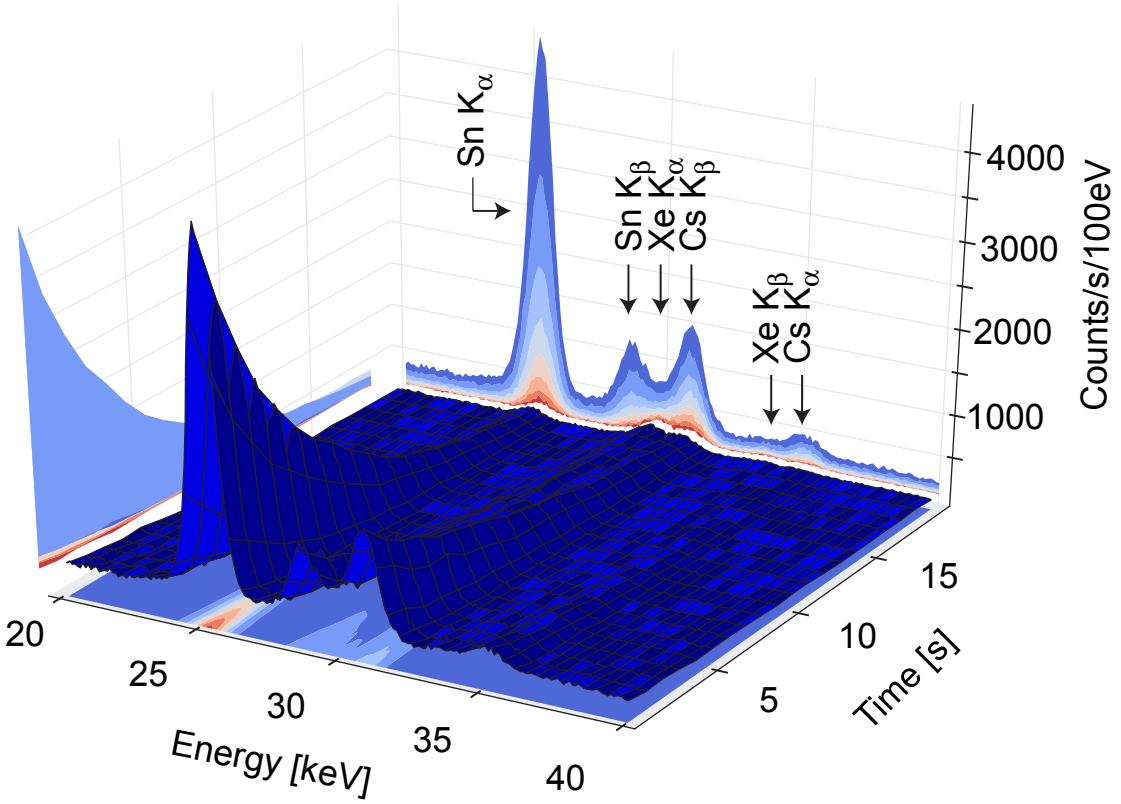

Figure 4.7: Three dimensional illustration of the ^{124}Cs and ^{124}In decays as a function of the trapping time displayed within an energy region of 20 keV to 40 keV to demonstrate the time-dependent structure of the data.

A three-dimensional, trapping-time dependent illustration of the radioactive decay within the X-ray region is presented in Fig. 4.7, where one observes the time- and energy-dependent intensity distribution.

4.1.3 EBIT extraction efficiency

In order to measure half-lives, complete ion extraction from the EBIT at the end of each cycle is essential. To study the extraction efficiency during the ^{124}Cs experiment, the full-trap spectrum is compared to the 5 s background spectrum recorded immediately after the ion expulsion as presented in Fig. 4.4. The background shows no trace of the decay of any of the three species. Especially, the fact that the Xe X-rays from the EC decay of the longer-lived ^{124}Cs ground state have vanished completely, emphasizes the $\sim$ 100% efficient ion extraction. Fig. 4.8 displays the two spectra within an energy region of 300 keV to 400 keV, where the 354 keV transition is visible in the full-trap spectrum, while the background shows

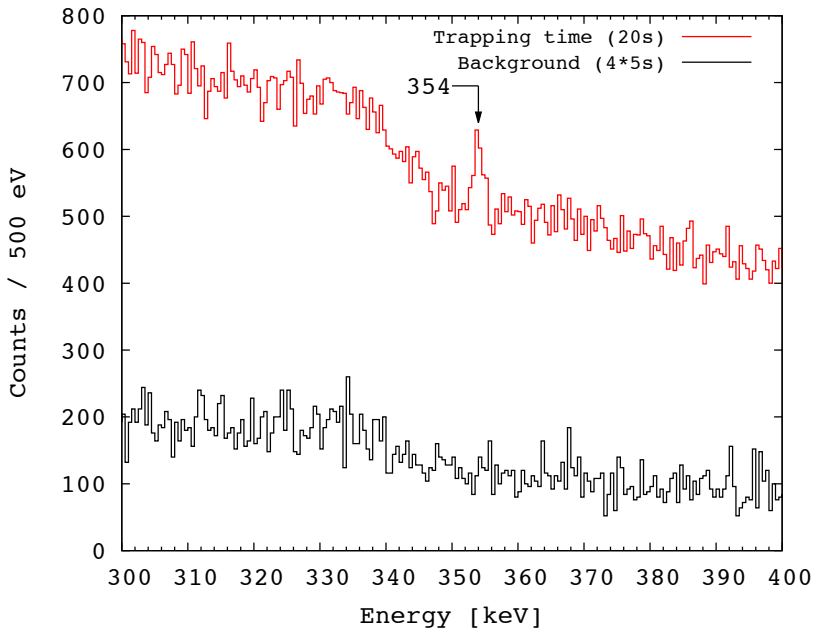

Figure 4.8: Comparison of the 354 keV transition in the 20 s full-trap part of the cycle with the background spectrum directly measured after ion extraction. The background spectrum has been scaled by a factor of 4 for a direct comparison with the time-integrated full-trap spectrum (20 s).

no evidence for the transition, thus also confirming the efficient removal of the ions from the trap. To estimate the environmental background during the experiment and further the possible background caused by beam losses in the RFQ or the beam line, the beam was dumped on FC_0 downstream of the TITAN-RFQ for 2 h while data was recorded. In Fig. 4.9 a comparison of two independent HPGe-spectra taken while ^{124}Cs was trapped inside the EBIT and one HPGe-spectrum taken while the beam was blocked on FC_0 as described above is presented. The HPGe detector did not feature a passive CuPb background shielding and was therefore more susceptible to radiation originating from outside the trap. One notes that the intensity of the 511 keV annihilation line is more than a factor of 2 higher in the background (red) spectrum than it is when ^{124}Cs is trapped and the β particles are guided out of the trap and unable to reach the detector. Contrary to this, the amount of the 354 keV transition is reduced in the background spectrum relative to the count rate recorded during an in-trap measurement. This observation is differs from a previous measurement on ^{124}Cs described in Ref. [146], where the 354 keV line was present in the background measurements.

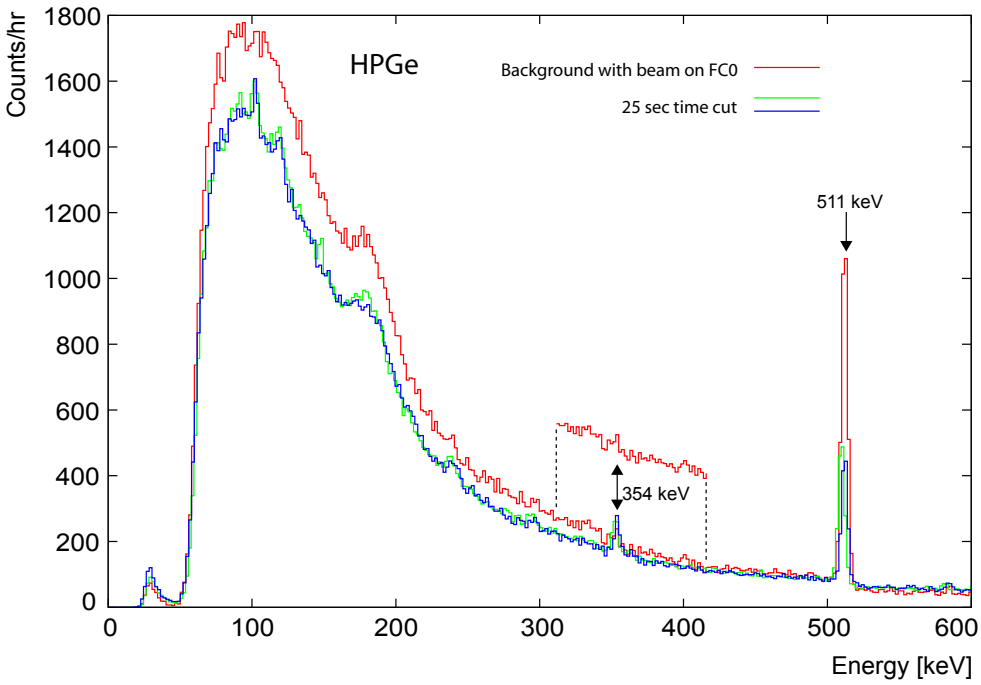

Figure 4.9: Comparison of two HPGe spectra (blue, green) taken while ^{124}Cs was trapped with a HPGe spectrum (red) taken while the ^{124}Cs beam was stopped on FC_0 downstream of the RFQ.

4.1.4 Beam-tune stability

In order to study the tune stability over the course of the ^{124}Cs experiment, the count rate of the ^{124}In K_α X-ray was extracted for each of the 18 runs as presented in Fig. 4.10. The study revealed rate fluctuations from ~ 0.6 to ~ 3.2 counts per second, where a decreasing trend for the first seven runs (760 - 766) is observed before it starts increasing from run 766 to 778. For the last five runs the rate decreases again continuously. Since tuning to higher electron-beam energies was realized after run 773, the tune switch did not affect the count rate. Another explanation are fluctuations of the ISAC beam intensity directly corresponding to less ions reaching the RFQ and consequently the EBIT. However, neither target- and ISAC-optics problems nor beam instabilities were reported over the course of the experiment. Minor drops of the proton current may have contributed to lower rates for some of the runs, but do not explain the clear upwards or, respectively, downwards trends. More likely is a misalignment of the EBIT injection optics, a fact which was indeed discovered after the ^{124}Cs experiment. The collector was found to be misaligned by a few

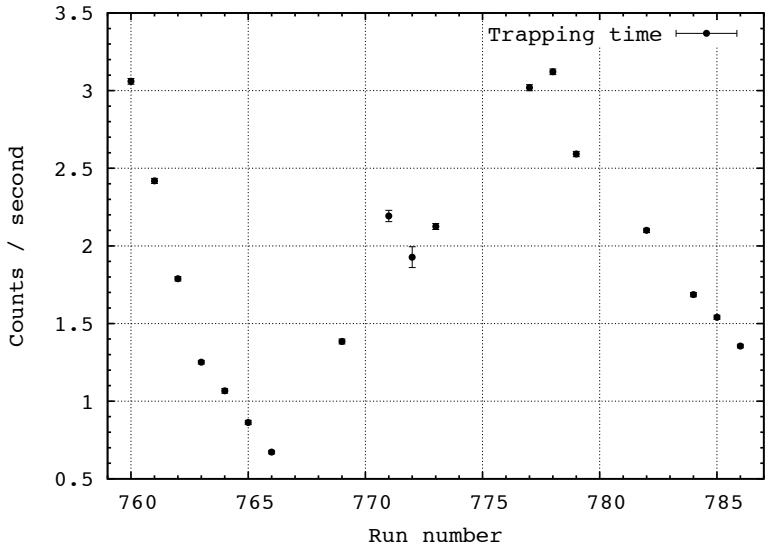

Figure 4.10: Comparison of the Sn K_α X-ray count rates recorded during the trapping time for each of the 18 runs taken during the ^{124}Cs beamtime.

cm, thus complicating the tune into the EBIT and resulting in an unstable injection. This affected the additional objective of the experiment to investigate the dependence of the EC rates on the charge state as it was not possible to increase the transport voltage from the RFQ to the EBIT in order to increase the electron-beam energy. Therefore, only the cathode voltage was changed to reach a slightly higher beam energy.

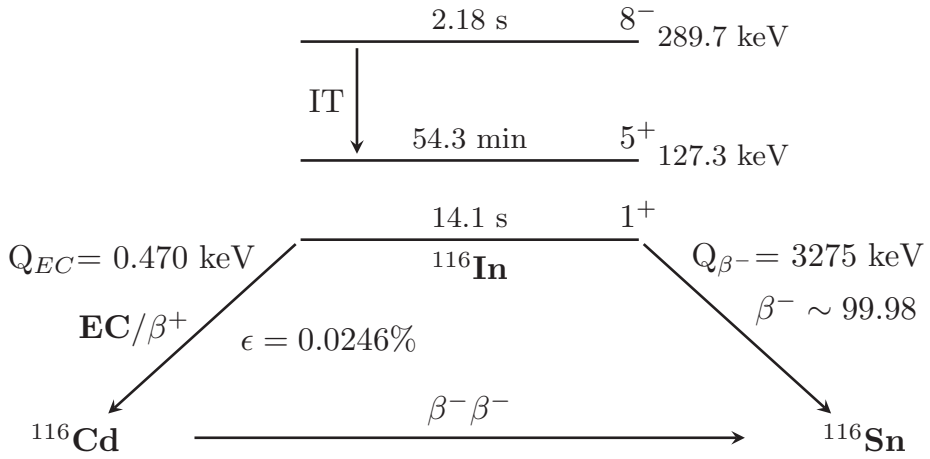

Figure 4.11: Partial decay scheme of ^{116}In including the lowest-lying isomeric states. The indicated value for the branching ratio is taken from Ref. [178].

4.2 A=116 in-trap decay

As a continued commissioning experiment, and a first attempt to measure an ECBR relevant for $\beta\beta$-decay nuclear matrix elements, the decay of ^{116}In was observed in the TITAN EBIT in November 2013.

^{116}In is the intermediate nucleus in the decay of ^{116}Cd with a ground-state half-life of 14.1 s [176]. The strong β^- branch of the ground-state decay of ^{116}In populates the ground state of ^{116}Sn at $\sim 99.98\%$ [169]. Additionally, ^{116}In features two isomers, a $J^\pi = 8^-$-state at 289.7 keV with $T_{1/2}$=2.18(4) s [169] that decays primarily via internal conversion, and a $J^\pi = 5^+$-state at 127.3 keV decaying 100% via β^- emission with $T_{1/2}$=54.3 min [75]. A partial decay scheme is presented in Fig. 4.11.

As the A=116 [^{116}Cd(0^+)-^{116}In(1^+)-^{116}Sn(0^+)] system has more favorable vibrational properties than for instance the A=100 [^{100}Mo(0^+)-^{100}Tc(1^+)-^{100}Ru(0^+)], it is a suitable system to test QRPA calculations [177]. Until recently, the measured ^{116}Cd ground-state EC branching ratio of $\epsilon = (0.0227 \pm 0.0063)\%$ [177] (B(GT)=0.47 $\pm$ 0.13) was in direct conflict with the value of $\epsilon = (0.0019 \pm 0.0003)\%$ deduced from the (^{3}He,t) charge-exchange experiment resulting in a B(GT) value of 0.032 $\pm$ 0.005 [179]. Due to problems with the target in the charge-exchange experiment, the B(GT) was revised to a value of 0.14 $\pm$ 0.03. The authors of Ref. [178] measured the electron-capture decay branch of ^{116}In to be [0.0246

$\pm$ 0.0044(stat.) $\pm$ 0.0039(syst.)]% using Penning trap-assisted decay spectroscopy and claim a corresponding B(GT) value of 0.402 $\pm$ 0.072(stat.) $\pm$ 0.064(syst.), which is compatible with the value (B(GT)=0.28 $\pm$ 0.03) extracted from the latest (p,n) charge-exchange experiment [180].

Current experiments aimed at observing the $0\nu\beta\beta$ decay in ^{116}Cd are already in operation, such as the COBRA experiment [32], which has already tested a prototype of four high-resolution semiconductor detectors made of cadmium zinc telluride (CZT). Furthermore, another ^{3}He,t charge-exchange experiment on ^{116}Cd has been proposed at the RCNP [181].

4.2.1 Setup and beam delivery

The A=116 radioactive beam was produced at the ISAC facility with a high-power tantalum target (proton-beam current of $\sim$ 70 μA) in combination with the resonant laser ionization source and delivered to the TITAN-RFQ at an energy of 20 keV. After loading the RFQ for 25 ms, the ion beam was transported and injected into the EBIT, where the ions were charge-bred to an average charge state of $q \approx 29^{+}$ by bombarding the ion cloud with an electron-beam with an energy of 1.7 keV, which was just low enough to keep the Ar-subshell configuration closed. The beam energy was determined by the transport energy of 1.35 kV to the EBIT and the cathode bias (-350 V). At that cathode bias the maximum stable electron-beam current available was 50 mA. The drift tube potential was set to 290 V (low value 1280 V) and the EBIT capture time was 0.1425 ms with a capture width of 0.0014 ms. The compressor supply pressure was between 1.90 MPa and 2.00 MPa and the EBIT $\vec{B}$-field was calculated to be at 3.96 T. The calculation assumes a loss of 1.2% in strength over 10.5 weeks, with an original value of 4.5 T when the magnet was ramped up.

Similar to the ^{124}Cs experiment, six Si(Li) detectors for X-ray detection were mounted perpendicular to the beam axis around the trap center. The detectors were mounted at the 45°, 90°, 180°, 270° and the 315° access ports of the EBIT and shielded with the cylindric CuPb background shields. The unshielded HPGe detector was positioned in front of the 225° port at a distance of $\sim$30 cm to the Be-window.

A ^{87}Sr pilot beam was delivered from ISAC and tuned through the RFQ. Due to a problem

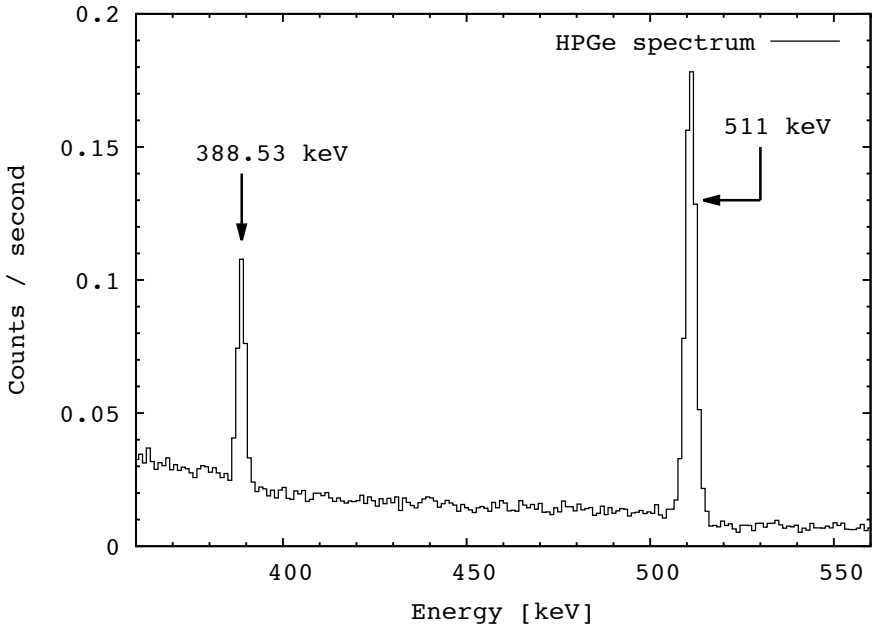

Figure 4.12: HPGe ^{87m}Sr decay spectrum presented within an energy region from 360 keV to 560 keV. One observes the 388.531(3) keV transition resulting from the IT-decay of the ^{87m}Sr isomer [169] in relation to the 511 keV positron-annihilation line from the ambient background.

with the switching logic of the kickers, it is possible that some ^{87}Sr beam was spilled into the RFQ. The latter was noticed by monitoring the HPGe spectrum, where the 388 keV γ-transition [169] resulting from the decay of the $J^{\pi} = 1/2^{-}$ ^{87m}Sr isomer ($T_{1/2}$=2.815(12) h, $I_{\gamma} = 82.4(3)\%$ [169]) into the ^{87}Sr ground state was observed in the spectrum. The HPGe spectrum is presented in Fig. 4.12 and shows the 388 keV transition relative to the 511 keV positron-annihilation line.

The 20 keV ^{116}In ion beam from ISAC delivered to TITAN's RFQ consisted of roughly [10^4:10^6:10^5] of ^{116}In$_{gs:m1:m2}$, respectively (compare Tab. 4.2). According to the ISAC operators, about 1000 pps of ^{116}Cs were observed at the yield station. However, this contamination was not noticeable in the Si(Li) or HPGe spectra of the decay-spectroscopy detector-array and would not have distorted the physics measurement since the Xe X-rays occur at higher energies than those for In, Cd or Sn. The 394 keV γ-transition, which accompanies the decay of the ^{116}Xe $J^{\pi}=2^{+}$ isomer into the ground state was not observed. Yield measurements were performed at the beginning, in the middle and at the end of the experiment showing that the yields for the two ^{116}In isomers as well as for the ground state

Measurement	^{116m2}In	^{116m1}In	^{116}In g.s.
1	2.28×10^5 ± 11.0% pps	4.08×10^6 ± 6.6% pps	2.95×10^4 ± 13.0% pps
2	2.41×10^5 ± 11.0% pps	3.82×10^6 ± 5.0% pps	2.91×10^4 ± 13.0% pps
3	1.90×10^5 ± 11.2% pps	3.37×10^6 ± 6.6% pps	2.41×10^4 ± 11.0% pps

Table 4.2: Overview of the three sets of yield measurements taken before, in between and after the ^{116}In experiment. Even though the yields measured after the experiment are slightly lower than for the previous two measurements, all three sets are consistent within the uncertainties.

remained stable over the data taking time. The ^{116}In decay scheme is displayed in Fig. 4.11, showing the EC and β^- decay into the ^{116}Cd and ^{116}Sn daughter nuclei.

4.2.2 Trapping cycle and peak identification

For the ^{116}In experiment multiple-ion stacking into the EBIT was employed in order to increase the number of ions in the trap [182]. A trapping cycle of 35 s in total was applied over the entire data taking time and consisted of three different parts, injection, trapping and extraction followed by a subsequent background measurement. The RFQ was loaded for 25 ms before each injection, where a total of 600 ion bunches was injected into the EBIT over an injection time of 15 s. Injection and extraction times were on the order of a few μs. After the injection stopped, the ions were trapped for 15 s and their radioactive decay was monitored with the Si(Li) detectors before the ions were extracted and 5 s of empty-trap background were recorded. This was the first time a multiple-ion stacking technique was employed in an EBIT with radioactive ions. Fig. 4.13 shows a time- and energy-dependent decay spectrum of the X-ray energy region demonstrating the ion-bunch stacking followed by the observation of the decay.

The ^{116}In data used for the analysis was taken during a total of 18 runs, which corresponds to a data taking time of 56193 s ($\sim$ 16 h). For the analysis, only the data taken by the three detectors, which were mounted on the large acceptance ports were taken into account because of the better energy resolution of the detectors. Tab. 4.3 gives an overview of those runs and lists the trapping-, injection- and background time separately for each run.

Fig. 4.14 shows the summed spectra for the individual parts of the trapping cycle within an energy region of 0 keV to 200 keV. The green spectrum corresponds to the injection time where 600 ion bunches from the RFQ (25 ms loading time) are injected into the EBIT. In

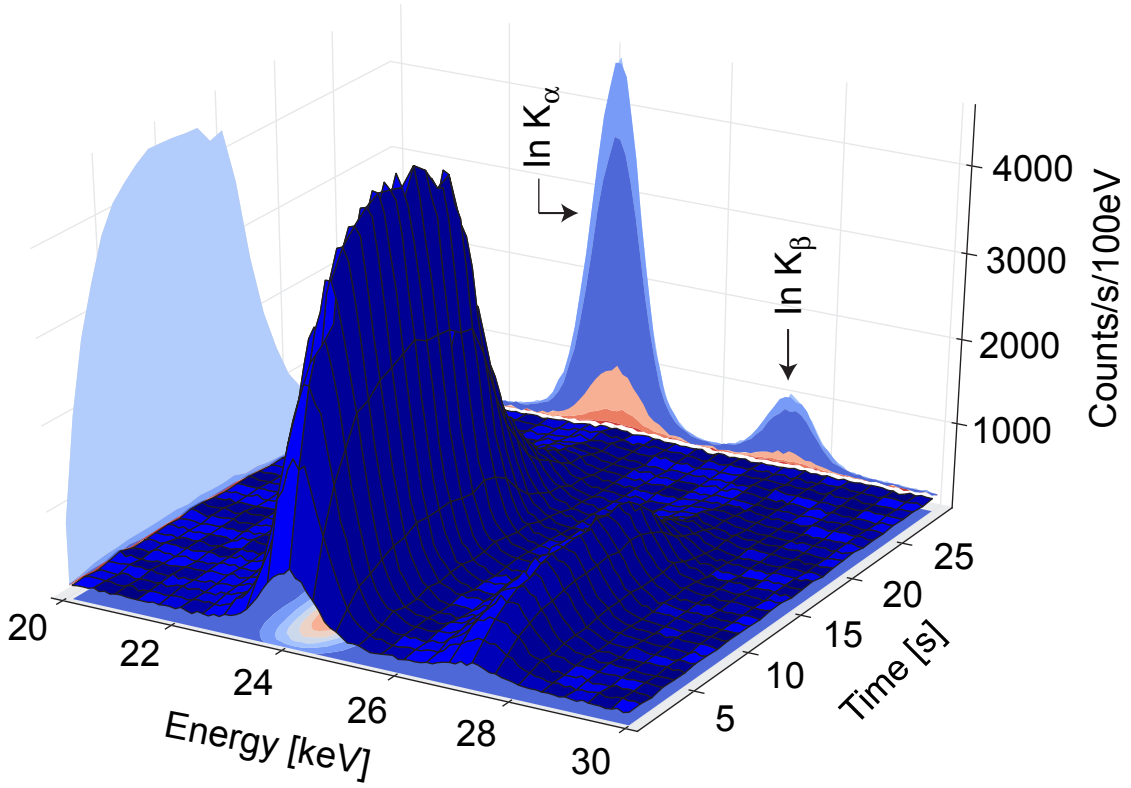

Figure 4.13: Time- and energy-dependent X-ray spectrum illustrating the time structure of the In X-rays resulting from the ^{116}In IT decay. The trap is filled for 15 s at a frequency of 15 ms, before the ions are stored for another 15 s, followed by a 5 s background measurement with an empty trap.

run	T_{run} [± 1s]	$T_{injection}$ [± 1s]	$T_{trapping}$ [± 1s]	$T_{background}$ [± 1s]	# of cycles
1291	4200	1800	1800	600	120
1294	3380	1449	1449	483	97
1296	5306	2274	2274	758	152
1297	2714	1163	1163	388	78
1299	3993	1711	1711	570	114
1300	3098	1328	1328	443	89
1301	2887	1237	1237	412	82
1302	2781	1192	1192	397	79
1303	2805	1202	1202	401	80
1304	2753	1180	1180	393	79
1305	2679	1148	1148	383	77
1306	2662	1141	1141	380	76
1307	2678	1148	1148	383	77
1308	2687	1152	1152	384	77
1309	2668	1143	1143	381	76
1315	3213	1377	1377	459	92
1316	2906	1245	1245	415	83
1317	2783	1193	1193	398	80

Table 4.3: Overview of the usable physics runs taken during the ^{116}In experiment. Injection- and trapping time as well as the empty-trap background-measurement time of the EBIT cycle are listed for each run in addition to the total number of EBIT cycles per run.

red, the actual trapping (closed trap) time is plotted. The sum of injection- and trapping time is shown in black.

An enlargement of the X-ray energy region (20 keV to 32 keV) is displayed in the bottom panel of Fig. 4.14. The peaks visible in the X-ray spectrum are an overlay of the X-rays from three different isobars, ^{116}In, ^{116}Cd and ^{116}Sn (compare Fig. 4.11), which originate from the decay of $^{116}\text{In}(8^-) \longrightarrow {}^{116}\text{In}(5^+)$ (IT), $^{116}\text{In}(1^+) \longrightarrow {}^{116}\text{Cd}(0^+)$ (EC) and the IT decay of several states in ^{116}Sn, whereby the β^- decay of the ^{116}In 5^+ isomer populates the 4^+ state at 3046 keV in ^{116}Sn. Details concerning the X-ray analysis are described in Sec. 5.6 of Ch. 5. In particular, the origin of a weak Sn K_α line noticeable at longer trapping times will be discussed in Sec. 5.6.4.

At 63.1 keV the Compton edge caused by the 162.39 keV γ-ray of the $J^\pi=8^-$ ^{116m2}In isomer at E_x=289.7 keV ($T_{1/2}$ = 2.18 s) is visible in the spectrum. The largest contribution can be observed in the injection-time spectrum (green), while the background spectrum (blue) shows no remains of the Compton edge or the 162.39 keV γ-ray. Note that the spectra for

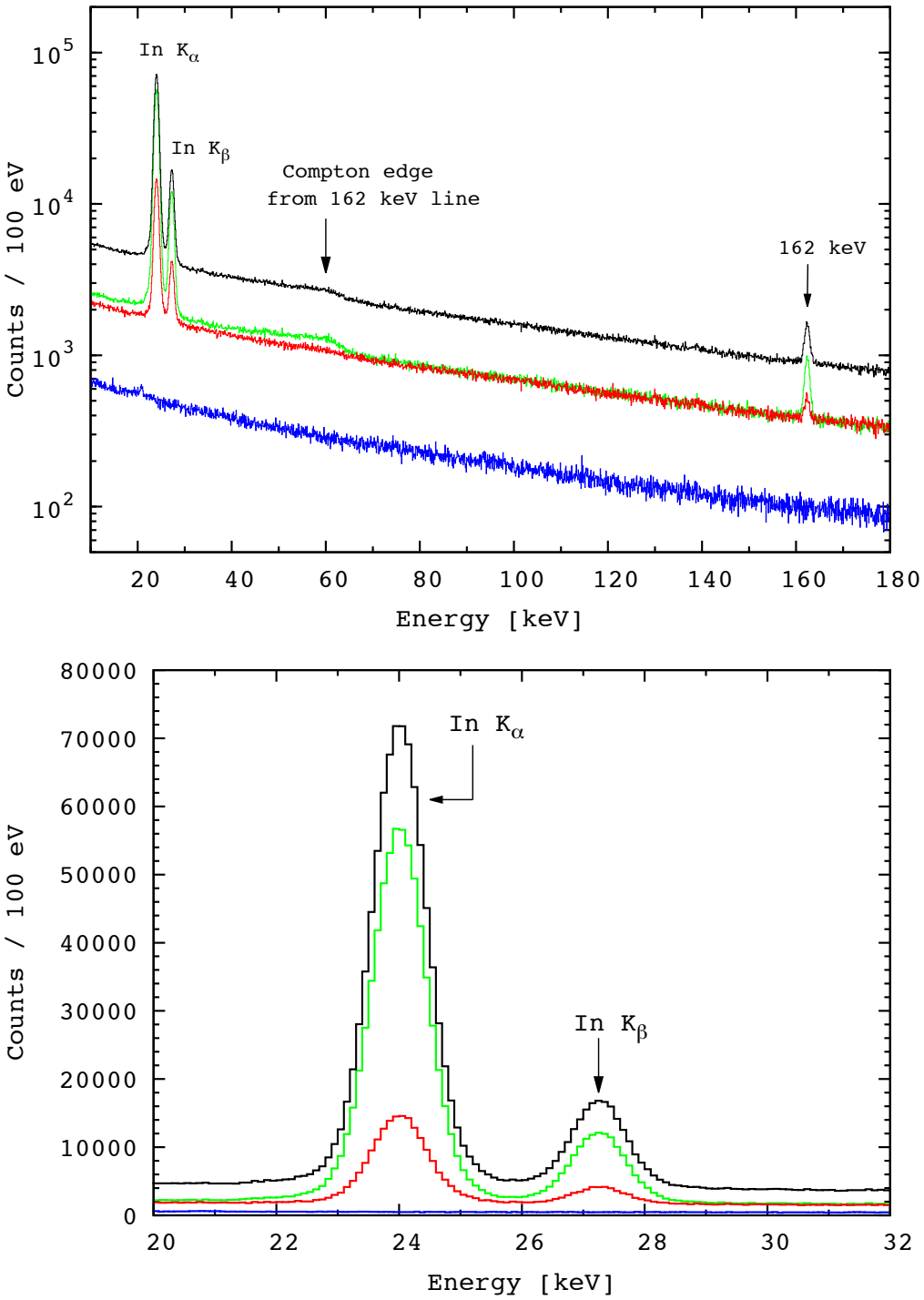

Figure 4.14: Top: ^{116}In spectra for the individual components of the trapping cycle from 0 keV to 180 keV. Each cycle is 35 s long and consists of three parts: 15 s injection time (green), 15 s trapping time (red) and 5 s empty-trap time (blue). The sum of the spectra taken during injection- and trapping time is illustrated in black. Bottom: X-ray energy region from 20 keV to 32 keV. To generate these spectra, the data of 18 runs taken by the Si(Li) detectors on the ports at 90°, 180° and 270° has been summed up.

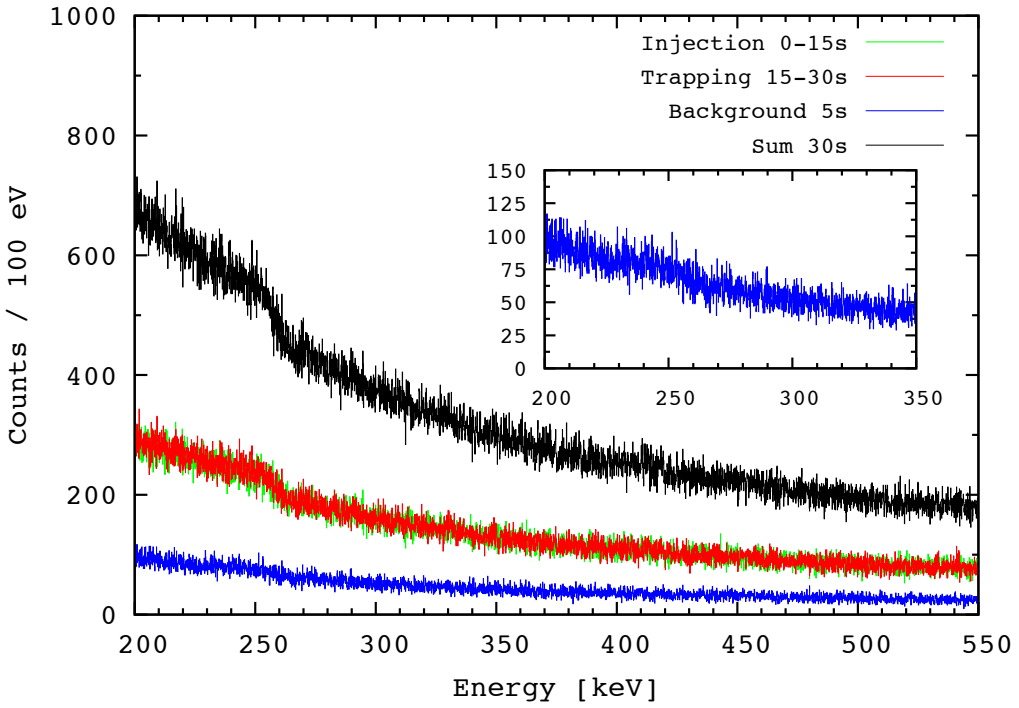

Figure 4.15: ^{116}In spectra for the individual parts of the trapping cycle from 200 keV to 450 keV. Each cycle is 35 s long and consists of three parts: 15 s injection time (green), 15 s trapping time (red) and 5 s empty-trap time (blue). The sum of the spectra taken during injection- and trapping time is illustrated in black. The inset shows the spectrum recorded during the empty-trap time between 200 keV and 350 keV to illustrate the remains of the Compton edge in the background spectrum at 257.7 keV.

injection- and trapping time have similar intensities above the Compton edge except for the energy of the 162.39 keV peak, whereas they differ in the region below the Compton edge. This indicates that above the Compton edge that one only sees background events in both cases.

In Fig. 4.15 the same spectra as in Fig. 4.14 are presented but in the energy region from 200 keV to 450 keV in order to show the Compton edge at 257.7 keV, which is caused by the 416.86 keV γ-ray (27.2% transition intensity) of the long-lived 54.3 min ^{116m}In $J^{\pi}=5^{+}$ isomer at E_x=127.3 keV. Though not visible in the Si(Li) spectra, the occurrence of the 416.86 keV transition can be verified in the HPGe spectrum shown in Fig. 4.17. The inset shows the background spectrum from 200 keV to 350 keV after ion extraction from the trap. Since remains of the Compton edge are still visible in the background spectrum one can conclude that a fraction of the long-lived $J^{\pi}=5^{+}$ isomer must have been accumulated

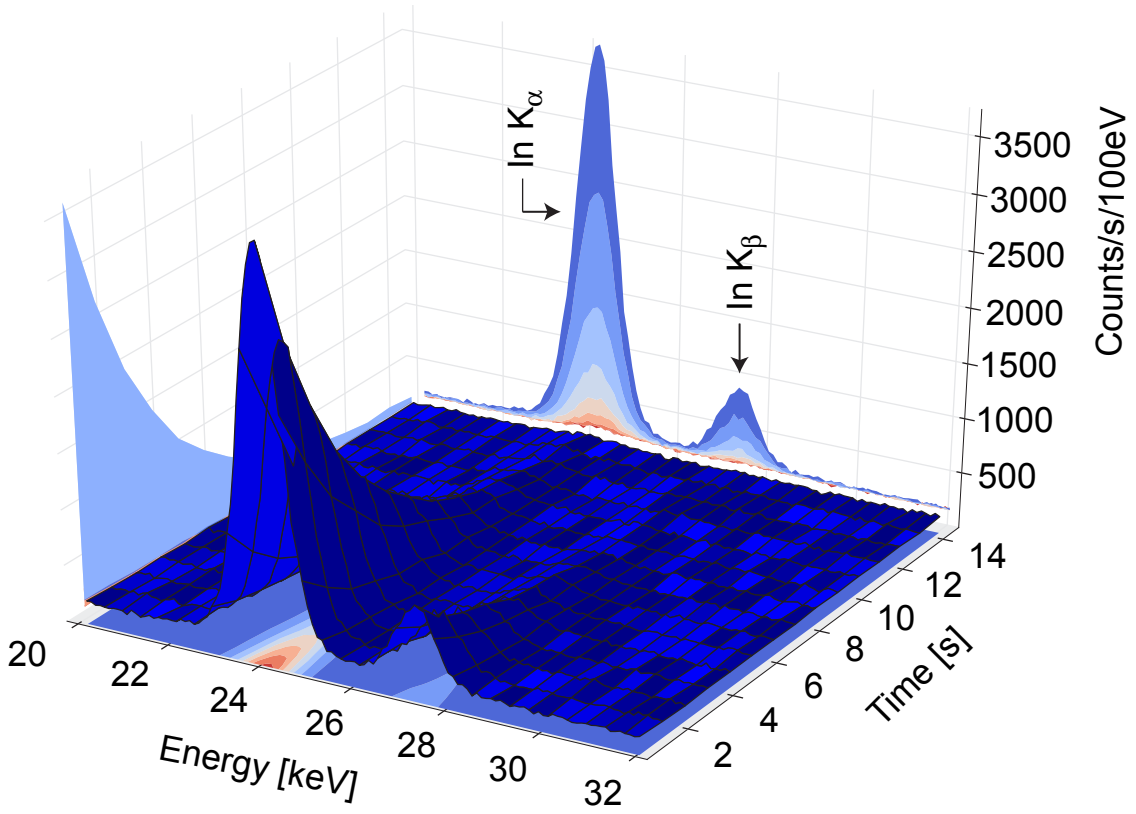

Figure 4.16: Time- and energy-dependent X-ray spectrum illustrating the time-structure of the X-rays from the ^{116}In IT decay within the 15 s of trapping time.

either in or close to the trap. The clean background spectrum at 162.39 keV must not be mistaken as an indication for efficient extraction since one has to consider the short half-life of $T_{1/2}$=2.18 s and that most of the $J^{\pi}=8^{-}$ isomer already decays during the trapping time as indicated by the 3-dimensional illustration of the decay spectrum shown in Fig. 4.16. The decay of the long-lived $J^{\pi}=5^{+}$ isomer populates states in ^{116}Sn (see Fig. 4.18). The decay of the 4^{+} state at an excitation energy of 2529 keV into the next 4^{+} state at 2391 keV features a γ-transition with 138 keV [169]. Due to the long half-life, this transition is ideal to estimate the extraction efficiency. However, due to its relatively low γ-ray intensity of 3.70(9)% and the low detection efficiency of the Si(Li) detectors at that energy in combination with the Compton background caused by the 417 keV transition from the decay of the 4^{+} state at 2391 keV in ^{116}Sn into the 2^{+} state at 2112 keV, only traces of the 138 keV transition can be observed in the Si(Li) spectra. In the germanium spectrum, however, the 138 keV transition is identified unambiguously (see Fig. 4.17). In addition to the 138 keV

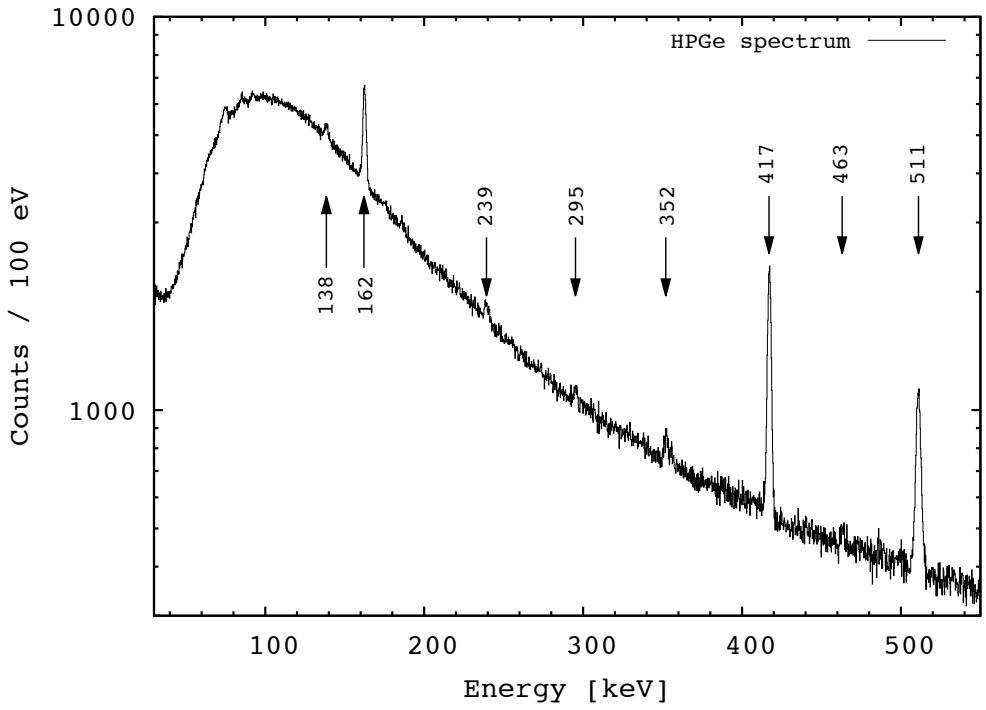

Figure 4.17: ^{116}In-decay spectrum taken with an HPGe detector during the ^{116}In experiment. One observes the γ-rays at 138.29 keV, 416.86 keV and 463.21 keV following the decay of the long-lived $J^{\pi}=5^{+}$ isomer into excited states in ^{116}Sn, as well as the 162.39 keV transition from the short-lived $J^{\pi}=8^{-}$ isomers. The ambient background peak at 238.6 keV results from the decay of ^{212}Pb(Th) and the lines at 295.3 keV and 351.9 keV from the decay of ^{214}Pb(U).

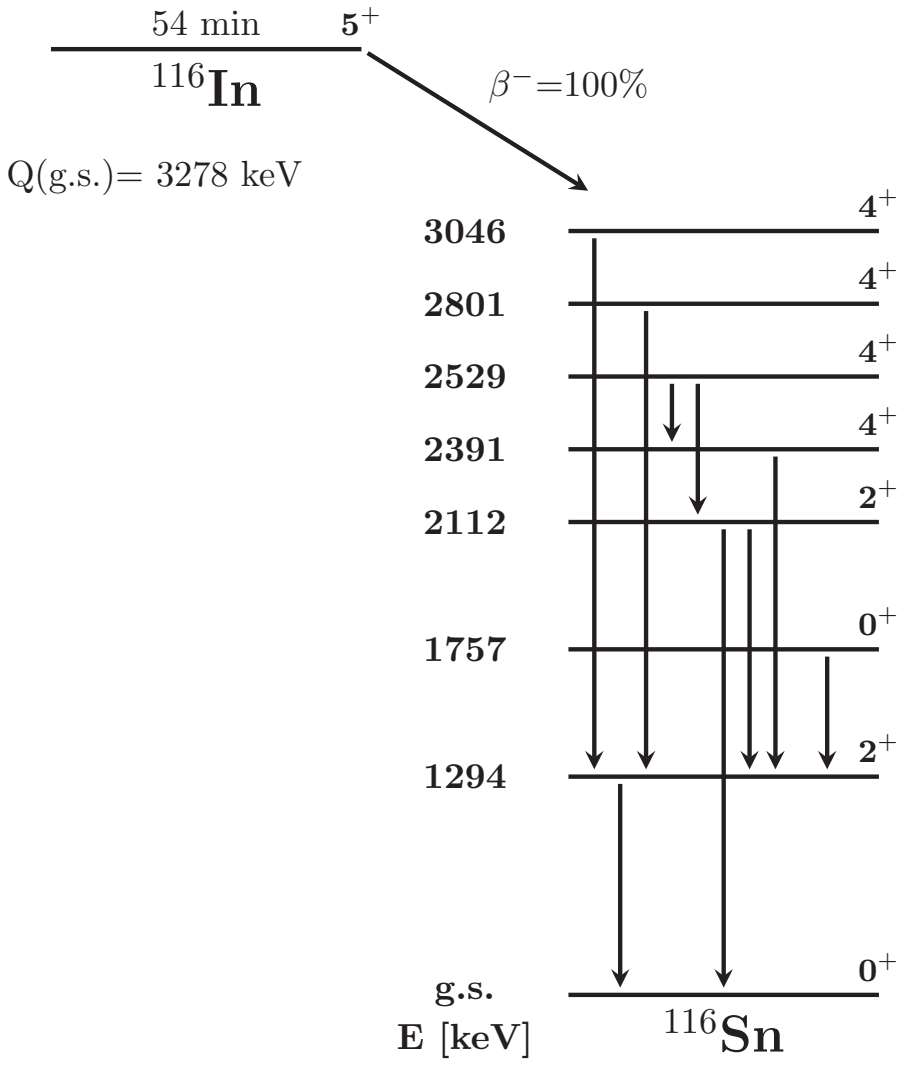

Figure 4.18: ^{116}Sn level scheme. Transitions observed in the HPGe spectrum are indicated by arrows.

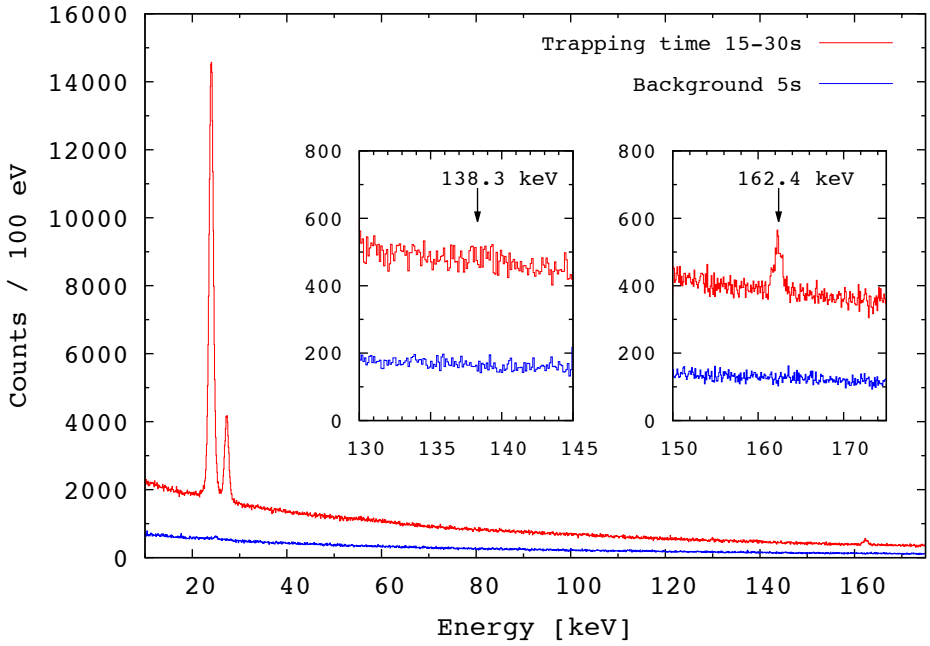

Figure 4.19: ^{116}In decay spectra showing the energy region from 10 to 175 keV. The red spectrum presents the summed data recorded within the trapping time of the EBIT cycle while the blue spectrum presents the 5 s background measurement. The insets display the energy region around the 138 keV and 162 keV transitions. The latter is visible in the Si(Li) spectrum, while the 138 keV line can only be identified in the HPGe spectrum due to its increased detection efficiency.

and 417 keV lines, the HPGe spectrum exhibits the 463 keV transition from the decay of the 0^+ state in ^{116}Sn at an excitation energy of 1757 keV long-lived $J^\pi=5^+$ isomer into the 2^+ state at 1294 keV, as well as the 511 keV annihilation line and several ambient background lines originating from the uranium thorium decay chain.

To verify that the appearance of the Compton edge at 257.7 keV originates from the 417 keV γ-transition, a GEANT4 simulation [175] was employed to generate decay spectra for the decay of the 54.3 min ^{116m}In $J^\pi=5^+$ isomer with and without the implementation of the 417 keV γ-transition. Fig. 4.20 presents an overlay of the simulated spectra within an energy region of 0 keV to 450 keV. Displayed in blue is the spectrum generated without a 416.86 keV transition and as a result the spectrum does not feature a Compton edge or respectively continuum, while the spectrum for which the simulation included the transition (red) exhibits the expected edge at 257.7 keV. Enlargements of the energy region between 350 keV and 450 keV indicating the appearance or respectively the disappearance of the

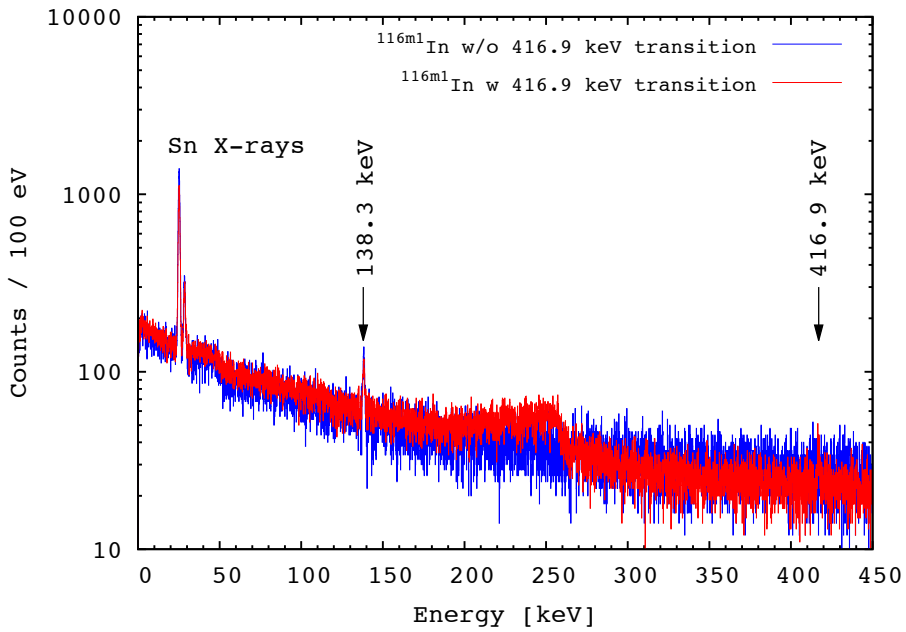

Figure 4.20: GEANT4 generated spectra of the 54.3 min ^{116m}In $J^{\pi}=5^{+}$ isomer decay within 0 keV to 450 keV. The spectrum displayed in blue has been simulated without a 417 keV γ-transition, while the spectrum shown in red was generated including that transition. The latter features a Compton edge at 257.7 keV. Also visible is the transition at 138 keV in both spectra, as well as the Sn X-rays at ∼25.2 keV and ∼28.4 keV [169]. The spectra have been normalized to the number of X-ray counts.

416.9 keV line are shown in Fig. 4.21.

4.2.3 Beam-tune stability

Comparing the normalized X-ray count rates for each run, as presented in Fig. 4.22, reveals an instability of the beam tune over the course of the ^{116}In experiment. An increased count rate can be observed after run 1298, which was used by the ISAC operators to perform yield measurements. The higher count rate observed subsequently of the yield measurement can be correlated directly to the ADC rate (Fig. 4.23), which was monitored during the experiment. An obvious explanation for the observed behavior is an increase in the ISAC beam intensity. However, the values for the beam intensity before the start of the ^{116}In beamtime, the yield measurement in run 1298 and the measurement at the very end of the experiment do not differ significantly enough to explain the trend of the rate (compare Tab. 4.2). Thus, the explanation for the lower count rate detected in the runs before the yield measurement has to be the result of technical difficulties. In this case the problems

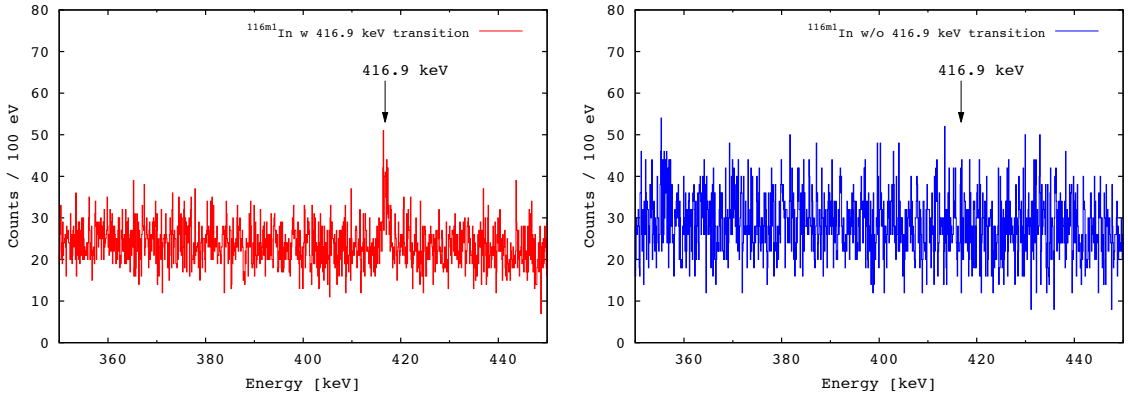

Figure 4.21: Left: GEANT4 simulated ^{116m}In $J^{\pi}=5^{+}$ spectrum generated with the 417 keV transition included. Right: Simulation without the 417 keV transition.

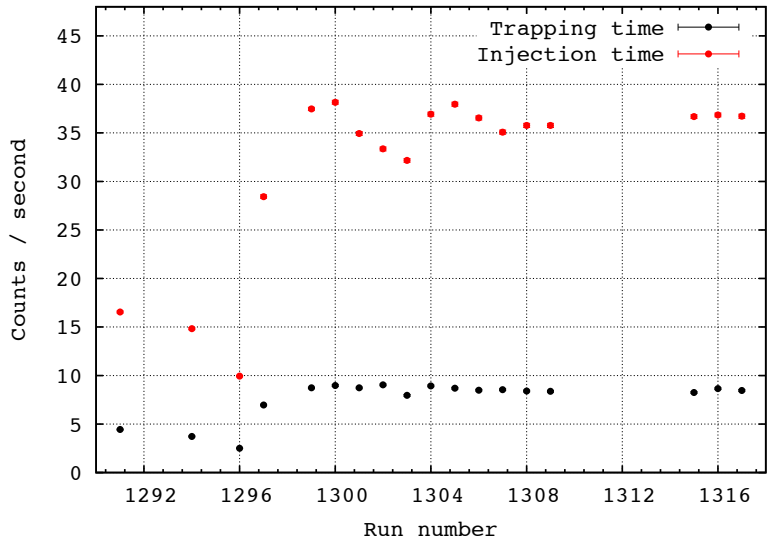

Figure 4.22: Comparison of the average In X-ray count rates recorded during the injection- and trapping time for each of the 18 runs taken during the ^{116}In beamtime. The average count-rate difference between injection- and trapping time is about a factor of 4. The statistical errors are smaller than the point size and, thus not visible in the figure above.

concerned one of the ISAC beam attenuators, which was reported to be stuck (partially) in the beam for several hours and did not respond to the ISAC controls.

4.2.4 Background studies

To gain insight into the origin of the background recorded during the empty-trap part of the cycle and to clarify if and where possible beam losses occur, the ^{116}In beam was dumped at different locations along the beamline, whereby each location was further away from the EBIT. The following locations were chosen for the beam dump:

- Faraday Cup 0 located after (downstream of) the RFQ
- Faraday Cup 3 located before (upstream of) the RFQ
- MCP2 located downstream of the RFQ in the switch yard section
- EBIT gate valves located on the injection side of the EBIT

To recall the position of these diagnostic devices, a schemtic view of the TITAN facility is shown again in Fig. 4.24. Each background run was of the order of a few minutes while the EBIT continued running with the 600 injections cycle consisting of 15 s injection time, 15 s trapping time and 5 s background time. The data was split into injection and trapping time and the background spectra normalized to counts per second for the four runs with the beam dumped at different locations were compared to one another. Tab. 4.4 lists the background runs including the run time and the beam-dump location. Fig. 4.25 presents an overlay of the background runs for the injection as well as for the trapping time, revealing no significant count rate dependence on the beam-dump location nor on the cycle part. No evidence of ^{116}In can be found in the spectra, which underlines the efficient background shielding and proves that the spectra are not contaminated by events from possible beam losses along the beam line or the RFQ. Further, it can be concluded that the background originating from Compton scattering of high-energy γ-rays was comparable to the nominal off-line background in the case of the A=116 experiment.

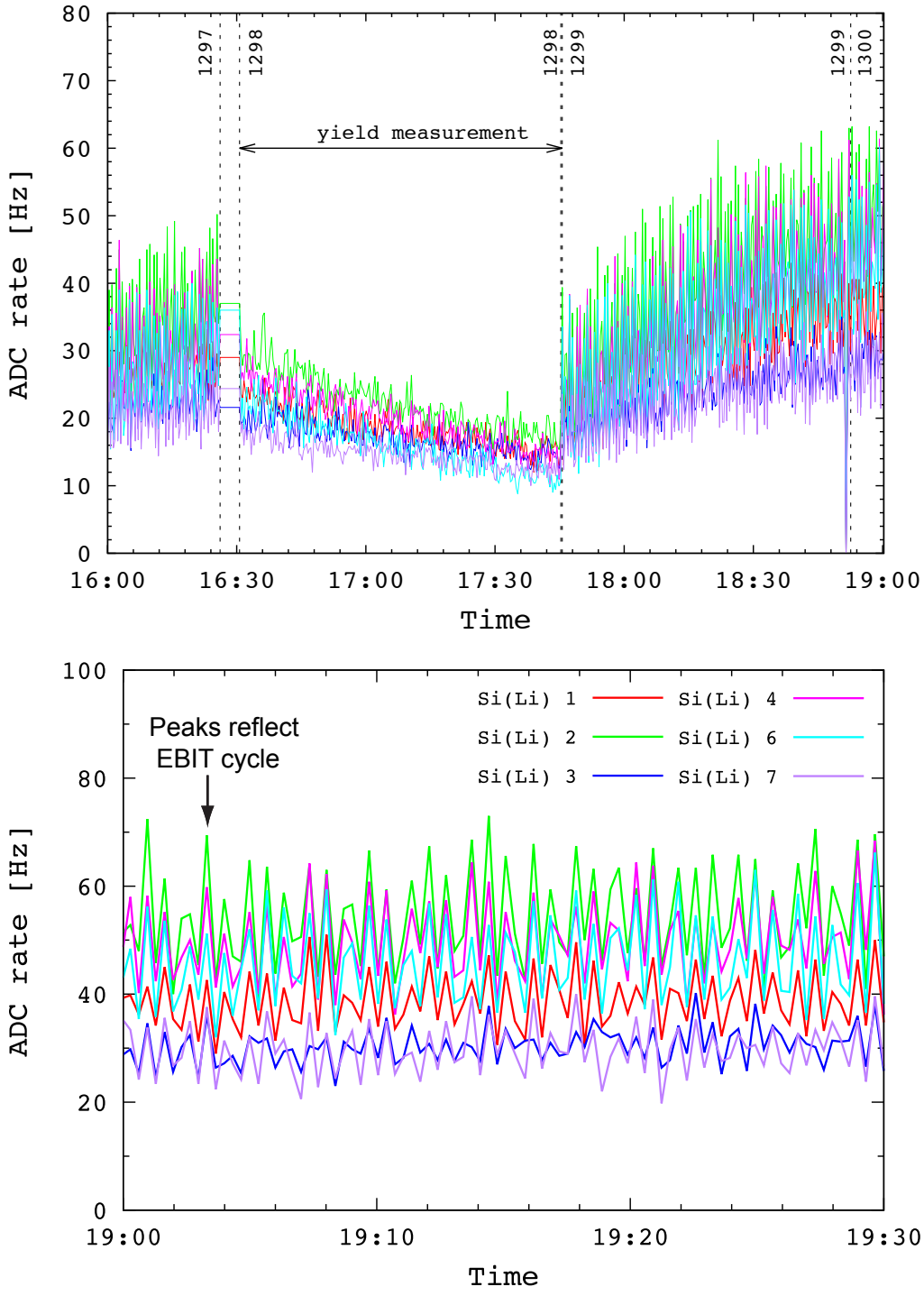

Figure 4.23: Top: ADC event rates during the experiment as a function of time. Displayed is an excerpt of three hours illustrating the increasing count rate after a yield measurement in run 1298. Bottom: Enlargement (1 h) of the ADC event rate to illustrate how the EBIT cycle is reflected in the ADC rates fluctuations. Each peak corresponds to one cycle.

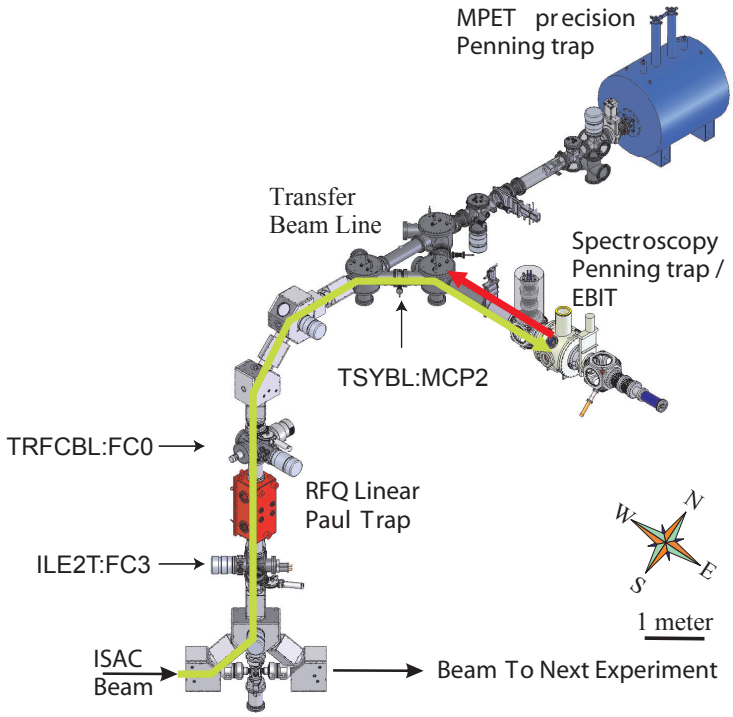

Figure 4.24: Schematic view of the TITAN facility. The Faraday Cups and MCPs used to dump the beam during the background studies are indicated by arrows. Figure adapted from Ref. [126].

run	T_{run} [± 1s]	location	distance to EBIT center
1311	431	FC3	∼ 5.5 m
1312	439	FC0	∼ 5.0 m
1313	447	MCP2	∼ 2.5 m
1314	428	EBIT IV0	∼ 1.0 m

Table 4.4: Overview of the background runs taken while the radioactive beam was dumped at various locations of the beam line. The distance to the trap center refers to the direct line of sight of the individual components.

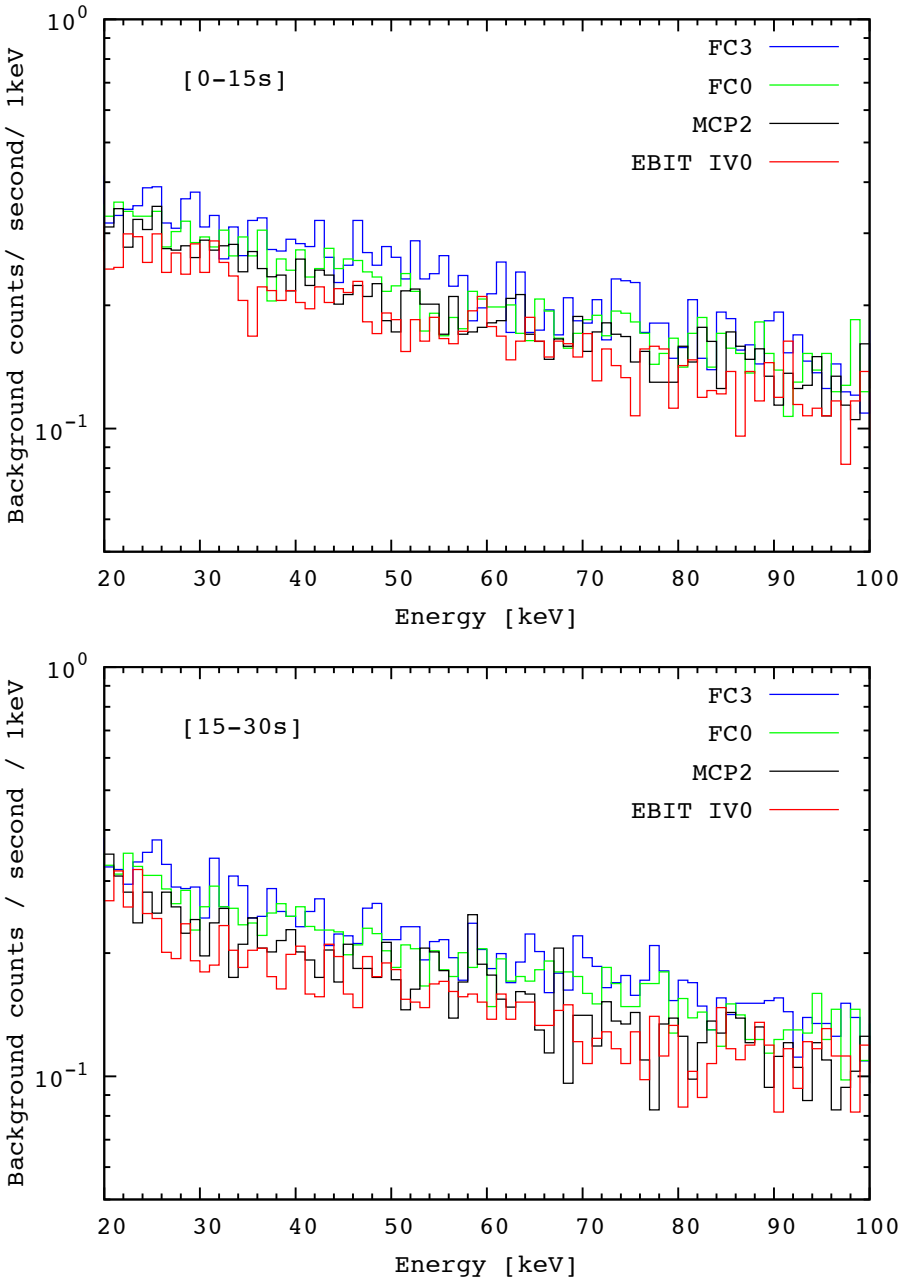

Figure 4.25: Overlay of the background spectra accumulated while the radioactive beam was dumped at various locations in the beam line. The upper panel shows the spectra from 20 to 100 keV for the first 15 s of the EBIT cycle, while the lower one displays the background recorded during the last 15 s of the cycle.

4.3 Conclusion

The above described studies demonstrate an efficient ambient background reduction as well as an efficient ion extraction from the trap. These features are essential for the measurement of weak decay signatures. Furthermore, the trapping cycles, which will be of importance for a time-dependent analysis were introduced.

After gaining insight into the technical details of the setup and beam related aspects of the experiments one can now engage into a detailed data analysis of the here introduced decay spectra, which will be subject of the following chapter.

Chapter V

DATA ANALYSIS

This chapter outlines the analysis procedure of the data recorded during the two experiments described in the previous chapter. At the beginning, the general data selection criteria are introduced, which is followed by a description of the photon-spectra generation and the energy-calibration method. Afterwards, a description of the data fitting routine is given by the example of the ^{124}Cs data, before a detailed analysis of the ^{124}Cs and the ^{116}In decay spectra is presented. The analysis comprises a study of the time structure of the data including half-life extraction, a comparison to simulations, a discussion of the number of ions in the EBIT and of the corresponding beam composition, as well as charge-breeding induced atomic structure effects, such as X-ray energy shifts and the observed X-ray intensity ratios.

5.1 Data selection

For the analysis of the ^{124}Cs as well as of the ^{116}In data only the data recorded with three of the six detectors were used (see Tab. 5.1). In both experiments, the remaining three Si(Li) detectors suffered considerably from the vibrations and electromagnetic interference, which led to a significantly deteriorated resolution ($\approx 2.7\%$) and high noise levels (≈ 40 mV). Since all detectors had been tested prior to the experiments, this behavior was already anticipated. Consequently, the more sensitive detectors were mounted at the smaller acceptance ports (about 1/2 less than for the large acceptance ports as described in Sec. 2.3.2), while the three large acceptance ports were occupied with those detectors that were expected to provide the best energy resolution. Fig. 5.1 shows X-ray spectra from all six detectors that were operational during the A=116 experiment in order to illustrate the decrease in energy resolution for Si(Li) #432 and #427. For Si(Li) #427 the ^{116}In K_α and K_β X-rays (about 3 keV apart) are not resolved anymore but merely a broad bump is observed in the spectrum. The resolution for Si(Li) #431 was slightly better than for #432, which made

	Port	angle	Det. #	resolution[%]
^{124}Cs	2	90°	404	1.6(1)
	4	180°	427	1.9(1)
	6	270°	405	1.8(1)
^{116}In	2	90°	404	1.8(1)
	4	180°	438	1.8(1)
	6	270°	405	1.8(1)

Table 5.1: List of Si(Li) detectors that were operational during the ^{124}Cs and ^{116}In experiments and used for the data analysis. The value for the energy resolution refers to the ^{133}Ba calibration measurements at 53 keV taken shortly before the experiments.

the detector suitable as a diagnostic tool to monitor intensity variations during the online multiple-injection tests carried out for the injection-tune optimization.

5.2 Generating the spectra

The TITAN-EC data acquisition (DAQ) uses a MIDAS (Maximum Integrated Data Acquisition System) based system [183], which is a general purpose software package for event-based DAQ developed at PSI and TRIUMF and is the standard DAQ system of the ISAC facility. The TITAN-EC DAQ uses the C++ based code for data communication, data control for run operation and data distribution for online analysis, as well as for online monitoring the run conditions like temperatures, vibrations, proton current, event rate, Si(Li) reset rate, LN_2 LEDs and EBIT related features, i.e., central drift tube voltages and electron-beam gun current.

After each run, the data is stored in a compressed binary file (mid.gz file), out of which a ROOT [184] tree is generated. The data for all runs were summed on a detector-by-detector basis, and a linear energy-scaling factor was applied by fitting a monoenergetic γ-line. Subsequently, a more sophisticated energy calibration was performed individually for each detector. The procedure is described in detail in the following section.

The calibrated spectra for all three detectors (compare Tab. 5.1) were summed for the analysis since the resolution and detection efficiency of all used detectors were similar, and the slight gain in resolution by using a single detector was small compared to the gain in statistics.

Further, all Si(Li) detectors were mounted on the larger acceptance ports, and had identical

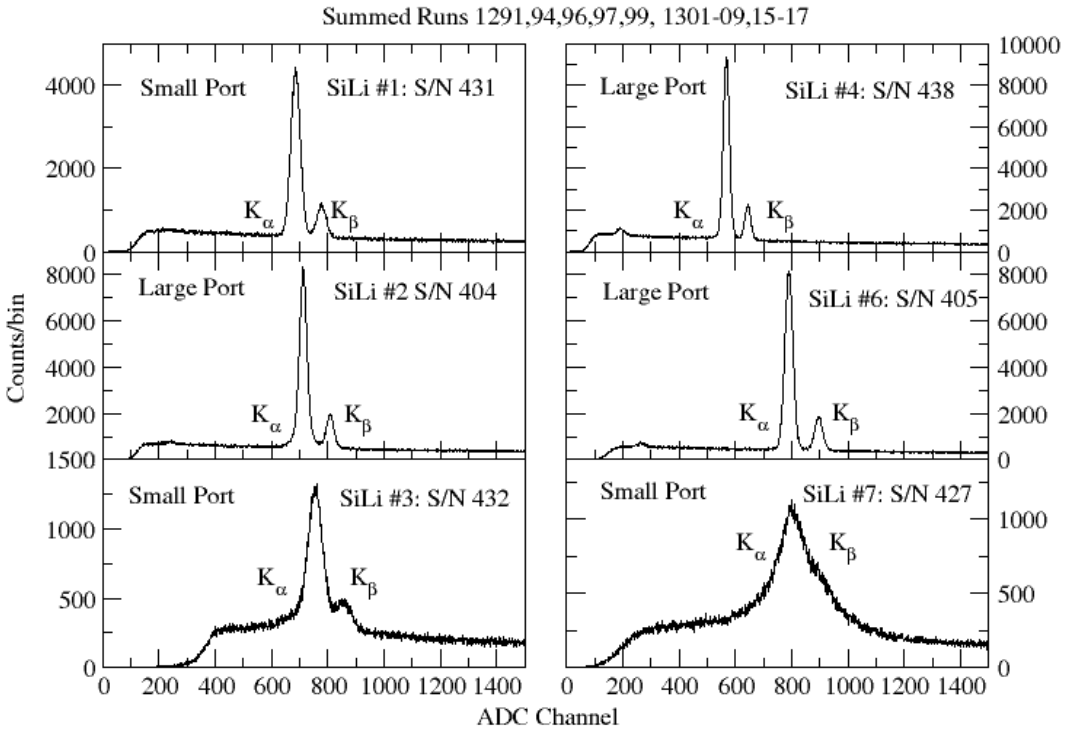

Figure 5.1: Overview of the X-ray spectra for the six Si(Li) detectors that were operational during the ^{116}In experiment in November 2013. While the data taken with the detectors #431, #438, #404 and #405 could be used for the data analysis, the data from #432 and #427 were not usable due to the insufficient energy resolution. Not inserted into the array for this experiment was Si(Li) #406, as it was not operational.

Port #	Angle	Det. #	F_i [keV/Ch]
2	90°	404	0.13334
4	180°	427	0.13174
6	270°	405	0.12081

Table 5.2: Linear calibration factors F_i for the A=124 spectra.

ambient background shielding. Therefore, the background recorded by all three detectors was comparable. The data were binned in 100 eV increments, and the specific region of interest for this work was from 0 - 600 keV. To analyze the spectra during the trapping time of the cycle, time cuts from 0 to 20 s were applied to the spectra with 1 s or 2 s wide binning. The data are then available in three formats:

1. as full 2-dimensional histograms (energy vs. time)
2. as projected 1-dimensional histograms (energy, all times)
3. as 1-dimensional energy spectra for all given time slices of 1 or 2 s bin width

The fitting procedures for the different types of spectra are described in Sec. 5.4.

5.3 Energy calibration

In preparation for a detailed data analysis an accurate energy calibration of the spectra was performed for each detector. As a constant calibration factor for the Si(Li) spectra was insufficient for energies higher than $\sim$ 180 keV, a quadratic function was used to calibrate each detector individually before summing the data. The iterative energy-calibration procedure for both, the ^{124}Cs and ^{116}In experiments are outlined below.

5.3.1 ^{124}Cs

The calibration is performed in two steps. First, each detector is calibrated with an initial factor gained from the ^{124m}In γ-lines at 103 keV and 120 keV, which is done to simplify the automation of the fitting procedure described below. The initial calibration factors (F_i), with i standing for the port number of each detector, are listed in Tab. 5.2. After the initial calibration, all γ-transitions of know energies up to 354.10 keV, as well as the ^{124}Sn K_α X-rays (see Tab. 5.3) were used as calibration points. Fitting the 25.044 keV ^{124}Sn $K_{\alpha 2}$

Peak energy [keV]	Species
25.0440(2) [185]	^{124}Sn $K_{\alpha 2}$ X-ray
25.2713(2) [185]	^{124}Sn $K_{\alpha 1}$ X-ray
58.20(5)	γ-ray from ^{124}Cs 7^+ isomer
89.50(5)	γ-ray from ^{124}Cs 7^+ isomer
96.55(5)	γ-ray from ^{124}Cs 7^+ isomer
102.91(5)	γ-ray from ^{124}In 8^- isomer
120.34(5)	γ-ray from ^{124}In 8^- isomer
354.10(4)	γ-ray from ^{124}Cs 1^+ g.s.

Table 5.3: Calibration peaks used for the energy calibration of the ^{124}Cs spectra. Values taken from Ref. [169] and [185].

and the $K_{\alpha 1}$ at 25.271 keV is realized by a correlated double-Gaussian function, where one peak is used as reference peak. The double-Gaussian function was necessary to separate the $K_{\alpha 1}$ and $K_{\alpha 2}$ transitions at 25.044 keV and 25.271 keV since they were not resolved as a result of the insufficient energy resolution. The double-Gaussian function for the ^{124}Sn K_α was applied within the energy region of 22 keV to 27 keV, where the distance of the peak centers (25.044 keV and 25.271 keV) as well as the intensity ratio of those two transitions were fixed for the second Gaussian function. The obtained centroid for the $K_{\alpha 2}$ X-ray was then corrected to be exactly 25.044 keV. That correction factor multiplied by the initial calibration factor F_6 or, respectively, F_2 and F_4 for the other detectors gives the exact peak centroid for that specific transition.

To extract the channel numbers for the other transitions (γ-rays) that were used to generate the calibration function, the same correction procedure was applied, only with single Gauss functions since all other peaks occur from monoenergetic γ-transitions. Due to the limited statistics at 354.10 keV in a spectrum taken by a single detector, the 354.10 keV fit was only sufficient enough to reliably extract the center value but not the count rate. The fits for Si(Li) 6 (#405) are presented in Fig. 5.2 and Fig. 5.3 as an example of the process used for all three detectors.

After determining the center values, the latter are plotted against the peak energy and fitted automatically with a quadratic function by the routine. The final calibration function is shown in the lower right panel of Fig. 5.3. The calibration functions for the individual

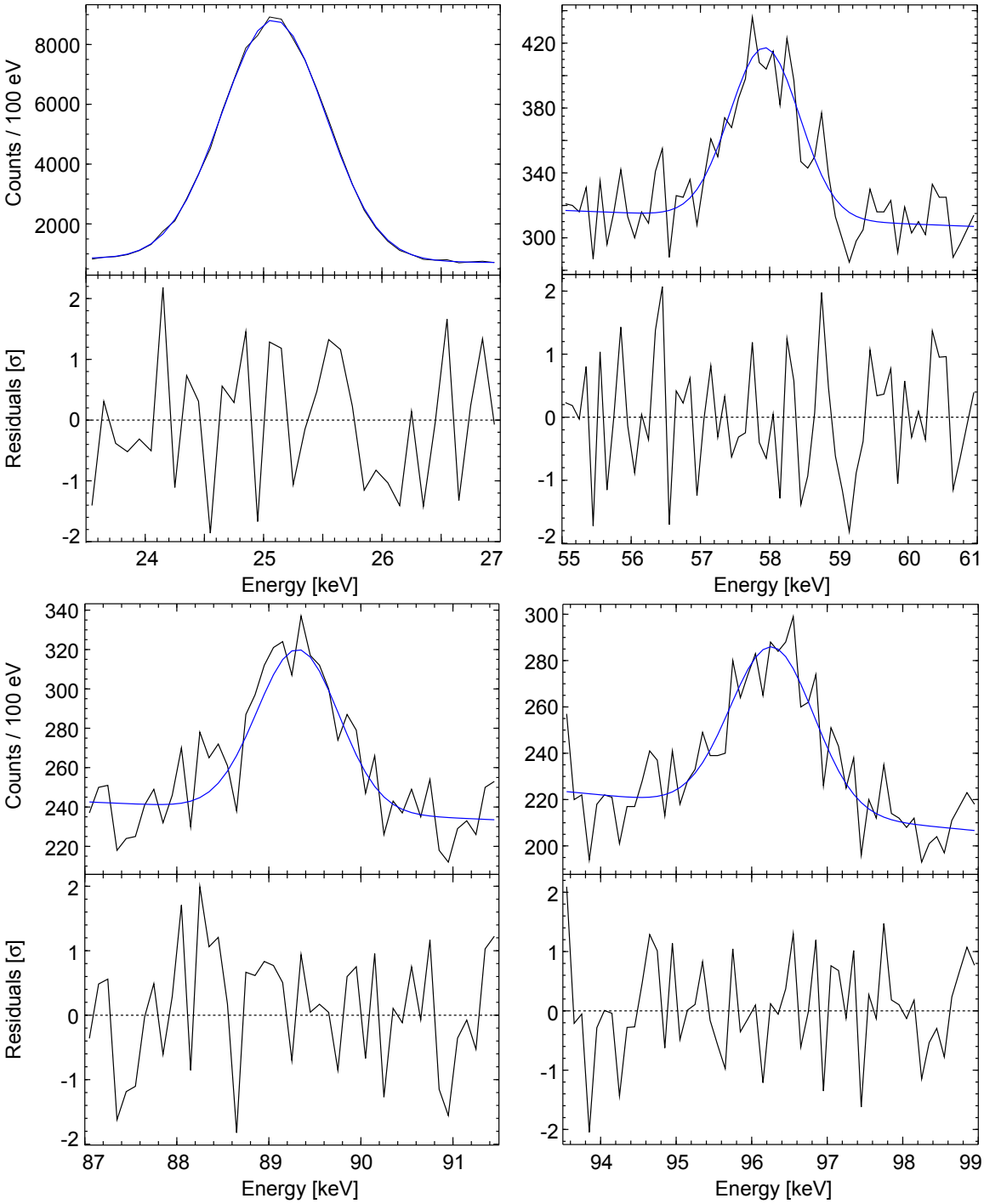

Figure 5.2: Fits used for the energy calibration of Si(Li) #405 after the linear calibration with the factor F_i. The upper left panel shows the double K_α peak at 25.044 keV and 25.27 keV, whereas the other three panels show the fits for monoenergetic γ-lines at 58.20 keV, 89.50 keV and 96.55 keV.

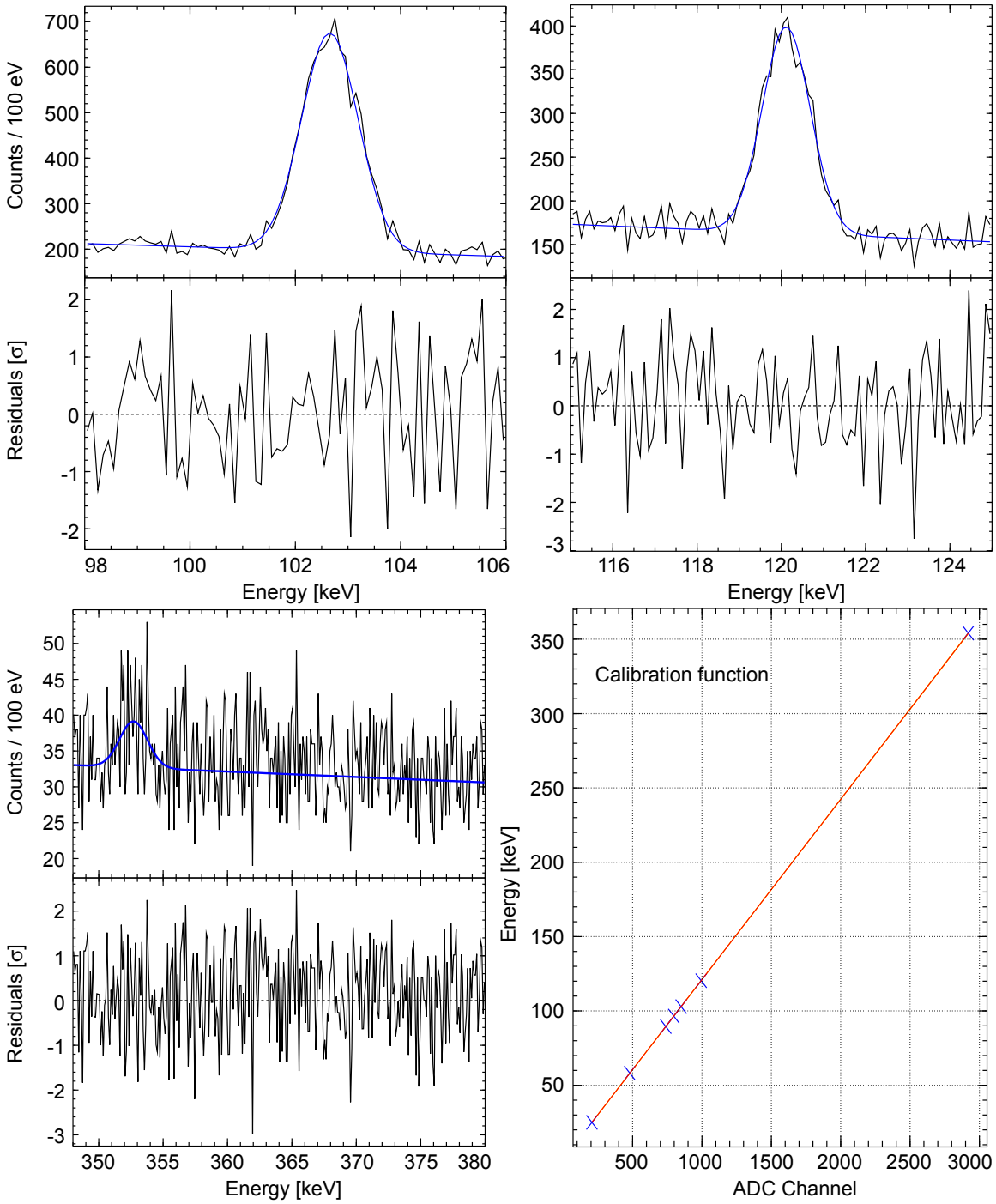

Figure 5.3: Gauss fits of the 103 keV, 120 keV and 354 keV lines after the linear calibration with the factor F_i. The lower right panel illustrates the final energy-calibration function.

Peak energy [keV]	Species
24.0020(2) [185]	^{116}In $K_{\alpha 2}$ X-ray
24.2097(2) [185]	^{116}In $K_{\alpha 1}$ X-ray
162.393(7)	γ-ray from ^{116}In 8^- isomer

Table 5.4: Calibration peaks used for the energy calibration of the ^{116}In spectra. Values taken from Ref. [186] and [185].

detectors are listed in the following:

$$f_2(x) = -1.00276351 * 10^{-8} * x^2 + 0.13338 * x - 0.0063, \tag{5.1}$$

$$f_4(x) = 5.92264643 * 10^{-8} * x^2 + 0.16993 * x + 0.0119, \tag{5.2}$$

$$f_6(x) = 1.42831272 * 10^{-8} * x^2 + 0.12077 * x + 0.0054, \tag{5.3}$$

with x = ADC channel. The functions presented above are directly taken from the output file of the calibration script and have not been rounded to the actual significant digits in order to avoid a bias for the given uncertainties. The statistical uncertainty on the calibration is 19 eV for Si(Li) 2 (#404), 17 eV for Si(Li) 4 (#427) and 21 eV for Si(Li) 6 (#405). Fig. 5.4 displays the calibration function with the corresponding uncertainty for Si(Li) #405 within the energy region of the Xe K_α peak.

To validate the calibration function for higher energies, the 354.1 keV transition was fitted after the data of three detectors was summed up. Fitting the peak resulted in an energy resolution of 1.4 keV, which is the expected value for the Si(Li) detectors at 354.1 keV according to the specifications.

5.3.2 ^{116}In

The energy calibration for the ^{116}In data was done analogously to the calibration for the ^{124}Cs data. The transitions that were used to generate a second order calibration function are shown in Tab. 5.4.

The calibration functions for the detectors used for the data analysis are:

$$f_2(x) = 1.1357862 * 10^{-7} * x^2 + 0.13515 * x - 0.091, \tag{5.4}$$

$$f_4(x) = -1.7049762 * 10^{-6} * x^2 + 0.17154 * x - 0.3148, \tag{5.5}$$

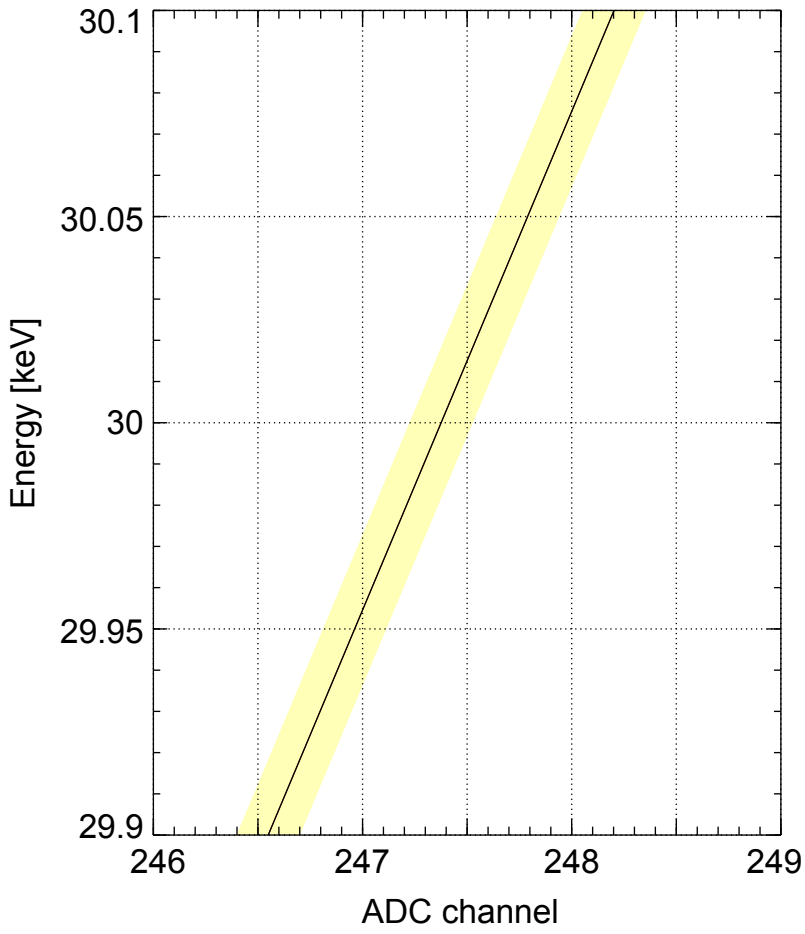

Figure 5.4: Energy calibration function for Si(Li) #405 within the energy region relevant for the Xe K_α peak. The yellow shaded region represents the uncertainty corresponding to 21 eV.

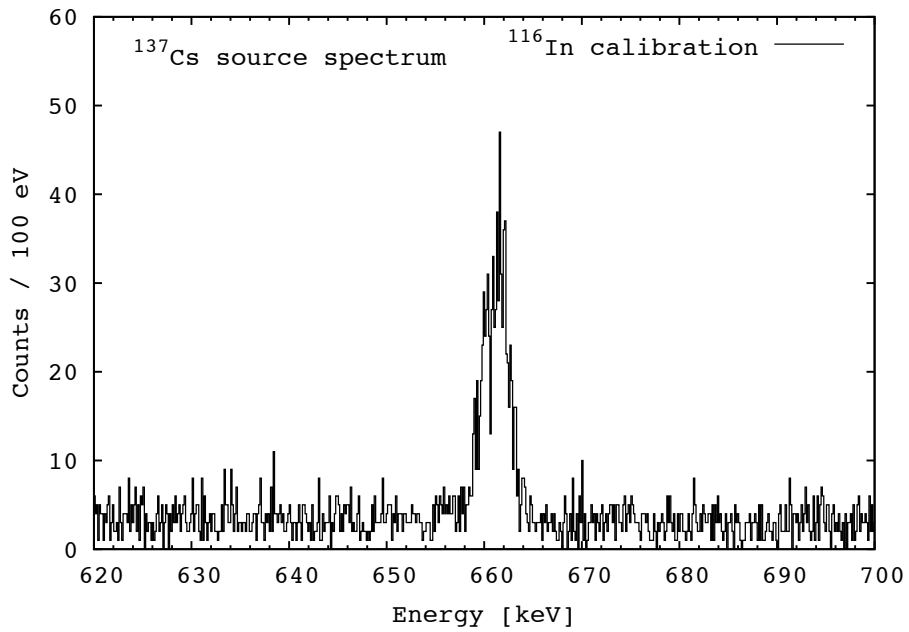

Figure 5.5: ^{137}Cs source spectrum calibrated with the calibration function generated from the ^{116}In data. Shown is the energy region from 620 keV to 700 keV to validate the uncertainty of the calibration at the 661.65 keV line.

$$f_6(x) = -4.5603190 * 10^{-7} * x^2 + 0.12265 * x - 0.2130. \tag{5.6}$$

The statistical uncertainty on the calibration is 30 eV for Si(Li) 2 (#404), 35 eV for Si(Li) 4 (#438) and 38 eV for Si(Li) 6 (#405).

Since the 162.39 keV transition was the calibration point with the highest energy, the reliability of the calibration functions for the ^{116}In spectra had to be validated for energies beyond 162.39 keV.

On that account, a ^{137}Cs source spectrum taken before the ^{116}In experiment was calibrated with the same function as the ^{116}In data. The spectrum is shown in Fig. 5.5. Even though the last calibration point from the ^{116}In data was set at 162.39 keV, the 661.65 keV γ-transition from the ^{137}Cs decay appears at the correct energy with a fitted value of 661.2 keV for the peak centroid. This validates the calibration for energies above 500 keV without an energy shift.

5.4 Fitting routine

Before going into a detailed description of the analysis of the spectra, the principles of the analytical fitting method will be explained in the following. In essence, the spectrum created out of the experimental data as described before is compared to a calculated spectrum where their difference is minimized towards a certain set of defined parameters. This minimization method is applying the Levenberg-Marquardt algorithm [187, 188] generally used to solve non-linear least-square problems, which involves an iterative improvement of the parameter values for reducing the sum of squares of the errors between the parameter-based calculated function and the measured data. In the particular case of the ^{124}Cs and ^{116}In data, a calculated spectrum consists of:

1. a spectrum for each ion species in the trap, calculated (not simulated) as the sum of a number of Gaussian peaks (from X-rays and γ-rays), with intensities and energies from the National Nuclear Data Center database (NNDC) [169] as starting values and,

2. a background function, that represent the actual measured ambient background and the simulated time-dependent Compton background of the spectra from the individual species.

Then an efficiency function is applied, which is derived from GEANT4 [175] simulations, which were cross-checked and compatible with results from both, PENELOPE [189] simulations, and experimental data. The efficiency curve appears in Sec. 3.5.1.

In the following the described fitting procedure is explained using the set of parameters applied to fit the ^{124}Cs data. In the specific case of ^{124}Cs the fit covers an energy region from 20 keV to 140 keV. In the simplest and first iteration, a fit needs 7 parameters, 6 as normalization for the three species (Xe, Cs, Sn K_α and K_β X-rays) contributing to the spectrum and a 7^{th} parameter for the background scaling. Then, in the second step, the peak energies and peak intensities for all species are free fitting parameters, for which one may define starting values. In the third step, another set of two parameters is added to

characterize the resolution as function of the energy, which is important for the calculation of the width of the Gaussian peaks. Taking into account the (dominant) statistical uncertainties of the data, i.e., the best fit in the least-squares sense is minimizing the sum of squared residuals, the number of counts for each X-ray peak and the corresponding number of decays for each species can simply be extracted from the calculated function.

5.4.1 Background function

Most of the background coming from inside the trap is time-dependent, as it results from the decay of the trapped ions themselves. However, the contribution from the ambient background has no such time dependence, which was deduced from the fact that the empty-trap spectrum remained constant over time and is consistent with previously measured ambient background spectra. Particular attention needs to be given to the Compton spectrum of the 102.91 keV and 120.34 keV γ-rays from the ^{124m}In 8^- isomer decay. According to the following formula [157]:

$$E_{Compton} = \frac{E_\nu}{1 + \frac{m_e c^2}{2E_\nu}}, \tag{5.7}$$

The Compton edges appear at an energy of 29.5 keV and 38.5 keV in the spectrum, and are thus located under the ^{124}Xe K_α peak. For completeness, the simulated background function includes the Compton spectrum of the 89.4 keV and 96.5 keV γ-transitions from the ^{124m}Cs 7^+ isomer decay, where the Compton edges occur at 23.2 keV and 26.5 keV.

In order to include the Compton background contribution into the fit function, the Compton spectrum had to be derived from the GEANT4 simulation, was turned into a spline function, and added to the fit with a fitted scaling factor as the background is directly coupled to the intensities of the γ-rays. The fact that the scaling factor of the Compton contribution is a variable, fitable parameter offers the opportunity to apply the Compton contribution for each time-slice of the data, independent of the size of the time bins.

The background fit function is based on the measured background during the empty-trap part of the trapping cycle, which is used to generate a spline function in the fit together with correct statistical fluctuations and uncertainties. As stated above, already implemented in the fitting procedure are the detector efficiencies, ambient and Compton background from

the decaying ^{124m}In and ^{124m}Cs contamination inside the trap as well as the feeding of the ^{124}Cs 7^+ isomer decaying into the ground state.

5.4.2 Low-energy tail

The energy region between 24 keV and 35 keV essentially features 12 X-rays from three different isobars, as there are $K_{\alpha 1,2}$ and $K_{\beta 1,3}$ from ^{124}Sn, $K_{\alpha 1,2}$ and $K_{\beta 1,3}$ from ^{124}Xe and $K_{\alpha 1,2}$ and $K_{\beta 1,3}$ from ^{124}Cs. The fit functions used to describe each of those 12 peaks consist of a Gaussian function, which has been convoluted with an exponential tail on the low-energy side of the distribution. This tail, or so called skewness of the Gaussian distribution arises from incomplete charge collection [157] resulting from the detector geometry as described previously in Sec. 3.5.3. Assuming a perfect energy resolution, the Gaussian distribution would simply be described by a delta function and the low-energy tail would be described by an exponential function. By convoluting the exponential tail with a Gaussian resolution function instead of a delta function results in the following description [190]:

$$y = constant \cdot \exp((x-c)/\beta) \cdot erfc((x-c)/(\sqrt{2}\cdot\sigma) + \sigma/(\sqrt{2}\cdot\beta)), \tag{5.8}$$

where $erfc$ is the complement of the error function, x denotes the centroid of the skewed Gaussian, c is the centroid of the normal Gaussian distribution, σ its standard deviation and the parameter β describes the decay constant of the exponential tail. Fig. 5.6 presents a schematic of the different components, which contribute to the final peak shape. For the X-ray spectra presented in this work, the fraction of the low-energy tail contributed $\sim 2.3\%$ to the total count rate in a single peak, with $\beta = 1.63$. A discussion of the asymmetry of X-ray peaks in Si(Li) detectors can be found in Ref. [166].

5.5 ^{124}Cs electron-capture decay

Having introduced the basics of the fitting routine, further details of the ^{124}Cs data analysis will be discussed in this section.

5.5.1 Fitted spectra

Figures 5.7, 5.8, 5.9 and 5.10 illustrate the fits for the 1 s time slices from 20 keV to 40 keV, where the presented fit function (red curve) contains the Gaussian distributions

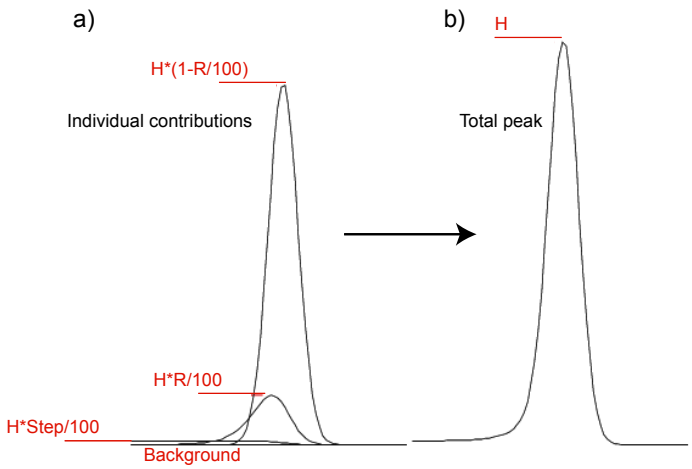

Figure 5.6: Schematic of a skewed Gaussian distribution. The parameter R, β and STEP define the peak shape, which is the sum of a Gaussian with the height $H \cdot (1 - R/100)$ and a skewed Gaussian with the height $H \cdot R/100$. β is the decay constant or skewness and STEP describes the relative height of a smoothed step function, which increases the background below each peak. Fig. adapted from Ref. [190].

modified according to Eq. 5.8 for all three species, as well as the background as explained above. The corresponding extracted efficiency corrected X-ray count rates per 1 s time bins for the three ion species are listed in Tab. 5.5, Tab. 5.6 and Tab. 5.7.

Fig. 5.11 presents four time slices within an energy region of 20 keV to 40 keV, where each spectrum contains 5 s of statistics of the 20 s trapping time (a) 0-5 s, b) 5-10 , c) 10-15 s and d) 15-20 s). Further, the individual fit functions for all three ion species are displayed. The red curve describes the fit for the Sn X-rays from the decay of the excited states in ^{124}Sn, which are populated by the ^{124m}In 8^- isomer. The fit of the Xe X-rays from the EC decay of the ^{124}Cs ground state into ^{124}Xe is indicated by the solid blue line and the green curve describes the fit of the ^{124}Cs X-rays from the decay of the ^{124m}Cs isomer into the ^{124}Cs ground state. The black dashed line denotes the background function, which includes the time-scaled measured empty-trap background as well as a time-dependent component originating from the Compton background induced by γ-rays from the decay of the ^{124m}In and ^{124m}Cs isomers. The grey curve is the sum of all species including the background. The figure emphasizes the different time-dependences of the various species. Due to the relatively long half-life of the ^{124}Cs ground state, the Xe X-rays at $E(K_\alpha) \sim 29.7$ keV and

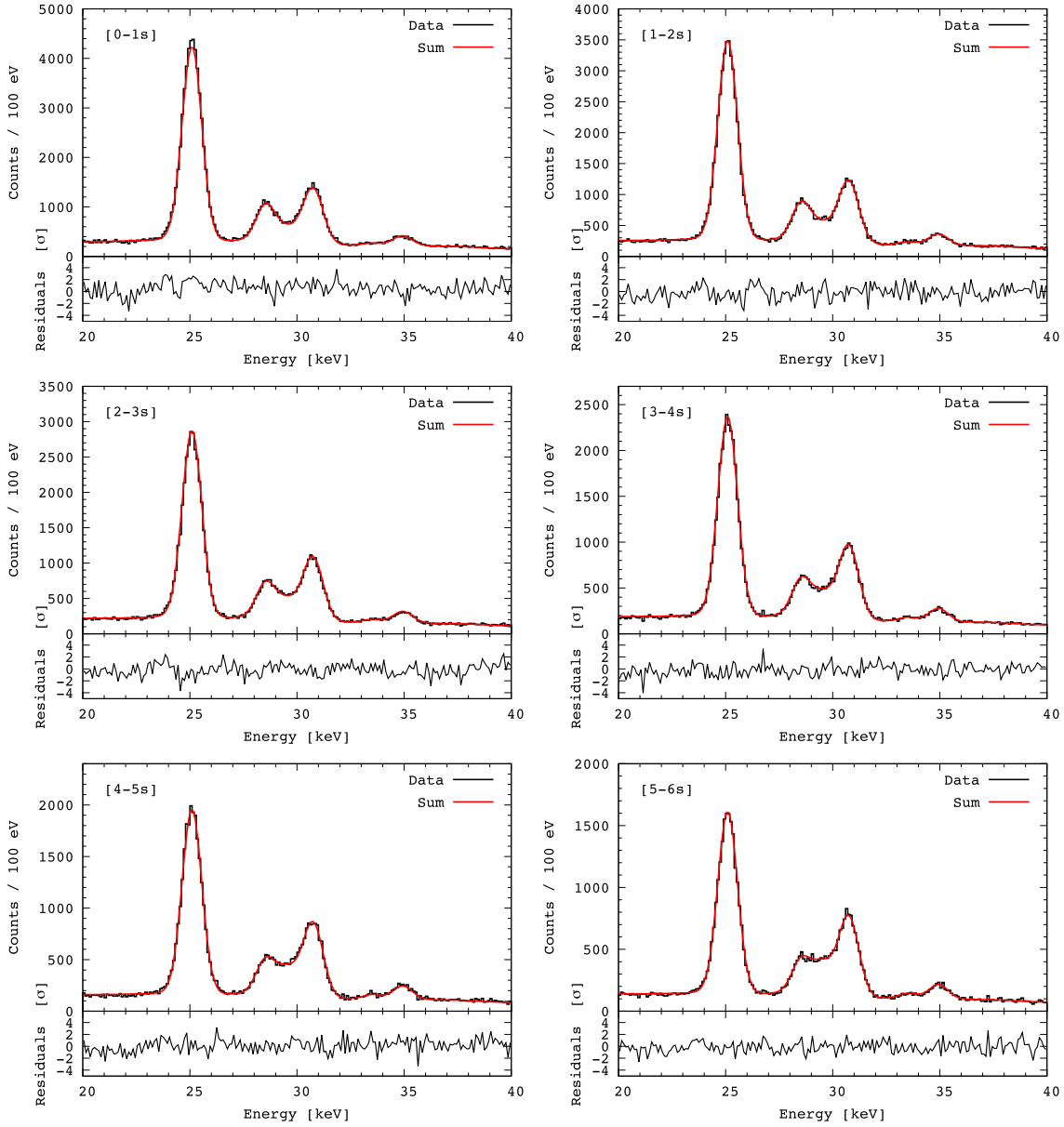

Figure 5.7: Displayed are the fits of the X-ray energy region (20 keV to 40 keV) for the first six 1 s time slices of the trapping time. Each panel shows one second of data and the corresponding fit function (red curve). The fit includes the 12 Gauss functions for the three different species as well as the background.

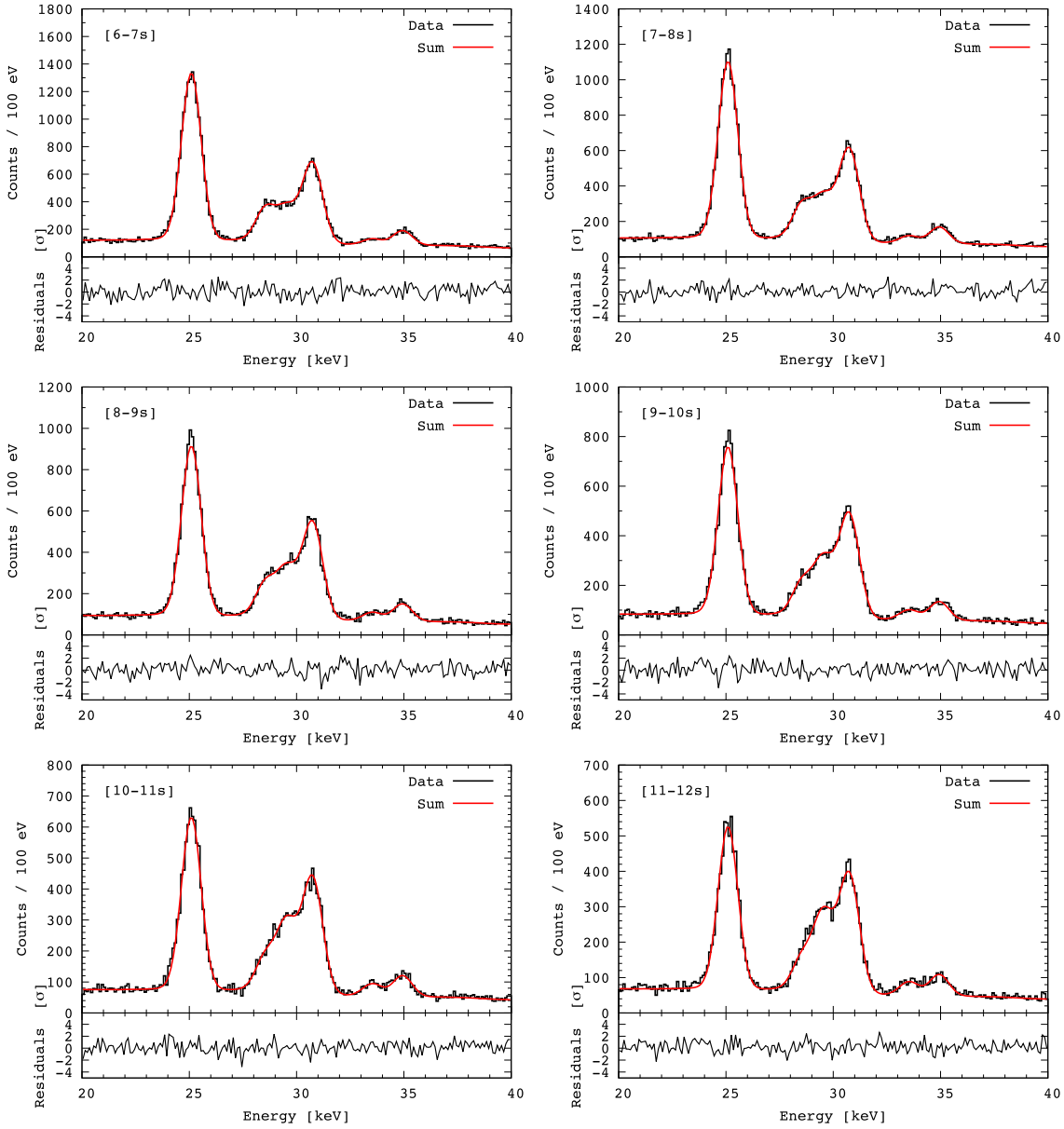

Figure 5.8: Fits of the X-ray energy region (20 keV to 40 keV) for the time slices within the 7 to 12 s time interval of the trapping time. Each panel shows one second of data and the corresponding fit function (red curve). The fit includes the 12 Gauss functions for the three different species as well as the background.

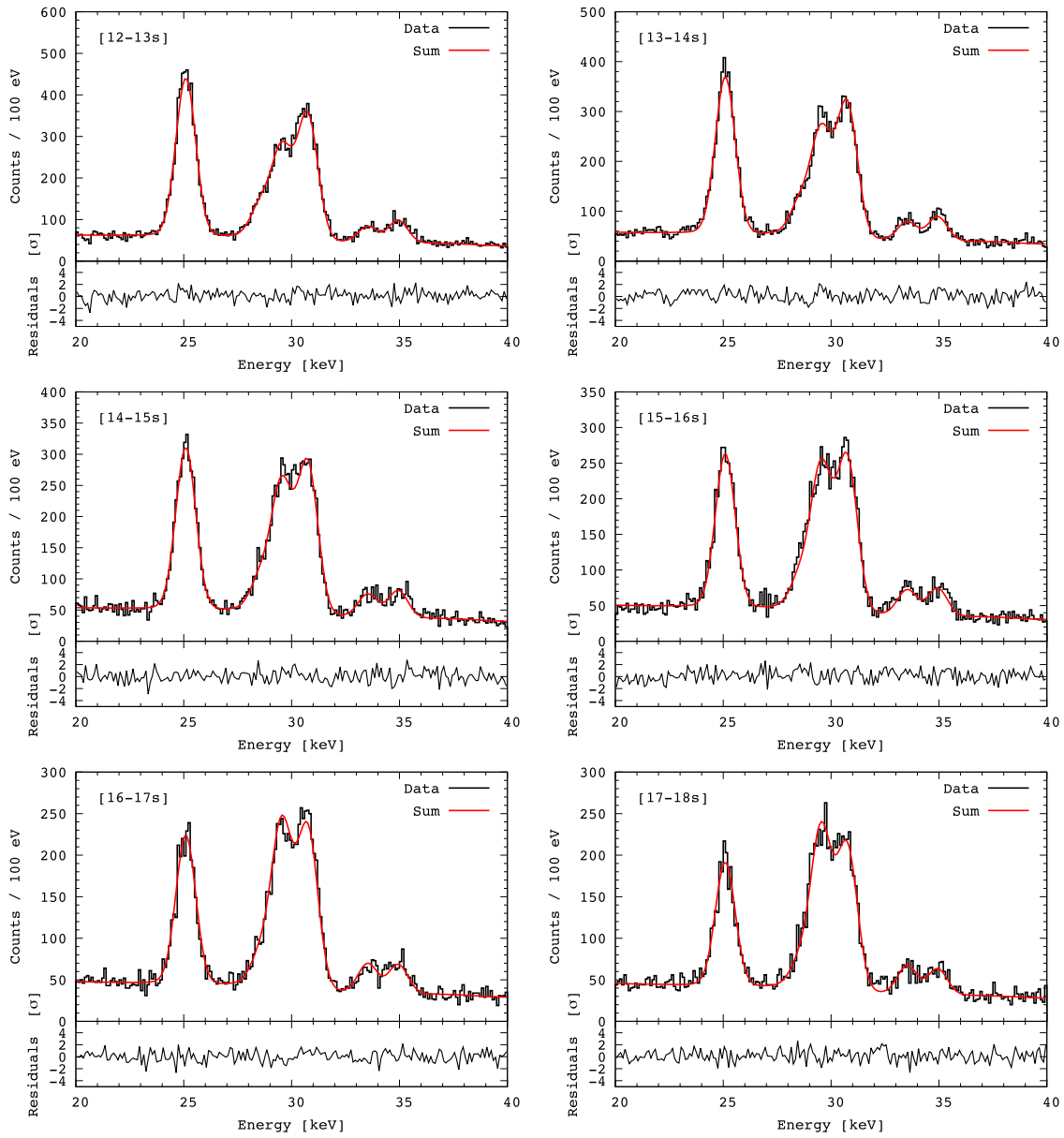

Figure 5.9: Fits of the X-ray energy region (20 keV to 40 keV) for the time slices within the 13 to 18 s time interval of the trapping time. Each panel shows one second of data and the corresponding fit function (red curve). The fit includes the 12 Gauss functions for the three different species as well as the background.

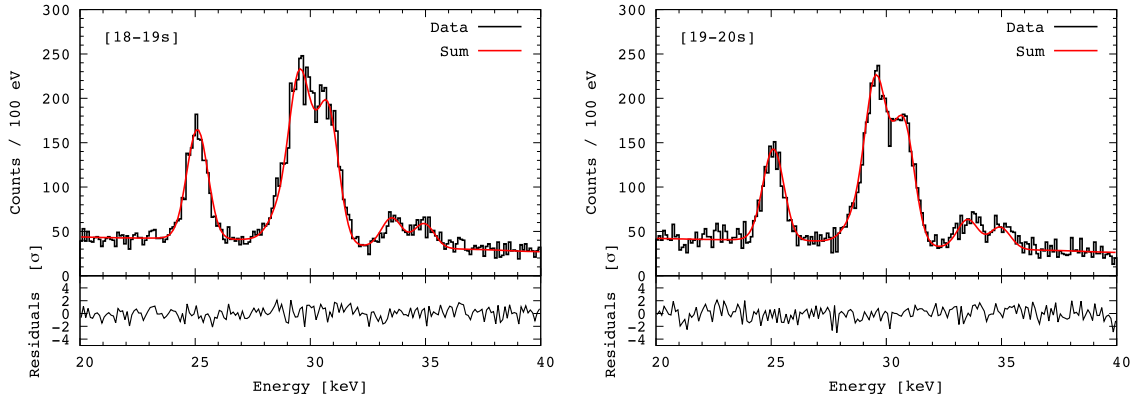

Figure 5.10: Fits of the X-ray energy region (20 keV to 40 keV) for the last two time slices of the trapping time. Each panel shows one second of data and the corresponding fit function (red curve). The fit includes the 12 Gauss functions for the three different species as well as the background.

^{124}Xe			
Time [s]	Counts/ϵ (K_α) $\times 10^3$	Counts/ϵ (K_β) $\times 10^2$	Counts/ϵ (total) $\times 10^3$
0.5	3.22(6)	6.6(3)	3.88(9)
1.5	3.05(6)	6.9(3)	3.74(9)
2.5	3.45(6)	6.4(3)	4.09(9)
3.5	2.98(6)	5.0(2)	3.49(8)
4.5	2.99(6)	5.9(2)	3.58(8)
5.5	2.83(5)	4.8(2)	3.31 (7)
6.5	2.66(5)	4.9(2)	3.15 (7)
7.5	2.71(5)	6.4(3)	3.35 (8)
8.5	2.71(5)	5.3(2)	3.24 (7)
9.5	2.47(5)	5.9(2)	3.06 (7)
10.5	2.41(5)	5.6(2)	2.97 (7)
11.5	2.56(5)	4.9(2)	3.05 (7)
12.5	2.41(5)	5.2(2)	2.92 (7)
13.5	2.51(5)	5.2(2)	3.03 (7)
14.5	2.47(5)	5.0(2)	2.97 (7)
15.5	2.24(5)	5.8(2)	2.82 (7)
16.5	2.10(5)	4.4(2)	2.53 (7)
17.5	2.08(5)	3.2(2)	2.40 (7)
18.5	1.95(4)	3.9(2)	2.34 (6)
19.5	2.02(4)	4.7(2)	2.48(6)
Sum	5.18(28) $\times 10^4$	1.06(8)$\times 10^4$	6.24(37)$\times 10^4$
Time-dependent result	5.17(11)$\times 10^4$	1.02(4)$\times 10^4$	6.19(13)$\times 10^4$

Table 5.5: Overview of the extracted count rates (detection efficiency corrected) for ^{124}Xe X-rays depending on the trapping time. The given errors for the K_α and K_β count rates are the statistical errors based on the count rates. The error for the total number of counts is the sum of the K_α and K_β count-rate uncertainties. The errors for the sum of all peak integrals as well as for the time-dependent result represent the statistical uncertainty resulting from the fit.

^{124}Cs			
Time [s]	Counts/ϵ (K_α) $\times 10^3$	Counts/ϵ (K_β) $\times 10^3$	Counts/ϵ (total) $\times 10^3$
0.5	14.46(12)	2.84(5)	17.30(17)
1.5	12.27(11)	2.50(5)	14.77(16)
2.5	10.95(11)	2.33(5)	13.27(15)
3.5	9.94(10)	2.01(5)	11.95(15)
4.5	8.82(9)	1.94(4)	10.76(14)
5.5	8.03(9)	1.78(4)	9.80(13)
6.5	6.91(8)	1.64(4)	8.54(12)
7.5	6.49(8)	1.58(4)	8.07(12)
8.5	5.60(8)	1.36(4)	6.95(11)
9.5	5.16(7)	1.24(4)	6.40(11)
10.5	4.48(7)	1.06(3)	5.53(10)
11.5	4.17(7)	0.83(3)	5.00(9)
12.5	3.86(6)	0.84(3)	4.71(9)
13.5	3.25(6)	0.77(3)	4.02(9)
14.5	3.06(6)	0.64(3)	3.70(8)
15.5	2.70(5)	0.65(3)	3.35(8)
16.5	2.58(5)	0.66(3)	3.25(8)
17.5	2.08(5)	0.49(2)	2.56(7)
18.5	1.96(4)	0.40(2)	2.35(6)
19.5	1.68(4)	0.41(2)	2.09(6)
Sum	$1.18(33)\times 10^5$	$2.60(11)\times 10^4$	$1.44(44)\times 10^5$
Time-dependent result	$1.18(24)\times 10^5$	$2.60(5)\times 10^4$	$1.44(29)\times 10^5$

Table 5.6: Overview of the extracted count rates (detection efficiency corrected) for ^{124}Cs X-rays depending on the trapping time. The listed errors for the K_α and K_β count rates are the statistical errors based on the count rates. The error for the total number of counts is the sum of the K_α and K_β count-rate uncertainties. The errors for the sum of all peak integrals as well as for the time-dependent result represent the statistical uncertainty resulting from the fit.

^{124}Sn			
Time [s]	Counts/ϵ (K_α) $\times 10^3$	Counts/ϵ (K_β) $\times 10^3$	Counts/ϵ (total) $\times 10^3$
0.5	49.07(22)	10.04(10)	59.11(32)
1.5	38.27(20)	7.93(9)	46.20(29)
2.5	32.88(18)	6.71(8)	39.59(26)
3.5	27.51(17)	5.34(7)	32.85(24)
4.5	23.01(15)	4.50(7)	27.51(22)
5.5	17.66(13)	3.57(6)	21.23(19)
6.5	13.77(12)	2.76(5)	16.53(17)
7.5	11.87(11)	2.46(5)	14.33(16)
8.5	10.23(10)	2.09(5)	12.32(15)
9.5	8.47(9)	1.75(4)	10.22(13)
10.5	7.01(8)	1.43(4)	8.43(12)
11.5	6.00(8)	1.30(4)	7.30(11)
12.5	4.19(7)	0.75(3)	4.94(9)
13.5	3.75(6)	0.58(2)	4.34(9)
14.5	3.39(6)	0.70(3)	4.09(8)
15.5	2.17(5)	0.52(2)	2.69(7)
16.5	2.00(5)	0.44(2)	2.44(7)
17.5	1.70(4)	0.30(2)	2.00(6)
18.5	1.25(4)	0.28(2)	1.53(5)
19.5	1.24(4)	0.23(2)	1.47(5)
Sum	$2.65(5)\times 10^5$	$5.37(11)\times 10^4$	$3.19(10)\times 10^5$
Time-dependent result	$2.66(3)\times 10^5$	$5.35(6)\times 10^4$	$3.19(3)\times 10^5$

Table 5.7: Overview of the extracted count rates (detection efficiency corrected) for ^{124}Sn X-rays depending on the trapping time. The given errors for the K_α and K_β count rates represent the statistical uncertainties based on the count rates. The error for the total number of counts is the sum of the K_α and K_β count-rate uncertainties. The errors for the sum of all peak integrals as well as for the time-dependent result represent the statistical uncertainty resulting from the fit.

$E(K_\beta) \sim 33.7$ keV become the dominant component of the spectra towards longer trapping times, while the signature of the short-lived Sn X-rays become less present in the spectrum.

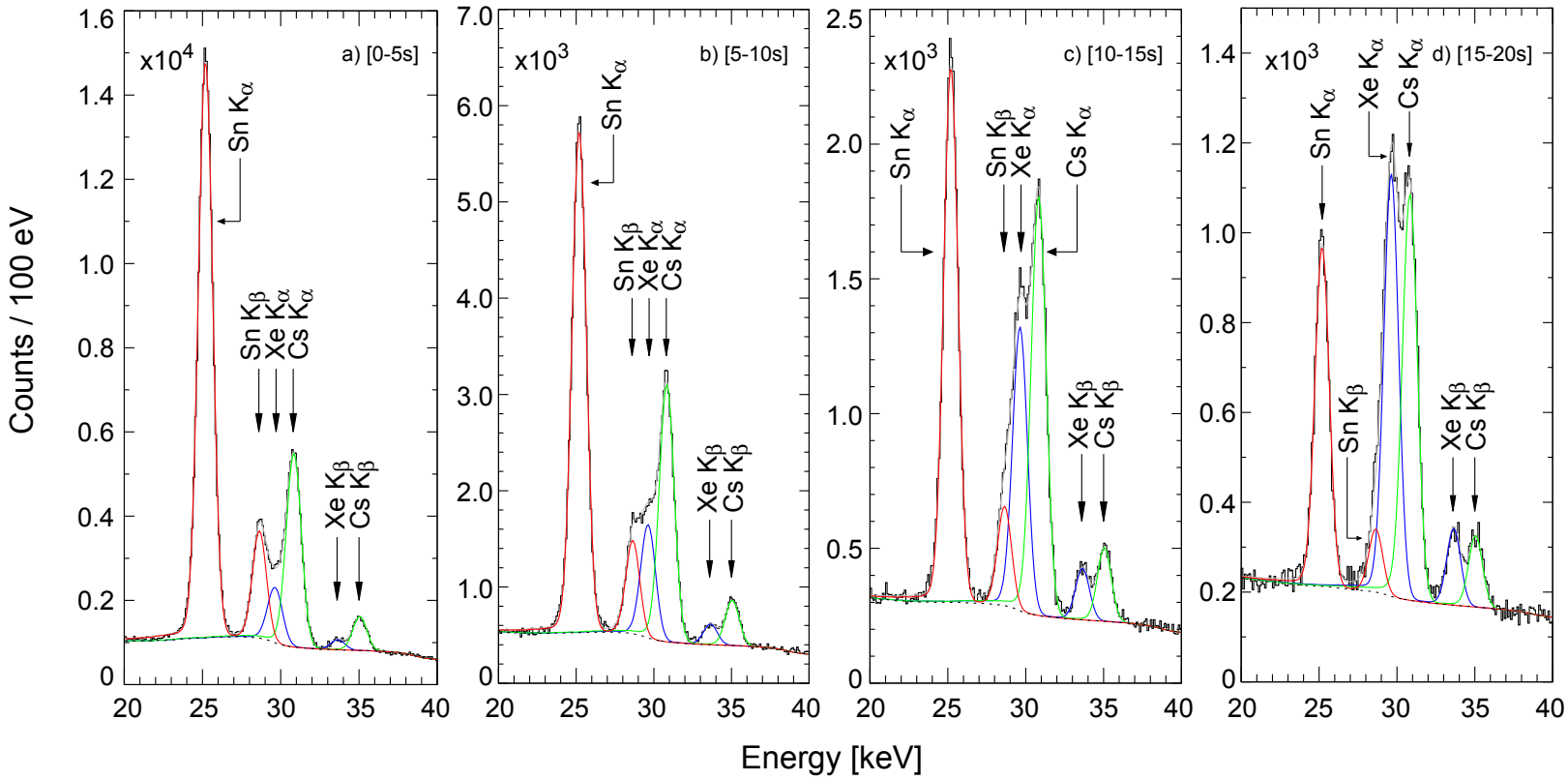

Figure 5.11: Time-sliced X-ray spectra displaying the X-ray energy region (20 keV to 40 keV) for the data recorded in four different time intervals of the trapping cycle: a) 0-5 s, b) 5-10 , c) 10-15 s and d) 15-20 s. The solid lines represent the individual contributions (red: ^{124}In isomer, blue: ^{124}Cs ground state, green: ^{124}Cs isomer) from the three species to the total analytical fit function (grey). The black dashed line denotes the background function, which includes the ambient background as well as a time-dependent component originating from the Compton background.

5.5.2 Time-dependent fitting method

In addition to the above described analysis, a time-dependent peak-fitting routine has been developed in parallel, to extend the analytical fit by a time dependency. For applying this procedure the data is not sliced into individual slices but the complete spectrum over the trapping time from 0 s to 20 s is fitted at once. Here, the basic fit function is the same as for the time-independent procedure but does not only apply a fit to the energy but has a second dimension, which is time.

The calculation of the spectra for each species is then extended by an exponential decay function by adding an additional fit parameter for each ion species and another one for the background alteration over time. This is possible as the data has already been processed to be available in form of a time- and energy-dependent spectrum.

For the time-dependent analytical method, the final fit functions for the three different species are applied to the integrated spectrum of 20 s trapping time, whereby the X-ray energies, intensities, half-lives, energy resolution and background scaling are free parameters for which starting values are given analogously to the time-independent routine described in Sec. 5.4. A fitted spectrum is presented in Fig. 5.12.

5.5.3 Half-lives

Since the timing information for each detected event was recorded for each measuring cycle, i.e., over 30 s relative to the ion-bunch injection, an extraction of the half-lives is possible. The half-lives of the three identified species (^{124m}In, ^{124m}Cs, ^{124}Cs g.s.) were determined by extracting the number of K_α and K_β X-ray counts (Sn, Cs, Xe) as a function of the trapping time. The time-dependent trends were described with a single exponential function for each species in order to extract the values for the half-lives as shown in Fig. 5.13. For the ^{124m}Cs isomer and ^{124}Cs ground state the decays yield values of $T_{1/2}$=6.41(7) s and $T_{1/2}$=31(3) s, which are in agreement with the literature values of $T_{1/2}$=6.3(2) s and $T_{1/2}$=30.9(4) s [169]. The decay of the ^{124m}In isomer into ^{124}Sn can be described by a half-life of $T_{1/2}$=3.68(3) s and is also consistent with the literature value of $T_{1/2}$=3.7(2) s [169].

A possibility to verify the extracted half-lives is given by using the result of the simultaneous

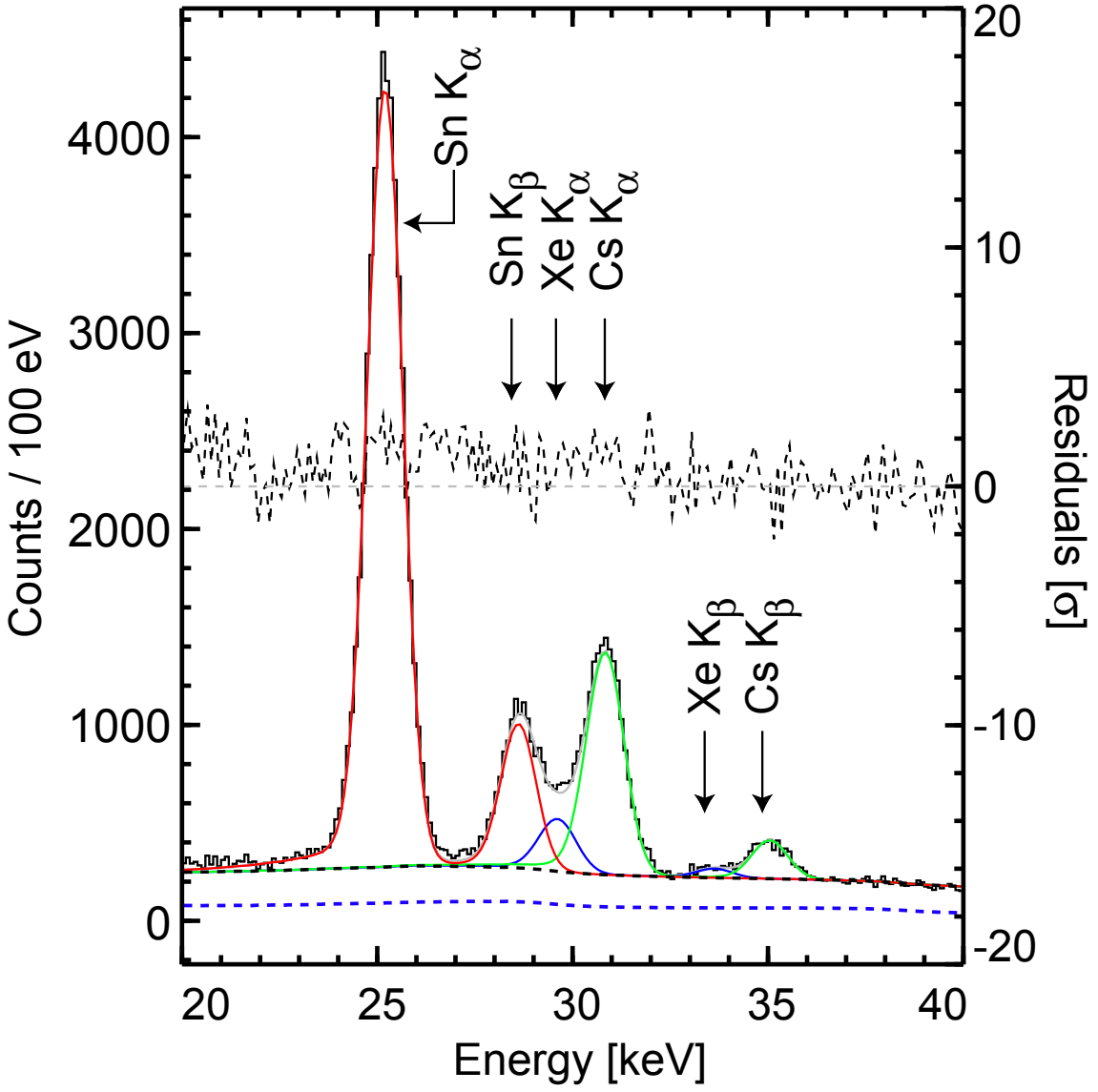

Figure 5.12: One-dimensional projection of the time-dependent fit of the X-ray energy region applied to the complete data set. Energy and time are fitted simultaneously. The grey curve represents the sum of all fit functions, the black, dashed line shows the background including the ambient and the time-dependent Compton background, whereas the blue dashed line shows the Compton background contribution only. The solid lines are the fits of the individual species: Xe (blue), Cs (green), Sn (red). The ordinate on the right corresponds to the residuals of the fit (black dashed line).

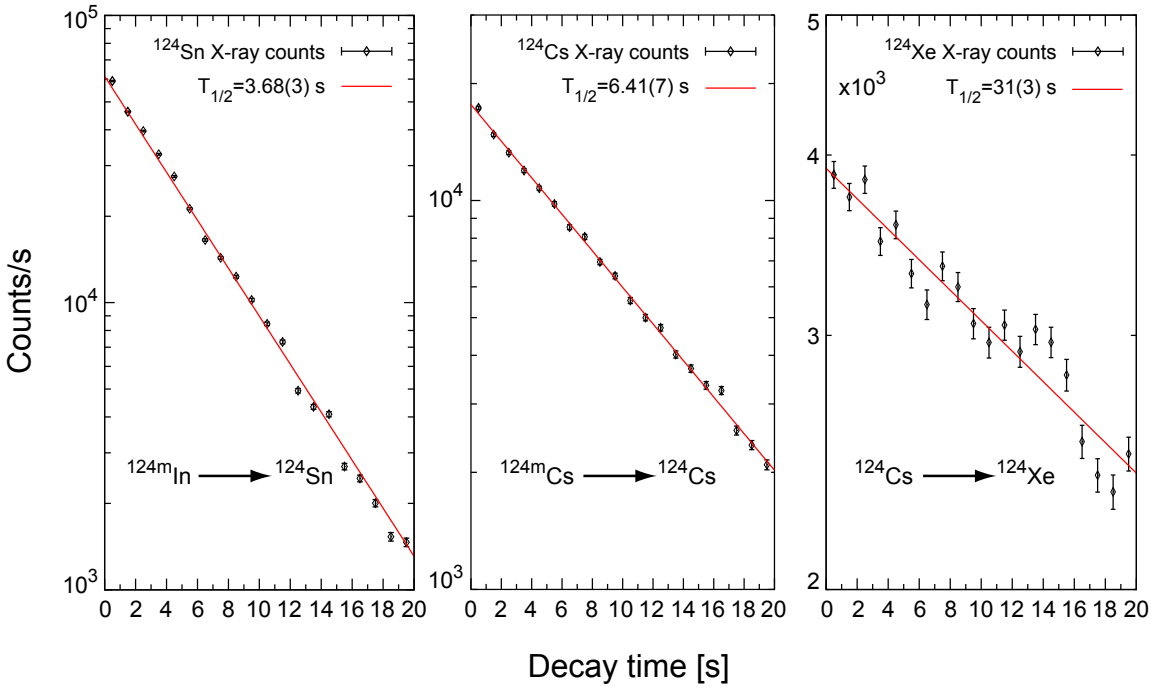

Figure 5.13: Decay curves of the ^{124}Cs ground state and isomer as well as the ^{124}In isomer presented on a half-logarithmic scale. The error bars correspond to the statistical uncertainty based on the count rate.

fit of energy and time, which has been constructed to directly fit the half-life during the minimization procedure. The results for both fitting procedures as well as the literature values are listed in Tab. 5.8. The half-lives extracted from an exponential fit of the count rates of the individual time slices as a function of time are consistent with the time-dependent fit of the complete data set over 20 s and further agree with the literature values. From these results, one can conclude that the ion trapping during the 20 s of decay time was $\sim$ 100% efficient and that possible ion losses were minimal and if present not detectable within the current sensitivity of the spectroscopy setup. Ion losses would manifest themselves in shorter measured half-lives, and deviate from the expected literature values given in Ref. [169].

5.5.4 Comparison to simulation

In order to prove the reliability of the analysis procedure, the fitting routine was tested by fitting a simulated Monte-Carlo (MC) spectra generated using GEANT4 and including

	$T_{1/2}$		
Species	Time-slices fit	Time-dependent fit	Lit. value
^{124}In (8^-)	3.68(3) s	3.71(2) s	3.7(2) s
^{124}Cs (7^+)	6.41(7) s	6.37(6) s	6.3(2) s
^{124}Cs (1^+)	31(3) s	31(2) s	30.9(4) s

Table 5.8: Measured half-lives for the ^{124m}In isomer, ^{124m}Cs isomer and ^{124}Cs ground state compared with the literature values taken from Ref. [185]. The values in brackets represent the statistical uncertainties.

the same three species as the experimental data taken during the A=124 experiment. The MC-simulation was benchmarked with radioactive source data and the experimental commissioning data is reproduced well within the energy region of 20 keV to 140 keV. The analytical fit takes the generated Compton background into account and describes the MC-spectrum correctly.

A comparison of the experimental data with the Monte-Carlo is shown in Fig. 5.14. The black curve represents the experimental A=124 data and the red one shows the MC-generated spectrum. In blue, the background taken during the 5 s measurement after ion extraction is shown. Within the energy region from 20 keV to 40 keV the X-rays from the three different isobars are observed. The major differences between MC and experimental data occur in this part of the spectrum, which is due to the fact that the Monte-Carlo input, i.e., intensities and energies, were taken from the NNDC database [169]. However, this deviation from the experimental data is expected as the values for energies and intensities from the database are those for neutral atoms, while the experimental data represents the decay spectrum of highly-charged ions, where the X-ray energies are shifted and the intensity ratios are affected (see Sec. 5.5.7). Further, the tail on the low energy side of the peaks, which is caused by charge collection is not included in the simulation and is the reason for the deviations on the low energy side of the peaks, which are most noticeable for the ^{124}Sn K_α X-ray.

Between 50 keV to 130 keV one can observe the γ-rays originating from the decay of the ^{124m}Cs isomer into the ^{124}Cs ground state at 53.85 keV, 58.20 keV, 89.50 keV and 96.55 keV as well as those from the decay of the ^{124m}In isomer at 102.91 keV and 120.34 keV, where

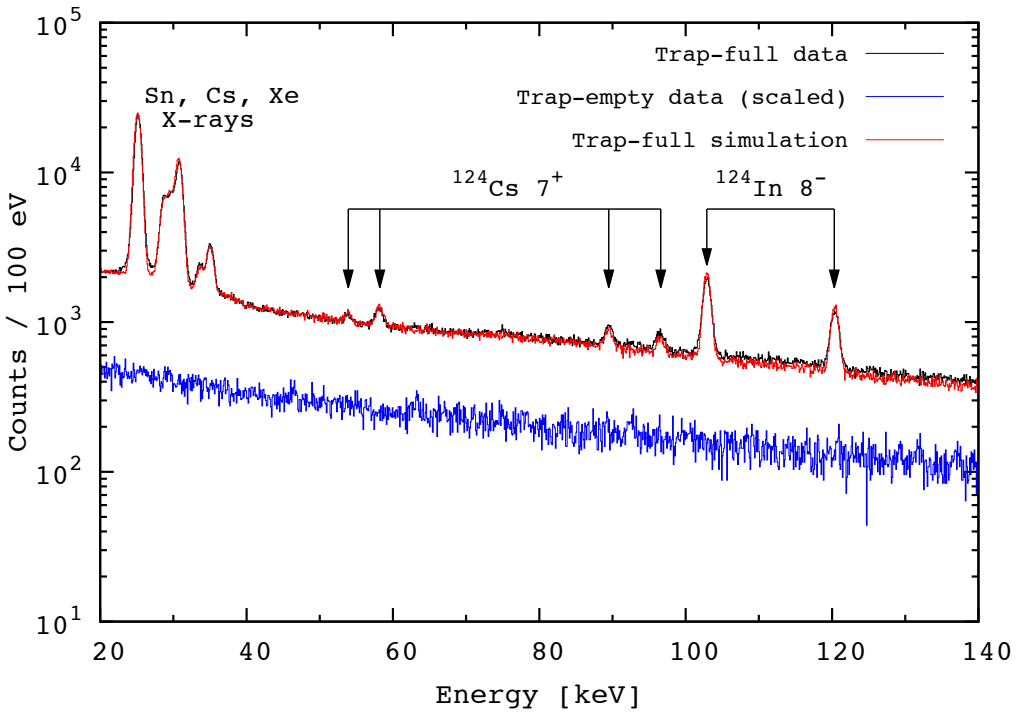

Figure 5.14: Overlay of the Monte-Carlo generated spectrum with the experimental data taken during the ^{124}Cs experiment within an energy region of 20 keV to 140 keV. The red spectrum shows the simulation of a full-trap A=124 spectrum, the black one the experimental ^{124}Cs data and the blue one the time-scaled background measured during the empty-trap part of the cycle.

the simulation is in good agreement with the experimental data.

5.5.5 Cross check of the ECBR normalization

The ^{124}Cs ground-state does not only decay into the ^{124}Xe ground state but also populates the first excited $J^{\pi} = 2^{+}$ state in ^{124}Xe at 354.1 keV with a relative transition intensity of 47% [169]. The 354.1 keV γ-ray is visible in the Si(Li) detectors and can be used to verify the normalization of the electron-capture branching ratio.

However, fitting the 354.10 keV photo peak is complicated by the appearance of a Compton edge at 340 keV (see Fig. 5.15), which is caused by traces of the positron annihilation line. Furthermore, one has to deal with low statistics due to the low intrinsic detection efficiency of the Si(Li) detectors ($\sim 0.1\%$) at this energy. Therefore, the fit function consists of four individual functions in order to avoid biases:

1. Two linear functions are generated to describe the background on either side of the Compton edge.

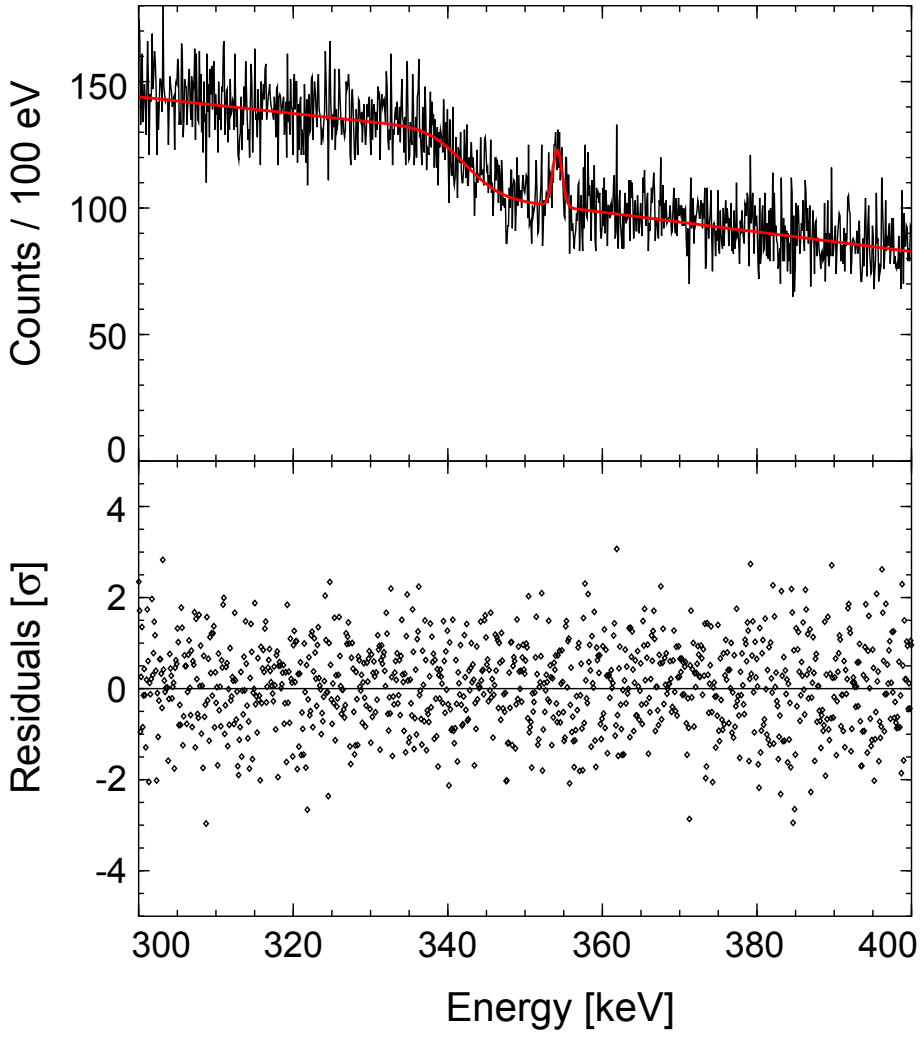

Figure 5.15: Displayed is the fit function (red) of the 354.10 keV γ-line within an energy region of 300 keV to 400 keV. The Compton edge is caused by remains of 511 keV annihilation photons and was included in the fit as described in the text. The bottom panel shows the residuals of the fit.

2. The step of the Compton edge is described by merging those two linear function with an error function that is adjusted to the data by minimizing it to its χ^2.

3. Then the actual Gauss function that describes the γ-ray is included.

The total number of counts is 352 ± 35. Taking into account the relative transition intensity of 47% [169] and the detection efficiency at 354.10 keV (ϵ_{354}=0.00104(5)) one gets for the number of ^{124}Cs ground-state decays:

$$N_{decays} = \frac{N_{counts}}{\epsilon_{354} \cdot I_\gamma} = \frac{352}{0.00104 \cdot 47} = 7.2(7) \times 10^3 \tag{5.9}$$

The consistency and reliability of the fitting procedure can be judged by the FWHM and the resulting energy resolution of 1.4 keV, which is the expected value according to the calculation based on the FWHM at lower energies (compare Fig. 3.10 in Ch. 3).
The number of decays has to be consistent with the number of EC decays extracted from the Xe X-rays. The number of ^{124}Cs ground-state decays is derived entirely from the X-rays in order to extract the number of electron-capture decays. The electron-capture decay also feeds excited states in ^{124}Xe (compare Fig. 5.16), which can decay via internal conversion producing additional Xe X-rays. To derive the contribution of IT X-rays, the BrIcc v2.3S (9-Dec-2011) internal-conversion coefficient calculator [169] was used to calculate the internal-conversion coefficients for the transitions with the major contributions:

- E2: 2^+(354 keV) $\longrightarrow$ 0^+(0 keV), $\alpha_C^{tot} = 0.0248(4)$, $\alpha_C^K = 0.0206(3)$, $I_{CE} = 0.973\%$, E_γ=354 keV,

- E2: 0^+(1269 keV) $\longrightarrow$ 2^+(847 keV), $\alpha_C^{tot} = 0.01456(21)$, $\alpha_C^K = 0.01223(18)$, $I_{CE} = 0.0062(8)\%$, E_γ=422 keV,

- M1+E2: 2^+(847 keV) $\longrightarrow$ 2^+(354 keV), $\alpha_C^{tot} = 0.00940(14)$, $\alpha_C^K = 0.00795(12)$, $I_{CE} = 0.034(5)\%$, E_γ=493 keV,

- E2: 4^+(879 keV) $\longrightarrow$ 2^+(354 keV), $\alpha_C^{tot} = 0.00785(11)$, $\alpha_C^K = 0.00666(10)$, $I_{CE} = 0.0028(4)\%$, E_γ=525 keV,

- E2: 2^+(847 keV) $\longrightarrow$ 0^+(0 keV), $\alpha_C^{tot} = 0.00236(4)$, $\alpha_C^K = 0.00202(3)$, $I_{CE} = 0.0028(4)\%$, E_γ=847 keV and
- E2: 0^+(1269 keV) $\longrightarrow$ 1^+(354 keV), $\alpha_C^{tot} = 0.00197(3)$, $\alpha_C^K = 0.001699(24)$, $I_{CE} = 0.0080(10)\%$, E_γ=915 keV.

From the internal conversion coefficients, the IT X-ray intensity I_{CE} can be calculated by further taking into account the intensity of the population for a particular state in ^{124}Xe by the ^{124}Cs ground state as indicated in Fig. 5.16. Summing the individual contributions yields a values of I_{CE}^K=1.0268(76)%. Given a total X-ray intensity of I_{EC}^K=8.14(56)%, the fraction of IT X-rays is 12.6(9)%.

To first order the number of EC decays can be compared with the number of decays in the 354 keV line to cross-check, whether one can reproduce the literature value of the branching ratio. From the efficiency corrected number of Xe K_α counts (compare Tab. 5.5) and a relative intensity of 6.92% one derives a total of $7.5(4)\times10^3$ EC decays. The same calculation can be performed for the Xe K_β (I=1.22%) counts, from which one calculates a total of $7.2(6)\times10^3$ EC decays. Both results are consistent with each other and with the number of decays extracted from the 354.10 keV peak (see Eq. 5.9), which confirms the quoted values for the intensities and proves the capability to measure ECBRs with the current experimental setup as well as the reliability of the data analysis.

5.5.6 Suppression of the 511 keV annihilation radiation

As explained in Sec. 2.3, the β decay induced charged particles (β^+ and β^-) are guided out of the trap, which results in a suppression of the 511 keV annihilation line in case of the β^+ decay. To experimentally quantify this capability, ^{124}Cs turned out to be an ideal test case, since the decay of the ^{124}Cs ground state features a strong β^+-decay branch (181% 511 keV annihilation [169]). A direct comparison of the efficiency-corrected peak areas of the 354.10 keV γ-line and the 511 keV peak was performed, to give an estimate of the lower limit for the suppression of the positron-annihilation background.

The fit for the 354.10 keV line is shown in Fig. 5.15 and yields 352 counts. The only evidence found for the existence of the 511 keV line is given by the appearance of the corresponding

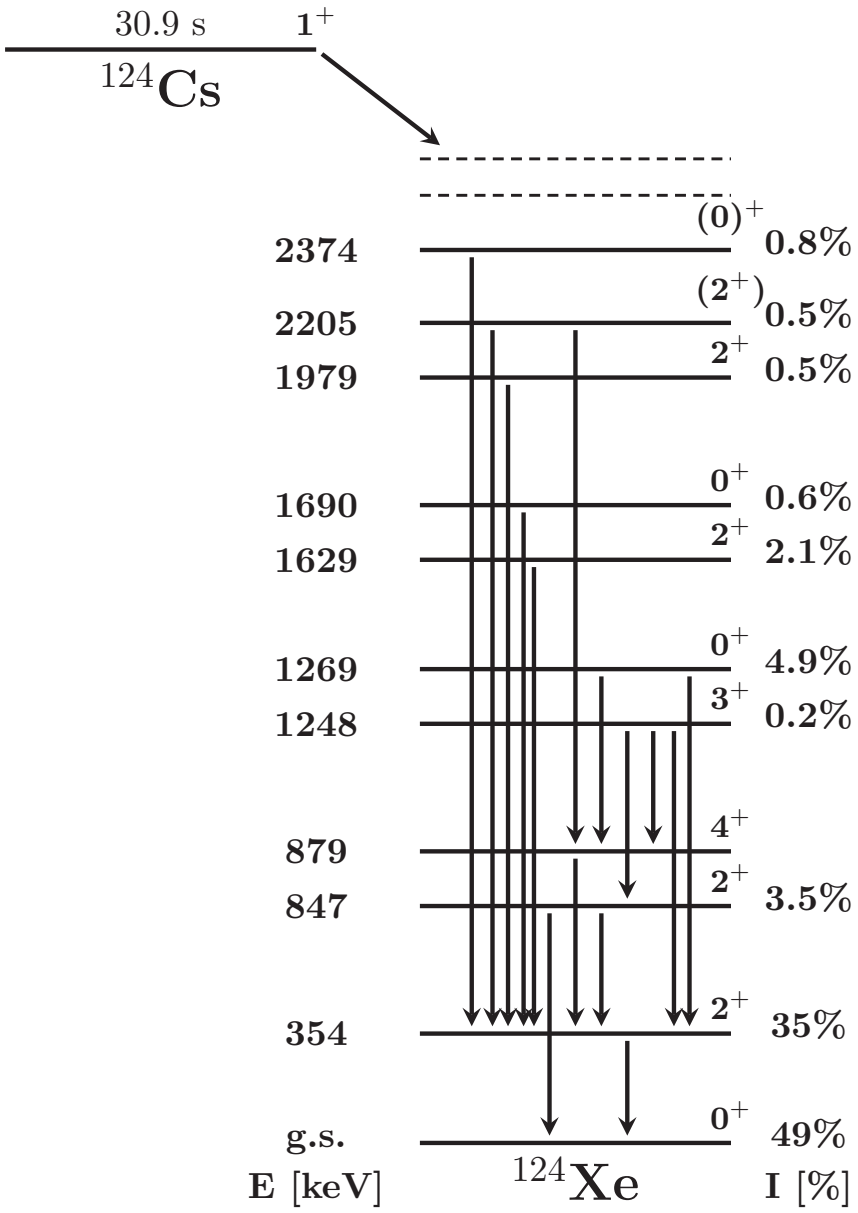

Figure 5.16: Partial level scheme for the decay of the ^{124}Cs ground state into excited states in ^{124}Xe. The transitions feeding the 354 keV state are indicated in addition to various other transitions within the excited states in ^{124}Xe. The intensity values refer to the population of that particular state by the ^{124}Cs ground state. The existence of several higher energy levels is indicated by the dashed lines. Values taken from Ref. [169].

Compton edge as mentioned in the previous section. An upper limit of 26 counts above background at 511 keV, representing the statistical uncertainty of 1 σ is used as input in Eq. 5.10 for the suppression-factor (S_{511}) calculation (see also Ref. [130]):

$$S_{511} = \left(\frac{I_{511}}{I_{354}}\right)_{lit.} \times \left(\frac{N_{354}}{I_{511}}\right)_{exp.} \times \left(\frac{\epsilon_{511}}{\epsilon_{354}}\right)_{sim} \approx 20, \tag{5.10}$$

where I represents the relative peak intensity found in the literature [169] and ϵ is the photo-peak detection efficiency (ϵ_{354}=0.001038, ϵ_{511}=0.0004), which has been derived from simulations. The latter were benchmarked to experimental radioactive source data. $\frac{N_{354}}{I_{511}} = \frac{352}{26}$ describes the count-rate ratio of the 354.10 keV and 511 keV line. Here it becomes obvious that a precise energy calibration up to $\sim$ 600 keV was essential to allow for a reliable summation of the spectra taken with different detectors in order to set a lower limit for the background suppression of the 511 keV annihilation line. This suppression factor comes to $\sim$ 20, which was verified additionally via a GEANT4 simulation, where no magnetic field was included and, hence, the 511 keV line was present in the simulated spectrum. The direct comparison of the experimental data to simulations in the 511 keV energy region is displayed in Fig. 5.17. Here, the 511 keV line is visible in the simulated spectrum while no evidence for a peak is found in the experimental data. The two spectra are shown relative to the background measurement.

5.5.7 Atomic-structure effects

Charge breeding provides significant advantages for ion trapping in terms of ion confinement and reduced trapping losses, but as a consequence of charge breeding, the atomic structure is altered in the process [109] as electron correlation, relativistic and quantum electrodynamical effects on the electronic-binding energies become larger with increased charge state [109] (compare Sec. 1.7).

This effect was studied with the commissioning data of the ^{124}Cs experiment in order to investigate its influence on X-ray energies, intensities and branching ratios. A comparison with theoretical calculations carried out with the FAC code [110] showed the consistency of the experimental data with theory. Additionally, the effect on the K_α/K_β ratio was investigated and is described in this section.

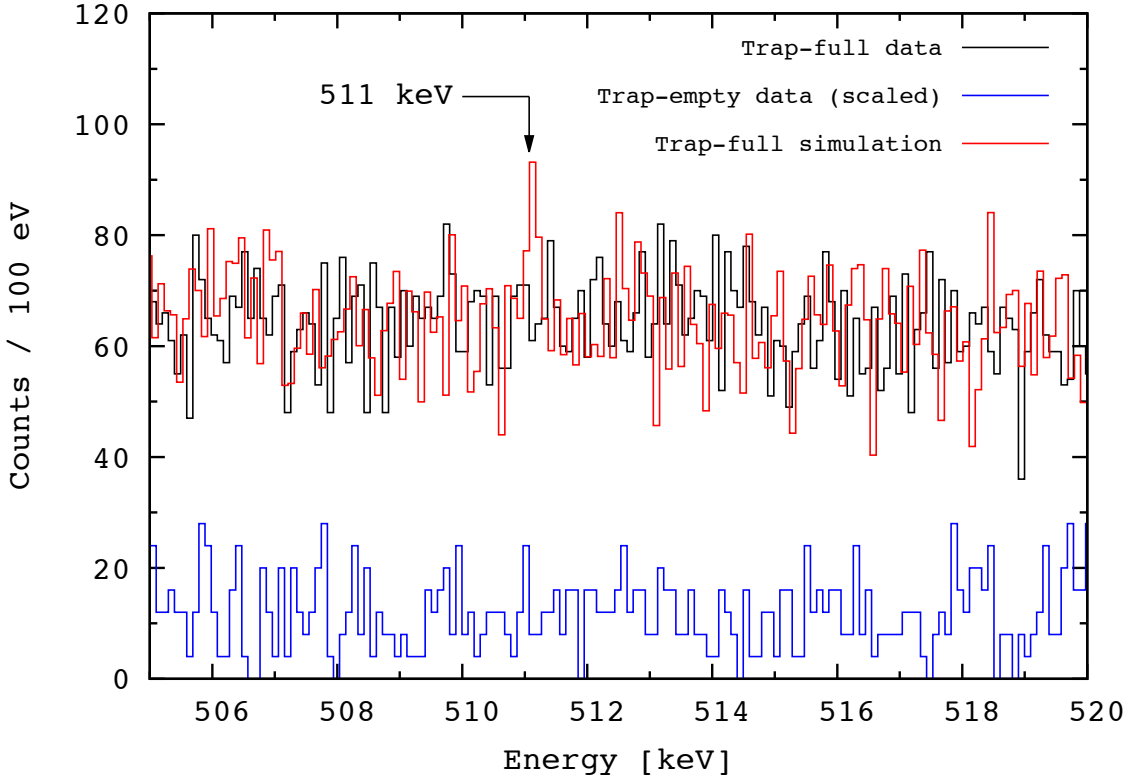

Figure 5.17: Energy region from 505 keV to 520 keV to illustrate the 511 keV annihilation suppression in the experimental data (black) relative to the simulated spectrum (red), which has been generated without 511 keV annihilation suppression, i.e., without the presence of a magnetic field. The measured background spectrum (blue) has been time-scaled up by a factor of 4 in order to be directly comparable to the full-trap data.

5.5.7.1 X-ray energy shifts

As the K_α X-ray from ^{124}Sn is used for energy calibration purposes it is not possible to determine absolute values for the energy shift of the K_α and K_β X-rays but merely the relative energy differences $[E(K_\beta) - E(K_\alpha)]_{q\approx 26-32}$ can be extracted and compared to the values for neutral atoms $[E(K_\beta) - E(K_\alpha)]_{q=0}$.

In order to test the sensitivity of the fitting procedure for extracting the energy shifts, an unbiased analytical analysis of a variety of simulated spectra with random X-ray energy shifts and half-lives was performed. The results reproduced the values for the shifts used to generate the spectra within 30 eV for not clearly separated peaks (Xe K_α) and within $\leq$ 10 eV for the Sn K_α, thus demonstrating the reliability of the fitting routine.

The energy shifts in the A=124 spectra were determined once for every 1 s time slice with a time-independent fit and once for the whole data set by applying the time-dependent method. The results are listed in Tab. 5.9. Here, the importance of a precise energy calibration to allow for quantitative statements about the atomic structure effects induced by charge breeding becomes obvious again.

As displayed in Tab. 5.9, the values for the shifts are 96(37) eV for Xe, 120(34) eV for Cs and 139(34) eV for the Sn X-rays, quoting the results for the time-slices weighted average. The results are consistent with a direct time-dependent fit. The average $\Delta\,[E(K_\beta) - E(K_\alpha)]$ values (red line) for ^{124}Xe and ^{124}Cs from all slices are presented in Fig. 5.18 and compared with the result from the time-dependent fit (black line). The corresponding values for ^{124}Sn are shown in Fig. 5.19.

While the individual values for every time-slice fit exhibit large trapping-time dependent variations especially for the Xe K_α, the average values of the 20 time slices are consistent with the results of the time-dependent fit. The deviations for the results from slice to slice are not only due to limited statistics within one slice, but also due to the different half-lives of the species and the corresponding, time-dependent alterations of the spectrum. In plain terms, at the beginning of the trapping time the Sn X-rays dominate the spectrum and are described better by the fit, while at longer trapping times, the Xe X-rays become the dominant component of the spectrum. As the nature of the time-dependent fit already

	$\Delta\left[E(K_\beta) - E(K_\alpha)\right]$		
Time [s]	Sn	Xe	Cs
0.5	98(34)	160(84)	84(37)
1.5	113(34)	150(55)	123(38)
2.5	117(36)	159(80)	133(39)
3.5	164(35)	93(92)	116(42)
4.5	135(37)	-18(66)	59(37)
5.5	107(38)	77(84)	101(41)
6.5	186(38)	71(94)	81(43)
7.5	137(43)	-64(78)	102(51)
8.5	171(44)	213(65)	111(44)
9.5	83(43)	132(100)	146(44)
10.5	222(47)	-36(81)	42(50)
11.5	193(52)	192(79)	160(51)
12.5	111(60)	146(80)	174(53)
13.5	74(62)	24(60)	171(48)
14.5	180(67)	100(67)	245(50)
15.5	337(94)	-18(84)	152(56)
16.5	67(85)	82(68)	114(55)
17.5	160(87)	119(63)	140(71)
18.5	135(76)	137(84)	86(93)
19.5	217(199)	162(66)	174(83)
Average	150(71)	94(84)	126(57)
Weighted average	139(34)	96(37)	120(34)
Time-dependent fit result	145(33)	87(34)	112(33)
FAC	143	92	111

Table 5.9: Listed are the extracted $\Delta\left[E(K_\beta) - E(K_\alpha)\right]$ values for the Sn, Xe and Cs X-rays for each 1 s time slice of the 20 s of trapping time as well as the average values in comparison to the results gained from the direct time-dependent fit. The values in brackets for the fitted shifts and for the time-dependent results represent the sum in quadrature of the statistical uncertainty of the fit obtained via the covariance matrix and the systematic uncertainty of the energy calibration (33 eV). The uncertainty for the weighted averages originate from the sum in quadrature of the corresponding internal errors and the systematic uncertainty, while the errors for the unweighted average values represent the combination of standard deviation and the systematic uncertainty. Since the theoretical values can be calculated to sub-eV precision, no uncertainties are given in this table.

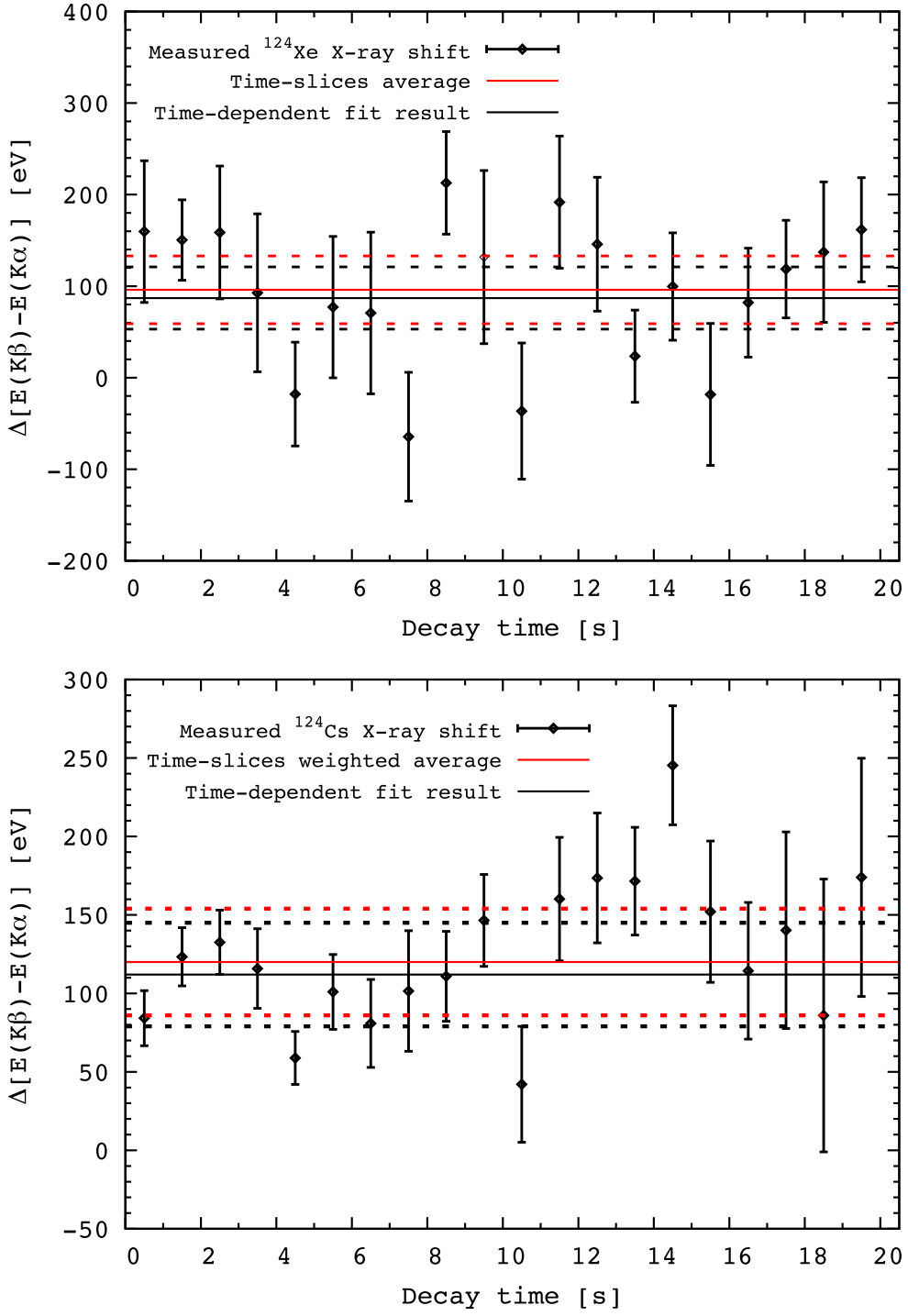

Figure 5.18: Top: $\Delta\left[E(K_\beta) - E(K_\alpha)\right]$ for ^{124}Xe for every time slice (1 s bins). Shown is a comparison of the weighted average value from all slices (solid red line) with the result from the time-dependent fit (solid black line). The errors of the individual data points represent the statistical uncertainty from the fit. Bottom: $\Delta\left[E(K_\beta) - E(K_\alpha)\right]$ for ^{124}Cs for every time slice (1 s bins).

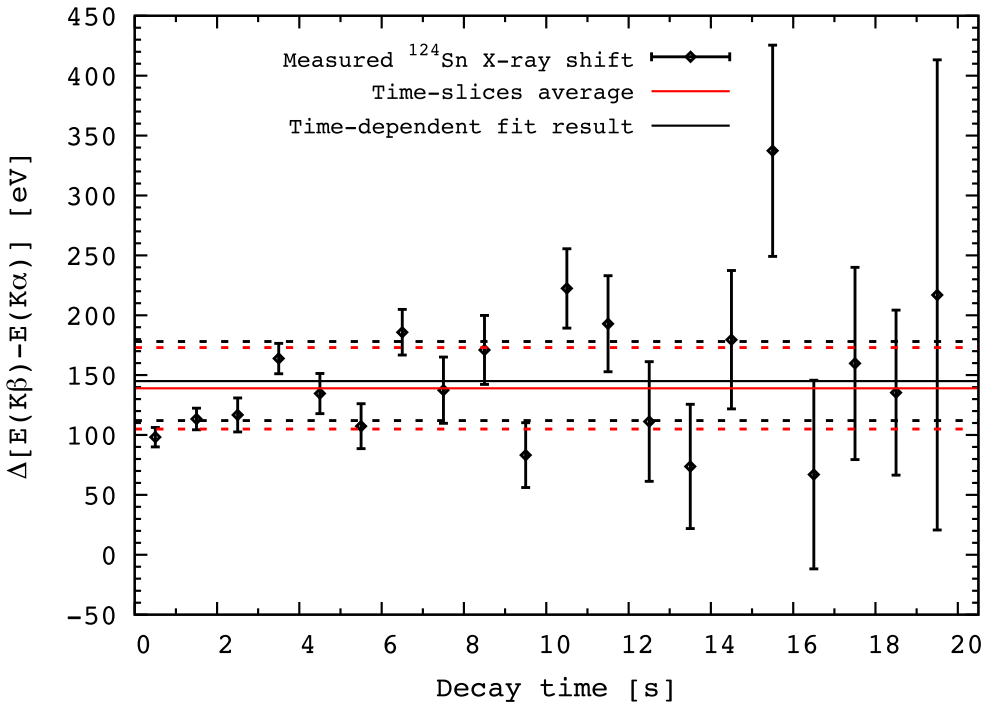

Figure 5.19: $\Delta\left[E(K_\beta) - E(K_\alpha)\right]$ for ^{124}Sn for every time slice (1 s bins). Shown is a comparison of the weighted average value from all slices (solid red line) with the result from the time-dependent fit (solid black line). The dashed red lines represent the uncertainties including the systematic error. The errors of the individual data points represent the statistical uncertainty from the fit.

	$\Delta\left[E(K_\beta) - E(K_\alpha)\right]_{exp.}$ [eV]			
E-beam energy [keV]	1.5	2.0	Average	All data
Sn	144(33)	136(33)	140(33)	144(33)
Cs	99(34)	114(33)	107(34)	112(33)
Xe	77(37)	67(35)	72(36)	87(34)

Table 5.10: Comparison of the $\Delta\left[E(K_\beta) - E(K_\alpha)\right]$ values extracted from data taken at different electron-beam energies to the results obtained from analyzing the complete data set. The average value combines the results from the shifts measured at an energy of 1.5 keV and 2.0 keV. The values in brackets represent the sum in quadrature of the statistical uncertainty and the systematic uncertainty resulting from the energy calibration.

accounts for the time-dependent change of the spectrum's structure, the values extracted by that method are consistent with the average fit values of the single time slices (see Tab. 5.9). The $\Delta\left[E(K_\beta) - E(K_\alpha)\right]$ values from Tab. 5.9 are illustrated in a bar chart in the top panel of Fig. 5.20. The average result from 20 time slices is shown in red, the weighted average in green and the value extracted via the time-dependent method is plotted in blue. While the analytical uncertainties of the weighted average of the individual 1 s time-slice fits and those of the time-dependent method are of the same order and relatively small, the statistical errors from the unweighted average are between 20% and 36%. Note that for both fitting methods the systematic uncertainty from the energy calibration, which is about 33 eV has to be taken into account for the absolute error and has been added in quadrature.

To verify whether the energy shifts observed at an electron-beam energy of 1.5 keV ($q \approx 27^+$) and 2.0 keV ($q \approx 32^+$) exhibit significant differences, the data obtained at different electron-beam energies was separated and analyzed individually. The resulting energy shifts are listed in Tab. 5.10 and illustrated in the bottom panel of Fig. 5.20. The observed alterations are within the uncertainties and the average value from the 1.5 keV and 2.0 keV results agree with the results obtained from the analysis using the complete data set. Due to the limited statistics, a direct time-dependent fit was used to obtain the values for the shifts in the individual spectra. Thus, those values are directly compared to the direct fit of the complete data set, instead of the result obtained from the time slices. This can be justified, as the results from both methods described above are consistent.

For all species, the experimental values for $\Delta\left[E(K_\beta) - E(K_\alpha)\right]$ are positive, resulting from

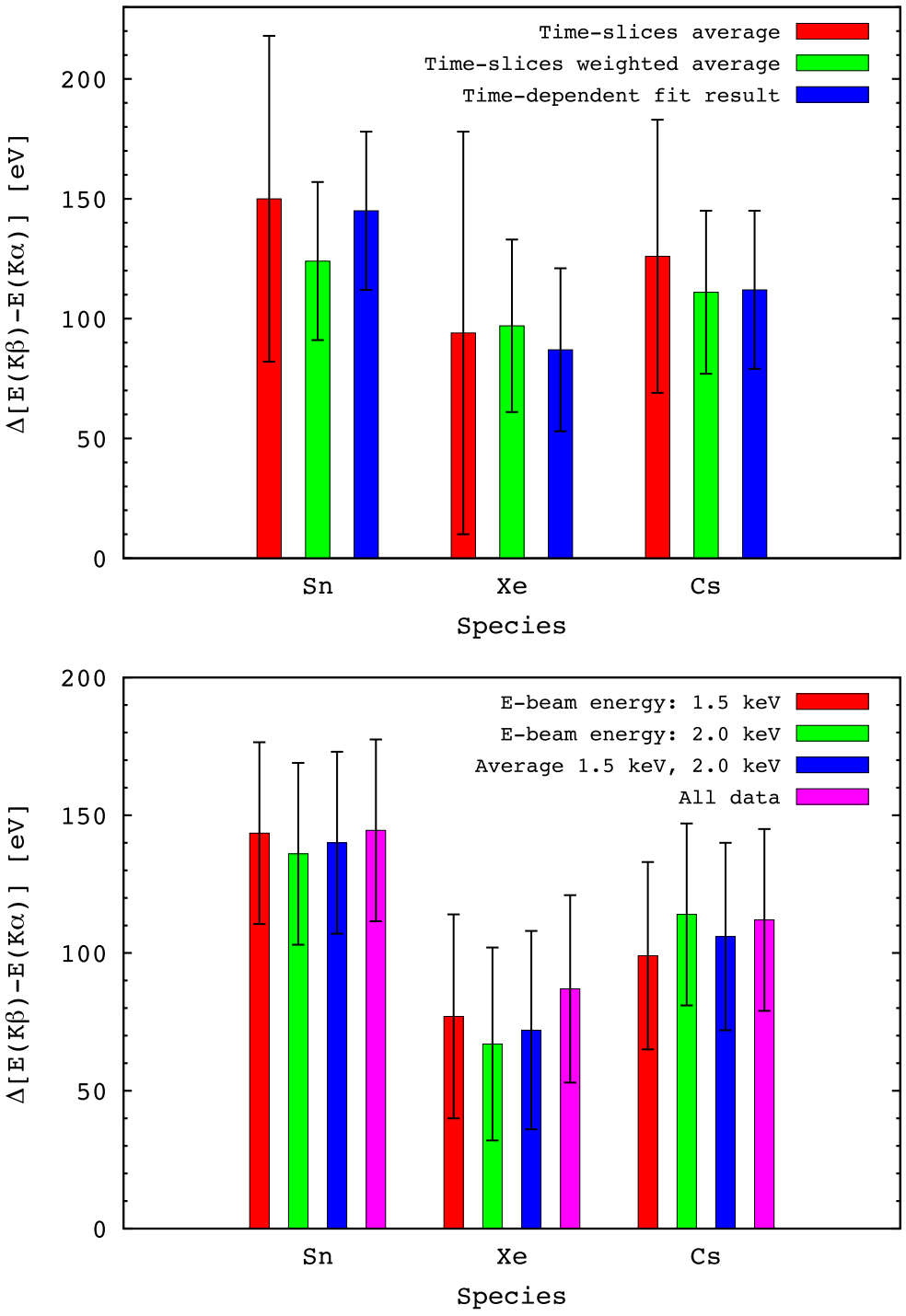

Figure 5.20: Top: Bar chart for the illustration of the $\Delta\left[E(K_\beta) - E(K_\alpha)\right]$ values depending on the fitting method and ion species. Red corresponds to the average value determined from individual fits of 20 time slices. The green bar represents the weighted time-slices average and the time-dependent result is shown in blue. The errorbars represent the statistical errors originating from the fitting procedure. Bottom: Bar chart for the illustration of the $\Delta\left[E(K_\beta) - E(K_\alpha)\right]$ values depending on the analyzed data set and ion species. Red corresponds to the data set measured at an electron-beam energy of 1.5 keV, green to the data collected at an energy of 2.0 keV, blue is the average of the former two values and the extracted value from the complete data set is shown on magenta. The plotted errorbars represent the statistical uncertainty.

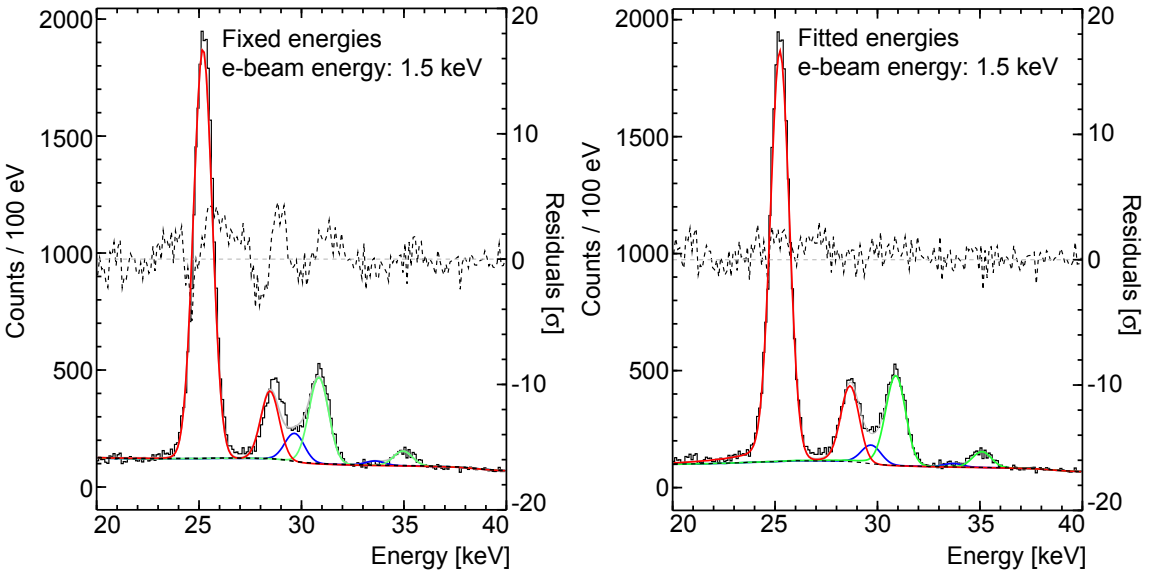

Figure 5.21: Comparison of the fit of the X-ray energy region with fixed energy parameters according to the literature values to the fit performed with free parameters for the peak energies. The fit range included the energy region from 20 to 140 keV. The fitted data was taken at an electron-beam energy of 1.5 keV. The black dashed line corresponding to the right ordinate represents the fit residuals, while the solid lines describe the three ion species and the black dashed line on the bottom describes the background.

the relativistic scaling of the fine-structure splitting, where higher angular-momentum states are driven apart as the charge state increases [107, 109].

To illustrate the sensitivity of the fit to the energy shifts, the fits with the energy as a free fitting parameter are compared to the fits to the data, where the energies were fixed to the literature values. The spectra taken at an electron-beam energy of 1.5 keV (see Fig. 5.21) and 2.0 keV (see Fig. 5.22) were fitted once individually and once as complete data set (see Fig. 5.23). For the fits performed with fixed X-ray energies, the worse quality of the fit relative to the fit with shifted energies is illustrated by the large fit residuals (black dashed line).

The experimentally derived shifts for the Xe X-rays (resulting from the Cs ground-state decay) were compared to theoretical calculations using the multiconfigurational, relativistic Dirac-Hartree-Fock code FAC [110] introduced in Sec. 1.7. Fig. 5.24 presents the theoretical prediction for the change in K_α and K_β energies as a function of the charge state. An

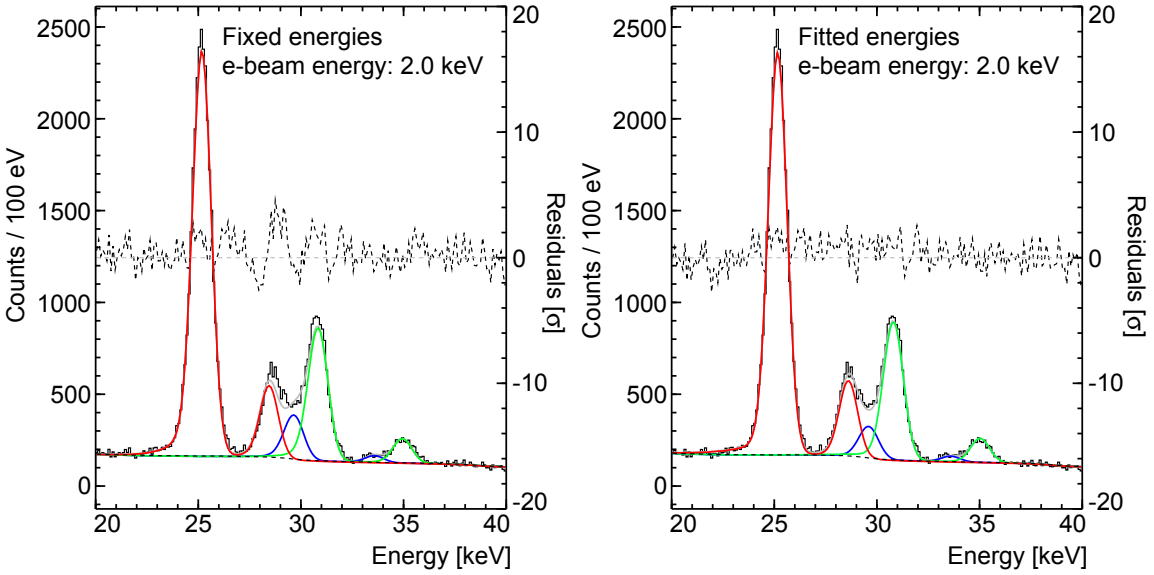

Figure 5.22: Comparison of the fit of the X-ray energy region with fixed energy parameters according to the literature values to the fit performed with free parameters for the peak energies. The fit range included the energy region from 20 to 140 keV. The fitted data was taken at an electron-beam energy of 2.0 keV. The black dashed line corresponding to the right ordinate represents the fit residuals, while the solid lines describe the three ion species and the black dashed line on the bottom describes the background.

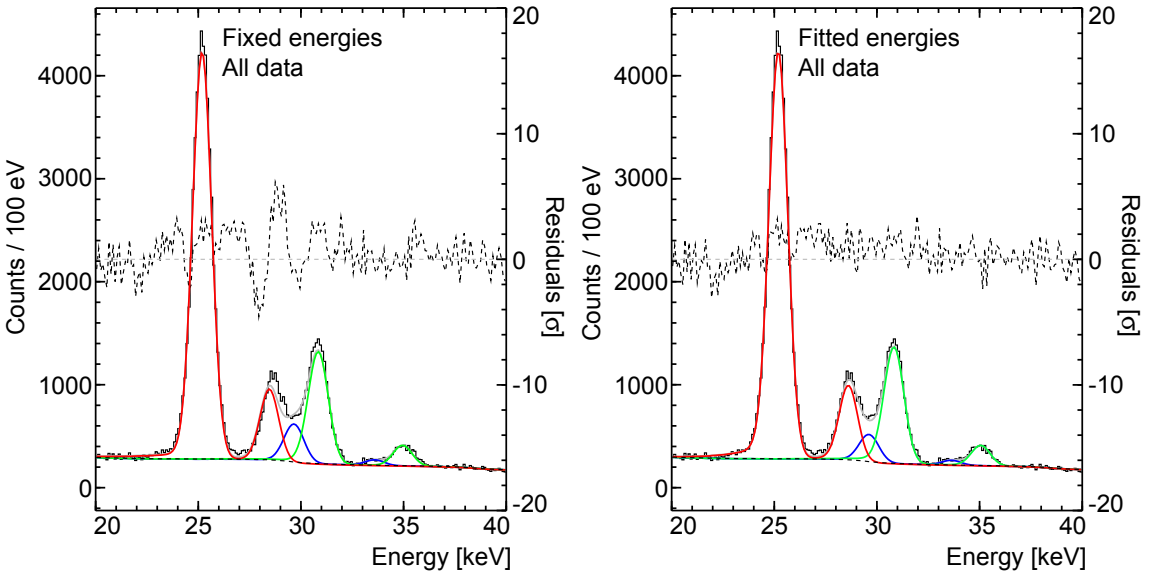

Figure 5.23: Comparison of the fit of the X-ray energy region with fixed energy parameters according to the literature values to the fit performed with free parameters for the peak energies. The fit range included the energy region from 20 to 140 keV. Displayed is the complete data set, where data taken at different electron-beam energies was summed up. The black dashed line corresponding to the right ordinate represents the fit residuals, while the solid lines describe the three ion species and the black dashed line on the bottom describes the background.

example for the input and output files can be found in appendix D. The corresponding $\Delta\left[E(K_\beta) - E(K_\alpha)\right]$ values for Cs ions derived from the FAC code are presented as a function of the charge state in Fig. 5.25.

As outlined in Sec. 1.4, the electron-capture branching ratios are mainly influenced by the electron densities of the inner-most shells and the experimentally observed shifts constitute less than 1% of the total electron-binding energies. Thus, one can conclude, that the high charge states reached within the here described experiment are not high enough to effectively change the nuclear-decay properties at those electron configurations.

5.5.7.2 K_α/K_β ratio

The ^{124}Cs and ^{124}In ions were charge-bred up to an average charge state of $q = 27^+$ or $q = 32^+$, depending on the electron-beam energy, which removed the N-shell electrons completely. With all electrons removed from the N-shell, the $K_{\beta 2}$ transition is non-existent. Fig. 5.26 illustrates that the $K_{\beta 2}$ X-rays result from the filling of a vacancy in the K_1 shell with an electron from the N_2 or N_3 shell. That the X-ray spectrum did not exhibit a $K_{\beta 2}$ transition could be deduced from the fact that the data could only be described well with a fit function that excluded $K_{\beta 2}$. Attempts to include that transition resulted in a significantly increased χ^2. For confirmation, two Monte-Carlo simulated spectrum were generated, one including and one excluding the $K_{\beta 2}$ transition and was fitted analytically in the same way as the experimental data. A comparison with the results from the experimental data revealed that the experimental data was consistent with the MC spectrum lacking the $K_{\beta 2}$ transition.

With the lack of the $K_{\beta 2}$ transition, one would further expect a change in the K_α/K_β ratio. Therefore, the effect was studied for the three different species. Fig. 5.27 and 5.28 present the K_α/K_β ratios for the Xe, Sn and Cs X-rays extracted from the individual 1 s time slices as a function of the trapping time relative to the average value of all time slices. In addition, the plots display the result from a direct time-dependent fit showing consistency.

The X-ray intensity ratio $R = K_\alpha/K_\beta$ for Sn was determined to be R=4.87(5), which is consistent with the value for a neutral atom ($R = 4.92$) including the $K_{\beta 2}$ transition,

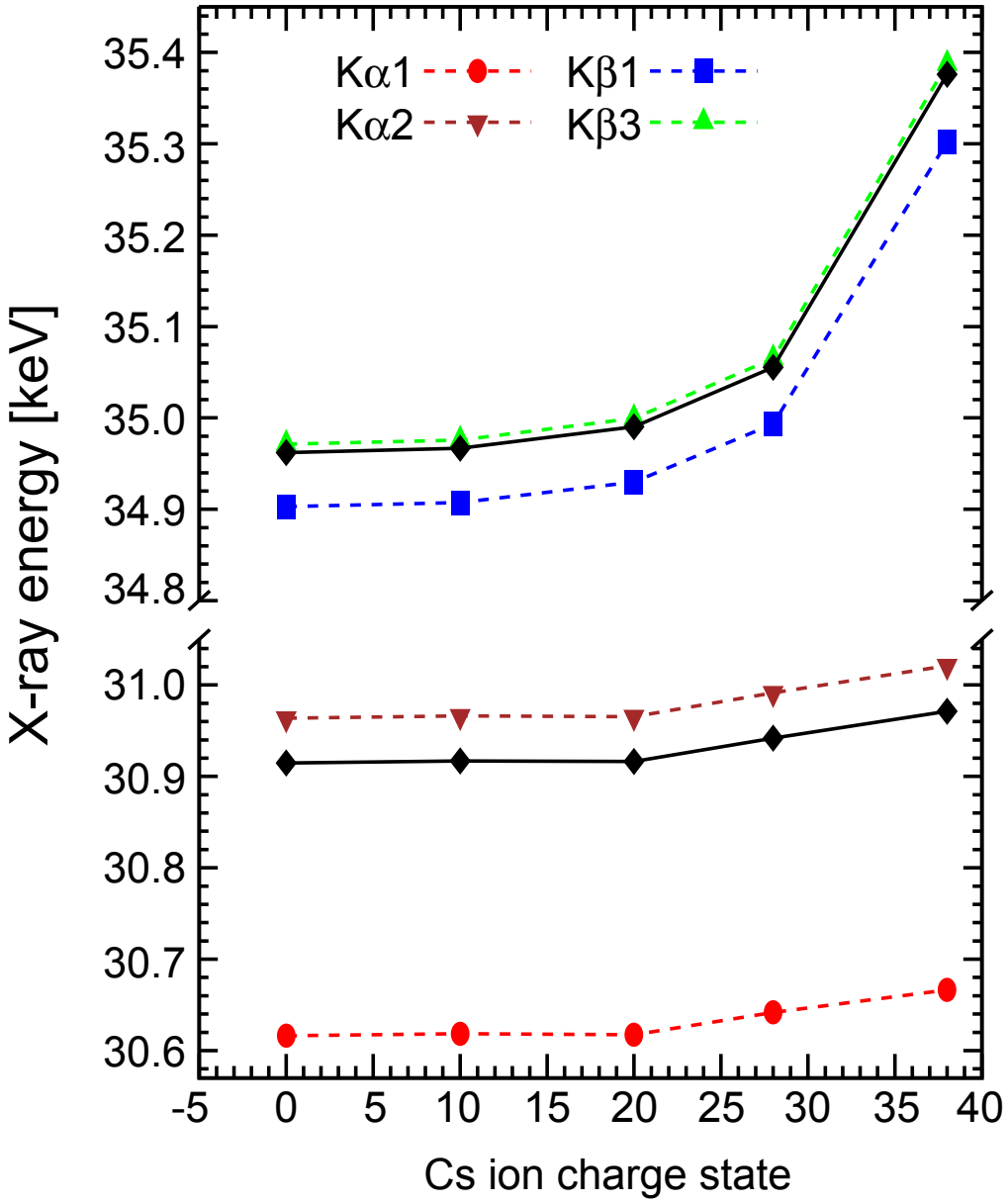

Figure 5.24: Theoretical values for the shifted Cs a) K_β and b) K_α X-ray energies as a function of the charge state. The multiconfigurational, relativistic Dirac-Fock code, FAC [110] was used to perform the atomic-structure calculations that showed the increase in binding-energy for K_α and K_β with increasing charge state. The increasing energy differences for $K_{\alpha 1}$, $K_{\alpha 2}$, $K_{\beta 1}$ and $K_{\beta 3}$ relative to the neutral Cs atom energies are indicated with the colored lines. Additionally, the plot includes two black lines that present the intensity-weighted average energy curves for K_α and K_β, which include the relative X-ray intensities. Those curves illustrate the energies that would be derived experimentally due to limited energy resolution.

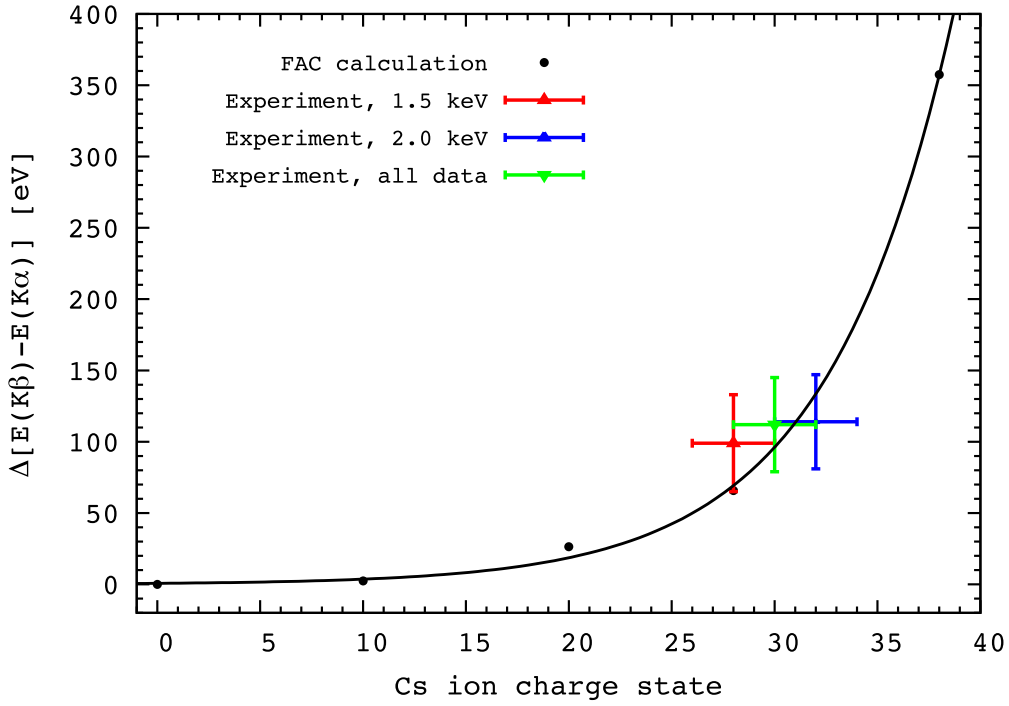

Figure 5.25: Relative X-ray energy shifts $\Delta[E(K_\beta) - E(K_\alpha)]$ for Cs ions as a function of the charge state. The data points represent theoretical calculations derived via the FAC code. The red triangle marks the experimental value from an average charge state from the data sets taken at two different electron-beam energies, while the blue and green triangles represent the experimental results from the individual measurements. The uncertainty in x-direction for the experimental values results from the fact that those values correspond to charge state distributions, while the calculated values refer to single charge states.

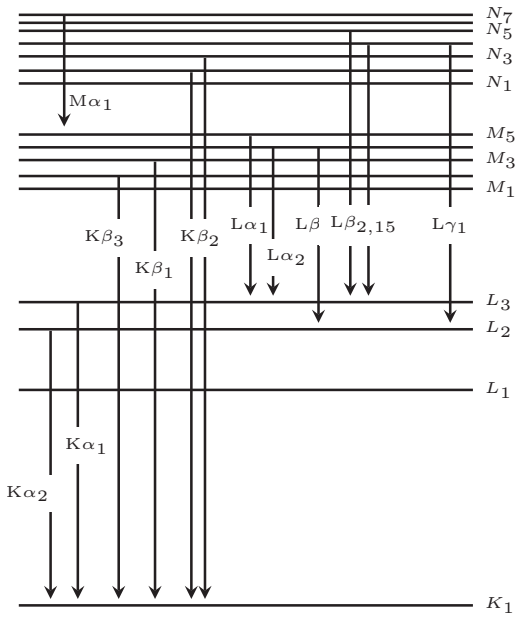

Figure 5.26: Schematic illustration of the characteristic K, L and M X-ray transitions. Only the strongest emission lines are indicated. Figure drawn according to Ref. [191].

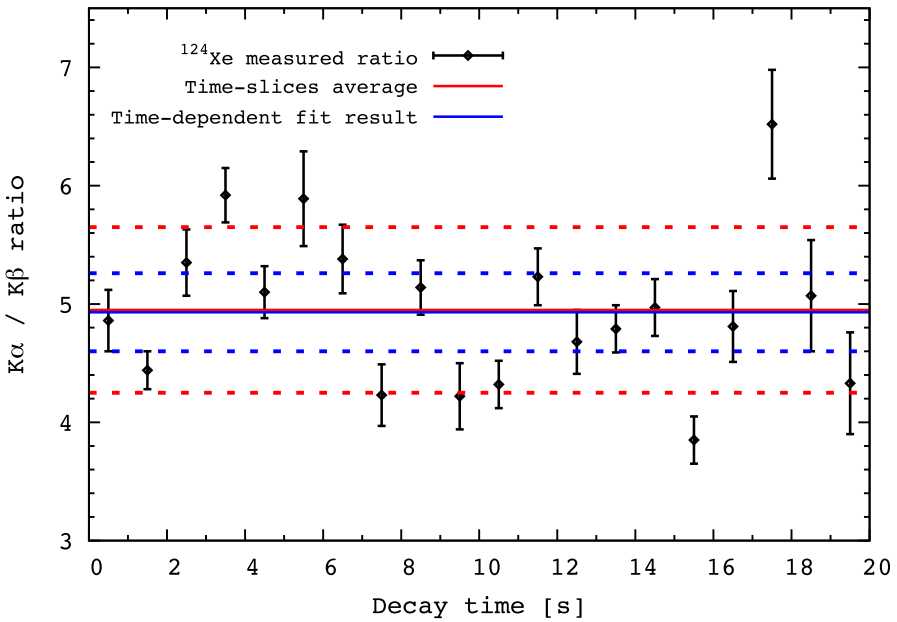

Figure 5.27: K_α/K_β ratios in dependence of the trapping time for ^{124}Xe X-rays. The errors of the individual data points represent the statistical uncertainty from the fit. The solid red line represents the average of all time slices and the corresponding standard deviation including an additional systematic uncertainty from the detection efficiency is indicated by the red dashed lines. For comparison the time-dependent fit result together with its upper and lower limit including the systematic uncertainty (dashed lines) is displayed in blue.

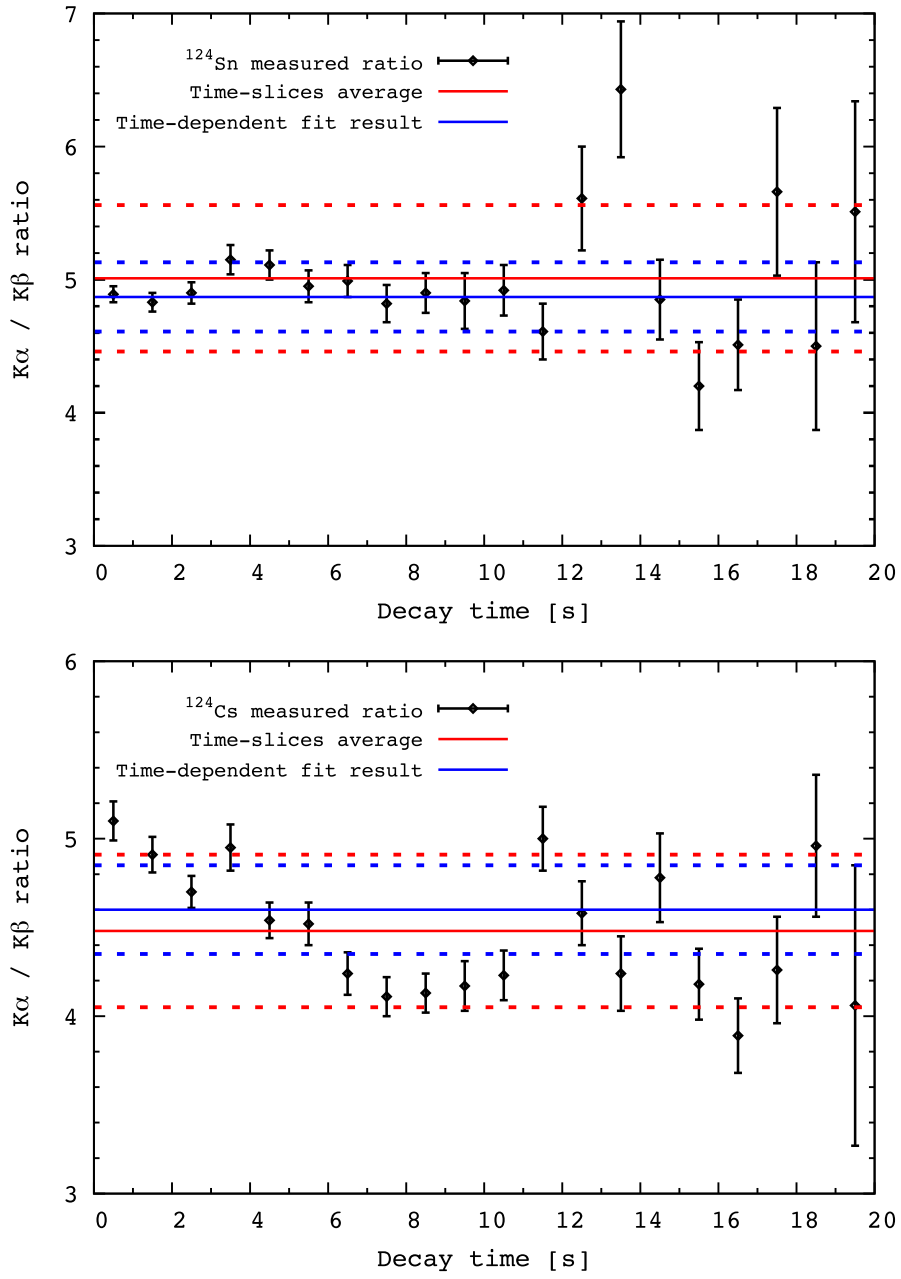

Figure 5.28: K_α/K_β ratios in dependence of the trapping time for ^{124}Sn (top) and ^{124}Cs (bottom) X-rays. The errors of the individual data points represent the statistical uncertainty from the fit. The solid red line represents the average of all time slices and the corresponding standard deviation including an additional systematic uncertainty from the detection efficiency is indicated by the red dashed lines. For comparison the time-dependent fit result together with its upper and lower limit including the systematic uncertainty (dashed lines) is displayed in blue.

	K_α/K_β ratio		
Time [s]	Sn	Cs	Xe
0.5	4.89(6)	5.10(11)	4.86(26)
1.5	4.83(7)	4.91(10)	4.44(16)
2.5	4.90(8)	4.70(9)	5.35(28)
3.5	5.15(11)	4.95(13)	5.92(23)
4.5	5.11(11)	4.54(10)	5.10(22)
5.5	4.95(12)	4.52(12)	5.89(40)
6.5	4.99(12)	4.24(12)	5.38(29)
7.5	4.82(14)	4.11(11)	4.23(26)
8.5	4.90(15)	4.13(11)	5.14(23)
9.5	4.84(21)	4.17(14)	4.22(28)
10.5	4.92(19)	4.23(14)	4.32(20)
11.5	4.61(21)	5.00(18)	5.23(24)
12.5	5.61(39)	4.58(18)	4.68(27)
13.5	6.43(51)	4.24(21)	4.79(20)
14.5	4.85(30)	4.78(25)	4.97(24)
15.5	4.20(33)	4.18(20)	3.85(20)
16.5	4.51(34)	3.89(21)	4.81(30)
17.5	5.66(63)	4.26(30)	6.52(46)
18.5	4.50(63)	4.96(40)	5.07(47)
19.5	5.51(83)	4.06(79)	4.33(43)
Time-slices average	5.01(49)	4.48(37)	4.95(66)
Time-dependent fit	4.87(10)	4.60(10)	4.93(22)

Table 5.11: Overview of the extracted K_α/K_β ratios for all three X-ray species as a function of the trapping time. The values in brackets represent the analytical uncertainties. For the average values of the time slices, the brackets contain the standard deviation. On top of the displayed uncertainties all values have an additional 5% uncertainty resulting from the uncertainty of the detection efficiency.

whereas the value for a neutral atom excluding the $K_{\beta 2}$ transition ($R = 5.81$) transition differs from the experimental result by about 19%. The measured X-ray intensity ratios for the slightly different charge-state distribution created with the two different electron-beam energies (1.5 keV, 2.0 keV) did not differ significantly.

The experimentally observed decrease of the K_α/K_β ratio ($R = 4.93(22)$ for Xe X-rays) relative to the expected value is consistent with the theoretical calculations carried out with the FAC code as presented for Cs ions in Fig. 5.29. For neutral atoms the Auger effect competes with X-ray emission and limits the emission probability of K_β X-rays. In the case of highly-charged ions, however, the Auger process is highly suppressed, which results in a higher K_β intensity. The calculations predict an overall decreasing K_α/K_β ratio with increasing charge state, whereas the neutral ratio yields a value of $R = 5.62$ without

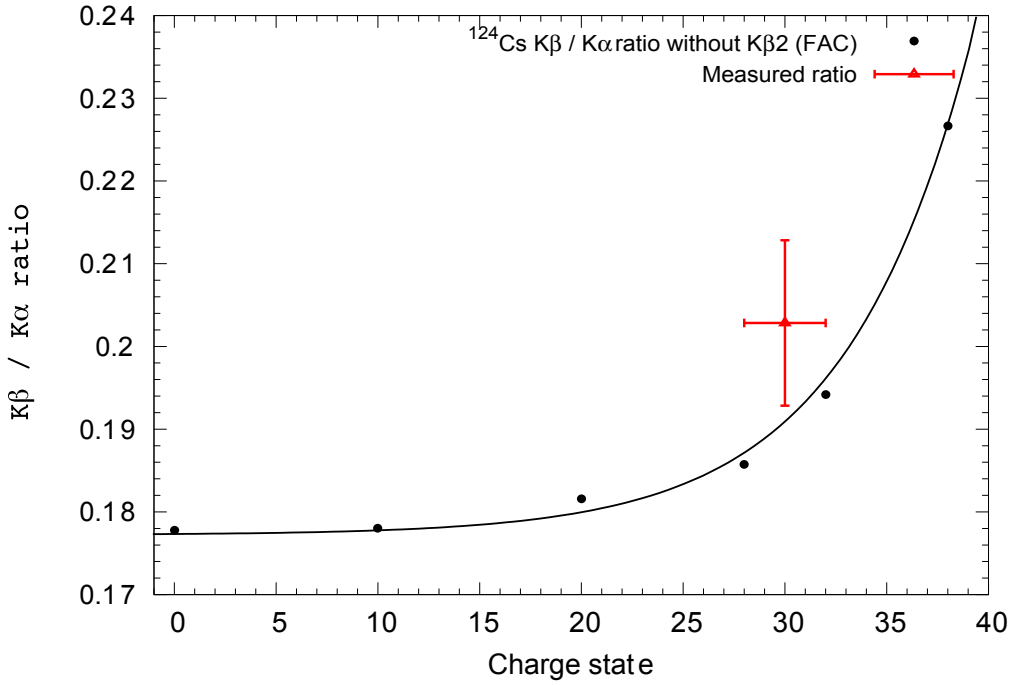

Figure 5.29: X-ray intensity ratios K_α/K_β for Cs ions as a function of the charge state. The red triangle marks the experimentally determined value for an average charge state of $q \approx 30^+$. The uncertainty in direction of the abscissa results from the fact that the experimental value corresponds to an average value of at least two charge states, while the calculation refers to a single charge state. The black dots are FAC calculated values and the black line is an exponential function to guide the eye.

including a $K_{\beta 2}$ transition. For the ratio at $q = 32^+$, one gets $R = 5.15$.

Though consistent within the uncertainty, the experimental value is lower than the calculated value, which is expected as the calculations do neither include any reduced Auger rates nor shakeoff rates in ions resulting from the empty outer shells [129]. Thus, an additional decrease of the calculated ratio would yield in a better agreement of theory and experiment. Even though the observed decrease of the K_α/K_β ratio is significant, the change did not affect the half-lives of the three ion species as the measured values agree with the literature values. Further, as expected, no effect on the ^{124}Cs EC branching ratio was observed, which could be concluded from the normalization cross check outlined in Sec. 5.5.5.

5.5.8 Beam composition

As outlined above, the radioactive ion beam consisted of three ion species (^{124}Cs ground state, ^{124m}Cs, ^{124m}In). Evidence for the ^{124}In ground state cannot be found in the spectra

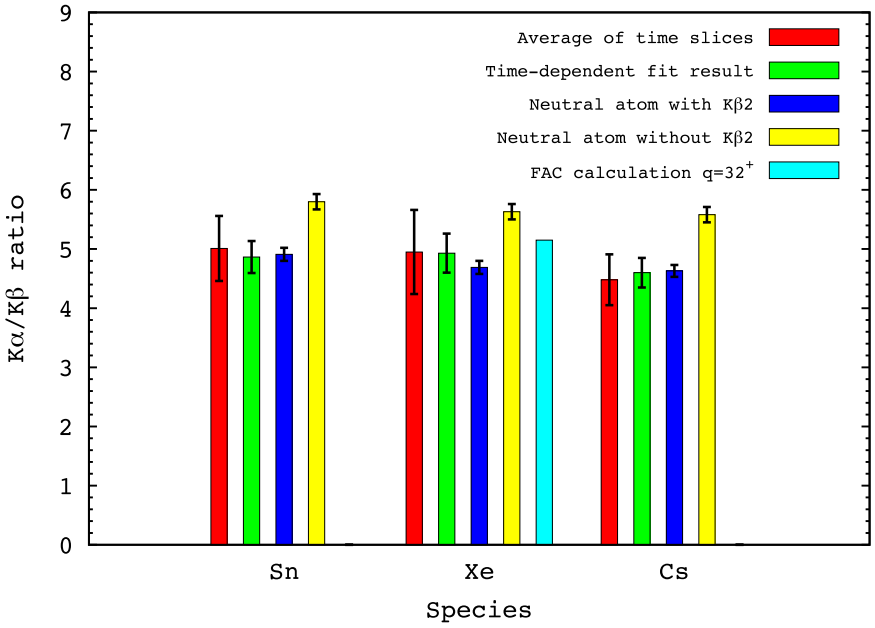

Figure 5.30: Comparison of the K_α/K_β ratios for Sn, Cs and Xe obtained experimentally from highly-charged ions (green and red) to the ratios of the neutral atoms including (dark blue) and excluding (yellow) the $K_{\beta 2}$ transition. For Cs, the ratio calculated with the FAC code (light blue) is presented as well. The error bars for the experimental values result from the sum in quadrature of the statistical errors of the fits and the 5% systematic uncertainty from the detection efficiency. The errors for the neutral atoms result from the uncertainties of the intensities quoted in the databases [169].

because of its direct decay into the ^{124}Sn ground state. The actual beam composition can be evaluated from the relative transition intensities, detection efficiencies and half-lives, which additionally allows calculating the number of ions trapped in the EBIT over the course of the experiment.

By extrapolating the exponential functions of the half-life fits shown in Fig. 5.13 to $t = 0$ s, one can determine the activity A($t = 0$ s) of each species at the beginning of the decay time. This allows calculating the number of ions N_{ions} at $t = 0$ s in the trap by the following formula:

$$N_{ions}(t = 0) = A(t = 0) \cdot T_{1/2}/(\ln 2 \cdot I \cdot \Omega \cdot \epsilon), \tag{5.11}$$

where I stands for the relative intensity, i.e., the branching ratio, of the transition used to extract the half-life, ϵ for the detection efficiency and Ω for the solid angle covered with the three Si(Li) detectors used for the analysis (Ω=0.9%). The extracted activities (detection efficiency corrected) at $t = 0$ s for the three individual species are:

- A(^{124}Cs g.s.): 3.90(7)$\times 10^3$ counts/s,
- A(^{124m}Cs): 1.76(2)$\times 10^4$ counts/s and
- A(^{124m}In): 6.14(10)$\times 10^4$ counts/s.

The values reflect the activities resulting from the complete set of statistics collected over $\sim$ 48 h. To calculate the resulting number of ions, one has to multiply the above listed activities with the K_α/K_β ratio (see Tab. 5.11 in Sec. 5.5.7.2) in order to separate the individual contributions from the K_α and K_β X-rays to the total X-ray activity. Then, one has to correct the activity of the individual contributions by their relative transition intensities. For the latter the literature values from Ref. [169] including the intensity for the $K_{\beta 2}$ transitions were applied in order to stay consistent with the measured K_α/K_β ratios. This is justified as the experimental intensities for the $K_{\beta 13}$ X-rays have to deviate from the literature values as otherwise the measured K_α/K_β ratios would not agree with the value for a neutral atom considering the missing $K_{\beta 2}$ transition. The N_{ions} was extracted from the number of K_α as well as from the number of K_β counts and compared to each

	Xe		
	K_α	K_β	Beam composition
Activity/ϵ [Counts/1s]	$(3.2 \pm 0.1)\cdot10^3$	$(6.6 \pm 0.3)\cdot10^2$	
Intensity (lit.) [%]	6.92(46)	1.464(96)	
Activity/ϵ/Intensity	$(4.7 \pm 0.3)\cdot10^4$	$(4.5 \pm 0.4)\cdot10^4$	$\sim 61\%$ ^{124}Cs g.s.
N_{ions}	$(2.1 \pm 0.2)\cdot10^6$	$(2.0 \pm 0.2)\cdot10^6$	
N_{ions} (Ω corrected)	$(2.3 \pm 0.2)\cdot10^8$	$(2.2 \pm 0.2)\cdot10^8$	
	Cs		
	K_α	K_β	Beam composition
Activity/ϵ [Counts/1s]	$(14.5 \pm 0.2)\cdot10^3$	3142(74)	
Intensity (lit.) [%]	139(14)	30.2(1.5)	
Activity/ϵ/Intensity	$(10.4 \pm 1.1)\cdot10^3$	$(10.4 \pm 0.6)\cdot10^3$	$\sim 3\%$ ^{124m}Cs
N_{ions}	$(9.5 \pm 1.0)\cdot10^4$	$(9.5 \pm 0.6)\cdot10^4$	
N_{ions} (Ω corrected)	$(1.1 \pm 0.1)\cdot10^7$	$(1.1 \pm 0.1)\cdot10^7$	
	Sn		
	K_α	K_β	Beam composition
Activity/ϵ [Counts/1s]	$(5.1 \pm 0.1)\cdot10^4$	$(10.5 \pm 0.2)\cdot10^3$	
Intensity (lit.) [%]	22.0(2)	4.47(41)	
Activity/ϵ/Intensity	$(23.2 \pm 0.6)\cdot10^4$	$(23.4 \pm 2.2)\cdot10^4$	$\sim 36\%$ ^{124m}In
N_{ions}	$(1.2 \pm 0.1)\cdot10^6$	$(1.2 \pm 0.1)\cdot10^6$	
N_{ions} (Ω corrected)	$(1.4 \pm 0.1)\cdot10^8$	$(1.4 \pm 0.2)\cdot10^8$	

Table 5.12: Listed are the quantities necessary to calculate the A=124 beam composition. The K_α and K_β activities for Xe, Cs and Sn as well as the literature values for the intensities and the corresponding number of ions calculated once from the K_α activity and once from the K_β activity are presented. The right column lists the contribution of each species to the total beam composition.

other. Tab. 5.12 gives an overview of the activities and the corresponding number of ions for all three species and the resulting contributions to the total beam composition. Using the numbers from Tab. 5.12 one gets a total number of $\sim 3.8\cdot10^8$ ions in the trap over the course of the experiment which leads to $\sim 6.8\cdot10^4$ ions in the trap per cycle injected from a single ion bunch supplied by the RFQ (1 s loading time). Regarding the contributions of the three ion species to the beam composition, not including a possible contribution from the ^{124}In ground state, one derives $\sim 61\%$ for the ^{124}Cs ground state, $\sim 3\%$ for the ^{124}Cs isomer and $\sim 36\%$ for the contribution of the ^{124}In isomer to the beam composition.

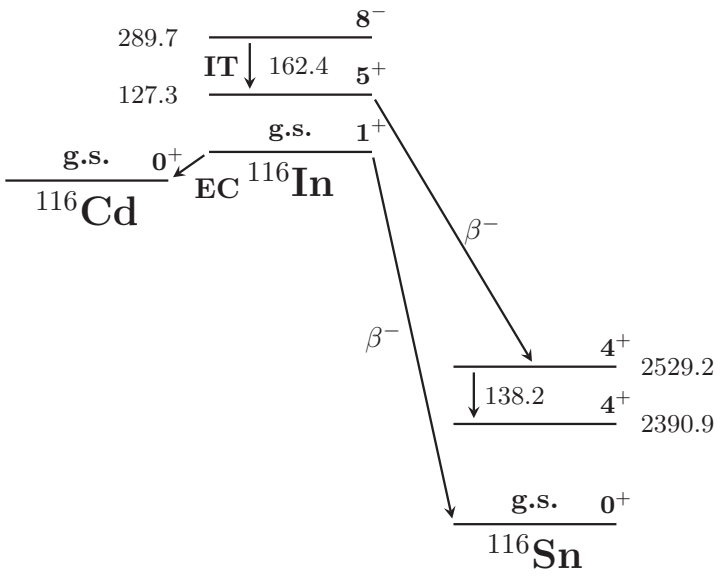

Figure 5.31: ^{116}In decay scheme showing the transitions and energy levels most relevant for the here presented analysis. Excitation and transition energies are given in units of keV.

5.6 A=116 in-trap decay

After the discussion of the data analysis recorded during the ^{124}Cs experiment, the ^{116}In data analysis will be described in this part of the chapter. A discussion of the X-ray spectra including half-lives and atomic structure effects will be followed by a section about multiple-ion bunch injection, where the trend of the injection scheme was analyzed by using the In X-rays.

5.6.1 Fitting routine

For the analysis of the A=116 X-ray spectrum, the data recorded during the 15 s of trapping time was sliced into 15 time slices with a bin width of 1 s after which an analytical fitting procedure analogously to the ^{124}Cs analysis described in Sec. 5.4 was applied to extract the X-ray peak integrals. As described in Sec. 4.2, the X-ray spectrum is dominated by In X-rays, which are produced by the internal-conversion decay (see Fig. 5.31) of the ^{116}In (8^-) isomer into the long-lived 54.29(17) min [169] (5^+) isomer.

The fits for all time slices are presented in Fig. 5.32, Fig. 5.33 and Fig. 5.34 illustrating the time dependence of the X-ray spectrum. Here the initially strong signature of the In

Time [s]	Counts/ϵ (In K_α) $\times 10^3$	Counts/ϵ (In K_β) $\times 10^3$	Counts/ϵ (sum) $\times 10^3$
0.5	45.55(21)	10.35(10)	55.87(31)
1.5	32.92(18)	7.41(9)	40.33(27)
2.5	24.14(15)	5.28(7)	29.42(22)
3.5	17.49(13)	3.91(6)	21.41(19)
4.5	12.84(11)	3.07(6)	15.89(17)
5.5	9.53(10)	2.04(5)	11.57(15)
6.5	6.70(8)	1.59(4)	8.28(12)
7.5	4.99(7)	1.14(3)	6.13(10)
8.5	3.56(6)	0.84(3)	4.39(9)
9.5	2.58(5)	0.54(2)	3.12(7)
10.5	1.97(4)	0.45(2)	2.42(6)
11.5	1.34(4)	0.31(2)	1.65(6)
12.5	1.11(3)	0.36(2)	1.47(5)
13.5	0.89(3)	0.18(1)	1.07(4)
14.5	0.69(3)	0.09(1)	0.78(4)
Sum	$1.66(3) \times 10^5$	$3.75(17) \times 10^4$	$2.04(10) \times 10^5$

Table 5.13: Overview of the extracted count rates (detection efficiency corrected) for the ^{116}In K_α and K_β X-rays. The listed values in brackets represent the statistical uncertainties based on the count rates.

K_α X-ray becomes less intense towards longer trapping times. The corresponding detection efficiency corrected count rates per time bin for the In X-rays at E_{K_α}=24.2 keV and E_{K_β} = 27.3 keV are listed in Tab. 5.13. At later times, a transition located at the high-energy shoulder of the In K_α becomes noticeable. This peak occurs at the energy of the Sn K_α X-ray.

A fit of the time-integrated X-ray spectrum for the complete 30 s including trapping and injection time for the summed data of all runs taken during the experiment is presented from 20 to 32 keV in Fig. 5.35. It shows the individual fit functions to describe the In X-rays (red curve) as well as the fit of the Sn K_α X-ray (blue) on top of the ambient background. The solid black line presents the summed fit function including all ion species as well as the time-scaled ambient background. Fig. 5.36 displays a fit of the complete data set recorded during the 15 s of trapping time only. A one-dimensional projection of the time-dependent fit for the data recorded during the trapping time is shown in Fig. 5.37. However, due to limited experimental time, the total collected statistics were not sufficient to observe the extremely weak ($\sim$ 0.02% [169]) EC branch of the ^{116}In ground state to ^{116}Cd with

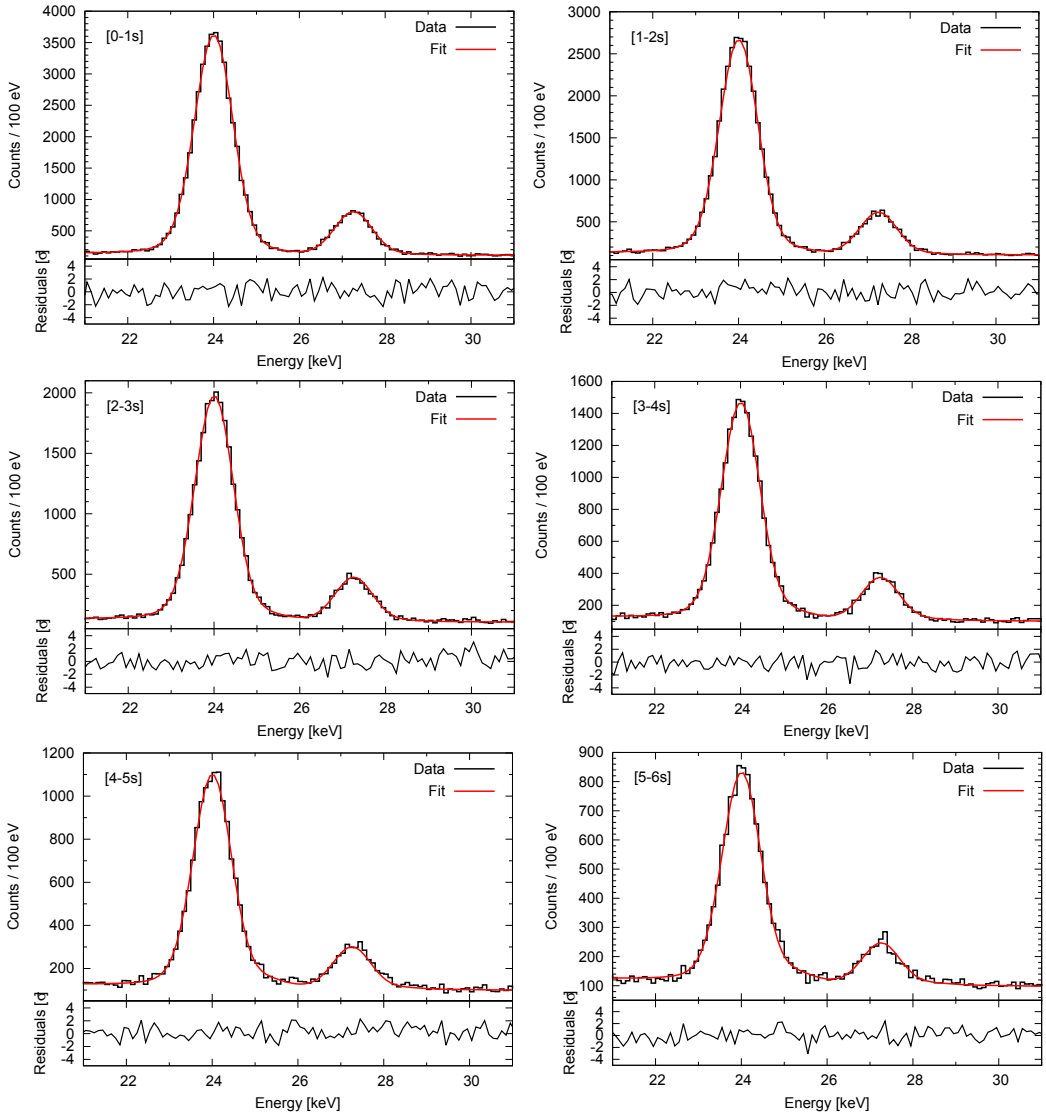

Figure 5.32: Fits of the X-ray energy region for the time slices within the first 6 s of the trapping cycle. Each panel shows one second of data and the corresponding fit function, which consists of the skewed Gaussian distribution for each X-ray species (In, Sn) including a low-energy tail as well as the scaled ambient background.

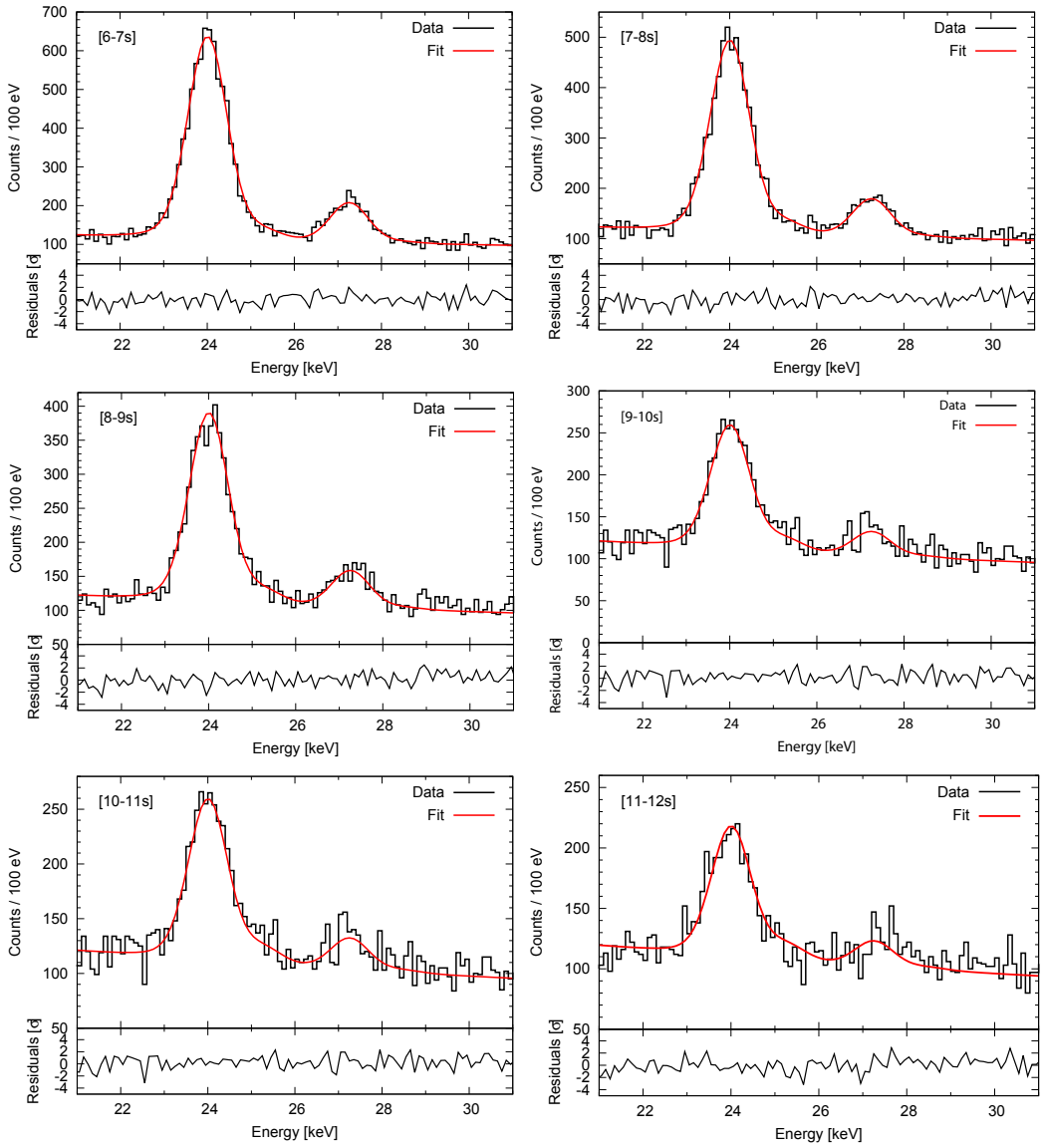

Figure 5.33: Fits of the X-ray energy region for the time slices within the 6-12 s time interval of the trapping cycle. Each panel shows one second of data and the corresponding fit function, which consists of the skewed Gaussian distribution for each X-ray species (In, Sn) including a low-energy tail as well as the scaled ambient background.

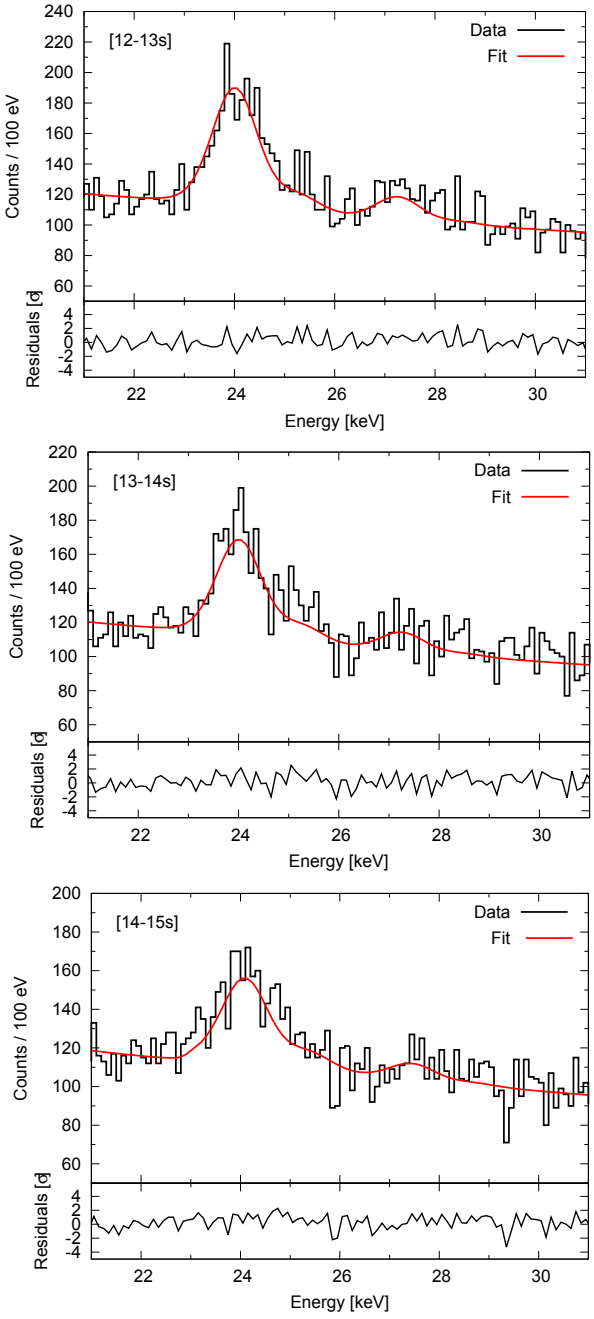

Figure 5.34: Fits of the X-ray energy region for the time slices within the 12-15 s time interval of the trapping cycle. Each panel shows one second of data and the corresponding fit function, which consists of the skewed Gaussian distribution for each X-ray species (In, Sn) including a low-energy tail as well as the scaled ambient background.

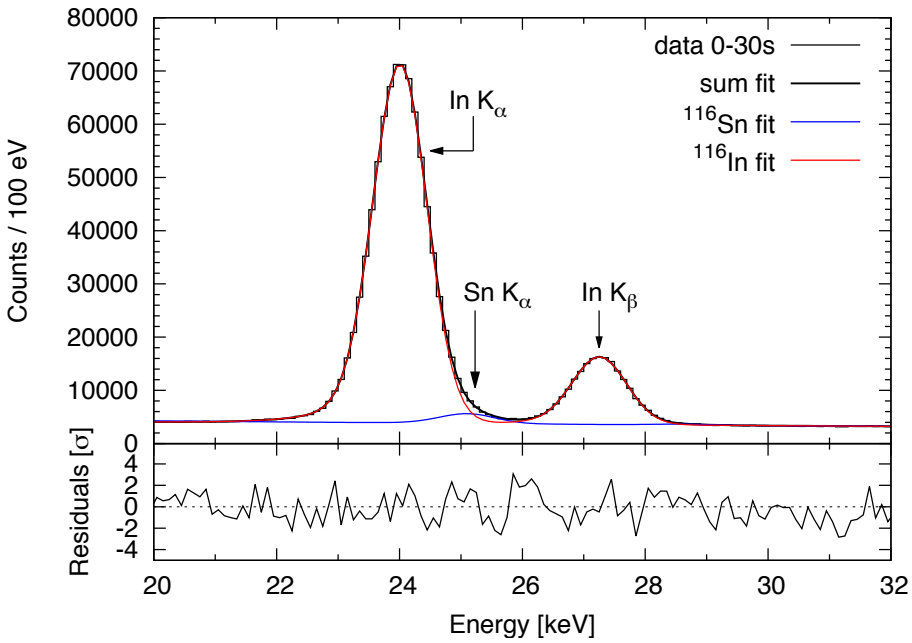

Figure 5.35: Fit of the time-integrated X-ray spectrum over the first 30 s of the EBIT cycle, including injection and trapping time. The red curve describes the fit for the In X-rays from the decay of the 8^- $^{116}In^{m2}$ isomer, whereas the blue curve represents the fit for the Sn X-rays. The curves represent the number of counts of the individual species on top of the ambient background. The grey line, marks the summed fit including both species as well as the background.

characteristic X-ray energies of $E_{K_\alpha} \sim 23.1$ keV ($I(K_\alpha) = 0.0138\%$) and $E_{K_\beta} \sim 26.0$ keV ($I(K_\beta) = 0.00267\%$) in any of the spectra, independent of the fitting procedure.

The 162.4 keV E3 γ-ray from the $8^- \longrightarrow 5^+$ transition in ^{116}In was observed in addition to the In X-rays, however due to the low detection efficiency of the array at this energy, the observed statistics were relatively low yielding a value of $(1.9 \pm 0.1) \cdot 10^5$ counts (efficiency corrected) for the summed data within the 15 s trapping-time interval. The corresponding Compton edge at $\sim$ 63 keV (compare Fig. 4.14 in Sec. 4.2.2) was observed as well.

5.6.2 Half-life of the ^{116}In 8^- isomer

In the same way as for the A=124 data, the half-life of the ^{116}In (8^-) isomer was extracted from the indium X-ray spectrum, by fitting the X-ray peak integrals as a function of the trapping time, whereby the decay can be described by a single exponential function. Fig. 5.38 depicts three decay curves for the ^{116}In (8^-) isomer (K_α, K_β and K_α + K_β) with a fitted half-life of $T_{1/2}$=2.19(1) s for the summed data of the K_α and K_β peak integrals, which is in agreement with the literature value of 2.18(4) s [169]. An overview of the fitted

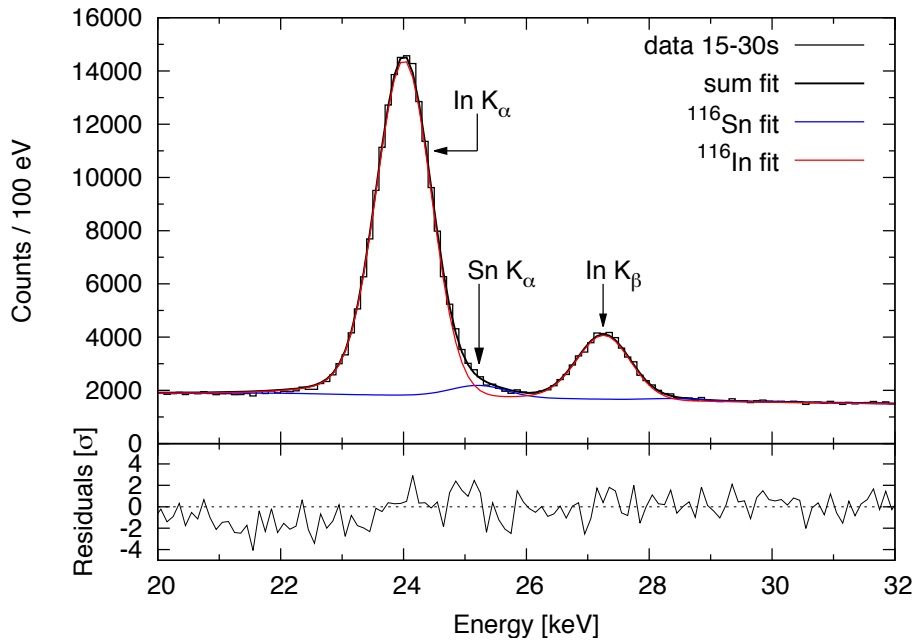

Figure 5.36: Fit of the time-integrated X-ray spectrum over the 15 s trapping time of the EBIT cycle. The red curve describes the In X-rays from the decay of the 8^- $^{116}In^{m2}$ isomer, whereas the blue curve represents the fit for the Sn X-rays. The curves represent the number of counts of the individual species on top of the ambient background. The grey line, marks the summed fit including both species as well as the background.

integrals for the In K_α and In K_β transitions used to generate the half-life curves can be found in Tab. 5.13.

5.6.2.1 Activities and internal conversion coefficients

Extrapolating the exponential fits shown in Fig. 5.38 to $t_{decay} = 0$ s gives the values for the activities for the K_α and K_β X-rays or, respectively, their sum at the moment in time when the trap is closed. One gets the following results for the activities:

- $A_0(K_\alpha)$: $5.30(4) \cdot 10^4$ counts/s
- $A_0(K_\beta)$: $1.19(2) \cdot 10^4$ counts/s
- $A_0(K_\alpha+K_\beta)$: $6.50(4) \cdot 10^4$ counts/s

Those values include the counts for all cycles over the complete data taking time. By correcting the activities for the X-ray intensities it is possible to extract the number of ions stored in the trap at $t_{decay} = 0$ s. The TOI [104] lists intensity values of $I(K_\alpha) = 29.00(12)\%$

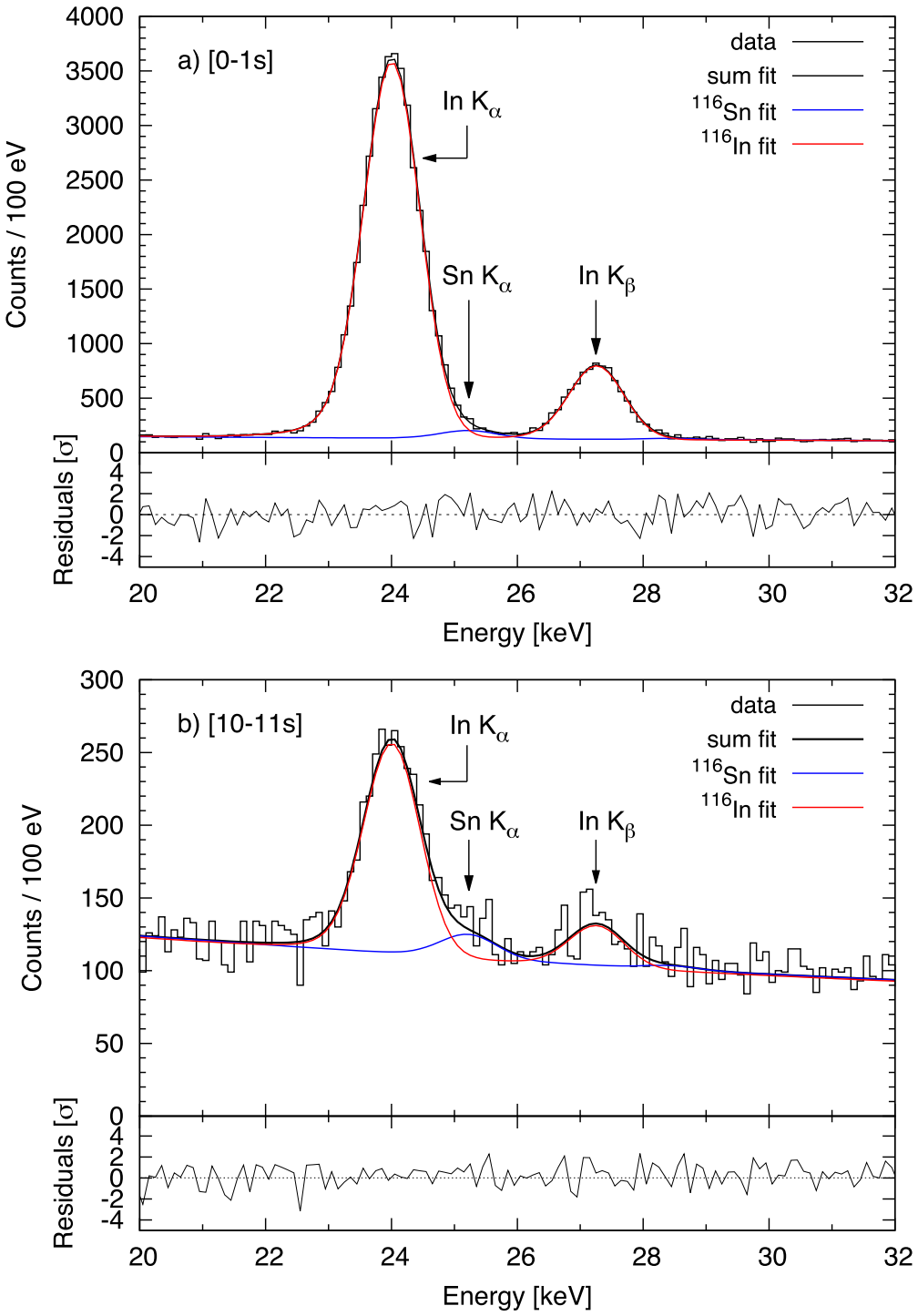

Figure 5.37: One-dimensional projection of the time-dependent fit of the time-integrated X-ray spectrum recorded during the 15 s trapping. The panel above shows the first second of data, while the lower panel displays the fit and data from 10-11 s to demonstrate the appearance of the Sn K_α peak. The spectrum is dominated by In X-rays resulting from the internal conversion decay of the 8^- isomer into the 5^+ isomer (shown in red), which has a characteristic half-life of 2.18(4) s [169]. X-rays from internal conversion in ^{116}Sn populated through the β^- -decay of the longer lived (54 min) $^{116}\mathrm{In}^{m1}$ were also observed, however with a much lower intensity.

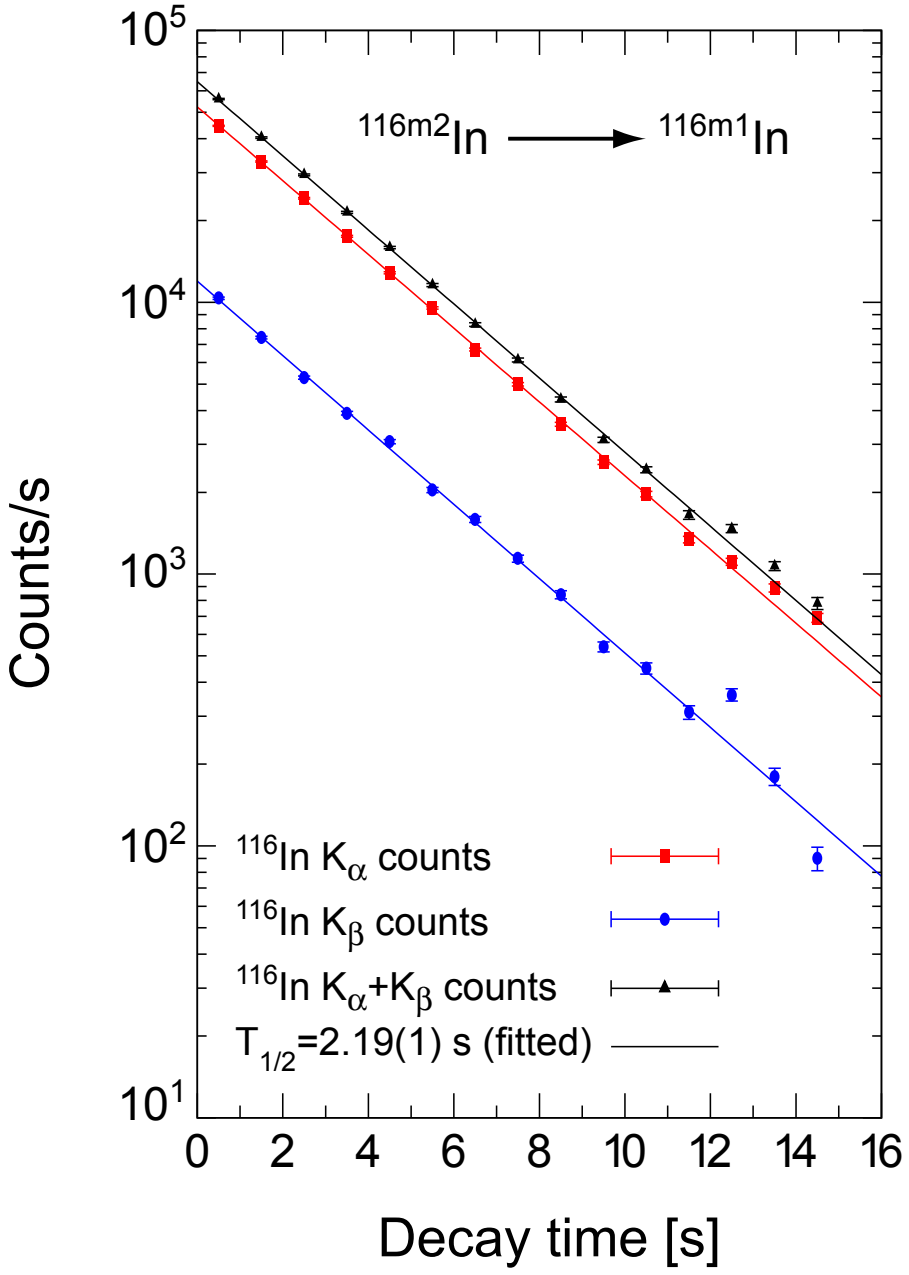

Figure 5.38: Number of ^{116}In X-ray counts per 1 s time bin as a function of the trapping time. The exponential functions, which are presented on a half-logarithmic scale, describe the radioactive decay of the ^{116m2}In 8^- isomer into the 5^+ isomer ($T_{1/2}$=54.29 min). The black curve describes the fitted decay curve for the sum of K_α and K_β counts with $T_{1/2}$=2.19(1) s, whereas the red and blue curves present the fits for the individual contributions from the K_α or K_β X-ray counts, respectively. The errors of the single data points denote the statistical uncertainties, whereby the ones for the sum of K_α and K_β result from the quadratic summation of the individual errors from the K_α and K_β peak integrals.

and $I(K_\beta) = 5.7(3)\%$ for the In X-rays. However, since the X-ray intensities are neither listed in the NNDC database [169] nor in the *LiveChart of Nuclides* of the *International Atomic Energy Agency (IAEA)* [185], the intensities were calculated in order to verify the values from the TOI.

On that account one calculates the total conversion coefficient α_C^{total}(In) for the 162.390(3) keV γ-transition [185] from the decay of the 8^- state in ^{116}In to the 5^+ state with an E3 multipolarity using the BrIcc v2.3S (9-Dec-2011) internal-conversion coefficient calculator [169], which yields a value of α_C^{total}(In)=1.716(24). The contribution from the K-shell comes to α_C^K(In)=1.098(16).

In order to derive the IC contribution to the total number of decays, the γ-intensity of the 162.4 keV transition is required, for which IAEA quotes a value of $I_\gamma = 36.819\%$. Hence, the remaining contribution of the decays (63.181%) have to originate from internal conversion. One can cross-check the calculated conversion coefficient α_K^C with the experimental data by determining the ratio of the In X-ray counts to the observed counts in the 162.4 keV γ-transition:

$$\alpha_K^C = \frac{N_{cts}(K_\alpha + K_\beta)}{N_{cts}(\gamma)} = \frac{1.63(2)\cdot 10^5 + 3.39(15)\cdot 10^4}{1.89(14)\cdot 10^5} = 1.04(4). \tag{5.12}$$

The experimental value of 1.04(4) for α_K^C is in agreement with the calculated value of $\alpha_K^C = 1.098(16)$, which implies that possible charge-breeding effects on α_K^C are smaller or of the order of our current sensitivity. To calculate the K-shell X-ray intensity contribution, the $\alpha_C^K/\alpha_C^{total}$ ratio (calculated values) is multiplied by the total percentage of internal-conversion decays (63.181%):

$$I(K) = \frac{1.098(16)}{1.716(24)} \cdot 63.181 = 40.4(8)\%. \tag{5.13}$$

The uncertainty for $I(K)$ represents the sum in quadrature of the uncertainties of the original fractional uncertainties. In the following the same procedure for the error calculation is applied.

The individual intensities for K_α and K_β are derived by correcting $I(K)$ from Eq. 5.13 by the K_α/K_β ratio ($R = 4.73(46)$, compare Sec. 5.6.5.2) after which one gets the following transition intensities:

- $I(K_\alpha)$: $(33.35 \pm 1.38)\%$
- $I(K_\beta)$: $(7.05 \pm 0.58)\%$

With those X-ray intensity values, the derived number of ions from the 8^- isomer in the trap at $t_{decay} = 0$ s for the sum of all cycles is:

$$N_{ions}(t=0) = \frac{A(K_\alpha) \cdot T_{1/2}}{\ln 2 \cdot I(K_\alpha) \cdot \Omega \cdot \epsilon} = \frac{(5.30(4) \cdot 10^4) \cdot 2.18}{\ln 2 \cdot 0.3348 \cdot 0.009} = (5.55 \pm 0.25) \cdot 10^7 \qquad (5.14)$$

or, respectively:

$$N_{ions}(t=0) = \frac{A(K_\beta) \cdot T_{1/2}}{\ln 2 \cdot I(K_\beta) \cdot \Omega \cdot \epsilon} = \frac{11901 \cdot 2.18}{\ln 2 \cdot 0.0696 \cdot 0.009} = (5.89 \pm 0.51) \cdot 10^7, \qquad (5.15)$$

when using the K_β transition to derive N_{ions}. The quantity Ω denotes the solid angle covered with three Si(Li) detectors positioned on the large acceptance ports and ϵ stands for the detection efficiency. These numbers correspond to the total number of ions of that particular species that were trapped over the course of the whole experiment.

To derive the number of ions that were stored in the trap at the beginning of a single trapping cycle (decay time 15-30 s), one has to account for the number of cycles (N_{cycles}=1606). Hence, one gets for the average number of ions from the second isomer at the beginning of a single trapping cycle:

$$N_{ions}(t=0) = \frac{5.55(25) \cdot 10^7}{1606(1)} = (3.5 \pm 0.2) \cdot 10^4, \qquad (5.16)$$

using the K_α X-ray, and

$$N_{ions}(t=0) = \frac{5.89(51) \cdot 10^7}{1606(1)} = (3.7 \pm 0.2) \cdot 10^4, \qquad (5.17)$$

when using the K_β X-ray transition. The two values derived from the number of K_α and K_β counts are consistent.

5.6.3 Decay of the long-lived ^{116m1}In 5^+ isomer

Next to the 8^- isomer, evidence for the decay of the long-lived 5^+ isomer in ^{116}In can be found in the Si(Li) spectra as outlined in Sec. 4.2.2, which is indicated by the Compton edge at at 257.7 keV from the 416.9 keV γ-transition. More transitions in ^{116}Sn can be identified

Energy [keV]	Fitted energy [keV]	Intensity [%]	Counts $\times 10^3$	$\sqrt{N}$
138.29(2)	138.54(10)	3.70(9)	10.6	103
416.90(2)	417.19(2)	27.2(4)	45.5	213
463.25(3)	463.22(10)	0.725(11)	4.5	67
818.68(2)	818.74(3)	12.13(14)	14.8	122
1097.28(2)	1098.12(1)	58.5(8)	665.3	816
1293.56(2)	1294.12(1)	84.8(12)	90.8	301
1507.59(2)	1507.33(3)	9.92(13)	10.5	102
1752.50(2)	1751.19(9)	2.36(3)	2.2	47
2112.29(2)	2109.28(3)	15.09(22)	13.2	115

Table 5.14: List of the observed γ-transitions in the HPGe spectrum, which result from excited states in ^{116}Sn populated by the decay of the ^{116m}In 5^+ 54 min isomer. The intensities and non-fitted energy values are taken from Ref. [169].

in the HPGe spectrum (compare Fig. 4.17), i.e., the 138.29(2) keV M1 γ-transition with $I_\gamma = 3.70(9)\%$ from the decay of the 4^+ state at 2529 keV into the 4^+ at an energy of 2391 keV in ^{116}Sn (see Fig. 5.31), for which only traces were visible in the Si(Li) spectra due to the low detection efficiency. The 138 keV transition is also converted and causes the long-lived contribution in the Sn X-rays. In particular one gets the following conversion coefficient with the BrIcc v2.3S (9-Dec-2011) internal-conversion coefficient calculator [169]:

- ^{116}Sn, 138.29 keV, M1: α_C^{total}=0.227(4), α_C^K=0.196(3)

Tab. 5.14 lists all transitions assigned to the decay of the 5^+ isomer decay from the HPGe spectrum, illustrated in Fig. 5.39.

5.6.4 The ^{116}Sn X-ray

As mentioned above, analyzing the X-ray spectrum as a function of time (compare Fig. 5.32, Fig. 5.33 and Fig. 5.34) revealed a transition at an energy of 25.23 keV. This energy was identified as the energy of the ^{116}Sn K_α X-ray transition. The latter only becomes noticeable at later trapping times, while it is hidden by the overlapping and more intense ^{116}In K_α peak at the beginning of the trapping time as well as in the summed, time-integrated spectra (Fig. 5.35, 5.36 and 5.37). In order to extract the peak integrals of the Sn K_α X-ray for every time bin, the 15 time slices were fitted in two slightly different ways. First, the FWHM of the Sn K_α peak was fixed to 1 keV, while the FWHM for the partly overlapping ^{116}In K_α X-ray as well as for the ^{116}In K_β were free fit parameters. The energies for the

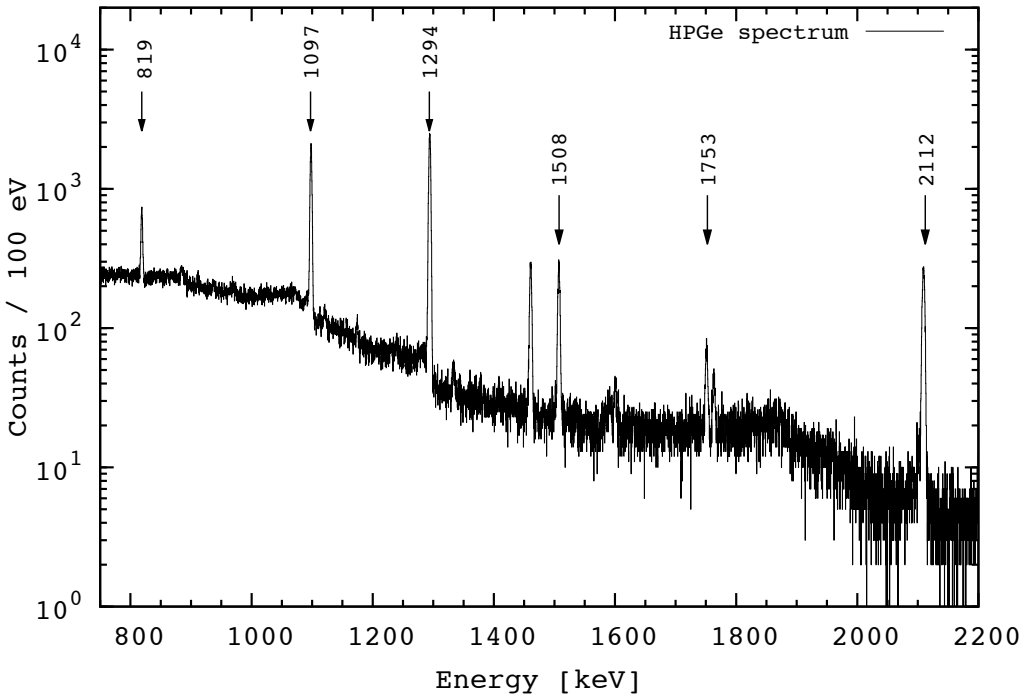

Figure 5.39: ^{116}In-decay spectrum taken with an HPGe detector during the ^{116}In experiment. The indicated transitions result from the decay of the long-lived $J^{\pi}=5^{+}$ isomer. The additional peaks in the spectrum result from the ambient background.

In X-rays were determined by a fit of the summed spectrum and then fixed for the fits of each time slice. To determine and fix the Sn K_{α} energy, a time slice of a later trapping time when that peak becomes more visible in the spectrum was fit with fixed In X-ray energies. The efficiency corrected counts per 1 s time bin for the Sn K_{α} peak resulting from that fitting procedure are plotted in Fig. 5.40 as a function of the trapping time. The data was fit once with a single exponential function (i(x), solid black curve) and once with a combination (solid red line) of an exponential function (f(x), blue, dashed curve) and a constant (black dashed line). From the fit of the single exponential function one can extract a half-life of $T_{1/2}$=(5.1 $\pm$ 0.8) s. When the function includes an exponential function and a constant, one gets a half-life of $T_{1/2}$=(2.8 $\pm$ 1.0) s with a constant of c=107 $\pm$ 45. The intersection of the exponential function with $T_{1/2}$=(2.8 $\pm$ 1.0) s with the ordinate at $t_{decay} = 0$ s gives 625 $\pm$ 97 counts/s. The observation of a short-lived component contributing to the count rate in the Sn K_{α} peak is unexpected because, according to the literature, the Sn X-rays are expected to occur from the decay of excited states in ^{116}Sn only populated by the long-lived

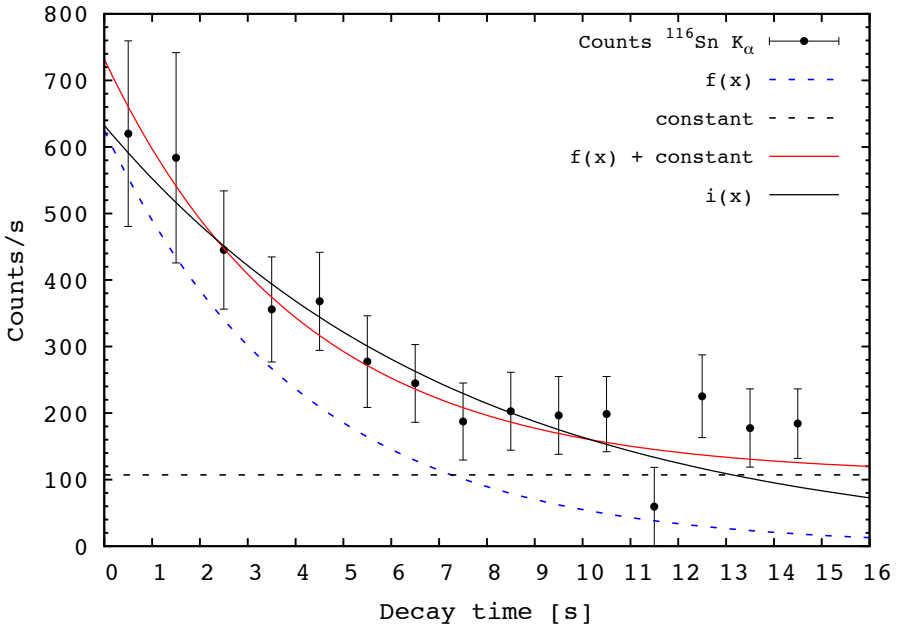

Figure 5.40: Count rate per time bin in the Sn K$_\alpha$ peak as a function of the trapping time. To extract the number of counts the FWHM for the peak was fixed to 1 keV. The black curve represents a single exponential function with $T_{1/2}$=(5.1 ± 0.8) s, while the red function consists of an exponential function (blue, dashed line) with $T_{1/2}$=(2.8 ± 1.0) s and a constant (c=107 ± 45) (black, dashes line).

^{116}In isomer.

The data was fitted a second time, whereby the FWHM of the Sn K$_\alpha$ was set to the same value as the FWHM of the In K$_\alpha$ (compare Tab. 5.15). Again, all energies were fixed. The overall trend of the data is similar to the values resulting from the first fitting procedure. In Fig. 5.41 the data and the fit functions are displayed analogously to the first data set. For the single exponential fit the extracted half-life is $T_{1/2}$=(7.1 ± 1.5) s, while the extracted value for $T_{1/2}$ is shorter ($T_{1/2}$=(2.5 ± 1.0) s, c=(176 ± 44) counts/s) when the data is fitted with a function including a constant in addition to the exponential decay. The intersection of the exponential with $T_{1/2}$=(2.5 ± 1.0) s with the ordinate at t=0 s yields 593 ± 141 counts/s.

Given an activity of A(t=0)=176 counts/s from the long-lived 5$^+$ isomer, one can derive

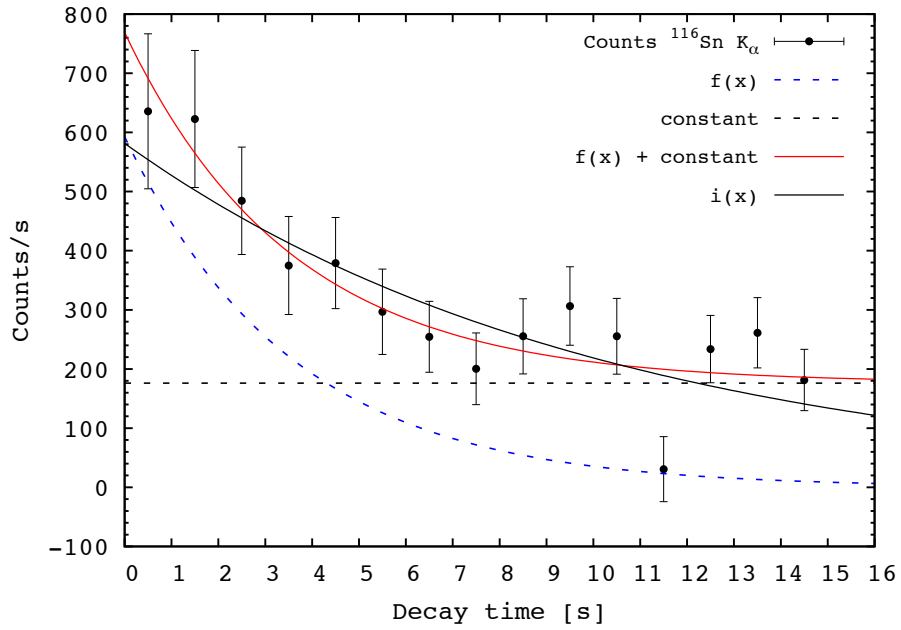

Figure 5.41: Count rate per time bin in the Sn K_α peak as a function of the trapping time. To extract the number of counts the FWHM for the peak was set to the value of the partly overlapping In K_α peak. The black curve represents a single exponential function with $T_{1/2}$=(7.1 ± 1.5) s, while the red function consists of an exponential function (blue, dashed line) with $T_{1/2}$=(2.5 ± 1.0) s and a constant (c=(176 ± 44) counts/s) (black, dashed line).

Time [s]	Counts/ϵ (Sn K_α) $\times 10^2$	
	Set 1	Set2
0.5	6.2 ± 1.4	6.4 ± 1.3
1.5	5.8 ± 1.6	6.2 ± 1.2
2.5	4.5 ± 0.9	4.8 ± 0.9
3.5	3.6 ± 0.8	3.8 ± 0.8
4.5	3.7 ± 0.7	3.8 ± 0.8
5.5	2.8 ± 0.7	3.0 ± 0.7
6.5	2.5 ± 0.6	2.5 ± 0.6
7.5	1.9 ± 0.6	2.0 ± 0.6
8.5	2.0 ± 0.6	2.6 ± 0.6
9.5	2.0 ± 0.2	3.1 ± 0.7
10.5	2.0 ± 0.6	2.6 ± 0.6
11.5	0.6 ± 0.6	0.3 ± 0.6
12.5	2.3 ± 0.6	2.3 ± 0.6
13.5	1.8 ± 1.2	2.6 ± 0.6
14.5	1.8 ± 1.6	1.8 ± 0.5
Sum	$(4.3 \pm 1.1) \times 10^3$	$(4.8 \pm 1.1) \times 10^3$

Table 5.15: Overview of the extracted count rates (detection efficiency corrected) extracted from the ^{116}Sn K_α X-ray with a FWHM set to 1 keV (set 1) and an adjusted FWHM (right) according to the FWHM of the In K_α peak. The listed errors result from the analytical fitting procedure.

	In		
	K_α	K_β	Beam composition
Activity [Counts/1s]	5.30(4)·10^4	1.19(18)·10^4	
Intensity (calc.) [%]	33.35 ± 1.38	7.05(58)	
Activity/Intensity	1.58(3)·10^3	1.71(5)·10^3	$\sim 0.5\%$ ^{116m2}In
N_{ions} ($\Omega\&\epsilon$ corrected)	5.55(25)·10^7	5.89(51)·10^7	
	Sn		
	K_α	K_β	Beam composition
Activity [Counts/1s]	176(44)	N/A	
Intensity (lit.) [%]	0.847(24)	N/A	
Activity/Intensity	208(52)	N/A	$\sim 99.5\%$ ^{116m1}In
N_{ions} ($\Omega\&\epsilon$ corrected)	1.1(3)·10^{10}	N/A	

Table 5.16: Listed are the quantities necessary to calculate the beam composition. The K_α and K_β activities for In and Sn as well as the values for the transition intensities and the corresponding number of ions calculated once from the K_α activity and once from the K_β activity are presented. The right column lists the contribution of each species to the total beam composition.

the number of ions from that particular isomer in the trap at $t_{decay} = 0$ s:

$$N_{ions}(t=0) = \frac{A(t=0)\cdot T_{1/2}}{\ln 2 \cdot I(K_\alpha)\cdot \Omega} = \frac{176 \cdot 54.29 \cdot 60}{\ln 2 \cdot 0.00847 \cdot 0.009} = 1.10(27)\cdot 10^{10} \tag{5.18}$$

For the average number of ions at the beginning of each individual trapping cycle (start of decay time) one gets:

$$N_{ions}(t=0) = \frac{1.10(27)\cdot 10^{10}}{1606} = (6.8 \pm 1.7)\cdot 10^6. \tag{5.19}$$

5.6.4.1 Beam composition

In order to make an estimate for the beam composition the extracted number of ions from the 5^+ isomer has to be compared to the number of ions deduced from the decay of the 2.18 s isomer. Tab. 5.16 lists the activities, N_{ions} and the X-ray intensities used for the calculation. According to these numbers the relative beam composition is:

- 5^+ isomer: 99.5%
- 8^- isomer: 0.5%

The yield measurements indicate a similar ratio. The fraction of the ^{116}In ground state contribution cannot be determined due to the lack of observed transitions.

Experimentally one gets for the ratio of the integrated activities $\frac{SnK_\alpha}{InK_\alpha}$:

$$\frac{A(SnK_\alpha)}{A(InK_\alpha)} = \frac{(4.8 \pm 1.1) \cdot 10^3}{(1.66 \pm 0.03) \cdot 10^5} = 0.029(7), \tag{5.20}$$

where the activity for the Sn K_α includes the sum of the long-lived and short-lived contribution. From the activities of the long-lived and short-lived component of the Sn K_α at $t_{decay} = 0$ s, $A_0(Sn_{long-lived})$=176(44) counts/s and $A_0(Sn_{short-lived})$=593(141) counts/s one deduces the relative contributions to the total number of counts. With a fraction of 77% for the short-lived component compared to only 23% for the long-lived component one can conclude, that the major contribution of the observed number of Sn K_α counts within the 15 s of decay time results from the decay of the unspecified short-lived component and not from the decay of the long-lived first isomer.

From the fraction of the long-lived component in the Sn K_α X-ray, one can estimate the required ground-state yield and measurement time for the observation of the Cd K_α X-ray originating from the EC decay of the ^{116}In ground state. Within 18 h of measurement time and at a yield of $\sim 3\times10^6$ pps for the 5^+ one extracts 1104±33 counts. Correcting this value by the intensity ratio $I_{K_\alpha}(Cd)/I_{K_\alpha}(Sn)$ and the half-life ratio $T_{1/2}(5^+)/T_{1/2}(8^-)$, one gets the following number of counts for the Cd K_α at a yield of $\sim 3\times10^6$ pps:

$$N_{counts} = 1104 \cdot \frac{0.0138\%}{0.847\%} \cdot \frac{3240\ s}{14\ s} = 4080 \pm 64. \tag{5.21}$$

As the yield measurements provided a value of $\sim 3\times10^4$ pps for the ground state, the number of Cd K_α counts detected in the experiment were at least two orders of magnitude lower than the number given in Eq. 5.21. The resulting ≤ 40 counts were not distinguishable from the background. This means, with a yield of 10^6 pps and a measurement time of $\leq$ 18 h, an observation of EC Cd X-rays becomes possible with the current setup.

5.6.4.2 Interpretation of the short-lived Sn component

Should the occurrence of this short-lived contribution not result from the fitting procedure itself, where one has to note that the fits for the first 6 s have large uncertainties, due to the dominant contribution of the ^{116}In K_α, one could consider the possibility of an additional decay branch (β^- decay) of the second isomer into a daughter level in ^{116}Sn as indicated

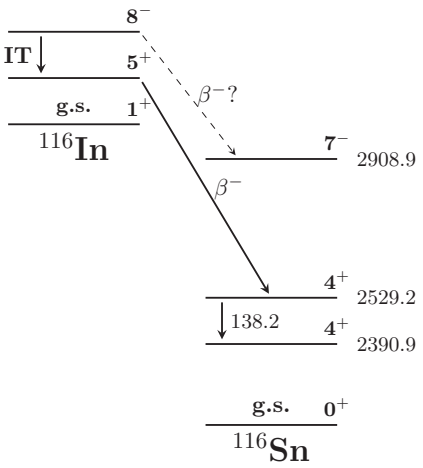

Figure 5.42: ^{116}In decay scheme showing the transitions relevant for the decay of the 8^- isomer. Excitation and transition energies are given in units of keV. The dashed arrow indicates a possible β^- decay of the 8^- into a daughter level in ^{116}Sn as explained in the text.

by the dashed arrow in Fig. 5.42. So far the second isomer is only know to decay 100% into the first isomer.

The TOI [104] quotes a 7^- state in ^{116}Sn at an energy level of 2908.8(1) keV. This state is the energetically highest state that could be populated by a β^- decay. Assuming the second isomer of ^{116}In β^--decays into that state via an allowed Gamow-Teller decay, one can derive a hypothetical log(ft) value, to verify whether the latter is consistent with a possible GT transition.

Given a ground-state to ground-state Q-value of Q_{β^-}=3278(4) keV, the energy of the 8^- level (289.660(6) keV) with $T_{1/2}$=2.18(4) s and the daughter level (2908.8(1) keV), one uses the experimental branching ratio for the transition intensity. The latter is calculated from the fitted activity at t_{decay}=0 s under the assumption that the short-lived component in the fit of the Sn K_α decay is real and due to a β^--decay branch. The activity at t_{decay}=0 s is 593(141) counts/s and the activity coming from the IT branch is extracted from the In K_α (53008(445) counts/s). Therefore, the branching ratio would be:

$$BR = \frac{A(\beta^-)}{A(\beta^-) + A(IC)} = \frac{593(141)}{593(141) + (5.30(4) \cdot 10^4)} = 1.11(2)\%. \tag{5.22}$$

However, the log(ft) value was calculated with the above mentioned values using the NNDC log(ft) calculator and comes to log(ft)=3.10(2), which contradicts the claim of a possible

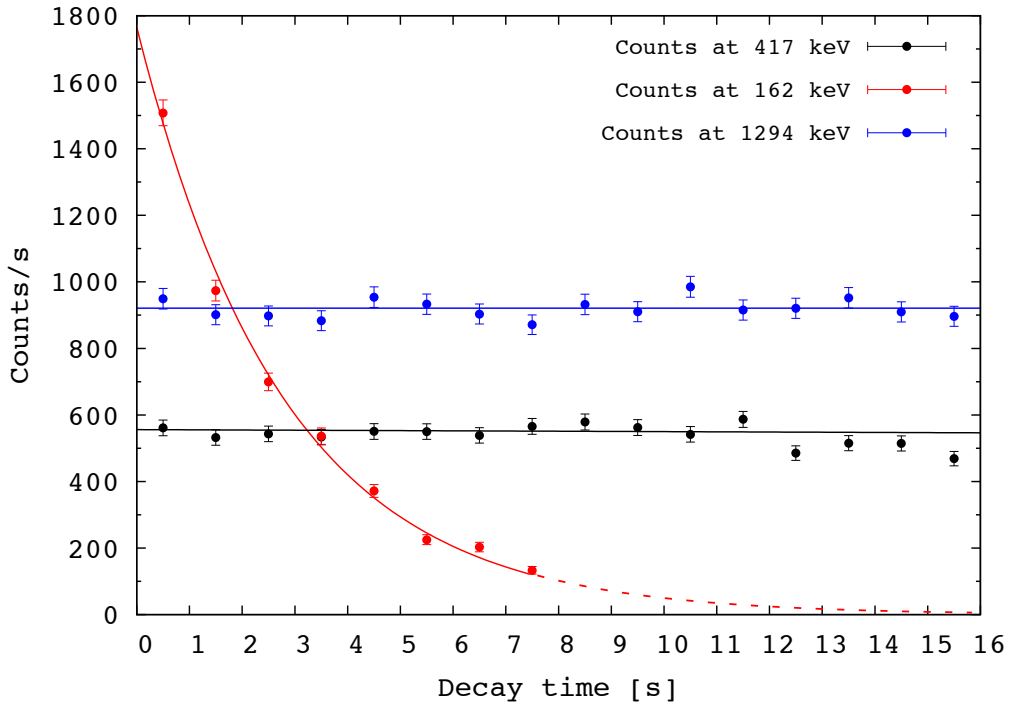

Figure 5.43: Displayed are the decay curves within 15 s trapping time extracted from the 1294 keV and 417 keV transitions directly compared with the decay curve generated from the 162.4 keV γ-line. While the rate of the 1294 keV and 417 keV transitions remains constant over the decay time (trap full and closed), the 2.18 s decay of the 8^- isomer can be described by a single exponential function.

GT-transition as it is even smaller than the $\log(ft)$ for most super-allowed Fermi decays. The expected value for an allowed GT transition is a $\log(ft)$ of $\sim$4.

Another argument that speaks against the possibility of a β^- decay of the second ^{116}In isomer into a daughter level in ^{116}Sn is the time structure of the higher γ-transitions in ^{116}Sn. To study whether γ-lines from the 54.3 min decay feature an additional short-lived component, the 1294 keV as well as the 417 keV transitions in the HPGe spectrum were analyzed as a function of time and the decay curves were compared to the decay of the 8^- isomer via the 162.4 keV transition as shown in Fig. 5.43. Measuring the 2.18 s decay of the 162.4 keV transition demonstrates the capability to extract the short-lived component in the HPGe spectrum, even though the detector is not located as close to the trap center as the Si(Li) detectors and further suffers from a higher background level.

In case of a β^- decay into the 7^- state at 2908.8(1) keV, the subsequent decay of that state

would feed the same states as the known β^- decay of the 54.29 min 5^+ state. Thus, the following γ-transitions would feature a short-lived component similar to the Sn K_α X-ray. The data shown in Fig. 5.43 confounds that argument, as the time structure for the 417 keV line as well as for the 1294 keV transition is a constant over the whole decay time of 15 s.

Since an unknown decay branch can be excluded, one can speculate whether the trap environment, i.e., observing the radioactive decay of a confined ion cloud, in combination with conversion electrons resulting from the IT decay of the 8^- isomer is the origin of the additional short-lived component in the time structure of the Sn K_α. The 8^- state mainly decays via internal conversion and is thus accompanied by the emission of internal-conversion electrons at an energy of:

$$E_e = (E_i - E_f) - E_B \approx 134\ keV, \tag{5.23}$$

where $E_B = 27.94$ keV denotes the atomic-electron binding energy of the K-shell [104], E_i is the excitation energy of the initial state and E_f is the energy of the final state. The minor fraction of electrons from the outer shells possess an even higher energy.

At a magnetic-field strength of 3.96 T the nonrelativistic cyclotron frequency f_c of the oscillating electrons is:

$$f_c = \frac{q_e B}{2\pi m_e} \approx 1.1 \times 10^{11}\ Hz. \tag{5.24}$$

At the same time their spiraling radius (to first order $r \sim 0.3$ mm) remains too small for the electrons to leave the ion cloud, which means, they continuously collide with the trapped ions, in particular stable Sn. Excitation and de-excitation of Sn will then result in the emission of Sn X-rays.

Given an average number of $\sim 3.4 \cdot 10^4$ ions in the 8^- state at the beginning of each cycle (see Sec. 5.6.2.1), out of which $\sim 63\%$ decay via IT decay, about $2.2 \cdot 10^4$ electrons are generated from the IT decay within the ion cloud. By considering the 2.18(4) s half-life of the 8^- state, one derives a current of:

$$\frac{2.2 \cdot 10^4\ e^-}{2.18\ s} \times 1.1 \times 10^{11}\ Hz \approx 1.1 \times 10^{15}\ \frac{e^-}{s}, \tag{5.25}$$

which corresponds to:

$$1.1 \times 10^{15} \frac{e^-}{s} \times (1.602 \cdot 10^{-19}) \frac{kg \cdot m^2}{s^2} \sim 0.2\ mA \tag{5.26}$$

The conversion electrons possess a sufficiently high energy for multiple ionizations of stable Sn, thereby imprinting the half-life of the 8^- isomer on the Sn K_α. Thus, one has to multiply the value for the current (0.2 mA) by the number of possible ionizations (~ 4), which yields ~ 0.8 mA. This estimate assumes at least 10^4 stable ^{116}Sn ions in the trap per cycle. With an electron-beam current of 50 mA, one gets the following ratio for the two currents:

$$\frac{0.8}{50} = 1.6\%. \tag{5.27}$$

This value reflects the measured ratio of 1.11(2)% in Eq. 5.22.

The electron-impact ionization cross section depends on the ion current generated by single electron impact, the current of the bombarding electrons with an energy E_e, the number density of the ion cloud ($\sim 6.8 \cdot 10^6$ ions/220 mm^3) and the collision-path length over which the measured ion current is collected [192].

Since accurate simulations for the TITAN EBIT are presently not available, one makes the assumption that the ionization cross section for the removal of 29 electrons with an electron-beam energy of 1.7 keV is to first order comparable to the cross section for the removal of an inner K-shell electron by the more energetic conversion electrons.

5.6.5 Atomic-structure effects

Analogous to the analysis of the ^{124}Cs data, the charge-breeding related atomic-structure effects were investigated for the ^{116}In spectrum.

5.6.5.1 X-ray energy shifts

The charge-breeding related X-ray energy shifts observed in the A=124 experiment were confirmed for the ^{116}In measurement. The relative energy shift Δ[E(K_β)-E(K_α)] for the indium X-rays was determined in the same way as for the ^{124}Cs measurement but since the analysis of the ^{124}Cs revealed no time dependence of the energy shift, the shifts were extracted by fitting the summed spectrum of all runs instead of each time slice individually.

Δ(E(K_β)-E(K_α))	
0 s - 30 s	15 s - 30 s
131 ± 12(stat.) ± 60(syst.)	141 ± 16(stat.) ± 60(syst.)

Table 5.17: X-ray energy shifts for In X-rays observed during the ^{116}In experiment. The given values were extracted from a direct time-dependent fit. All values have a statistical uncertainty resulting from the fits, which was obtained via the covariance matrix and a systematic uncertainty from the energy calibration ($\sim$ 60 eV). The uncertainties for the $\Delta[E(K_\beta) - E(K_\alpha)]$ values result from the sum of the errors from the K_α and K_β values.

It was differentiated between the summed spectrum over 30 s including the injection time and the spectrum accumulated over the last 15 s (15 s to 30 s) of the trapping cycle (decay time only). The extracted values for both time-integrated spectra are given in Tab. 5.17 and are consistent with each other as well as with the observed shift in the A=124 experiment.

5.6.5.2 K_α/K_β ratio

In addition to the energy shifts, the K_α/K_β X-ray intensity ratio was determined for every time slice (1 s bins) with a time-independent fit as well as for the whole data set with the time-dependent fitting method as described above for the ^{124}Cs data (see Ch. 5.4). The individual ratios extracted from every time slice of the decay time and the corresponding average value in comparison to the value of the ratio extracted from the time-dependent fit are listed in Tab. 5.18 and are presented in Fig. 5.44. Both results are consistent with each other. The experimentally determined K_α/K_β ratio yields a value of $R = 4.73(46)$, quoting the time-slices average result with a more conservative uncertainty. As illustrated in Fig. 5.45 this value agrees with the literature value for the X-ray ratio of a neutral atom which includes the $K_{\beta 2}$ transition ($R = 4.98(14)$ [104]) and deviates from the ratio expected for a neutral atom which lacks the $K_{\beta 2}$ transition ($R = 5.86(17)$ [104]). This observation confirms the results of the A=124 data, where the measured ratios of the highly-charged ions agreed with the ratio for a neutral atom, even though the $K_{\beta 2}$ transition is highly suppressed at the charge states discussed in this thesis, and an increased K_α/K_β ratio would be expected.

Time [s]	Ratio K_α/K_β
0.5	4.77(13)
1.5	4.82(15)
2.5	4.96(15)
3.5	4.85(18)
4.5	4.53(19)
5.5	5.07(27)
6.5	4.58(26)
7.5	4.73(36)
8.5	4.60(48)
9.5	5.15(96)
10.5	4.77(88)
11.5	4.66(1.02)
12.5	3.34(72)
13.5	5.38(2.43)
14.5	8.76(6.38)
Average	4.73(46)
Neutral w $K_{\beta 2}$	4.98(14)
Neutral w/o $K_{\beta 2}$	5.86(17)
Time-dependent fit	4.81(4)

Table 5.18: Overview extracted K_α/K_β ratio depending on the trapping time. The given errors represent the statistical uncertainties. Note that all values have an additional 5% systematic uncertainty resulting from the uncertainty of the detection efficiency. The average was determined by discarding the ratio at 15 s and the given uncertainty is the corresponding standard deviation. The uncertainties for the neutral atom ratios result from the uncertainties of the X-ray intensities, while the uncertainty for the time-dependent result comes directly from the time-dependent fit (covariance matrix).

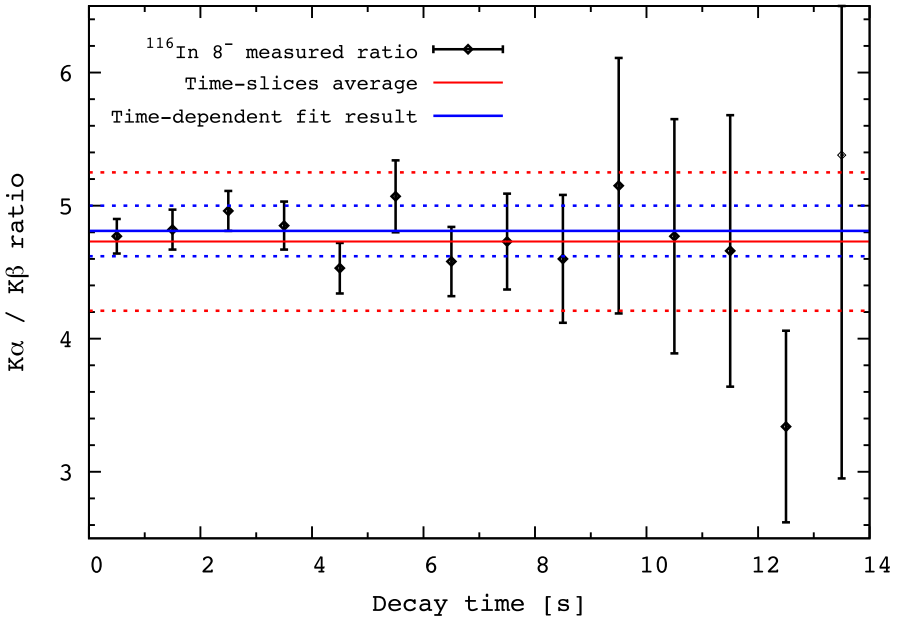

Figure 5.44: K_α/K_β ratios depending on the trapping time for ^{116}In X-rays. The solid red line represents the average of all time slices and the corresponding standard deviation including an additional systematic uncertainty from the detection efficiency is indicated by the red dashed lines. For comparison the time-dependent fit result together with its upper and lower limit also including the systematic uncertainty is displayed in blue.

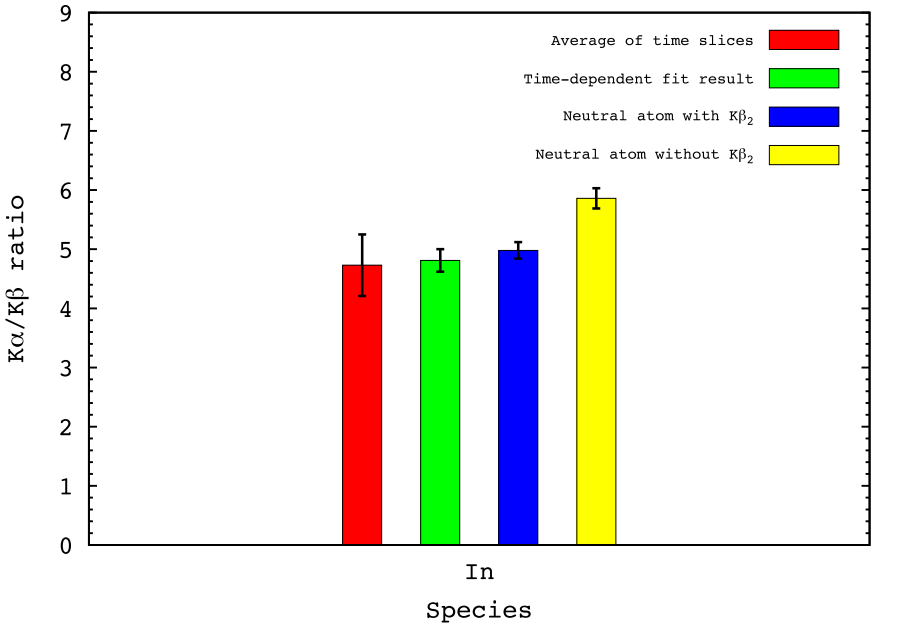

Figure 5.45: Comparison of the values for In X-ray K_α/K_β intensity ratio determined with two independent methods compared with the literature values including and excluding the $K_{\beta 2}$ transition. The plotted error bars for the experimental values result from the sum in quadrature of the statistical errors of the fits and the 5% systematic uncertainty from the detection efficiency. The errors for the neutral atoms result from the uncertainties of the intensities quoted in the databases [169].

5.6.6 Multiple-injection technique

For the realization of weak (10^{-2} to 10^{-5}) electron-capture branching-ratio measurements relevant for $\beta\beta$ decay, it is essential to store a sufficient number ($\geq 10^7$) of ions in the spectroscopy trap to collect enough statistics within the limited time (4-6 12 hr shifts) of an online experiment. The limiting factor for the number of injected ions into the EBIT is the space-charge limit of the RFQ ($\sim 10^5$-10^6 ions) [127]. As a result, ISAC beams with high intensities ($\geq 10^6$ pps) are effectively wasted, and cannot be utilized to their full potential. Therefore, it was necessary to employ a novel EBIT-injection scheme to overcome the RFQ space-charge limit.

In order to maximize the number of ions in the EBIT, multiple bunches of singly-charged ions from the RFQ were extracted, subsequently injected into the EBIT and charge-bred to $\sim q = 29^+$. Due to the fact that the effective potential depth for HCIs is deeper than for SCIs, it is possible to continuously inject ions, without losing those, that are already highly-charged and consequently trapped in the potential. This so called multiple-ion bunch-stacking [193] scheme was applied over the course of the ^{116}In experiment with 25 ms accumulation time in the RFQ and a total of 600 injections during the 15 s of injection time without extraction. Fig. 5.46 displays the summed number of ^{116}In X-ray counts (K_α and K_β) of all runs as a function of the cycle time. The first 15 s present the multiple-stacking technique, and show an efficiency of $\sim 100\%$ for injection up to 8.5 s (relative to ion implantation (Eq. 5.28)), at which point the space-charge-limit of the trap is reached. After 8.5 s of injection, or, respectively, ~ 340 ion bunches from the RFQ, the number of counts reaches its maximum, which will be referred to as "turn-over point" in the following. The data before the turn-over point can be described by the function for radioactive growth and decay (compare Fig. 5.46):

$$\frac{dN}{dt} = R - \lambda N, \tag{5.28}$$

with the ion-injection rate R, the number of radioactive nuclei N and the decay constant $\lambda = \ln(2)/T_{1/2}$.

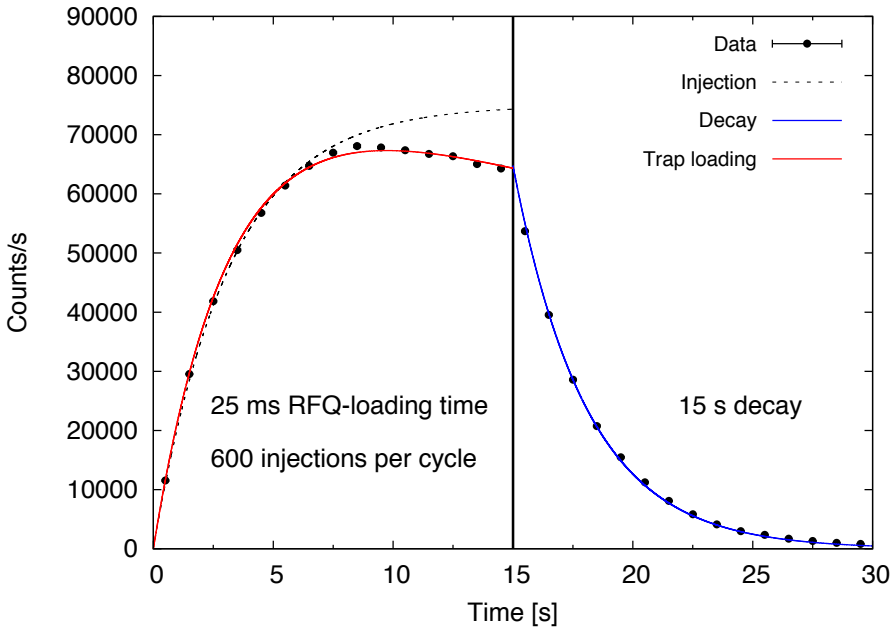

Figure 5.46: Sum of ^{116}In K_α and K_β X-ray counts per 1 s time bin depending on the cycle time. For the first 15 s the trap is filled constantly and the number of counts increases until it reaches its maximum after 8.5 s. 15 s of injection is then followed by 15 s of decay time, where the decay of the 2.18 s isomer is visible. The radioactive growth within the first 8.5 s of trap filling (black dashed line) is described according to formula 5.29. The radioactive decay over the last 15 s is described by a simple exponential fit (blue line). An attempt to describe the data over the first 15 s, including the turn-over point is presented by the red curve.

The solution for the produced activity is then:

$$\lambda N(t_{inj}) = A(t_{inj}) = R(1 - \exp(-\lambda \cdot t_{inj})), \tag{5.29}$$

where t_{inj} stands for the injection time. After the turn-over point, the number of counts decreases slightly until the injection stops at t_{inj}=15 s. Subsequently, the trap is closed, at which point the data represents pure statistical radioactive decay of the ^{116}In 8^- isomer. A fit to these data results in a half-life of $T_{1/2} = 2.19(1)$ s, which is in good agreement with the value of 2.18(4) s given in Ref. [176] for the ^{116}In 8^- internal-conversion decay and confirms that there are no trapping related losses which would be identified by an additional component in the decay curve.

According to Eq. 5.29 one would expect a stationary with increasing time ($t_{inj} \rightarrow \infty$), where the implantation rate and decay rate reach an equilibrium:

$$R = A_{max}. \tag{5.30}$$

After three half-lives the maximum obtainable activity should have been reached.
While the maximum is observed after 8.5 s, the equilibrium $R = A_{max}$ is not reached. Instead, the activity slightly decreases until the end of the injection part of the cycle (t_{inj}=15 s).

In order to understand this observation, the correlation of the radioactive decay and grow-in of the three species (^{116}In g.s., ^{116}In 8^- state and ^{116}In 5^+ state) delivered in the ISAC beam in as well as the space-charge limit of the EBIT has to be taken into account. The number of ions in the 8^- state in the trap, only depend on the injection rate and the half-life:

$$N'_{8^-}(t) = \frac{R_{8^-}}{\lambda_{8^-}} \left[1 - \exp(-\lambda_{8^-} \cdot t)\right]. \tag{5.31}$$

The number of ions in the 5^+ state depends on the injection rate as well as on the IT-decay of the 8^- isomer:

$$
\begin{aligned}
N'_{5^+}(t) &= \lambda_{8^-} \cdot N_{8^-}(t) + \frac{R_{5^+}}{\lambda_{5^+}} \left[1 - \exp(-\lambda_{5^+} \cdot t)\right] \\
&= -\frac{\lambda_{8^-}}{\lambda_{8^-} - \lambda_{5^+}} \cdot N_{10} \cdot \left[\exp(-\lambda_{8^-} \cdot t) - \exp(-\lambda_{5^+} \cdot t)\right] \\
&\quad + N_{20} \cdot \exp(-\lambda_{5^+} \cdot t) + \frac{R_{5^+}}{\lambda_{5^+}} \left[1 - \exp(-\lambda_{5^+} \cdot t)\right], \qquad (5.32)
\end{aligned}
$$

where one assumes a population of $N_{20} = 0$ for the initial condition at t=0 s for the 5^+. The number of ions in the ground-state depends on the injection rate and the decay of the 5^+ state:

$$
\begin{aligned}
N'_{g.s.}(t) &= \lambda_{5^+} \cdot N_{5^+}(t) + \frac{R_{g.s.}}{\lambda_{g.s.}} \left[1 - \exp(-\lambda_{g.s.} \cdot t)\right] \\
&= -\frac{\lambda_{5^+}}{\lambda_{5^+} - \lambda_{g.s.}} \cdot N_{20} \cdot \left[\exp(-\lambda_{5^+} \cdot t) - \exp(-\lambda_{g.s.} \cdot t)\right] \\
&\quad + N_{30} \cdot \exp(-\lambda_{g.s.} \cdot t) + \frac{R_{g.s.}}{\lambda_{g.s.}} \left[1 - \exp(-\lambda_{g.s.} \cdot t)\right], \qquad (5.33)
\end{aligned}
$$

with $N_{30} = 0$ for the initial condition at t=0 s for the ground state.

Ideally, the decay of the 5^+ state and the ground state would not affect the grow-in of the 8^- state, as it is not fed by any of the other two states. However, the injection and decay of the other species limit the available space charge in the EBIT.

The attempt to model the behavior over the total 15 s of injection time by an analytical expression was realized with the following modified trap-loading function T_{load} [194]:

$$
T_{load}(t_{inj}) = \frac{dN}{dt_{inj}} = R^{\epsilon \cdot t_{inj}} \cdot N^{-\frac{\lambda}{t_{inj}}}, \qquad (5.34)
$$

where ϵ describes the injection efficiency of the observed species (8^-), which depends on the beam composition as well as on the space charge limit of the EBIT. It essentially combines the radioactive decay and grow-in for all three species. The solution of Eq. 5.34 is then employed to describe the data for the first 15 s:

$$
T_{load}(t_{inj}) = -\frac{(2^{-t_{inj}/T_{1/2}} - \epsilon^{t_{inj}}) \cdot R \cdot T_{1/2}}{\ln(2) + T_{1/2} \cdot \ln(\epsilon)}, \qquad (5.35)
$$

The injection rate is R=2.52(1)·10^4 counts/s. Note that this includes all cycles over the about 18 h of data taking time. If one calculates the average rate for one cycle, one gets

R=(2.52(1)·10^4)/1606=16(1) counts/s, which corresponds to $\sim$ 1.6·10^4 ions/s in the 8^- state. Comparing this value to the average yield for the 8^- (see Tab. 4.2) shows that $\lesssim 6\%$ of the ions reaching the RFQ are effectively injected into the EBIT.

To confirm that the trend of the multiple-injection scheme does not purely follow the function for exponential growth as generally observed for the implantation of radioactive beam on a tape, the spectrum of the HPGe was analyzed in addition to the Si(Li) spectra.
The data was sliced in 1 s time bins and the count rate in the 162.4 keV line was extracted for each time-slice. The fit results, or, respectively, number of counts are presented in Tab. 5.19. Fig. 5.47 illustrates the HPGe data together with the functions used to describe the experimental data. The same trend as for the X-ray counts in the Si(Li) spectra is observed for the 162.4 keV line in the HPGe spectrum. The first 8 s can be described by Eq. 5.29 until the turn-over point is reached and a continuous count-rate decrease is observed until the end of the injection time.

The data after the trap has been closed follows pure exponential decay, however, the limited statistics only allow for an extraction of the count rate in the 162.4 keV line for the first 7 s of the trapping time. The fitted half-life comes to $T_{1/2}$=2.2(3) s and therefore agrees with the value determined by using the X-rays as well as the value quoted in the literature [169]. By comparing the multiple-injection schemes of transitions in the Si(Li) spectra (Fig. 5.46) to those in the HPGe (Fig. 5.47), one can conclude that the trend of the count rate does not depend on the energy of the emitted photons, as the behavior is similar for the X-ray region and the 162.4 keV transition. This confirms that the observed trend of the injection scheme is not related to any atomic effects but purely an effect of the decay and injection of multiple species with different half-lives. The space-charge limit of the trap as well as the number of ions in the 5^+ and the ground state determine the maximum number of ions for the 8^- state, for which the grow-in and decay can be monitored.

	Time [s]	counts	stat. error
Injection	0.5	326	18
	1.5	644	25
	2.5	961	31
	3.5	1249	35
	4.5	1343	37
	5.5	1541	39
	6.5	1586	40
	7.5	1656	41
	8.5	1737	42
	9.5	1711	41
	10.5	1712	41
	11.5	1633	40
	12.5	1645	41
	13.5	1650	41
	14.5	1612	40
Decay time	15.5	1508	39
	16.5	974	31
	17.5	699	26
	18.5	536	25
	19.5	372	19
	20.5	225	15
	21.5	203	14

Table 5.19: Extracted count rates and their statistical errors from the 162.4 keV γ-line in the HPGe spectrum. The upper part of the table lists the results for the 15 s injection time, whereas the lower part gives an overview of the counts during the decay time.

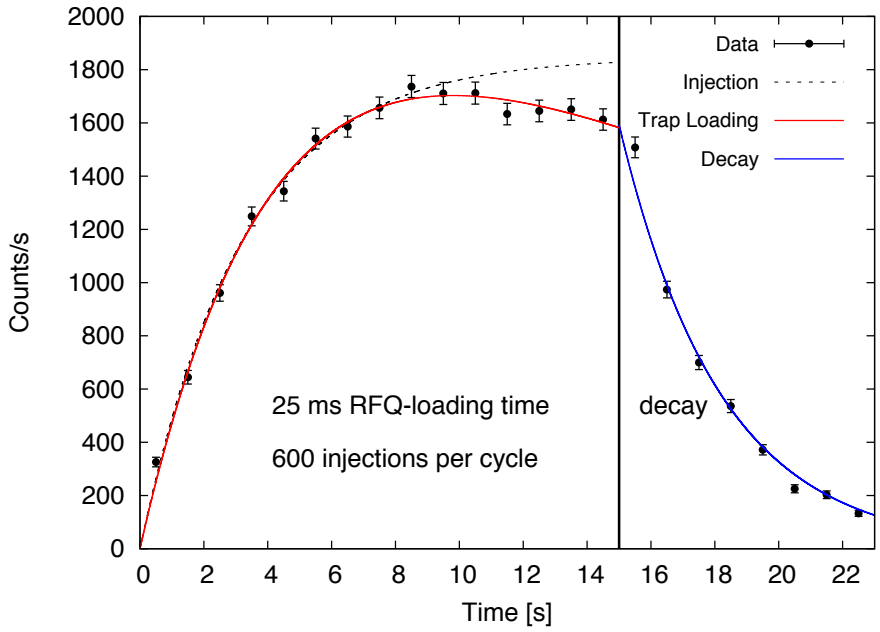

Figure 5.47: Presented is the number of counts in the 162.4 keV peak in the HPGe spectrum as a function of the trap-loading time from 0 s to 15 s as well as for the first 6 s of the decay time. The maximum number of counts is reached after $\sim$ 8 s of trap loading. The function for the radioactive growth is illustrated with the black, dashed line. The modified trap-loading function is indicated in red. After 15 s the exponential decay (blue) can be monitored. Due to a lack of statistics, the extracted number of counts is only shown for the first 6 s of the decay time. Displayed errors are statistical.

Run	RFQ loading time [ms]	#injections	$T_{injection}$ [s]	run time [s]
1319	25	1200	30	1509
1322	15	2000	30	1518
1326	10	3000	30	995

Table 5.20: Listed are the runs and the corresponding RFQ-loading times as well as the number of injections for each scheme, that was tested for the multiple-injection studies. The right column lists the total run time. Extraction times were of the order of a few μs.

5.6.6.1 Systematics

To what extend the RFQ-loading time influences the trap-loading efficiency was studied during the ^{116}In experiment with three different tunes or, respectively, RFQ-loading times (25 ms, 15 ms, 10 ms). The general trap-loading process, i.e., the injection rate as a function of time, as well as the radioactive growth and the point of stationary of the injection time was investigated. For each setting the trap was filled for 30 s, with up to 3000 injections in one cycle as listed in Tab. 5.20.

Fig. 5.48 displays the extracted number of counts for the sum of the ^{116}In K_α and K_β X-ray transitions for the tunes with 15 ms and 25 ms RFQ-loading time. Both data sets were fitted with two different functions each. First with a standard function for radioactive growth (compare Eq. 5.29), and secondly with the trap-loading function from Eq. 5.35. The overall trend for both data sets is similar, i.e., one observes a grow-in for the first 8 s (T_{RFQ}=15 ms) to 9 s (T_{RFQ}=25 ms) before the turn-over point is reached and the rate decreases for about 11 to 12 s. At t_{inj} ≈20 s the rate reaches a relatively constant level for the remaining injection time. By fitting the data with the trap-loading function one can determine a value for the injection rate R:

- $R_{25ms} = 568 \pm 18$ counts/s
- $R_{15ms} = 664 \pm 40$ counts/s

This corresponds to the following rate per cycle:

- $R_{25ms} = 11.3(4)$ counts/s
- $R_{15ms} = 13.1(8)$ counts/s

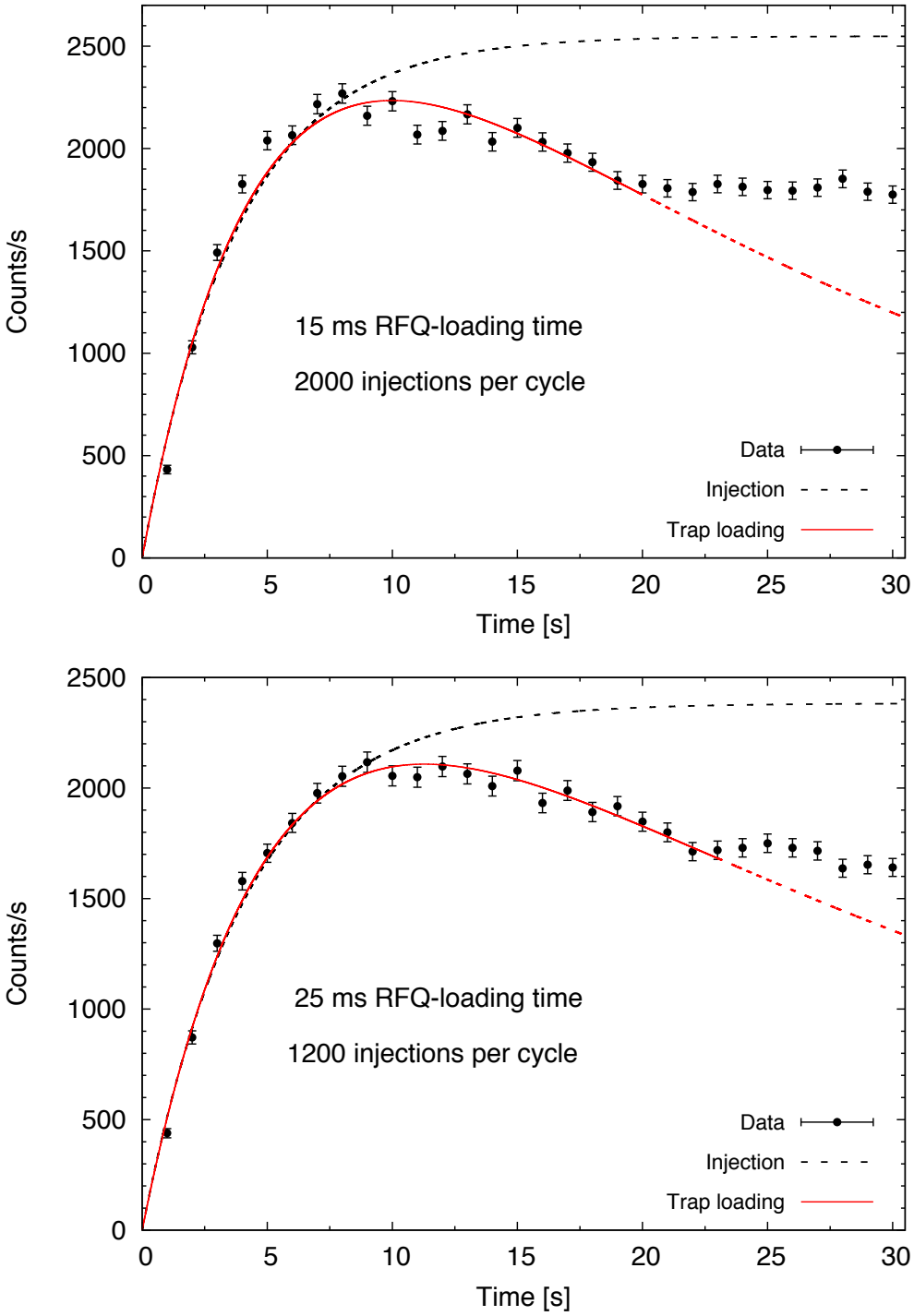

Figure 5.48: Top: Number of counts per 1 s time bins as a function of the filling time for a 30 s multiple-injection scheme. A total of 2000 ion bunches from the RFQ were injected into the EBIT every 15 ms during each cycle. The black, dashed curve describes the fit of the first 15 s of the data with a function for exponential growth (compare Eq. 5.29). The red line presents the fit of the first 23 s with trap-loading function (Eq. 5.35). Bottom: count rate for a scheme with 25 ms RFQ-loading time.

These values are consistent with the observed times for the turn-over point of the 18 h data set with 15 s injection time. The maximum rate is reached slightly earlier (after 8 s) for the 15 ms loading scheme with the higher injection rate than for the 25 ms scheme (9 s to maximum). Hence, the RFQ-loading time of 15 ms was more effective than the tune with 25 ms loading time.
To ensure that the observed trend of the multiple-injection scheme is not due to statistical fluctuations, the data was additionally binned in 2 s time bins. Alternating the size of the time bins from 1 s to 2 s results in an injection rate of:

- $R_{25ms} = 910 \pm 134$ counts/2s
- $R_{15ms} = 1066 \pm 124$ counts/2s

which is consistent with the results for the 1 s binning.

An injection scheme with only 10 ms RFQ-loading time was tested in addition to the 15 ms and 25 ms schemes, but resulted in a significantly lower count rate as illustrated in Fig. 5.49. The maximum count rate is reached after 10 s, which is $\approx$ 2 s later than for the other two schemes. Further, the maximum number of counts is about 36% lower than for the 15 ms scheme.

In summary, one can conclude that the fact that the data does not follow the same trend as the function used to describe the implantation on a tape, i.e., that it does not end up in a saturation, is correlated to reaching the space-charge limit of the EBIT, which is filled up with three ion species, each featuring a different half-life. Even though one only observes the grow-in and decay of one species, the curve is still affected by the other two species. The fact that the beam contamination occupies space in the trap, limits the maximum number of ions of the species of interest in the trap. This limitation will be minimized by implementing a multi-reflection time-of-flight (MR-TOF) spectrometer [195] into the TITAN system. The understanding of the various processes in detail and the dependence of the scheme on the trap depth, which was at $\sim$ 100 V for this experiment, however, requires

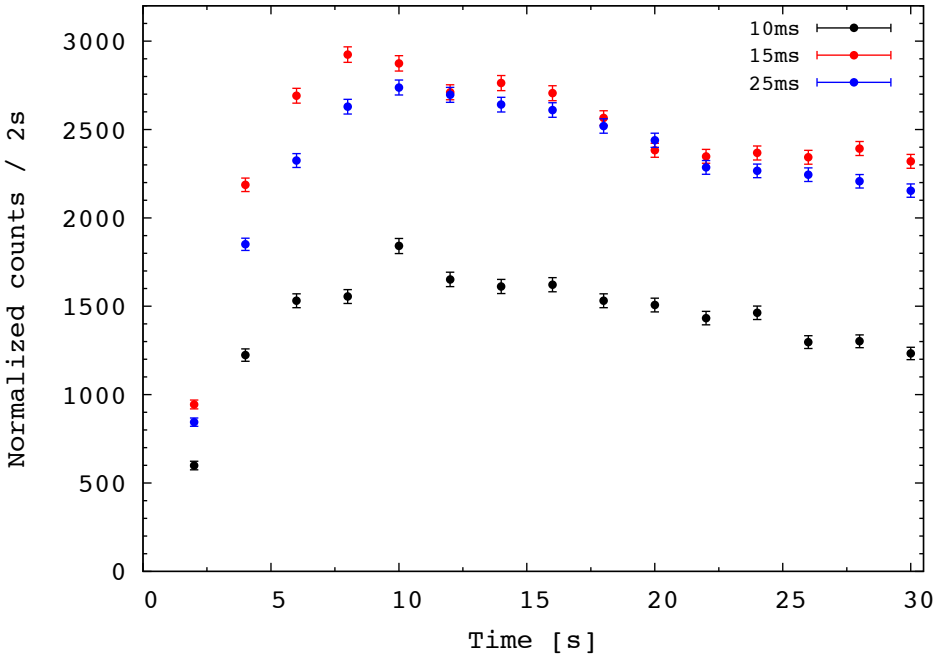

Figure 5.49: Comparison of the count rate for the three multiple injection schemes with different RFQ-loading times. Due to limited statistics at the T_{RFQ}=10 ms scheme, the count rate is presented per 2 s time bins. For a direct comparison, the count rates for the 15 ms and 25 ms schemes were normalized to the run time of the 10 ms scheme.

further investigation.

One can further conclude that for both detector types and the wide range of photon energies one gets consistent results for the trend of the multiple-injection scheme. The number of injections or, respectively, the injection frequency does not influence the trend, but only the time at which the maximum number of counts is reached. An expected charge state and half-life dependence has not been investigated yet.

Furthermore, the possibility to give an estimate for the number of ions, which are injected into the EBIT as a function of time can be used as diagnostic tool to monitor the transport efficiency from upstream of the RFQ to the EBIT.

Chapter VI

FURTHER APPLICATIONS OF IN-TRAP SPECTROSCOPY WITH TITAN

The decay-spectroscopy apparatus at the TITAN facility was originally designed for the purpose of performing EC branching-ratio measurements in a low-background environment crucial for the detection of the weak EC signature. However, the detection system in its present state also allows for performing general diagnostics in the EBIT, which is of particular interest during charge breeding for the mass-measurement program at TITAN. Depending on the half-life of the ion species, the ISAC yield, and the trapping time, it is possible to identify characteristic X-rays or γ-lines following radioactive decay occurring inside the EBIT. Further, the first measurements with the TITAN-EC setup demonstrated the potential and sensitivity of the spectroscopy apparatus to investigate decay properties of highly-charged ions, as discussed in the second part of this chapter (Sec. 6.2).

6.1 In-trap feeding for Penning trap mass spectrometry

The decay-spectroscopy experiments outlined in this thesis demonstrated that trapping of highly-charged ions in the EBIT for minutes is possible without suffering from significant ion losses. This feature, in combination with the detector system for diagnostics, offers the possibility for the so called "in-trap feeding" technique. The ion species of interest is generated by storing the parent nucleus in the EBIT and subsequently sending the daughter nucleus to MPET. Thus, this technique allows for Penning-trap mass spectrometry to be performed on ions which the ISAC facility is unable to produce and deliver to TITAN, while the detector array functions as the diagnostic tool to observe the radiation accompanying the decay of the parent nucleus into the daughter. In addition, one can gain information about the trapping efficiency in dependence of the charge-breeding time and the electron-beam energy.

This section deals with the analysis of in-trap decay spectroscopy data that was not collected for the purpose of an electron-capture branching-ratio measurement, but during a mass measurement on highly-charged ^{30}Mg, ^{30}Al, ^{34}Mg and ^{34}Al. The objective of that experiment was to perform a detailed binding-energy survey of the island of inversion at the region around N = 20 [133, 134]. The breakdown of the N=20 shell closure results from nuclear deformation, which leads to an inversion of the standard *sd*-shell configuration and *pf*-shell intruder configuration and consequently to the formation of this region in the nuclear chart known as the "island of inversion" [196]. In the past, the TITAN collaboration has performed detailed binding-energy surveys of part of this island of inversion. This section outlines evidence for the in-trap decay of ^{30}Mg $\longrightarrow$ ^{30}Al $\longrightarrow$ ^{30}Si for the first TITAN mass measurement with ions produced via the in-trap feeding technique.

6.1.1 EBIT operation and cycling

During this experiment, the EBIT was operated in a cycling mode consisting of three parts: injection, trapping/charge-breeding and extraction followed by a background measurement. Injection and extraction times were of the order of μs, while the trapping and charge-breeding times were altered from a few 100 ms up to 1.5 s. The timing of the drift-tubes was controlled by the programmable pulse-generator (PPG) of the EBIT and correlated to the ADC clock to time-stamp each event registered in the Si(Li) detectors and the HPGe detector.

In contrast to the in-trap decay spectroscopy experiments performed for ECBR measurements, the ion trapping did not occur in the central drift tube, but rather in the drift-tube section closer to the electron-beam ion gun to decrease the time spread of the extracted ions [194]. At the beginning of the experiment, the electron-beam energy was at 3.0 keV, before it was increased to 3.9 keV. In order to monitor the decay of ^{30}Mg $\longrightarrow$ ^{30}Al $\longrightarrow$ ^{30}Si inside the EBIT, the HPGe detector located in front of the 225° port at a distance of 30 cm to the outer Be-window of the port as well as four Si(Li) detectors were operational during the experiment.

Run	T_{run} [± 1s]	T_{trap} [s]	T_{bgd} [s]	E-beam energy [keV]	Comment
2011	596	1	0	3.0	
2012	636	0	0	3.0	background
2014	622	1.5	0	3.0	
2015	629	0	0	3.0	background
2018	329	1	0	3.9	
2019	441	0	0	3.9	background
2020	1203	4	0	3.9	
2021	1278	0	0	3.9	background
2049	752	1	0.5	3.9	Time-stamp start
2052	6511	1	0.3	3.9	
2053	4052	0.5	0.3	3.9	
2071	7204	0.9	8	3.9	
2072	2386	0.9	8	3.9	sames as 2071
2075	2043	0.1	0	3.9	beam-loss test
2077	2162	0.1	0.1	3.9	
2079	1128	0.1	0.1	3.9	10x attenuator
2080	6772	0.3	1.0	3.9	

Table 6.1: Overview of the runs taken to investigate the decay of ^{30}Mg $\longrightarrow$ ^{30}Al $\longrightarrow$ ^{30}Si inside the EBIT. The times for the individual parts of the cycles are listed for all runs. Ion extraction and injection happened on the order of a few μs.

As the objective of this experiment was to prove the in-trap decay of ^{30}Mg $\longrightarrow$ ^{30}Al $\longrightarrow$ ^{30}Si, the main focus was set on detecting γ-rays within an energy region from 200 keV up to 3.5 MeV, for which only the HPGe was usable due to its higher detection efficiency at those energies. The four Si(Li) detectors were mounted at the 45° (#431), 90° (#404), 135° (#432) and 270° (#438) ports and were running in order to monitor the low-energy region and potentially observe X-rays from the charge-breeding process. The singly-charged A=30 beam with a yield of $\sim 1.4{\cdot}10^6$ pps was delivered at $\sim$ 20 keV to the TITAN RFQ by ISAC. The ultimate goal was to trap and charge breed ^{30}Mg in the EBIT for several half-lives until it decayed into its daughter ^{30}Al followed by delivering highly-charged ^{30}Al to MPET for a mass measurement. For systematic background tests, a number of runs with and without radioactive beam in the EBIT were taken, whereby the electron-beam energy as well as the charge-breeding and background times were varied (see Tab. 6.1). The analysis of those spectra is described in the following sections.

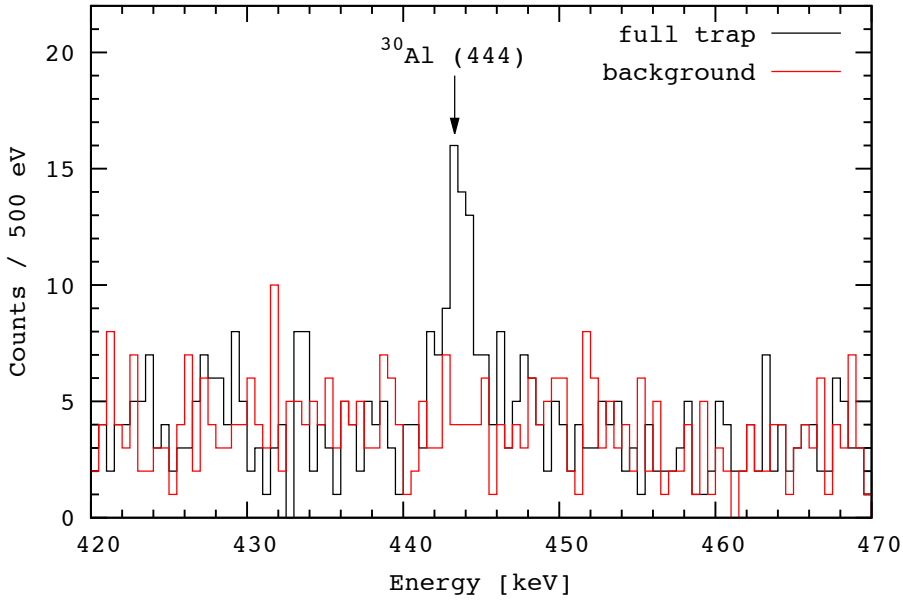

Figure 6.1: Direct comparison of a 10 min spectrum with ^{30}Mg beam injected into the EBIT every 1.5 s (black) and a 10 min empty-trap background spectrum (red). In the full-trap spectrum one observes the 444 keV γ-transition from the decay of the ^{30}Al 1^+ isomer into the 2^+ isomer.

6.1.2 Identifying transitions

^{30}Mg decays to ^{30}Al 100% via β^- decay with a half-life of $T_{1/2}$=335(17) ms, which in turn decays 100% via β^- decay ($T_{1/2}$ = 3.62(6) s) into the stable ^{30}Si. The first step was to verify whether it was possible to observe γ-lines characteristic for the decay of ^{30}Mg as well as from its daughter ^{30}Al. To that end, $\sim$ 10 min runs with radioactive beam in the EBIT followed by $\sim$ 10 min background measurements for which the radioactive beam was blocked by a faraday cup were taken. The comparison of the background and full-trap spectra for two runs (2014, 2015) is shown in Fig. 6.1. The full-trap spectrum clearly shows the 443.63(4) keV [185] γ-transition in ^{30}Al from the decay of the 1^+ isomer at 687.5 keV, populated by the decay of the ^{30}Mg ground state, into the 2^+ isomer at 243.9 keV in ^{30}Al (see Fig. 6.2), whereas the background lacks that transition. The same observation was made for the runs 2011, 2012, 2018, 2019, 2020, and 2021. The statistics in run 2020 are lower than for 2011 and 2018 due to the longer trapping time and the resultant lower number of injections.

During the online monitoring it was possible to identify two transitions in ^{30}Al following

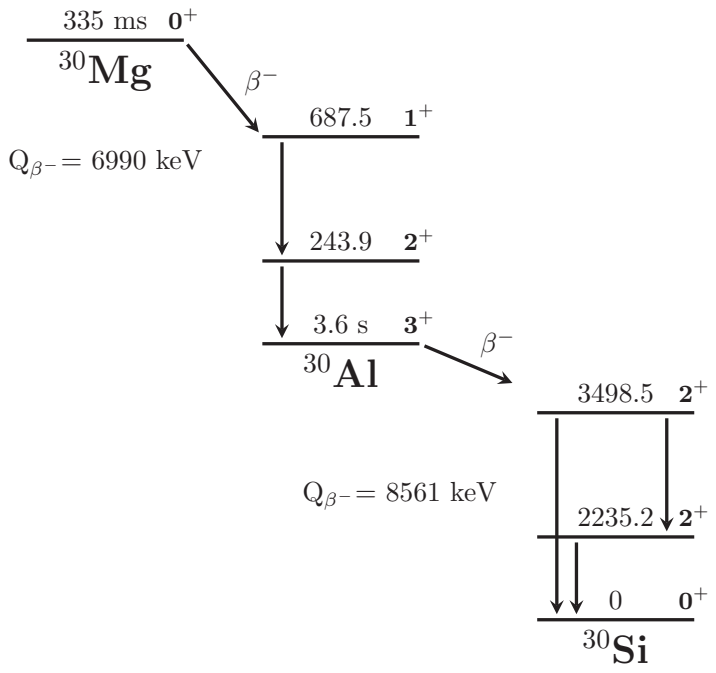

Figure 6.2: Decay scheme of the ^{30}Mg $\longrightarrow$ ^{30}Al $\longrightarrow$ ^{30}Si decay displaying only those energy levels and transitions which are of relevance for this analysis. Energies are given in units of keV. The arrows indicate the transitions observed during the experiment.

the decay of the ^{30}Mg g.s. to the 1^+ isomer in ^{30}Al (see Fig. 6.2):

- E_γ=243.90(8) keV, I_γ = 74(10)% [185], $2^+ \longrightarrow 3^+$, M1
- E_γ=443.63(4) keV, I_γ = 71(10)% [185], $1^+ \longrightarrow 2^+$, M1

and three transitions in ^{30}Si following the decay of the ^{30}Al 3^+ ground state to the 2^+ isomer in ^{30}Si:

- E_γ=1263.13(3) keV, I_γ = 40% [186], $2^+ \longrightarrow 2^+$, M1+E2
- E_γ=2235.23(2) keV, I_γ = 65% [186], $2^+ \longrightarrow 0^+$, E2
- E_γ=3498.37(4) keV, I_γ = 32% [186], $2^+ \longrightarrow 0^+$, E2

Fig. 6.3 shows a summed ^{30}Mg decay spectrum of four runs. The observed γ-transitions in ^{30}Al are marked by arrows. The ^{211}Bi transition at 351.9 keV is a background line as well as the peak from ^{214}Pb at 295.5 keV. Spectra illustrating the transitions at 1263 keV ($2^+ \longrightarrow 2^+$) and 2235 keV ($2^+ \longrightarrow 0^+$) from the excited states in ^{30}Si are presented in Fig. 6.4.

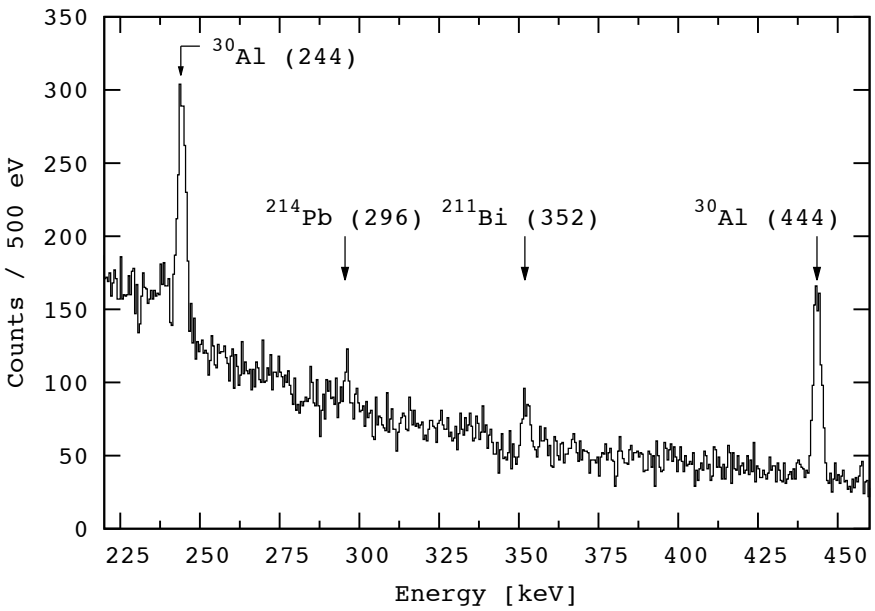

Figure 6.3: Shown is a summed ^{30}Mg decay spectrum within 220 keV to 460 keV of four runs with ^{30}Mg trapped inside the EBIT. The arrows indicate the transitions in ^{30}Al following the ^{30}Mg decay into ^{30}Al. Additionally, one observes the background lines of ^{211}Bi at 351.9 keV and of ^{214}Pb at 295.5 keV.

6.1.3 ^{30}Mg half-life

In order to extract the half-life for ^{30}Mg the data from several compatible runs (2052, 2053, 2071, 2072) had to be added and the trapping time (500 ms) was sliced into 100 ms time bins. An attempt to slice data from single runs with longer trapping times and consequently more data points failed due to limited statistics. An exponential fit of the number of counts in the 444 keV transition as a function of time is presented in Fig. 6.5 (top) and resulted in a fitted half-life of $T_{1/2}$=(305 $\pm$ 34) ms, which is in agreement with the literature value of $T_{1/2}$=(335 $\pm$ 17) ms [169]. The extracted half-life from the 244 keV transition, however, came out to be $T_{1/2}$=(240 $\pm$ 26) ms, which deviates from the literature value and the value extracted from the 444 keV transition.

The deviation from the literature value in case of the half-life extracted from the 244 keV transition has to be a result from the higher background level at that energy and the overall low statistics. A reduced half-life as a consequence of ion losses due to a less efficient trapping in the drift-tube section close to the electron gun cannot be excluded. However,

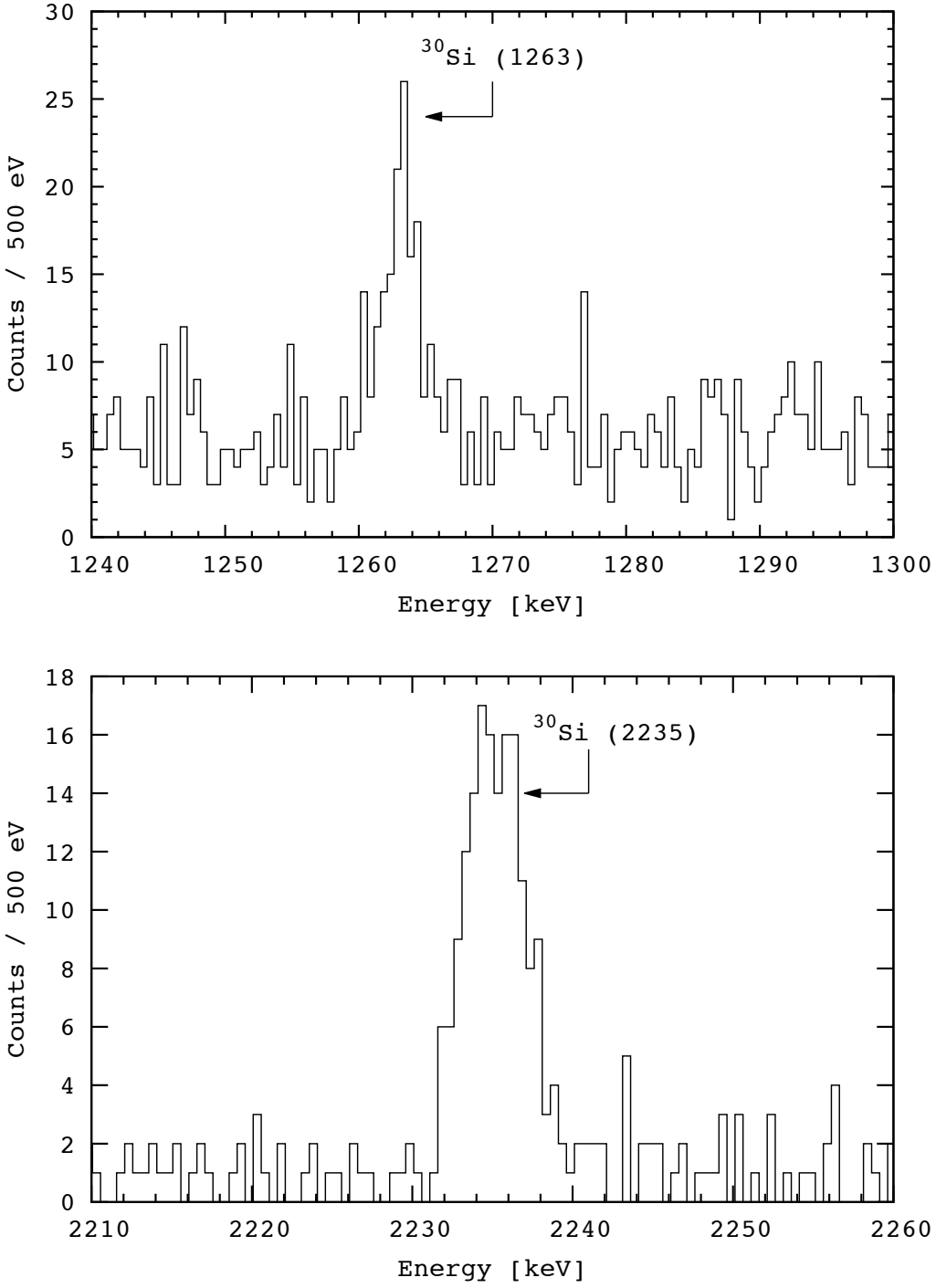

Figure 6.4: Top: Summed spectra within 1235 keV to 1300 keV of four runs with ^{30}Mg trapped in the EBIT. The arrow indicates the transition at 1263 keV resulting from the decay of excited states in ^{30}Si following the decay from ^{30}Al to ^{30}Si. Bottom: Summed spectra within 2210 keV to 2260 keV. The transition at 2235 keV also results from the decay of excited states in ^{30}Si.

the extracted half-life for the 444 keV transition still agrees with the literature value.

6.1.4 Count-rate dependence on charge-breeding time

To study the effect of different charge-breeding times on the count rate and to optimize the beam tune, the intensities of the ^{30}Al and ^{30}Si transitions in the different spectra were compared. First, the runs 2011 and 2014 where the electron-beam energy was at 3.0 keV were compared to each other (compare Fig. 6.6). The fit results are listed in Tab. 6.2. The

Run	Peak energy [keV]	$T_{breeding}$ [s]	Count rate [cts./s]	Count rate [cts./cycle]
2011	243.90(8)	1.0	3.7(7)	3.7(7)
2014	243.90(8)	1.5	2.1(6)	3.1(8)
2011	443.63(4)	1.0	2.8(5)	2.8(5)
2014	443.63(4)	1.5	2.0(3)	2.9(5)
2011	2235.23(2)	1.0	0.7(1)	0.7(1)
2014	2235.23(2)	1.5	0.3(1)	0.4(1)

Table 6.2: Count-rate dependence on the charge-breeding time with a constant electron-beam energy of 3.0 keV. Column 4 presents the count rate normalized to the total run time, whereas column 5 shows the number of counts per trapping cycle. The large uncertainties result from the lack of statistics and, hence, a larger uncertainty of the analytical fit.

loss in count rate at 1.5 s of charge-breeding relative to the rate with 1.0 s charge-breeding time is 43(15)% at 244 keV, 29(7)% at 444 keV and 57(21)% at 2235 keV. On average the loss is $\sim$ 43%, which can be directly related to the 50% longer charge-breeding time of 1.5 s reducing the overall number of duty cycles. Hence, one expects a reduction in statistics as the studied sample is about 50% smaller.

Comparing the number of counts per cycle shows a loss of about 17% at 244 keV, $\sim$ 7% at 444 keV and $\sim$ 44% at 2235 keV. An attempt was made to compare the count rates detected in the runs 2018 and 2020, with charge-breeding times of 1.0 s or 4.0 s, but the statistics given in run 2020 were too low to extract a meaningful value.

6.1.5 Count-rate dependence on electron-beam energy

How the count rate was affected by the electron-beam energy was investigated by comparing the spectra taken at an electron-beam energy of 3.0 keV to those taken at an energy of 3.9 keV while the charge-breeding time stayed constant at 1 s (runs 2011 and 2018). The energy of 3.0 keV corresponds to a charge-state distribution with a maximum at $q = 9^+$

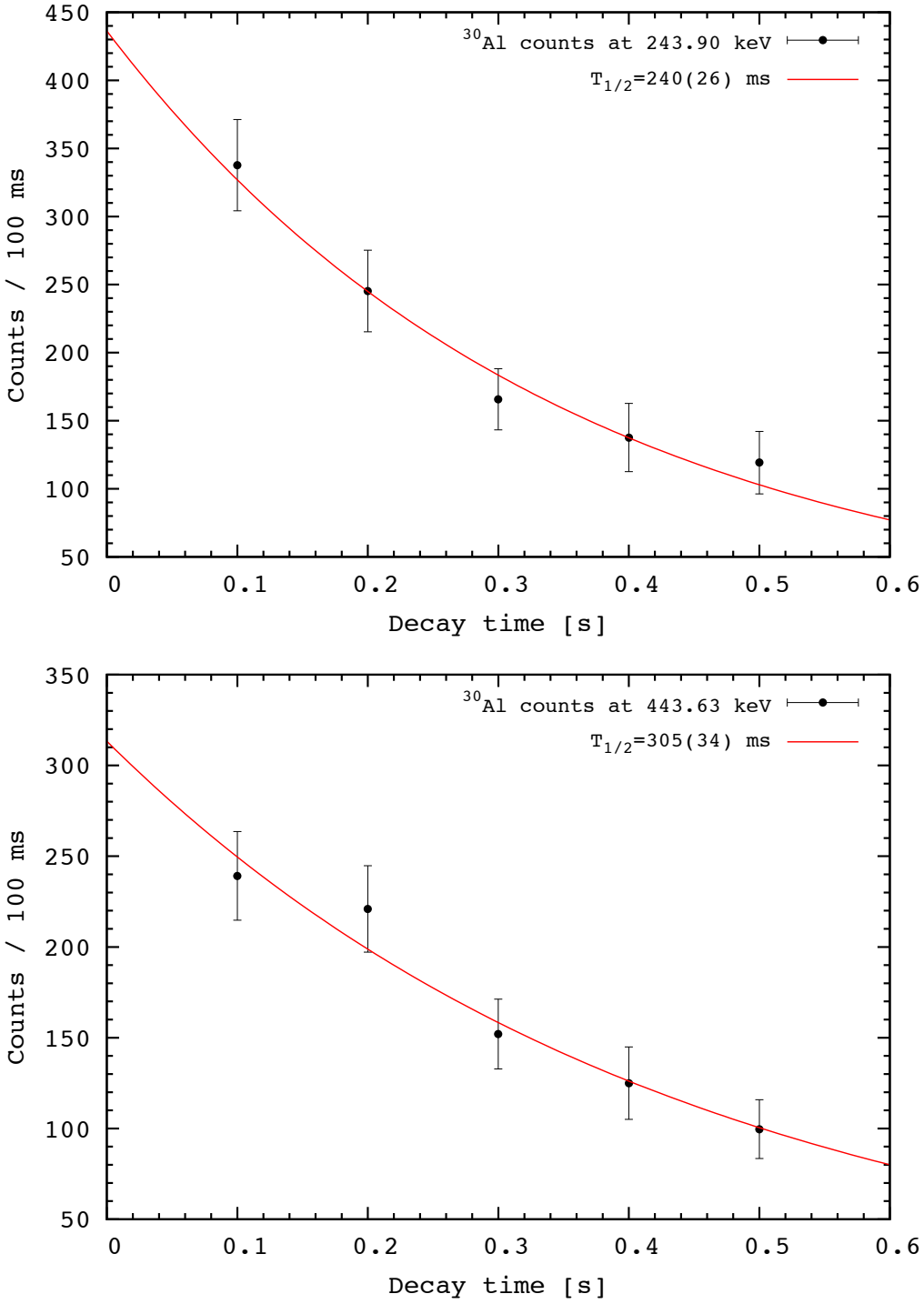

Figure 6.5: Top: Decay curve of the decay from ^{30}Mg into ^{30}Al for the 244 keV transition. The decay time was sliced into 100 ms time bins. Bottom: Decay curve of the decay from ^{30}Mg into ^{30}Al for the 444 keV transition. The decay time was sliced into 100 ms time bins.

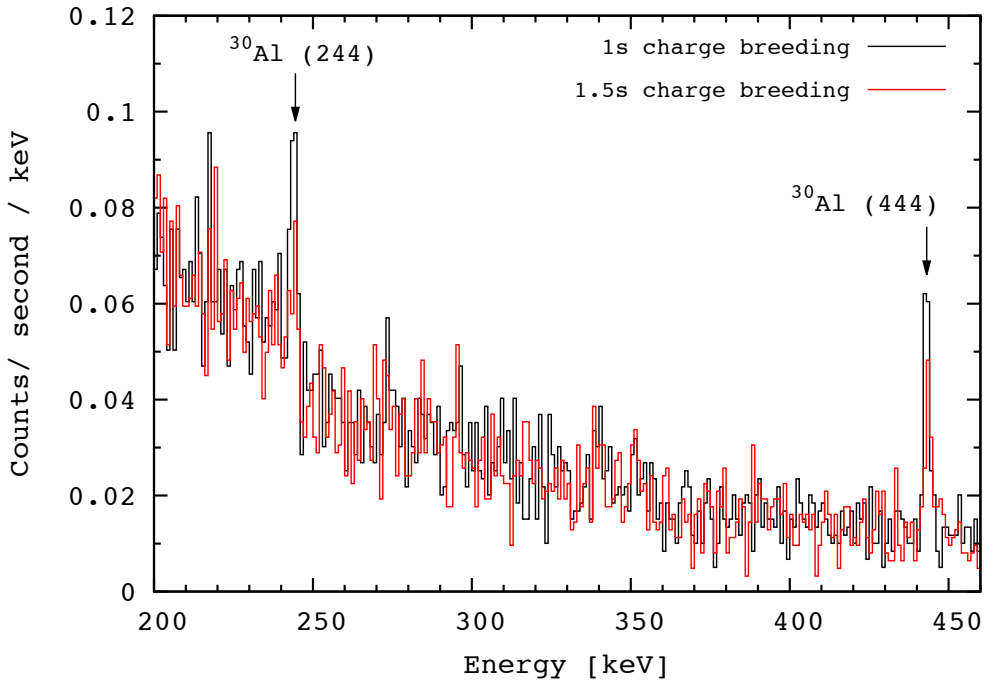

Figure 6.6: Comparison of in-trap decay spectra taken with 1 s and 1.5 s charge-breeding time at an electron-beam energy of 3.0 keV. The above shown spectra were normalized to the total run time.

for ^{30}Mg and $q = 10^+$ for ^{30}Al, while the electron-beam energy of 3.9 keV corresponds to $q = 10^+$ for ^{30}Mg and $q = 11^+$ for ^{30}Al at charge-breeding times of $\geq$1 s. Fig. 6.7 shows an overlay of the two spectra within an energy region from 200 keV to 460 keV normalized to the total run time. While the number of counts in the 444 keV peak coincides within the uncertainties for both spectra, it deviates significantly at 244 keV by $\sim$ 49%. Values are given in Tab. 6.3. The low statistics at higher energies do not allow for a comparison of the count rates at the energies of the ^{30}Si transitions. Further, the lack of transitions below 244 keV does not allow for studying whether the differences between the two spectra exhibit an energy dependence. However, one should note that the 244 keV transition does not only show a count-rate deviation at different electron-beam energies, but also features a lower half-life value (compare Sec. 6.1.3).

6.1.6 Background studies

To further investigate in-trap loss mechanisms, the empty-trap background spectra were compared to the full-trap decay spectra. Fig. 6.8 shows a direct comparison of the full-trap

Run	Peak energy [keV]	E-beam energy [keV]	Count rate [cts./s]
2011	243.90(8)	3.0	3.7 ± 0.7
2018	243.90(8)	3.9	7.2 ± 1.5
2011	443.63(4)	3.0	2.8 ± 0.5
2018	443.63(4)	3.9	3.1 ± 0.6

Table 6.3: Count-rate dependence on the electron-beam energy at a constant charge-breeding time of 1 s. Column 4 lists the count rate normalized to the total run time.

with the empty-trap spectra from run 2052 (1000 ms trapping time, 300 ms background) in three different energy regions. In the upper panel, one observes the ^{30}Al lines at 244 keV and 444 keV in the full-trap spectrum, which effectively disappear in the background spectrum. However, due to the short half-life of 335(17) ms the former observation cannot definitely prove an effective extraction, since most of the ^{30}Mg has already decayed when the 300 ms background measurement is started. The two bottom panels of Fig. 6.8 illustrate the energy regions around the 1263 keV and 2235 keV transitions, which are still visible in the background spectrum. Therefore, one has to look at the time structure of the longer lived ($T_{1/2}$=3.62(6) s) daughter nucleus ^{30}Al. The decay of ^{30}Al to excited states in ^{30}Si is followed by three main γ-lines of which those with an energy of 1263 keV and 2235 keV are presented in Fig. 6.8 and Fig. 6.9.

While Fig. 6.8 only compares the background to the full-trap spectrum, the full-trap spectrum is presented in 300 ms bins in Fig. 6.9. After the ion extraction from the EBIT one expects no events at the peak energy of 1263 keV or 2235 keV, however, the data exhibits a number of events above background even in the empty-trap spectrum, which was confirmed by studying the intensity distribution at the ^{30}Si peak at an energy of 2235 keV as a function of time as presented in Fig. 6.10. The highest count rate is detected after the extraction. This observation implies incomplete ion extraction, which is likely caused by the fact that the trapping did not occur in the central drift tube but closer to the electron gun. This significantly smaller region may suffer from spilled beam.

To investigate whether there was evidence for ^{30}Al and ^{30}Si lines in the background spectra of runs with different trapping cycles, those spectra were separated in background- and

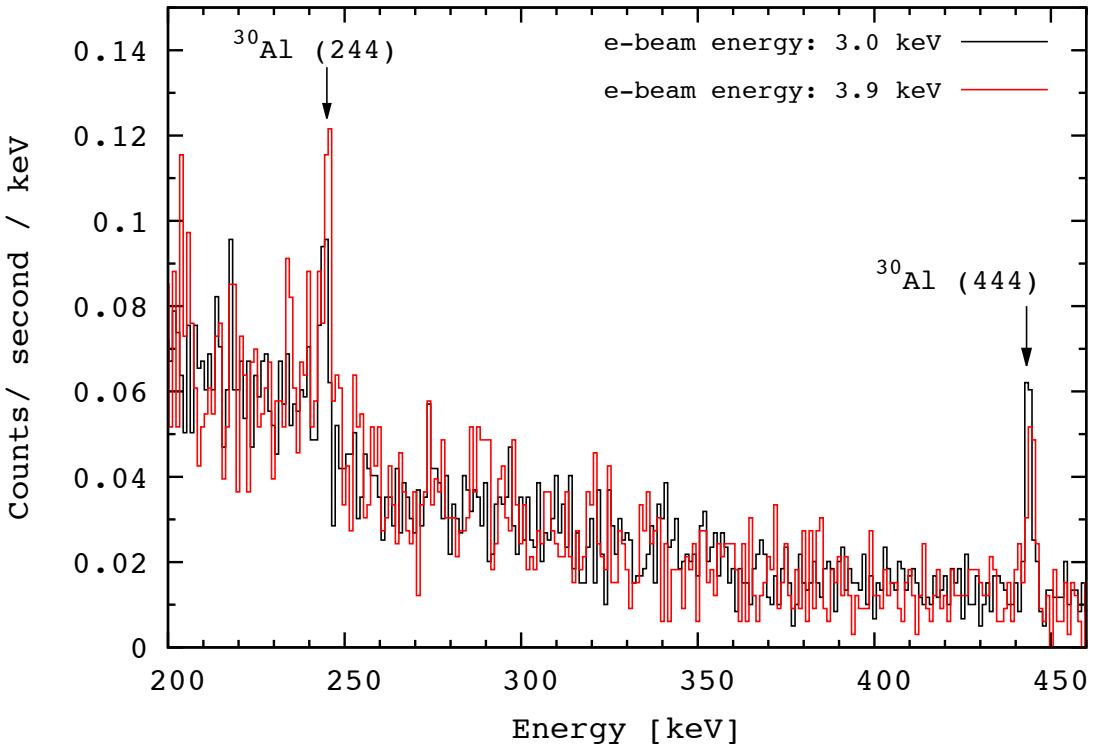

Figure 6.7: Comparison of in-trap decay spectra taken with 1 s charge-breeding time at two different electron-beam energies (3.0 keV and 3.9 keV). The above shown spectra were normalized to the total run time.

full-trap spectra and analyzed as well. The fit results for the runs 2052, 2053 and 2080 are shown in Tab. 6.4. The spectrum for run 2053, with 500 ms of trapping- and 300 ms of background time is shown in Fig. 6.11. Fig. 6.12 shows the intensity and energy-dependent count-rate distribution for run 2053. Again, the intensity within the 300 ms after extraction is relatively high, which indicates insufficient extraction as described above. The time-sliced spectrum for run 2080 with 1000 ms background measurement time and 300 ms trapping time is presented in Fig. 6.13. The ^{30}Al and ^{30}Si transitions are dominant in the background spectrum, indicating a problem on the extraction side and possibly spilled beam inside the trap.

During the online monitoring it was already observed, that the background spectra were not free of transitions originating from the ion species in the radioactive beam, as it was the case for the decay-spectroscopy experiments on ^{124}Cs and ^{116}In before. Therefore, runs

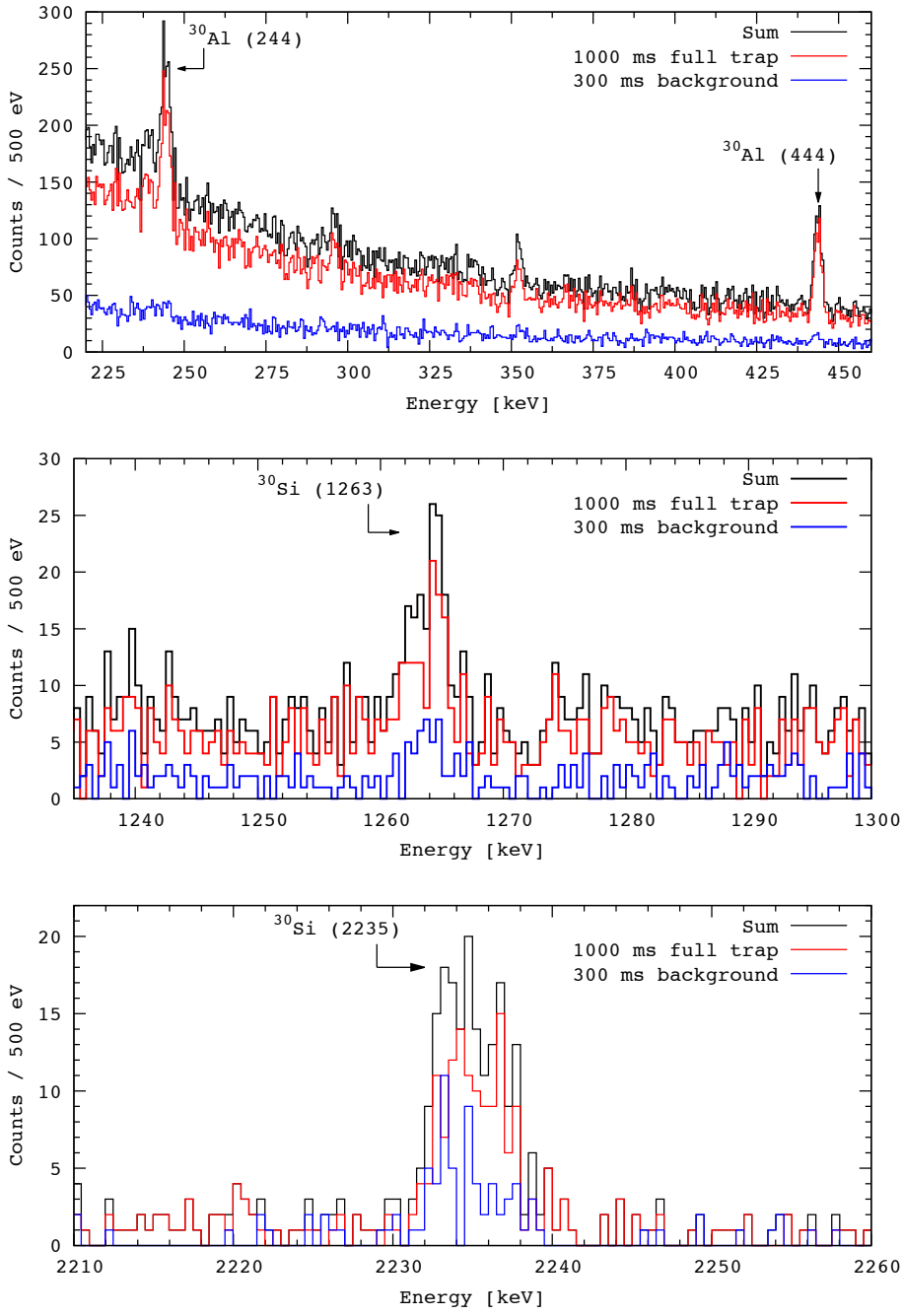

Figure 6.8: Comparison of the 1000 ms full-trap spectrum (red) with the background spectrum (blue) taken over 300 ms after extraction of the ions out of the EBIT. The two ^{30}Al lines at 244 keV and 444 keV as well as the 1263 keV and 2235 keV ^{30}Si transitions can be identified in the full-trap spectrum.

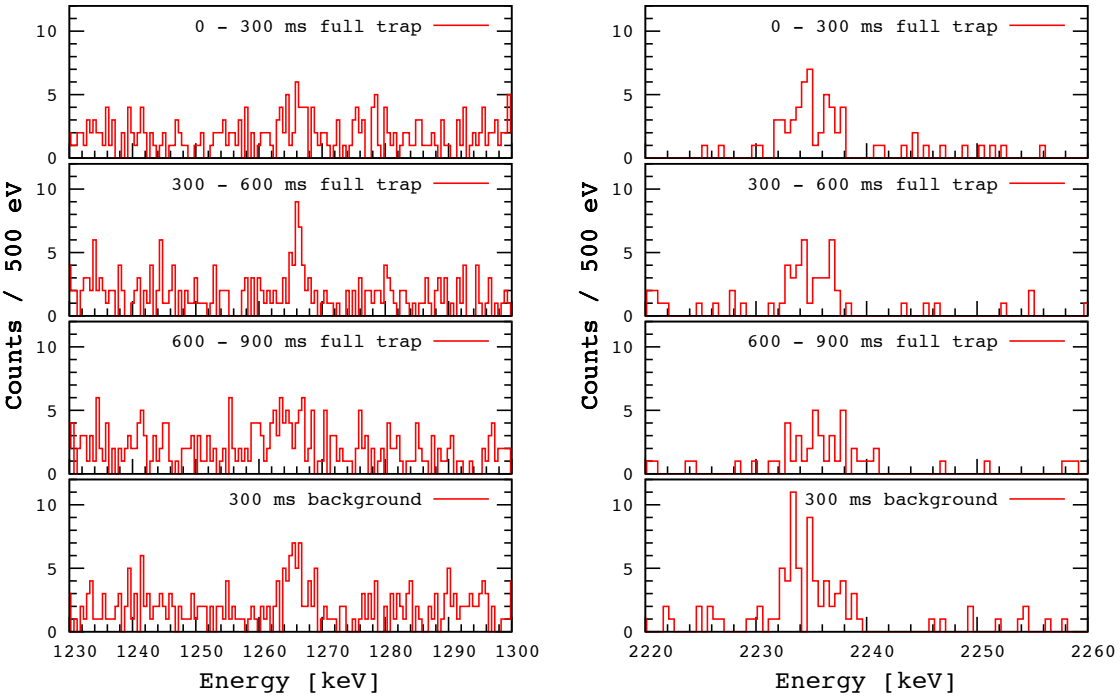

Figure 6.9: Left: Time-sliced spectra of run 2052 showing the 1263 keV γ-transition following the decay of ^{30}Al into ^{30}Si. Each panel corresponds to 300 ms of the cycle time. Right: Time slices illustrating the time structure of the 2235 keV line.

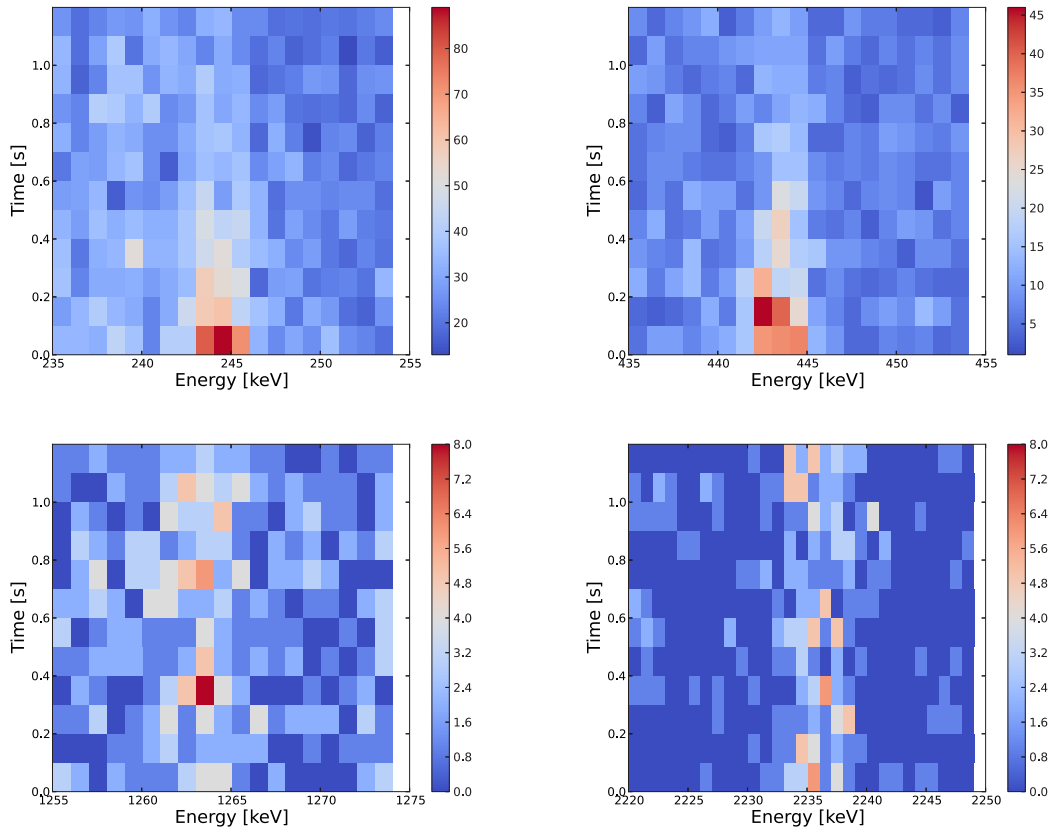

Figure 6.10: Time- and energy-dependent intensity distributions of the ^{30}Mg and ^{30}Al decays. The first 1000 ms contain data with ^{30}Mg beam inside of the EBIT, whereas the last 200 ms show data after ion extraction. Top: The transitions of excited states in ^{30}Al following the decay of ^{30}Mg $\longrightarrow$ ^{30}Al with $T_{1/2}$=335 ms are visible at 244 keV and 444 keV. Bottom: At 1263 keV and 2235 keV one observes the ^{30}Si transitions following the decay of ^{30}Al $\longrightarrow$ ^{30}Si with $T_{1/2}$=3.6 s.

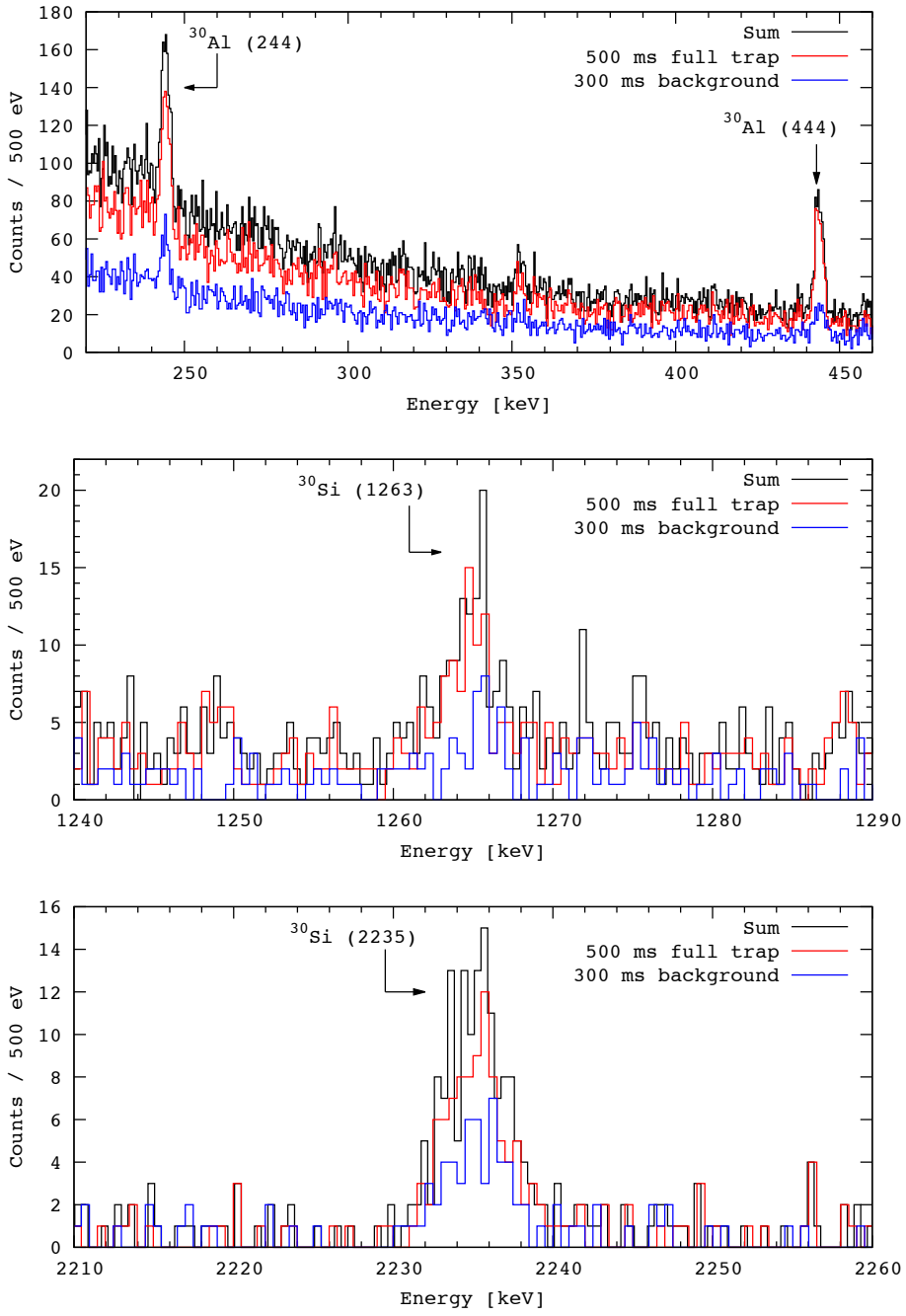

Figure 6.11: Comparison of the full-trap spectrum (500 ms) of run 2053 with the background (300 ms) for three different energy regions.

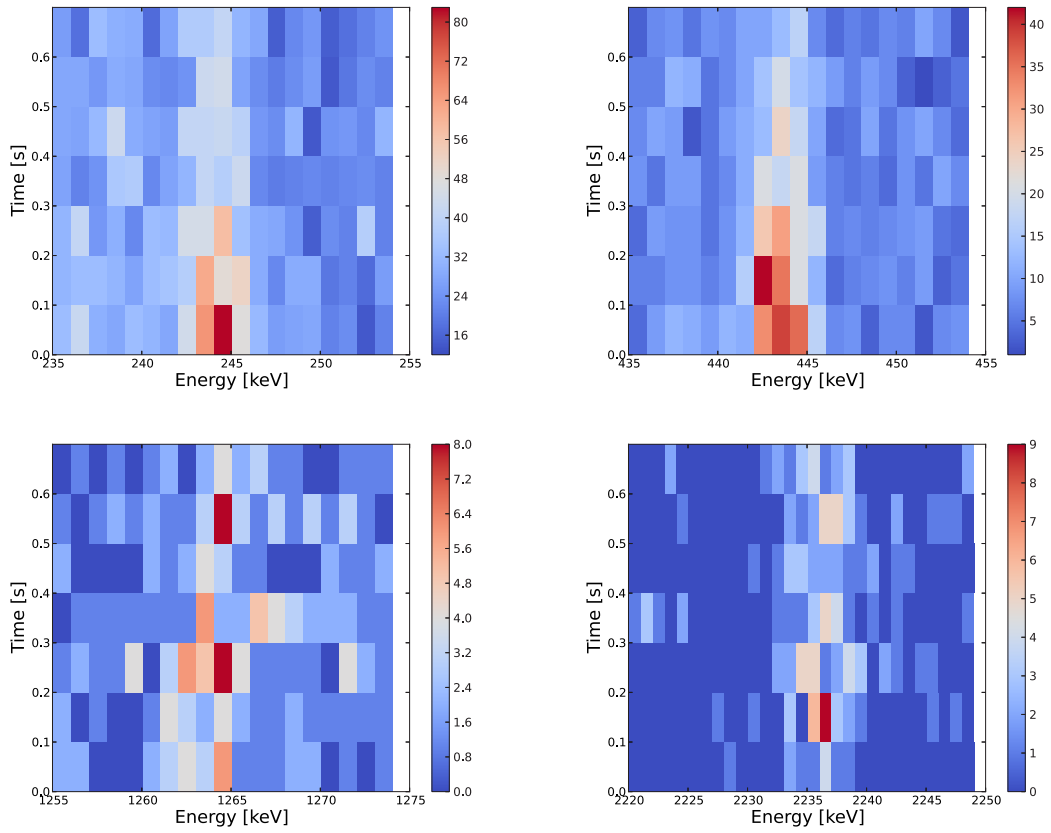

Figure 6.12: Time- and energy-dependent intensity distributions of the ^{30}Mg and ^{30}Al decays. The first 500 ms contain data with ^{30}Mg beam inside of the EBIT, whereas the last 200 ms show data after ion extraction. Top: The transitions of excited states in ^{30}Al following the decay of ^{30}Mg $\longrightarrow$ ^{30}Al with $T_{1/2}$=335 ms are visible at 244 keV and 444 keV. Bottom: At 1263 keV and 2235 keV one observes the ^{30}Si transitions following the decay of ^{30}Al $\longrightarrow$ ^{30}Si $T_{1/2}$=3.6 s.

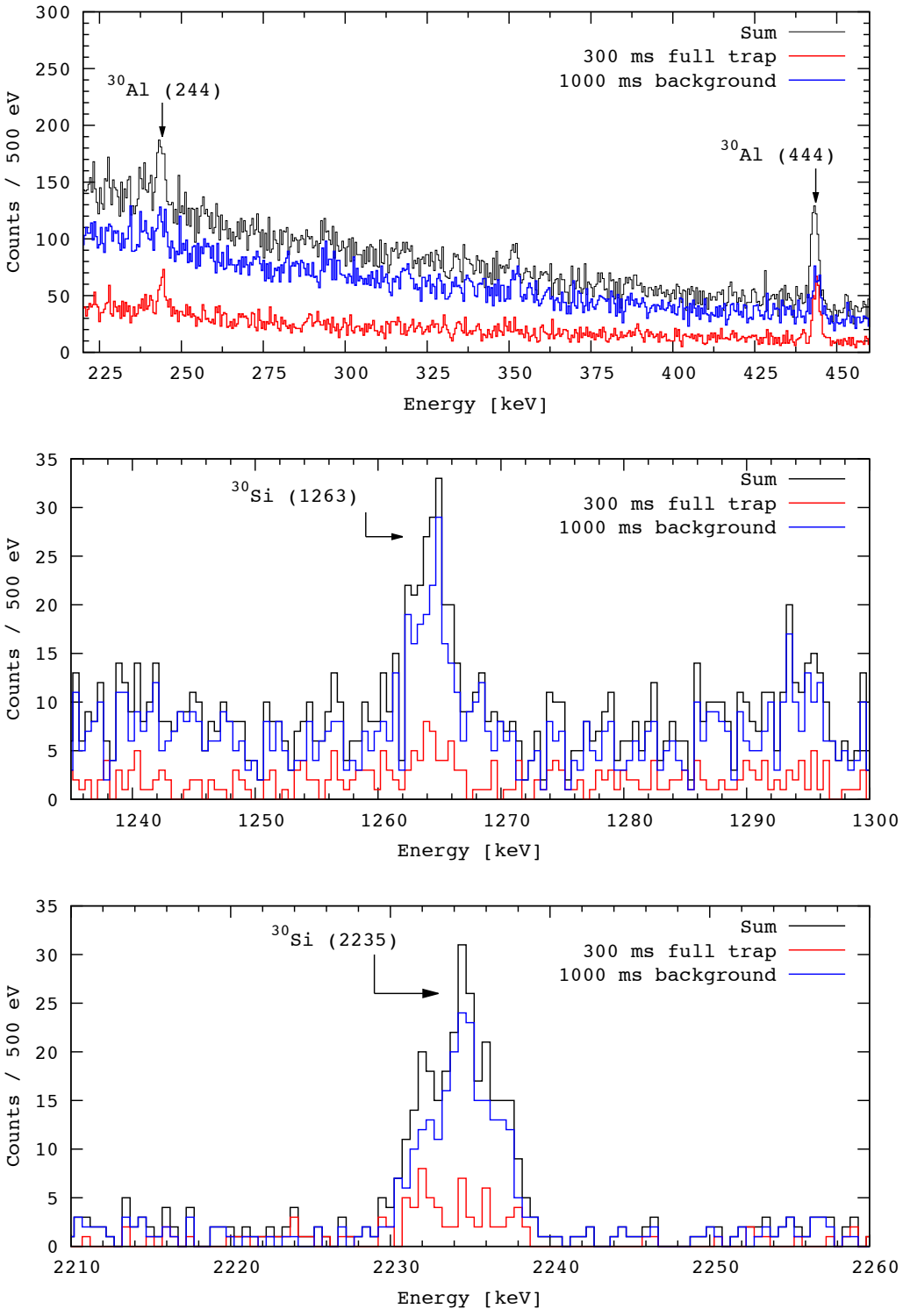

Figure 6.13: Comparison of the 300 ms full-trap spectrum of run 2080 with the 1000 ms background spectrum for three different energy regions.

Run	2052		2053		2080	
Energy [keV]	full [cts]	backg. [cts]	full [cts]	backg. [cts]	full [cts]	backg. [cts]
	$\times 10^3$		$\times 10^3$		$\times 10^3$	
243.90(8)	17.3 ± 1.4	1.5 ± 0.9	11.6 ± 1.0	4.1 ± 0.6	4.3 ± 0.7	3.7 ± 0.8
443.63(4)	11.2 ± 0.8	1.1 ± 0.3	9.1 ± 0.7	2.7 ± 0.4	6.6 ± 0.6	5.7 ± 0.8
1263.13(3)	1.9 ± 0.3	0.7 ± 0.2	1.4 ± 0.3	0.5 ± 0.1	0.7 ± 0.2	3.0 ± 0.5
2235.23(2)	2.5 ± 0.2	0.8 ± 0.1	2.0 ± 0.2	1.1 ± 0.1	1.0 ± 0.1	5.1 ± 0.3

Table 6.4: Overview of the fitted number of counts for the runs 2052, 2053 and 2080, which were taken with different EBIT cycles. Note that the energy binning was already accounted for in the number of counts shown in this table. The values in brackets represent the statistical uncertainty of the fit.

2071 and 2072 were taken with a trapping cycle of 900 ms full-trap (charge-breeding) and 8 s background measurement after ion extraction in order to study whether beam was spilled in the trap. The long background measurement was supposed to clarify whether one observed a time-dependent count-rate alteration at the energies of the ^{30}Al γ-transitions. However, the statistics taken during that run are not sufficient to allow for an extraction of the ^{30}Al half-life but only allow for a statement about which transitions are still visible in the background. The background spectrum is free of ^{30}Al transitions (see top panel in Fig. 6.14), which indicates that one does not observe any background from the beam blocked before the RFQ at those energies. The ^{30}Si γ-transitions, however, can still be observed at 2235 keV (Fig. 6.14) and 3498 keV, whereby the evidence for the latter is only given by a few counts above background. The fact that there are no counts above the background level at 1263 keV (Fig. 6.14) indicates that the main part of the still observed counts at 2235 keV and 3498 keV cannot result from decays occurring inside the trap. While the 2235 keV and 3498 keV γ-rays have a high enough energy to reach the HPGe from the RFQ, the γ-rays with an energy of 1263 keV or, respectively, 244 keV and 444 keV do not possess enough energy. A Geiger counter was also used to measure the radiation level at various points along the beamline during different EBIT injection and extraction schemes. This study revealed increased ion losses during the ion extraction compared to injection, which is consistent with the observations made during the background studies. Towards the end of the experiment, the extraction was optimized by tuning the Sikler lenses.

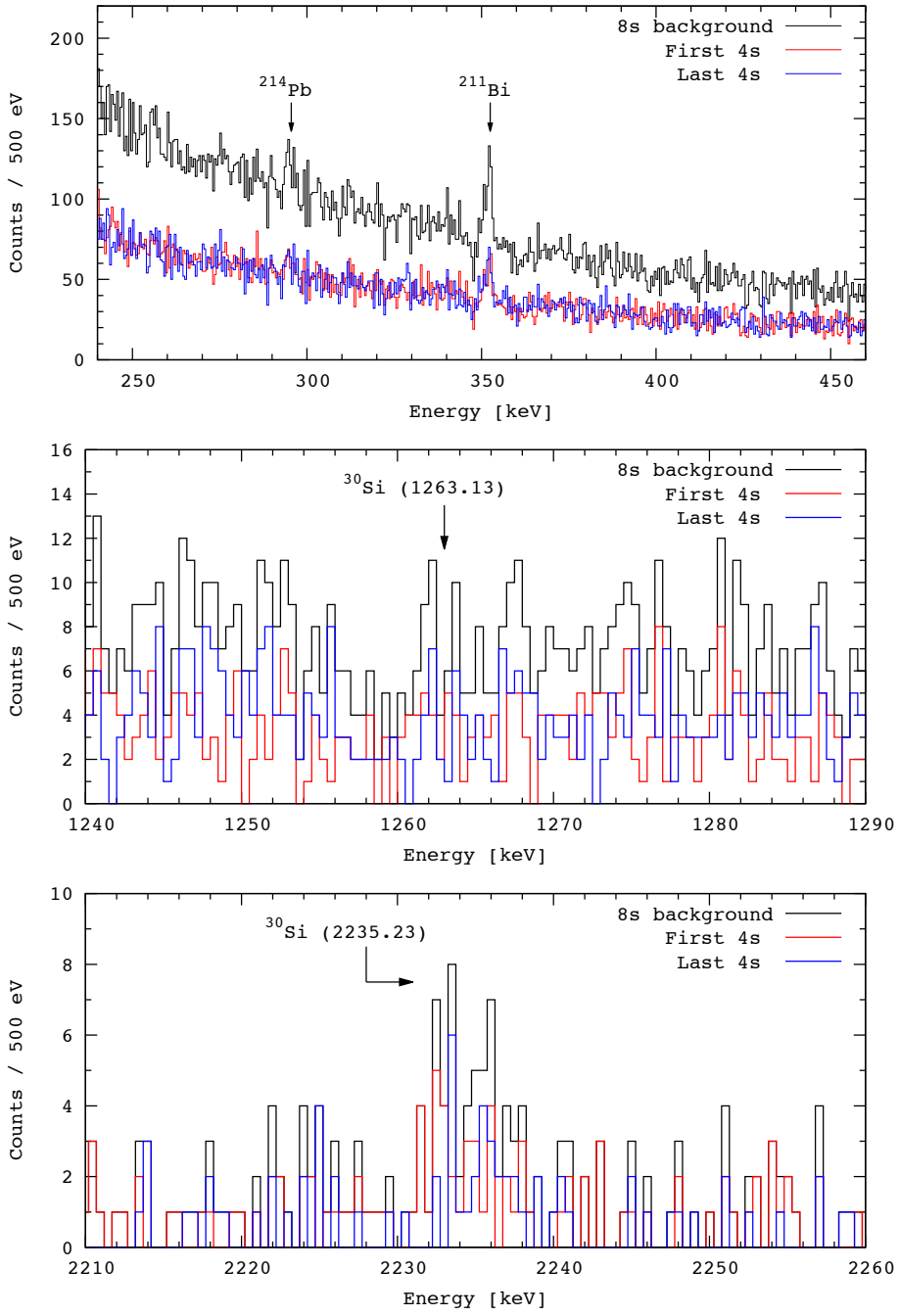

Figure 6.14: Background spectrum accumulated over 8 s of the EBIT cycle after a trapping time of 900 ms. The ^{30}Al lines at 244 keV and 444 keV are not visible in the spectrum anymore. The 1263 keV transition is absent, while the 2235 keV transition from the ^{30}Al decay is visible in the bottom spectrum.

6.1.7 Conclusion

The in-trap decay of ^{30}Mg was confirmed by the γ-spectra recorded with the HPGe detector. Further, three γ-transitions from the decay of excited states in ^{30}Si following the decay of ^{30}Al to ^{30}Si were identified. Blocking the radioactive beam on FC_0 showed a ^{30}Al free spectrum, which proves that the spectra taken with the HPGe are dominated by decays coming from locations inside the EBIT, or at least close to the trap. Active background shielding would allow for a better differentiation between events caused by high-energy γs from outside and inside the trap. Despite the fact that the collected statistics for this experiment are extremely low, it was possible to extract the half-life for ^{30}Mg by using the timing information. Summing up four individual runs and slicing the data into 100 ms time bins provided enough statistics to extract the count rates for the transitions at 244 keV and 444 keV. The extracted half-life value from the 444 keV transition is in agreement with the literature value.

The extraction efficiency during this experiment was not ideal or comparable to the close to 100% efficient extraction observed during the ^{124}Cs and ^{116}In ECBR experiments. The background spectra, measured right after ion extraction were not free of ^{30}Al or ^{30}Si transitions. This can be explained by the fact that the ions were not trapped in the central drift tube as it was the case for the ECBR experiments, but in the section closer to the electron gun. Further, it is possible that the beam was spread in the central drift tube right after ion extraction from the drift-tube section closer to the electron gun. While trapping closer to the gun was favorable for the ultimate goal to perform a mass measurement of the daughter nucleus, the conditions were not optimal to perform decay spectroscopy. Further tests with longer background spectra (8 s) revealed that the spectra were free of lines associated with the decay of ^{30}Mg, while they still exhibited lines following the decay of ^{30}Al to ^{30}Si. Since only those transitions with energies higher than $\sim$ 2 keV were visible in the spectra one can conclude that γ-rays from decays inside of the RFQ with high enough energies can contaminate the background spectrum of an unshielded detector.

In addition to the different trapping method compared to previous in-trap spectroscopy

experiments, the HPGe detector position was further away from the trap center than the Si(Li) detectors are during an experiment. The HPGe was not designed to be mounted on the EBIT and was not shielded by a CuPb shield or the EBIT itself. Therefore, it detected more ambient background radiation than the Si(Li)s would have. Due to the low efficiency at higher energies and the low statistics collected during this measurement, the Si(Li) detectors were not usable to detect the γ-lines discussed above.

6.2 Investigation of highly-charged ions and their decay properties

Demonstrating that the sensitivity of the in-trap spectroscopy setup is suitable for detecting atomic structure effects in highly-charged ions opens up the opportunity for studies of exotic decay modes [197]. These measurements require a low-background environment, the accessibility of rare isotope beams, and the possibility to modify the charge state of the ions. Of particular interest are electron-capture rates of highly-charged ions compared to the neutral atoms for studies of nuclear decay modes under stellar conditions. Under these extreme conditions, one expects significant changes in the decay rates compared to neutral atoms, which substantially influences the nucleosynthesis in stars [198, 199]. The nuclear orbital electron-capture process ($p + e_b^- \longrightarrow n + \nu_e$) is highly suppressed in the absence of orbital electrons, and the half-lives of nuclei which primarily decay via those processes are prolonged or even made stable for bare ions [199]. Thus, the decay rate of an excited nuclear state depends on the electron configuration of the inner atomic shells. Given that the de-excitation energy of an isomeric state is lower than the required energy for the excitation of a K-shell electron into the continuum, an excitation to higher-lying bound orbitals can occur [200]. Consequently, pure EC emitters would become stable after a complete removal of all electrons.

Re-creating stellar conditions in the laboratory to alter the electron density in an environment of extreme temperatures and pressure, however, is not yet possible to the required extent. A possibility to influence the electron density is given by storage rings (i.e., ESR

at GSI in Darmstadt [199, 201]) or by electron-beam ion traps, where the electrons are stripped until a H-like or He-like configuration is reached. Combining an EBIT with a photon-detection system thus offers the opportunity to measure the EC rates of highly-charged ions in the desired electron configuration.

A proposal for a proof-of-principle measurement at TITAN to study the changes in the EC rates of highly-charged ^{48}Cr and ^{64}Cu has recently been accepted [202], where the weak decay branches will be detected via photon counting with a combination of the presently used Si(Li) detectors and HPGe detectors. ^{48}Cr predominantly decays via EC (EC/$\beta^+ \geq 90\%$) [203] to the second excited state ($J^\pi = 1^+$) in ^{48}V, which decays further into the first excited state ($J^\pi = 2^+$) under the emission of a γ-ray with $E_\gamma = 112.3$ keV detectable with the photon counters. The EC decay (61.5%) of ^{64}Cu into the ^{64}Ni ground state will be determined via the corresponding K_α X-rays occurring at ~ 8 keV. The actual difference in the decay rate for different charge states can be measured by directly comparing the relative photo peak intensities.

As outlined in Sec. 2.2.2, charge breeding generally does not result in the production of a single charge state but in a charge-state distribution. Threshold charge breeding allows for predominantly populating the threshold charge state. Simulations of those charge-state distributions for the cases of interest are presented in Fig. 6.15 [202].
As the in-trap spectroscopy setup further allows for the measurement of half-lives, the measured half-lives can be compared to the expected value for highly-charged ions. From the classical assumption one would always expect a longer $T_{1/2}$ for orbital EC decay with $T_{1/2}$(H-like)=2·$T_{1/2}$(neutral) and $T_{1/2}$(He-like)=$\frac{9}{8}$·$T_{1/2}$(neutral) [197]. However, first experiments in storage rings performed on highly-charged ^{140}Pr^{58+} and ^{142}Pm observed a different behavior with $T_{1/2}$(H-like)=$\frac{9}{10}$·$T_{1/2}$(neutral). This observation can be explained by a spin-dependency of the EC rates on the hyperfine structure of the H-like ion, whereby the ratio for allowed EC-decay probabilities of H-like and He-like ions can be expressed in

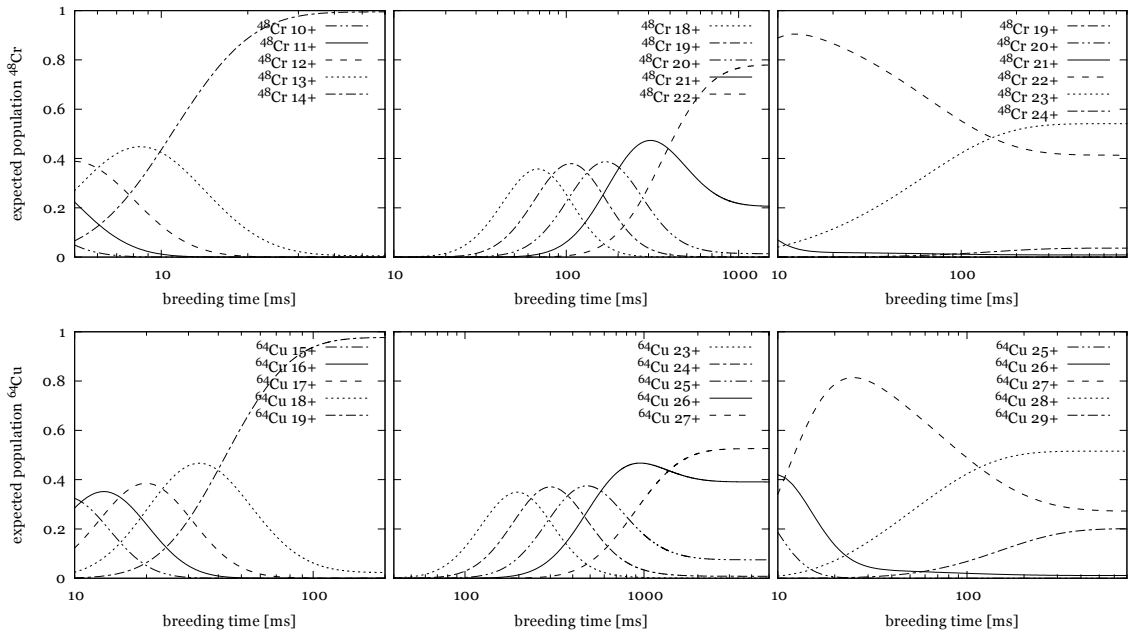

Figure 6.15: Simulations of the expected charge-state distributions for ^{48}Cr (top) and ^{64}Cu (bottom) as a function of the breeding time with optimized EBIT parameters for Ne-like (left), He-like (middle) and H-like (right) charge state configurations. Figure taken from Ref. [202].

the following way [197]:

$$\frac{P_{EC}^{H}}{P_{EC}^{He}} = \frac{2I_i + 1}{2I_i + 1}, \tag{6.1}$$

where F_i is the total angular momentum and I_i the nuclear spin of the initial state.

The proposal in Ref. [202] aims to confirm these effects, towards measuring more exotic highly-charged ions phenomena [197].

Chapter VII

CONCLUSIONS AND OUTLOOK

This thesis presents the development and commissioning of a novel low-background in-trap decay spectroscopy setup developed for the observation of the weak electron-capture branching ratios of the intermediate nuclei in double-beta decay. Experimental data on ECBRs are crucial for benchmarking theoretical models, however, a measurement of the weak EC signature is especially challenging due to its suppression by several orders of magnitude relative to their β^- counterpart. The TITAN-EC setup provides background reduction from any β-decay induced charged particles inside the trap as they are guided out of the trap on axis while only decay photons reach the Si(Li) detectors. Another important advantage of this setup is the backing-free storage of the ions in the trap, thereby avoiding possible contamination from a target-backing material.

Two commissioning experiments on the nuclei ^{124}Cs and ^{116}In demonstrated the performance and advantages of an EBIT for efficient ion storage in combination with a detection system as a tool for in-trap X-ray and γ-spectroscopy. The effective background reduction in the trap environment via spatial separation between decay photons and decay positrons was proved experimentally. β-decay induced particles were successfully guided out of the trap by the strong magnetic fringe field of the EBIT, while passive shieldings of the photon detectors reduced the ambient background. By making use of the space charge of the electron beam and the resulting improved confinement for highly-charged ions as well as the deeper trapping potential, the trapping efficiency was significantly enhanced compared to previous work, where the EBIT was operated without utilizing the electron beam. The agreement of the extracted half-lives with the literature values demonstrated the efficient ion storage for timescales on the order of minutes. Additionally, the timing information recorded for each event can be used to identify radioactive isobars in the trap resulting

from beam impurities.

With the improved ion-storage efficiency, the space-charge limit of the RFQ becomes the limiting factor for the number of ions in the EBIT. In order to overcome that space-charge limit, the EBIT operation was optimized by modifying the cycle by an extended injection part, where multiple-ion bunches from the RFQ were injected into the trap. Injection schemes with up to 2000 injections were successfully tested, thereby opening up the opportunity to perform measurements even on isotopes with low ISAC yields. As a consequence of charge breeding, the atomic structure of the ions was altered and resulted in a change of the electron-binding energies and thus, a shift of the detected X-ray energies relative to the energies of a neutral atom. In addition, a deviation of the X-ray intensity ratios from the expected value was found. However, the half-lives and EC branching ratios for the charge states presented in this thesis were found to be consistent with literature.

In the near future, the TITAN-EC program will attempt to measure the ECBR of ^{110}Ag, which is the intermediate nucleus in the $\beta\beta$ decay of ^{110}Pd. The 1^+ ground state has a half-life of $T_{1/2}$=24.56(11) s [169], which is favorable for storage and half-life measurements in the EBIT as it has been demonstrated on ^{124}Cs. Further, ^{110}Ag features an isomeric 6^+ state at 117.6 keV, however, with a long half-life of $T_{1/2}$=249.7 d. It mainly decays via β^- emission (98.6%) but features a 1.36% IT-branch producing ^{110}Ag X-rays. A de-excitation of the isomeric state through EC is not possible. The ground-state EC branching ratio has been measured in 1965 through production of ^{110}Ag by neutron activation [204]. The presently assumed EC branching ratio of $\epsilon = 0.3\%$ translates into a $\log(ft) = 5.1$. The β^- decay populates the ground state of ^{110}Cd with a 94.9% branch and the first excited 2^+ state at 657.8 keV at a level of 4.4%. The 6^+ isomer populates high-lying states in ^{110}Cd. However, because of the long half-life, it presents no concern to the experiment. Furthermore, the production of ^{110}Ag in its isomeric state at ISAC is likely suppressible with the new ion guide laser ion source (IG-LIS). The selective ionization of the 1^+ ground state will be an ideal test for the performance of the source and would provide clean beams

for the experiment.

In order to realize a ^{110}Ag ECBR measurement, the multiple ion-bunch injection technique has to be applied to collect enough statistics within the limited time of an experiment. Figure 7.1 (top) shows an overlay of three ^{110}Ag decay spectra within 15 to 45 keV simulated with different injection schemes to demonstrate the increase in count rate for a 10 shots injection scheme relative to the default 1 shot filling scheme. The ^{110}Pd X-rays are presented relative to ^{124}Xe X-rays simulated according to the experimental data recorded in 2012. The ECBR normalization can be achieved via the 657.5 keV γ-line, either directly or/and via the associated Compton edge as presented in Fig. 7.1 (bottom) in combination with the Monte-Carlo simulations. In case a ^{110}Ag yield of at least 10^6 pps for the ground state can be delivered without any significant ^{110}In contamination by the ISAC facility to the TITAN-RFQ, a ^{110}Ag ECBR measurement is possible with the current TITAN-EC setup within 6-8 12 hr shifts.

Given a successful ECBR measurement of ^{110}Ag for which 5 shifts are scheduled for the end of 2015, an ECBR measurement of ^{100}Tc, which is the intermediate nucleus in the double-beta decay of ^{100}Mo will be attempted. This case is not only of interest for double-beta decay, where the nuclear matrix element for ^{100}Mo is the largest for all $\beta\beta$ candidates, but also for measuring the solar neutrino flux through the charged-current reaction and the supernova ν flux, where the EC matrix element is crucial to determine absolute fluxes. With a ground-state half-life of $T_{1/2}$=15.8 s the EC decay of ^{100}Tc will only populate the ^{100}Mo ground state as there are no excited states below 168 keV in ^{100}Mo. The β^--decay branch of ^{100}Tc into the ^{100}Ru ground state has an intensity 93% with a log(ft) of 4.60. The authors of Ref. [205] measured an EC ratio of $\epsilon = (1.8 \pm 0.9) \cdot 10^{-3}$%, which corresponds to a log(ft) of $4.44^{+0.30}_{-0.18}$ and a $B(GT)$ of 0.42 ± 0.21 [205]. That $B(GT)$-value is consistent with the value of $B(GT) = 0.31 \pm 0.01$ extracted from a recent (^{3}He, t) charge-exchange reaction experiment [70]. However, those values are in conflict with a measurement performed by the authors of Ref. [206], where the extracted ECBR of $(2.6 \pm 0.4) \cdot 10^{-5}$ corresponds to a ground-state $B(GT)$ of 0.60 ± 0.09. Therefore, a re-measurement with the TITAN-EC

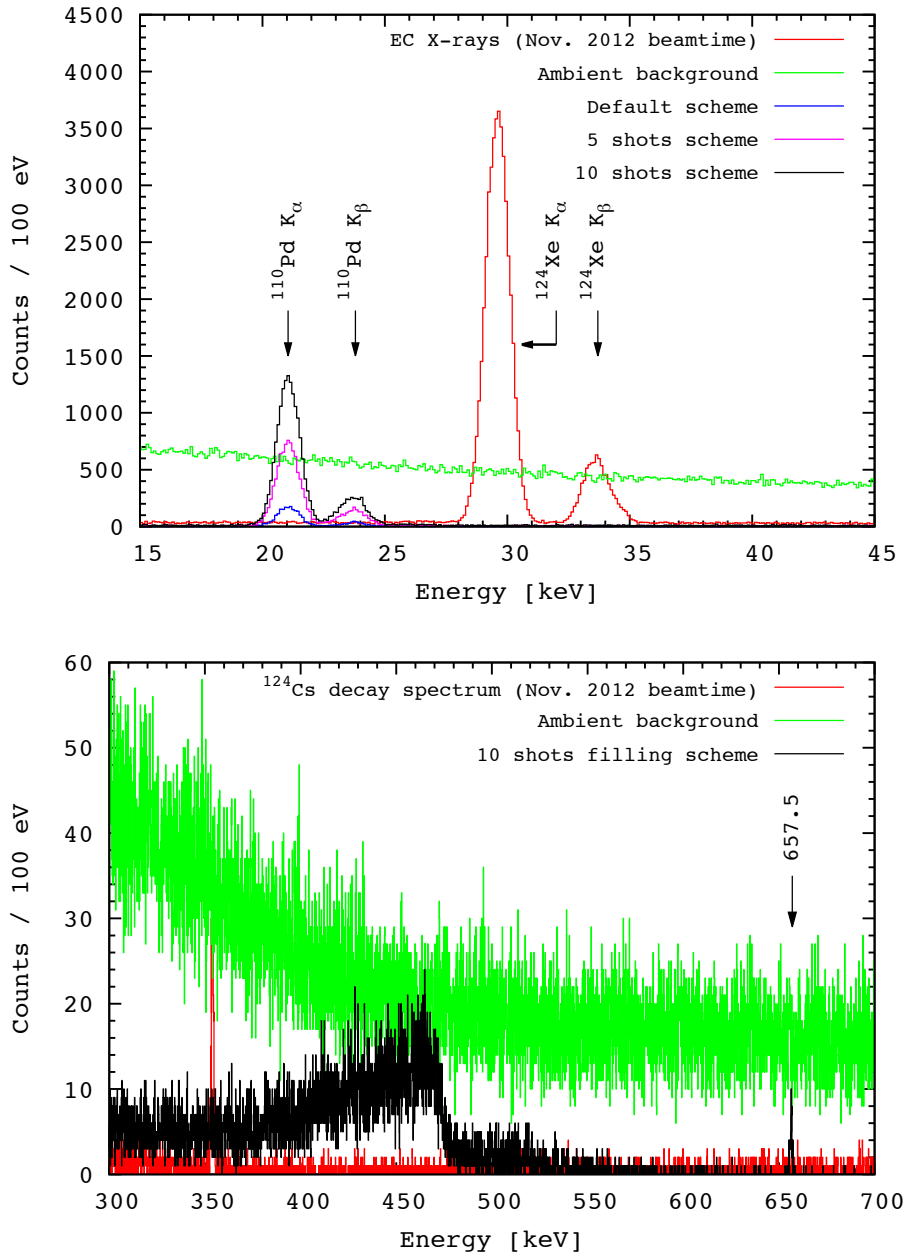

Figure 7.1: Top: Displayed are three simulated ^{110}Ag decay spectra for different injection schemes in relation to a ^{124}Cs ground-state decay spectrum simulated according to the A=124 experiment. For a realistic prediction of the detectable ^{110}Pd X-rays, the spectra represent the number of counts detected with 3 Si(Li) detectors over $\sim$ 180000 s at a ^{110}Ag ground-state yield of 10^6 pps. Dark blue: EBIT is filled with one shot only (20 s measurement, 5 s background cycle). Magenta: EBIT is filled with 5 shots from the RFQ before the measurement is started. Black: EBIT is filled with 10 shots from the RFQ. Green: time-scaled ambient background, measured with a shielded Si(Li) detector on trap. Red: ^{124}Cs decay spectrum with 20 s measurement time, 5 s background cycle. Note, that the individual spectra have to be added on top of the background. Bottom: Compton edge associated with the 657.5 keV γ-line, which can be used for normalization.

system would be conducive to solve that discrepancy.

Future work to extend the scientific reach of the device will include observing photons at energies above $\sim$ 100 keV. The de-commissioning of the 8π γ-ray spectrometer [207] at TRIUMF has allowed for up to seven HPGe detectors to be available for use in the open ports of the decay-spectroscopy setup implemented around the EBIT. Due to the latest modification of the detector support structure, and the compatible size of the HPGe detectors, it is possible to integrate them into the system without major modifications. Each detector features a cylindrical HPGe crystal with a 2.65 cm radius and a thickness of 6.0 cm located in a heat- and vacuum-shielded LN_2 cryostat similar to the Si(Li) detectors. The possibility to use HPGe detectors will increase the experimental capabilities and versatility of the spectroscopy apparatus.

Further prospects are possible due to the fact that the in-trap spectroscopy setup is integrated into a multi-trap system, thus allowing for further beam purification prior to ion storage inside the EBIT. In order to deliver isobarically clean singly-charged ion beams to the EBIT, a multi-reflection time-of-flight (MR-TOF) spectrometer [195] is presently integrated into the TITAN system and will be installed downstream of the RFQ to further increase the sensitivity for weak ECBR measurements.

As outlined in Ch. 6, the application of the TITAN-EC system is not limited to ECBR measurements in context of double-beta decay, but has already been employed as a diagnostics system during "in-trap feeding" prior to a mass measurement with TITAN, thereby extending the range of isotopes accessible for high-precision mass measurements. Even though the observed atomic structure effects induced by charge breeding were merely a byproduct of the improved ion storage, these effects open up the opportunity for a large range of studies of the nuclear decay properties of highly-charged ions in the future. Due to the capability to perform decay spectroscopy on highly-charged ions in a low-background environment the system has the potential to provide input to nuclear astrophysics.

The novel in-trap spectroscopy facility at TITAN presented in this work represents a unique device that will bring high-sensitivity decay spectroscopy into a new era worldwide.

Appendix A

DRAWINGS - BERYLLIUM WINDOWS

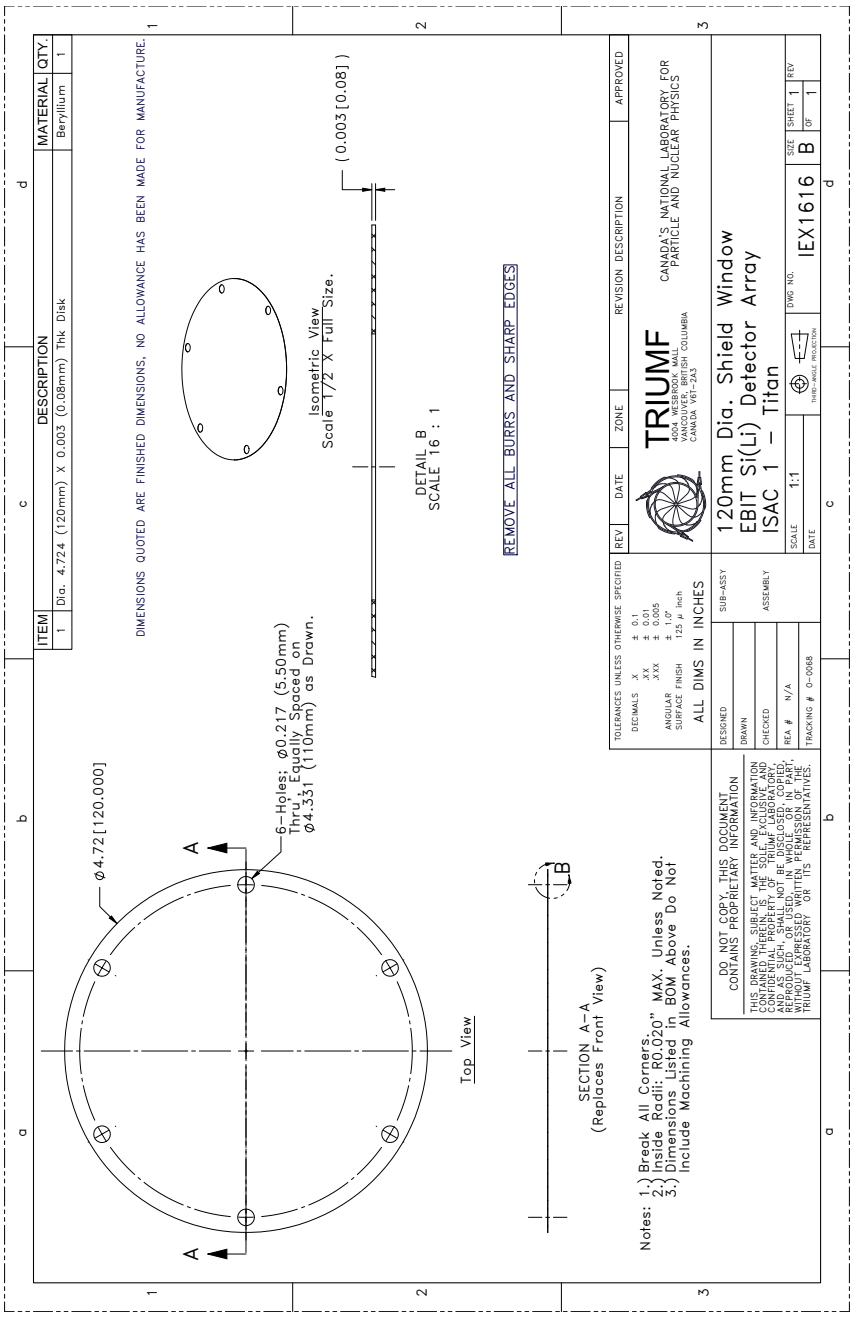

Figure A.1: Technical drawing of the 120 mm diameter heat shield window [172].

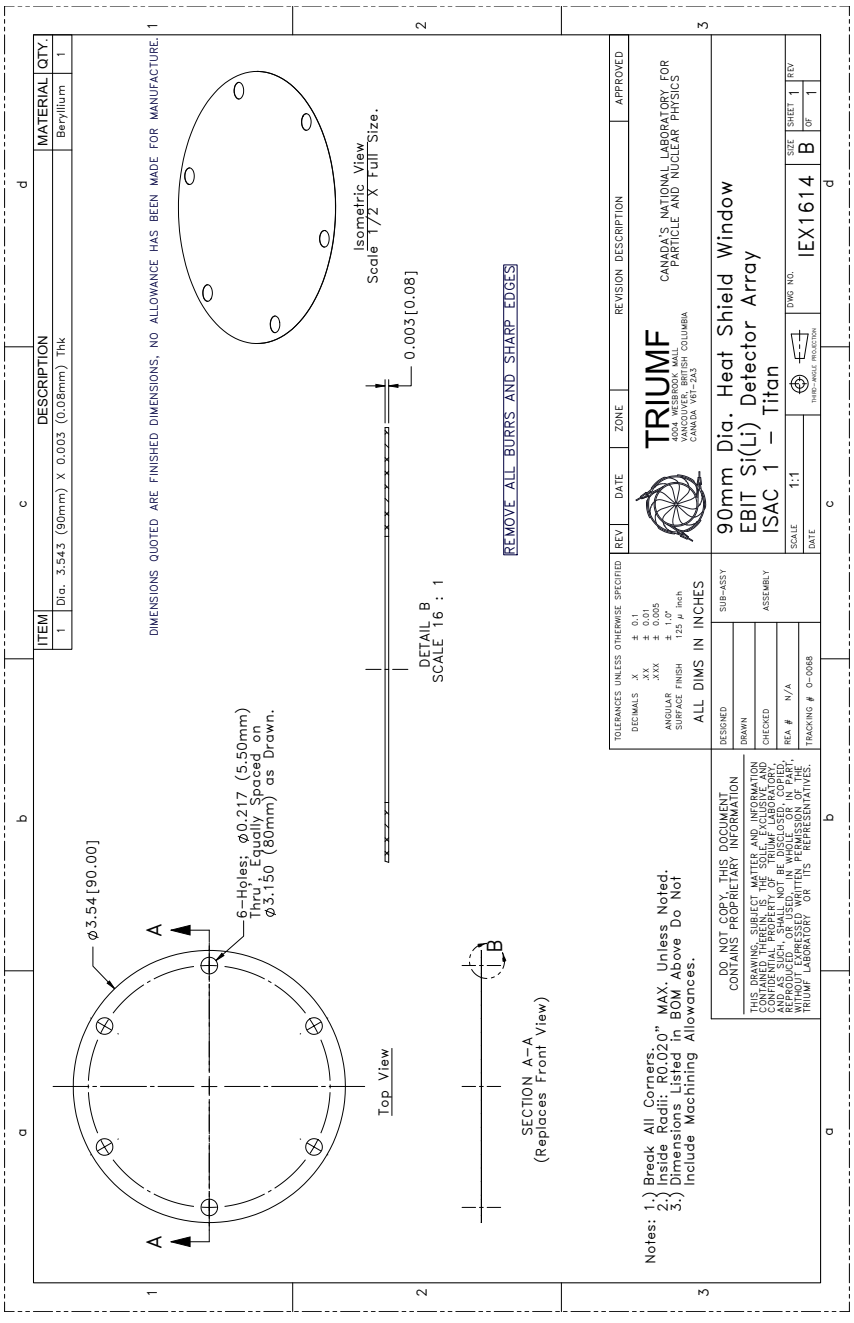

Figure A.2: Technical drawing of the 90 mm diameter heat shield window [172].

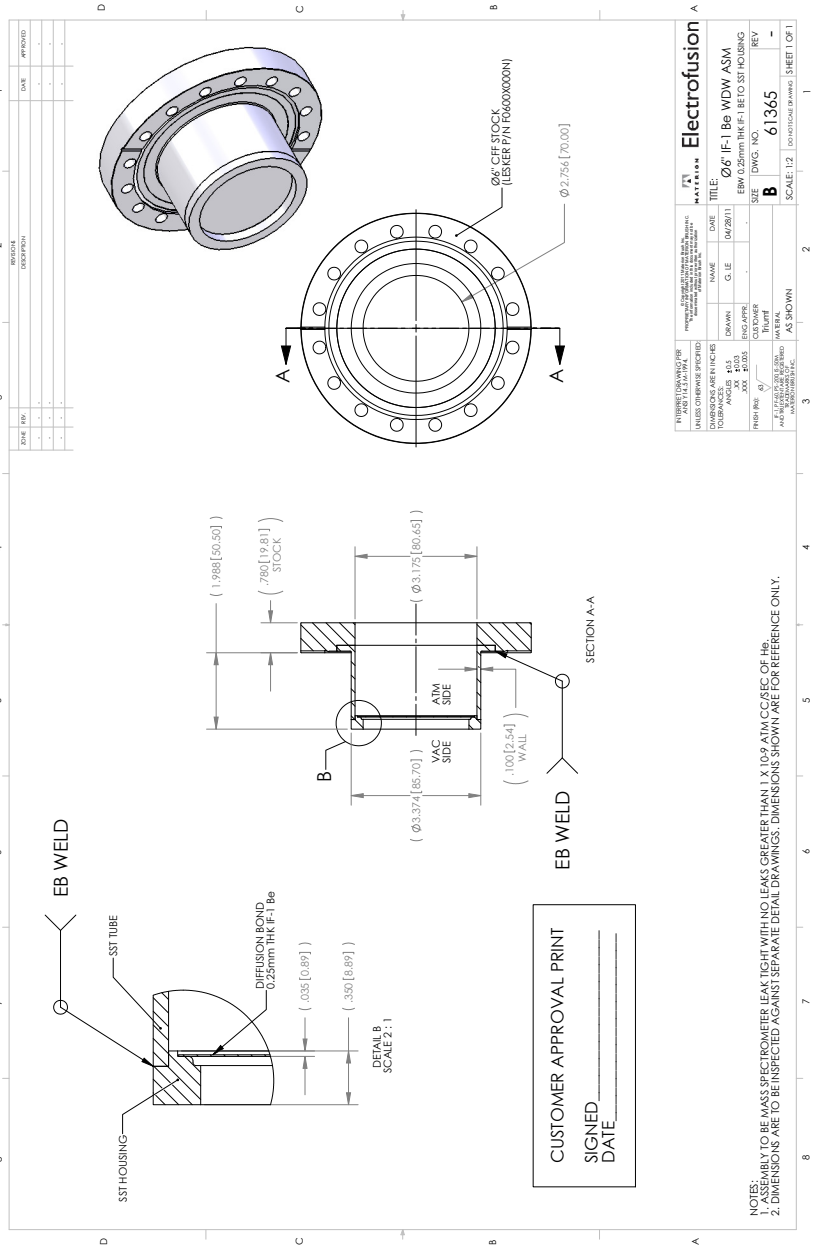

Figure A.3: Technical drawing of the 6″ diameter Be-window assembly [172].

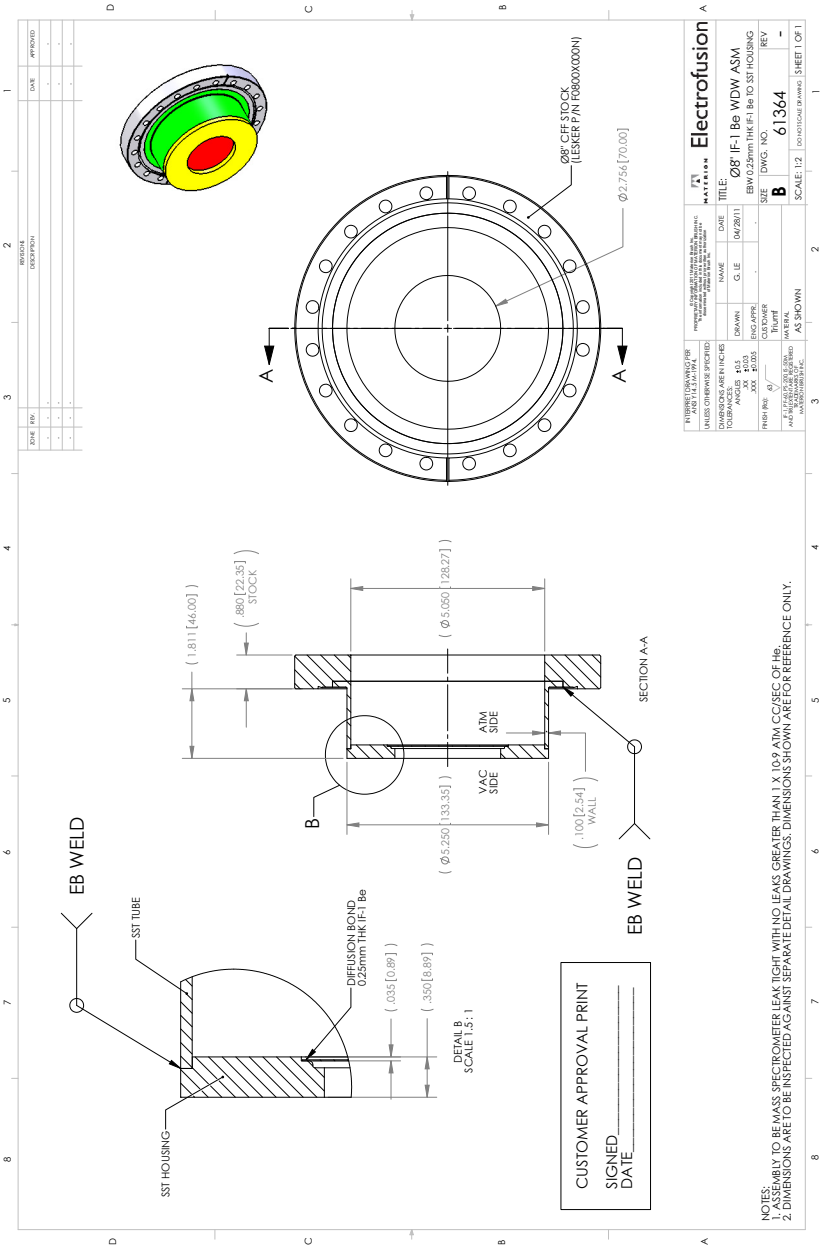

Figure A.4: Technical drawing of the 8″ diameter Be-window assembly [172].

Appendix B

DRAWINGS - DAMPING MATERIAL SHEETS

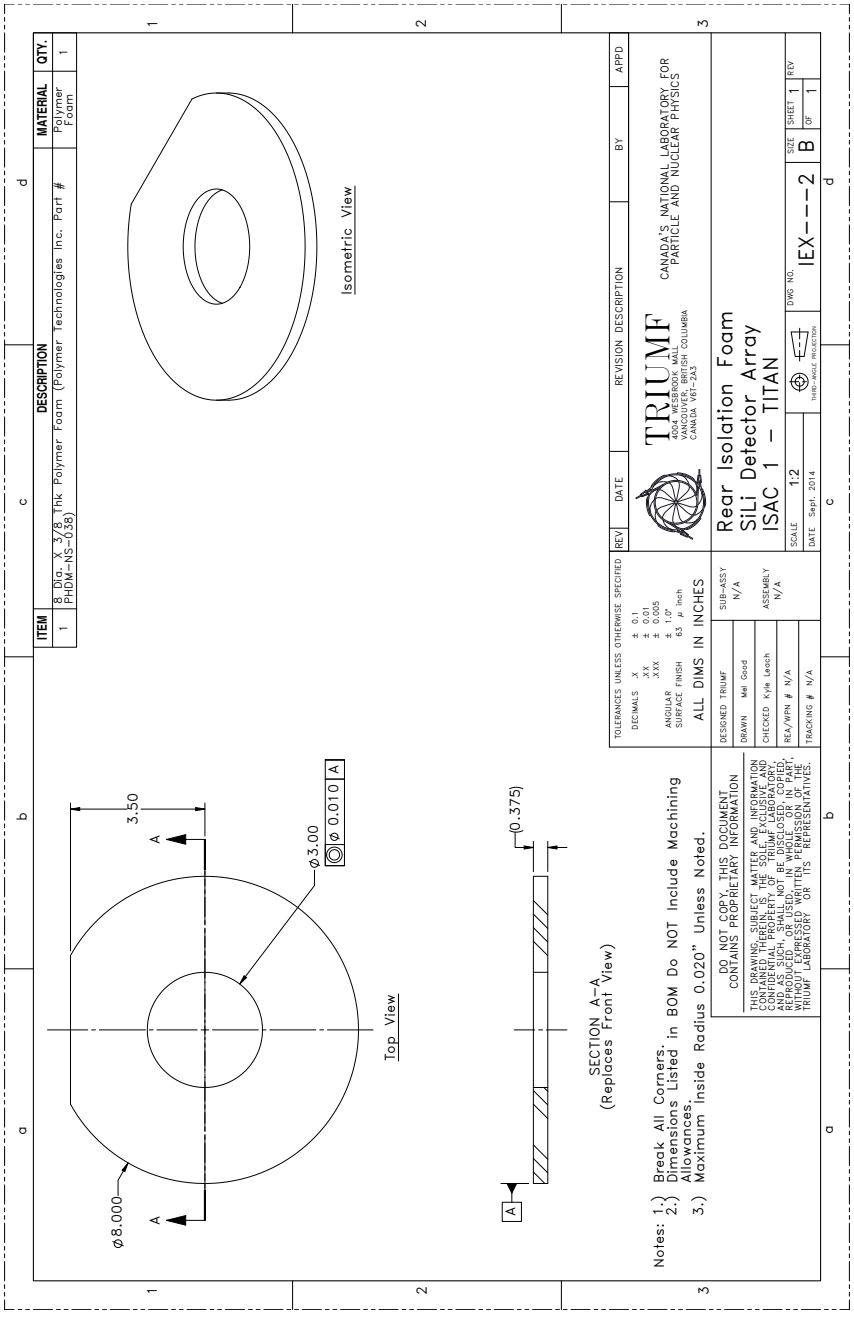

Figure B.1: Technical drawing of the rear isolation foam parts [172].

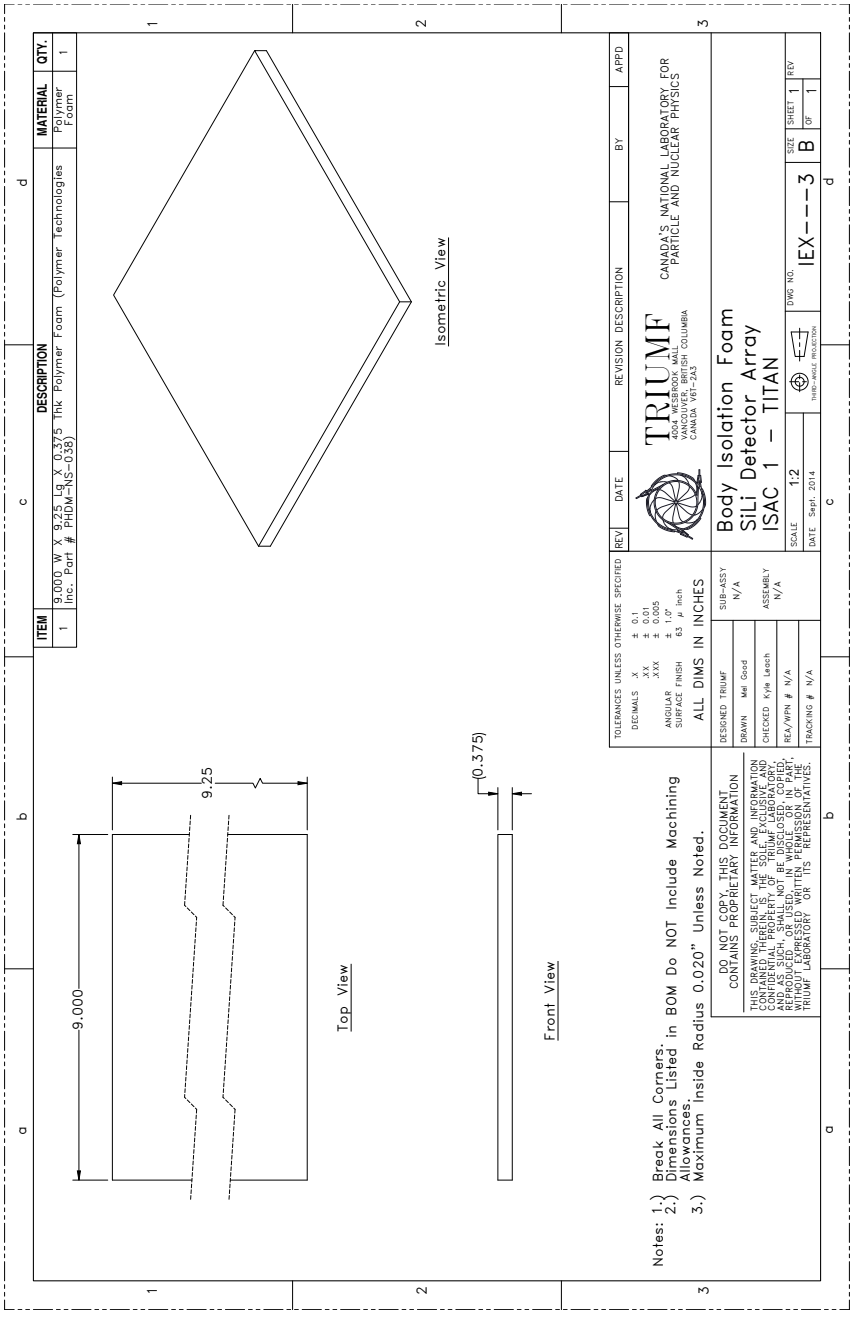

Figure B.2: Technical drawing of the body isolation foam parts [172].

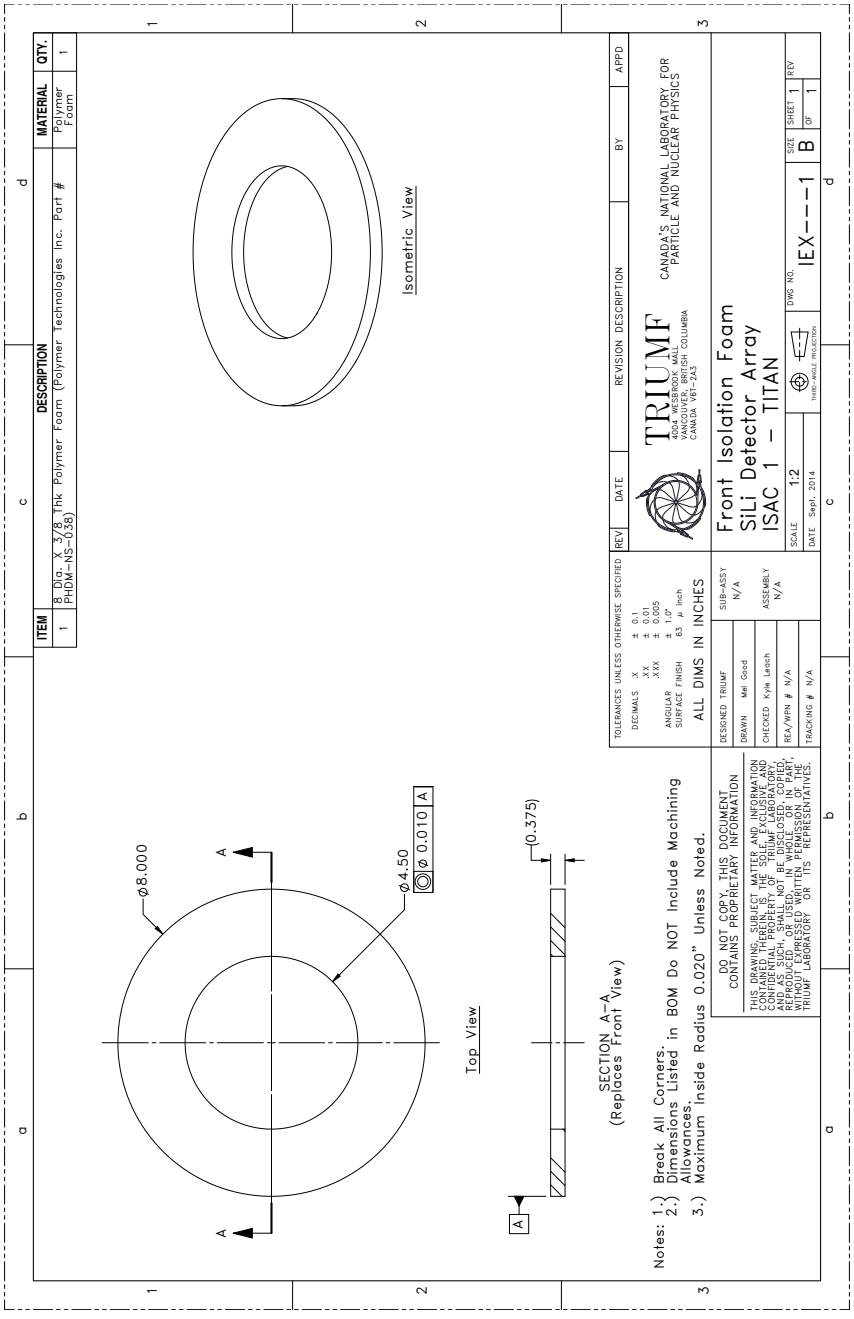

Figure B.3: Technical drawing of the front isolation foam parts [172].

Appendix C

RECORD OF THE DETECTOR STATUS: MODIFICATIONS AND CURRENT OPERATION

The present performance status of the seven planar Si(Li) detectors on- and off-trap as well as with and without vibration damping are presented to define the current (status April 2015) operational status of the Si(Li) array.

All detectors suffer from some form of vibration sensitivity, which in some cases makes them unusable when operated in the EBIT environment. The differences between the sensitivity levels may be due to different crystal qualities and differences in the electronics, i.e., FETs, high-voltage filters or reset triggering LEDs. Further, soldering, connections, electrical isolation, cabling and grounding turned out to be insufficient. Therefore, electrical modifications including grounding optimization and also more severe changes concerning the high-voltage filter were performed for some of the detectors.

To study the detector performance in the trap environment (on-trap), each Si(Li) detector was mounted on the horizontal access port at 90° without any CuPb shielding. A collimated ^{133}Ba source was placed on the opposite port (270°) of the EBIT and decay spectra were recorded with and without vibration-damping material (PHU-40 and PHDM-NS) around the cryostat (compare Sec. 3.6). Those spectra were compared to a reference measurement performed outside of the trap environment on the TITAN platform (off-trap) while the detectors were resting on two layers of foam for vibration isolation. The source-to-crystal distance was $\sim$ 26 cm. The usability of each detector for an online experiment was evaluated based on the achieved energy resolution at 53 keV (γ-transition in the ^{133}Ba spectrum). All detectors with an energy resolution of 2.3(1)% or better (corresponds to a FWHM of

about 1 keV) were considered usable for data taking. Details on the detector history and modifications as well as the results of the performance tests for each individual detector are described below.

C.1 Si(Li) #427 - Status: usable (with damping)

C.1.1 History

Si(Li) #427 is one of the three detectors that were sent to Vancouver in October 2011 and despite its vibration sensitivity, it was usable with a decent on-trap resolution of about 2.0(1)% while mounted on the 180° port underneath the EBIT for the ^{124}Cs experiment in November 2012. Shortly before the ^{116}In experiment in November 2013, Si(Li) #427 became unusable on-trap and also off-trap the resolution decreased significantly. The X-ray spectrum recorded during the ^{116}In experiment (compare Sec. 4.2) featured a broad bump and the K_α and K_β X-rays (about 3 keV apart) were not resolved anymore. The origin of this performance deterioration is still unknown, however degrading components or broken/lose connections after prolonged exposure to vibrations are possible explanations.

C.1.2 Previous operation

Before any modifications were performed on this detector, the structure of the reset signal for Si(Li) #427 was tested with the detector on-trap, once with the He-compressor off and once with the compressor running. The magnetic field remained off for all resolution test measurements. Scope images of the reset signal are shown in Fig. C.1. The signal revealed a relatively high noise level of 40-50 mV even without the compressor on. The He-compressor induced vibrations caused a microphonia structure in the reset-signal ramp-up which severely deteriorated the energy resolution and made the detector unusable for data taking in the trap environment.

C.1.3 Hardware changes/fixes

As this detector was unusable for an experiment it was modified twice in the detector lab at the TRIUMF facility. The following changes were performed:

- Improved grounding (connection between HV ground and post-amp ground)

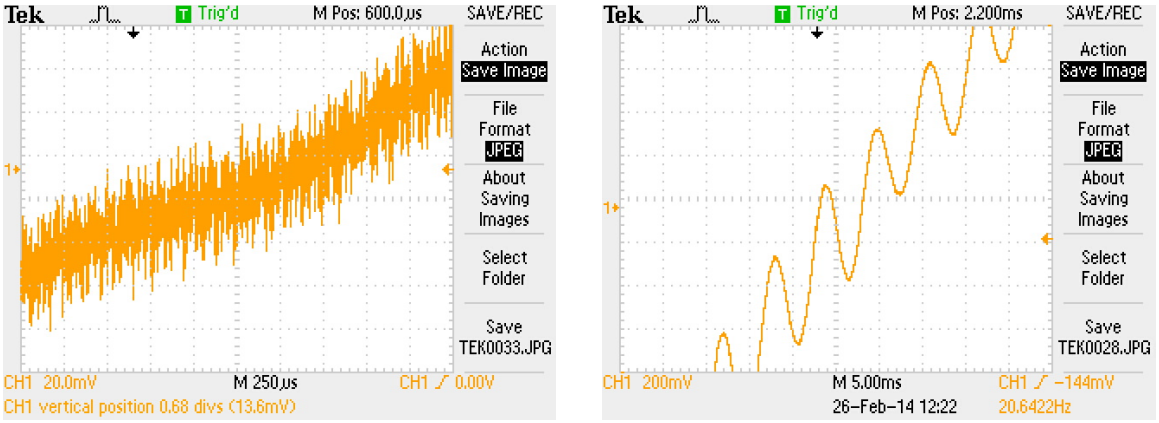

Figure C.1: Direct reset signals for Si(Li) #427. The signal features a high noise level of 40-50 mV (left) even without the compressor running. The vibrations caused by the compressor induce a microphonia structure in the signal (right) in addition to the noise.

- Exchange of high-voltage insulation, as it was different than for all other detectors
- FET source (pre-amp ground) connected to post-amp ground
- Twisted pair included
- Copper-tape around housing
- Support screws isolated to avoid contact to "dirty" ground

C.1.4 Current operation

After those modifications, the detector was tested again on- and off-trap with a collimated ^{133}Ba source. The off-trap reference spectrum was taken with the detector resting on foam for vibration isolation and an energy resolution of 2.0(1)% was achieved. This was a major improvement compared to the performance before the modifications, considering that the energy resolution of Si(Li) #427 was insufficient to even record data off-trap. A spectrum (black curve) is presented in Fig. C.2.

A feature in the low energy region exists due to a threshold change during the run to test the low-energy noise sensitivity. The low-energy noise in the spectrum has been reduced significantly through the modifications, which allows to detect events with energies of roughly 4 keV. However, the vibration sensitivity itself was not reduced.

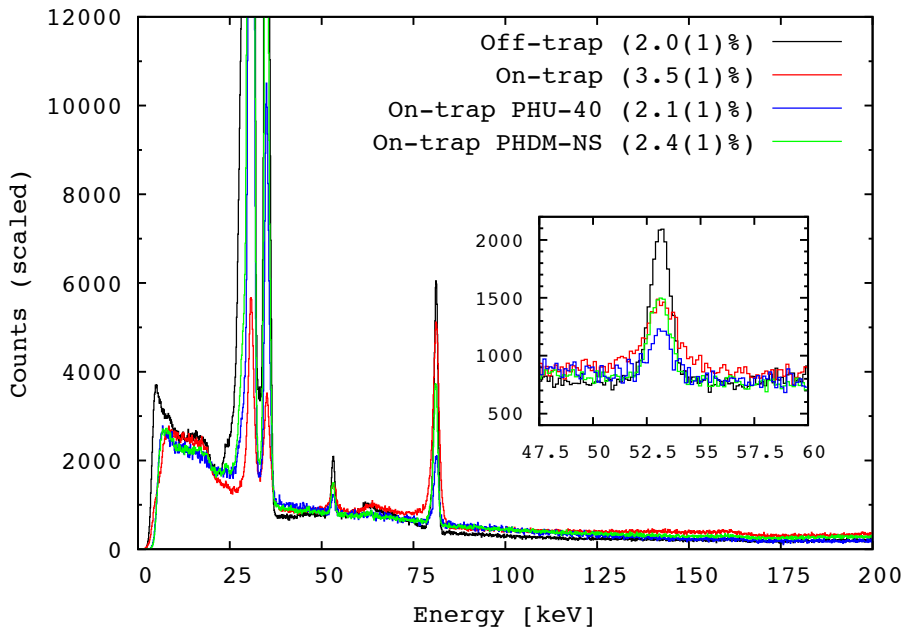

Figure C.2: Comparison of the ^{133}Ba spectra taken with different settings for Si(Li) #427. The black curve shows the spectrum taken off-trap, blue and green are on-trap spectra with two different types of damping materials around the cryostat and the red curve presents an on-trap spectrum taken without vibration damping.

On-trap ^{133}Ba spectra recorded with Si(Li) #427 mounted on the 90° access port compared to the off-trap spectrum taken after modifying the detector are shown in Fig. C.2. The corresponding fit values for the 53 keV γ-transition are given in Tab. C.1. The energy resolution decreased to 3.5(1)% for an on-trap spectrum taken without vibration damping. Clearly, the vibration sensitivity of this detector remains a serious problem. Nevertheless, the overall performance of the detector was improved as the noise level was reduced to around 10 mV compared to $\geq$ 40 mV beforehand. Furthermore, the high frequency pattern in the signal vanished on- and off-trap, making the detector usable in a low-vibration environment. By using the PHDM-NS vibration-damping material it was possible to achieve an energy resolution of 2.1(1)% on-trap, which is comparable to the resolution achieved off-trap.

Setting	FWHM [Ch]	Peak center [Ch]	Resolution [%)]
Off-trap	8.4(1)	411(2)	2.0(1)
On-trap	13.2(1)	380(2)	3.5(1)
On-trap - PHU40	9.3(1)	380(2)	2.4(1)
On-trap - PHDM-NS	8.0(1)	378(2)	2.1(1)

Table C.1: Si(Li) #427 fit values of the 53 keV γ-line.

C.2 Si(Li) #431 - Status: usable (with damping)

C.2.1 History

Detector #431 arrived at TRIUMF in 2013 but had to be send back to Canberra for implementing a reset-triggering LED. The same behavior was observed for the detectors #432 and #438. After its return to TRIUMF and further tests, its energy resolution was found to be insufficient for a spectroscopy experiment and did not match the specifications assigned by Canberra. Consequently, it had to be send back to the manufacturer a second time with the request to examine the electronics as well as the soldering material. After implementing a larger amount of indium for mechanical stability (compare Sec. 3.1), an attempt was made to use the detector for an online experiment. It performed with an energy resolution of 2.9(1)% on the down-facing port at 45° during the experiment in November 2013 (see Fig. 5.1) and was used for the online multiple-injection tests but not for the analysis of the X-ray spectra, since its data could not be added to the data of the other three operational detectors without broadening the peaks and, hence, decreasing the overall resolution.

C.2.2 Hardware changes/fixes

The detector has not been modified so far as the reset signal did not show any vibration related noise or microphonia structures whether the He-compressor was running or not. However, it may be beneficial to send the detector to the lab for a detailed review of the electronics even though it was possible to reproduce the off-trap resolution by using the PHDM-NS damping material in the new support structure.

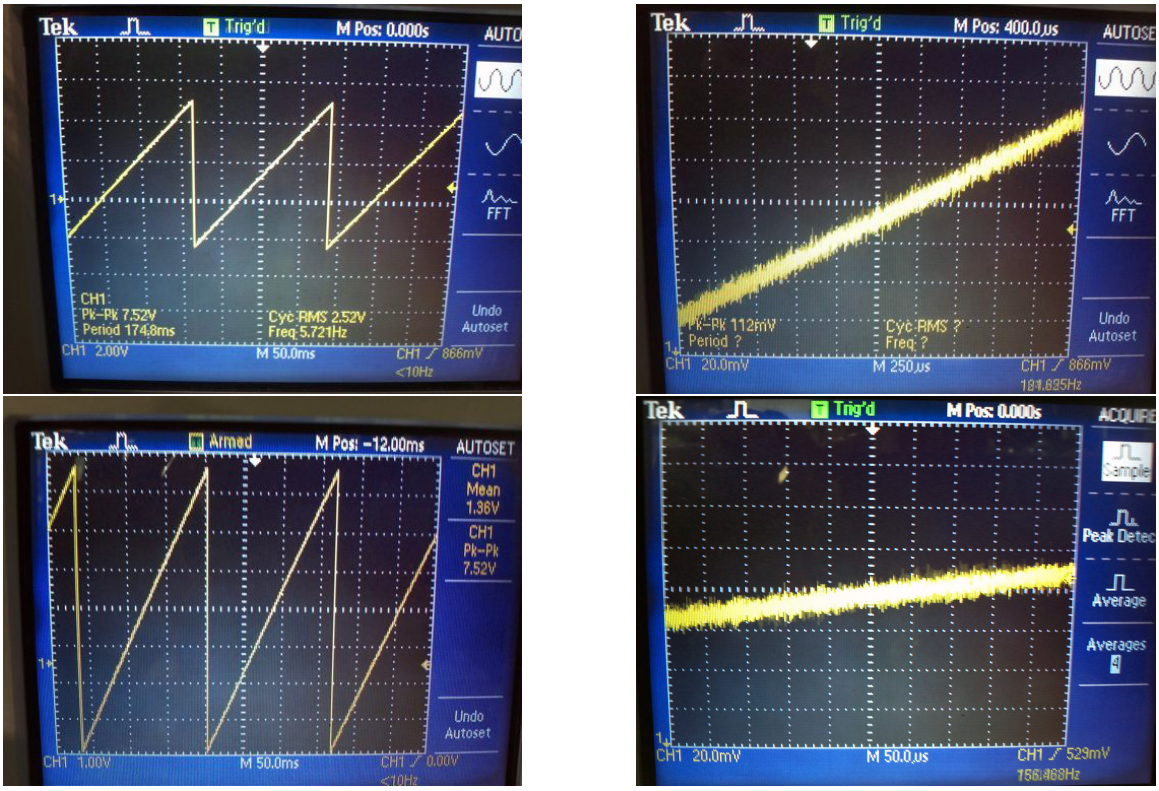

Figure C.3: Direct reset signals for Si(Li) #431. The upper two panels show the signal on two different scales with the detector on-trap while the He-compressor was off. The bottom two panels present the signal when the compressor was switched on.

C.2.3 Current performance

Fig. C.3 contains images of the direct reset signal of Si(Li) #431 on-trap mounted undamped on the 45° port with and without the EBIT compressor running. The reset signal is stable around 5 Hz to 10 Hz and for both cases, compressor off and compressor on, the noise level is below 20 mV. Further, no vibration related microphonia structure is visible, even when the compressor is on. Nevertheless, spectra taken on-trap without any vibration damping, do not yield the required energy resolution to perform a spectroscopy experiment. However, with the new support structure in combination with the PHDM-NS damping material it is now possible to use the detector for an online experiment. Fig. C.4 shows the on-trap ^{133}Ba spectra taken with the two types of damping materials compared to the off-trap and on-trap spectra taken without damping. Tab. C.2 contains the corresponding values for the FWHM, channel number of the peak centroid and energy resolution at 53 keV. The PHDM-NS material turned out to be more effective for vibration damping than the

Setting	FWHM [Ch]	Peak center [Ch]	Resolution [%]
Off-trap	7.6(1)	375(2)	2.0(1)
On-trap	10.1(1)	356(2)	2.8(1)
On-trap - PHU-40	9.5(1)	357(2)	2.7(1)
On-trap - PHDM-NS	7.6(1)	375(2)	2.0(1)

Table C.2: Si(Li) #431 fit values of the 53 keV γ-line.

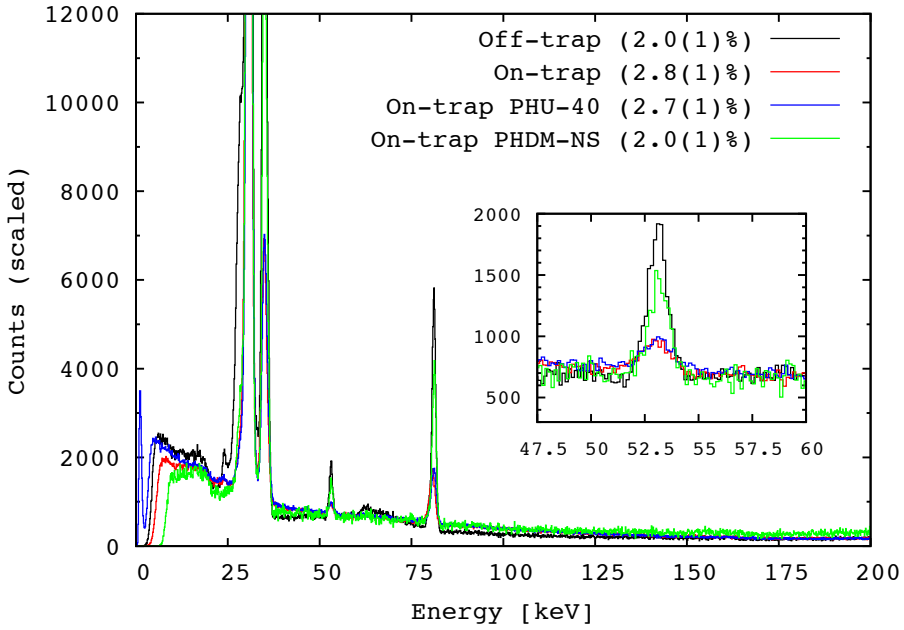

Figure C.4: Comparison of the ^{133}Ba spectra taken with different settings for Si(Li) #431. The black curve shows the spectrum taken off-trap, blue and green are on-trap spectra with two different types of damping material around the cryostat and the red curve presents an on-trap spectrum taken without vibration damping.

PHU-40 material, which makes it possible to use detector #431 for data taking during an experiment.

C.3 Si(Li) #432 - Status: usable (with damping)

C.3.1 History

Si(Li) #432 was shipped to Vancouver in 2013 and had to be send back to Canberra for implementing a reset triggering LED, as the detector would stop resetting after the high-voltage ramp-up was completed. It was sent back to Canberra a second time to change the soldering material as the material used before did not contain a sufficient amount of indium, which resulted in an extreme vibration sensitivity of this detector.

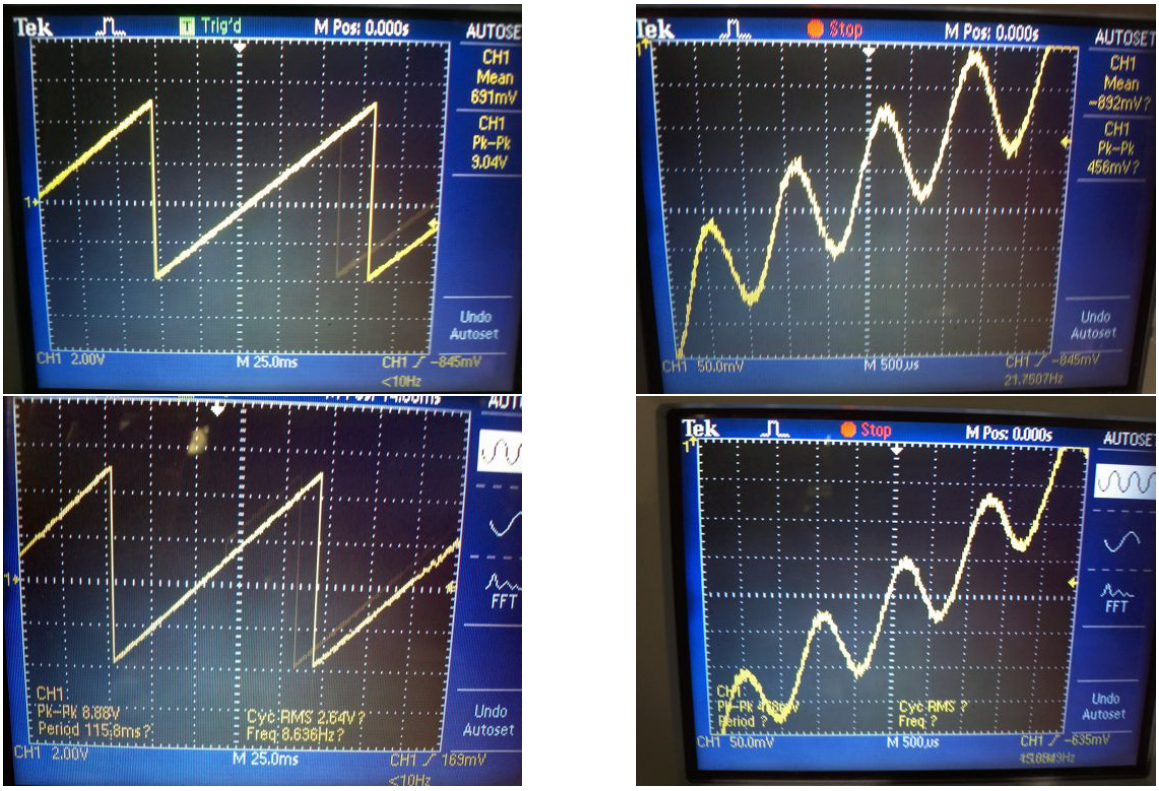

Figure C.5: Direct reset signals for Si(Li) #432. The upper two panels show the signal on two different scales with the detector on-trap while the He-compressor was switched off. The bottom two panels present the signal when the compressor was switched on.

C.3.2 Previous operation

Even after the two modifications conducted by the manufacturer, the detector was not usable for an experiment (see Fig. 5.1). Low-energy noise and a broad bump around 30 to 40 keV were characteristic for every spectrum taken with that detector. Optimizing the pulse-shaping parameters did not result in any significant performance improvement.

C.3.3 Hardware changes/fixes

For this detector the same modifications to optimize grounding and to reduce high-frequency noise as for Si(Li) #427 were performed.

C.3.4 Current operation

After the modifications from the detector lab at TRIUMF, the high-frequency component in the signal could be reduced. Therefore, it was possible to take off-trap data with an energy

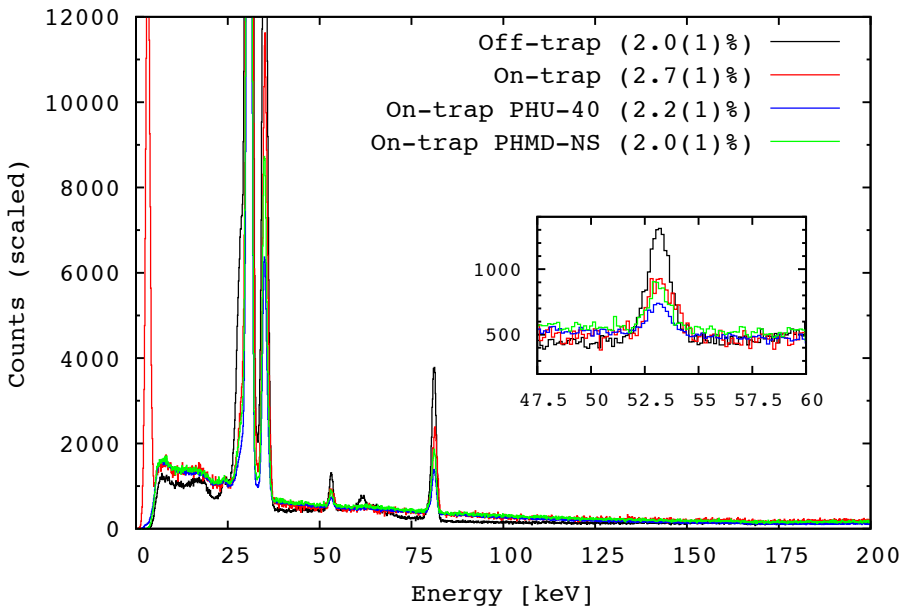

Figure C.6: Comparison of the ^{133}Ba spectra taken with different settings for Si(Li) #432. The black curve shows the spectrum taken off-trap, blue and green are on-trap spectra with two different types of damping material around the cryostat and the red curve presents an on-trap spectrum taken without vibration damping.

Setting	FWHM [Ch]	Peak center [Ch]	Resolution [%]
Off-trap	8.8(1)	415(2)	2.0(1)
On-trap	10.2(1)	383(2)	2.7(1)
On-trap - PHU40	8.5(1)	384(2)	2.2(1)
On-trap - PHDM-NS	7.7(1)	381(2)	2.0(1)

Table C.3: Si(Li) #432 fit values of the 53 keV γ-line.

resolution of 2.1(1)%. Especially the low-energy region remained clean of any noise, which allowed for observing X-rays around 4-6 keV originating from charge breeding. However, the detector remains sensitive to vibrations even though it was possible to take an on-trap spectrum at the 135° (up-facing) with a noise-free low energy region. A comparison of the off-trap spectrum with the on-trap (damping and no damping) spectra is given in Fig. C.6 and the fit values to determine the energy resolution are listed in Tab. C.3. By applying vibration damping for on-trap measurements, the detector becomes usable (2.0(1)%) for an experiment.

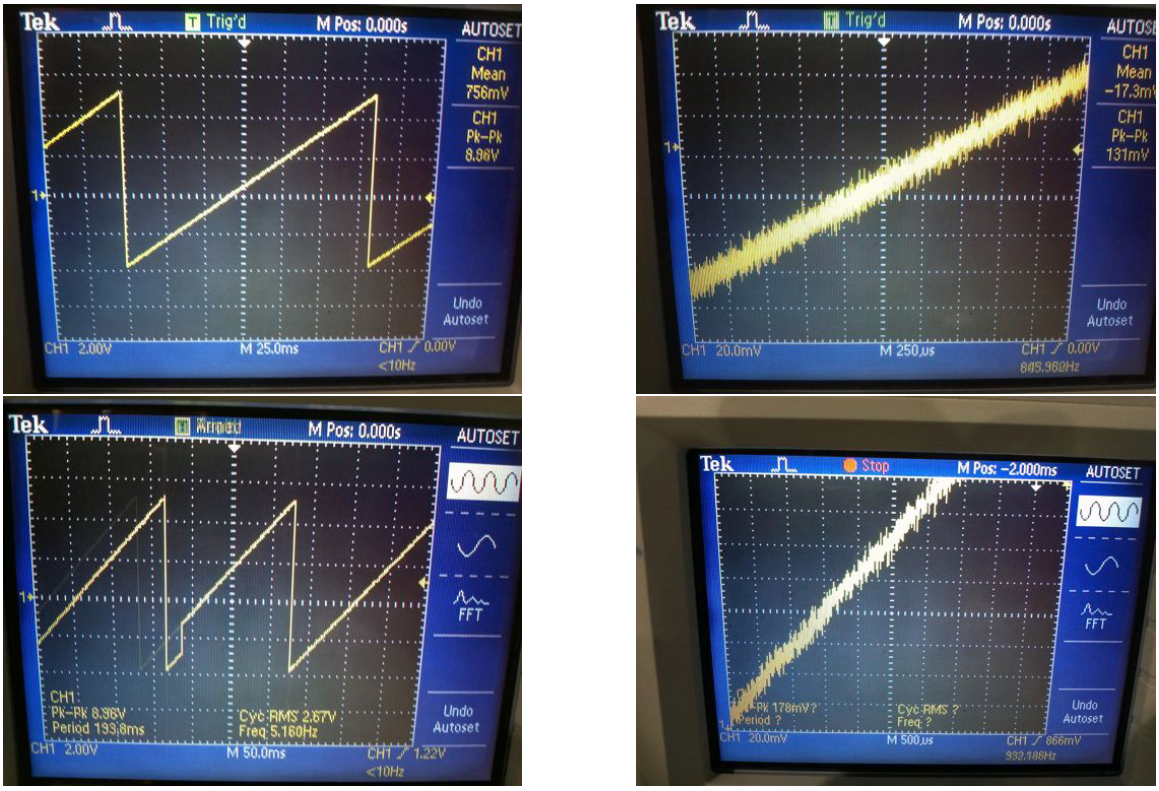

Figure C.7: Direct reset signals for Si(Li) #438. The upper two panels show the signal on two different scales with the detector on-trap while the He-compressor was off. The bottom two panels present the signal when the compressor was switched on.

C.4 Si(Li) #438 - Status: usable (with damping)

C.4.1 History

This detector arrived in Vancouver in 2012 and was send back to Canberra as it exhibited the same problem as Si(Li) #431 and #432, which was solved by implementing an internal reset triggering LED. Further tests at TRIUMF revealed an extreme vibration sensitivity, which made the detector unsuitable for usage on-trap. The lack of indium in the soldering material was partially responsible for this extreme sensitivity as it had been observed for the detectors Si(Li) #431 and #432. To exchange the soldering material the detector was shipped to Canberra again in 2013 and arrived back in Vancouver in October 2013.

Si(Li) #438 was used for data taking during the ^{116}In experiment in November 2013 on the 180° port (compare Fig. 5.1) located underneath the EBIT and performed with a comparably good energy resolution of 2.0(1)% like the two detectors on the horizontal ports (#404,

#405). Note, that the 180° port was the only port Si(Li) #438 could be used on, since the mechanical vibrations were less severe on the port underneath the EBIT than for the other six ports.

C.4.2 Previous operation

Though usable on the port underneath the EBIT, any type of vibrations still had a strong effect on the reset signal. The noise level reached about 50 mV and the signal became unstable. The direct reset signal with compressor on and off, while the detector was mounted on the 180° is shown in Fig. C.7. The noise level was about 18 mV and the signal was clean from microphonia, whether the compressor was running or not. Nevertheless, the signal was less stable whenever the compressor was running.

C.4.3 Hardware changes/fixes

For this detector the same modifications to optimize grounding and to reduce high-frequency noise as for Si(Li) #427 were performed.

C.4.4 Current operation

A spectrum taken with Si(Li) #438 off-trap and isolated from vibrations with foam is shown in Fig. C.8 relative to spectra recorded on-trap (90° port) with and without vibration damping, which were taken after the modifications employed by the detector lab at TRIUMF. Off-trap this detector performs according to the data sheets with an energy resolution of 1.9(1)% at 53 keV. However, depending on which port Si(Li) #438 is mounted, it is either completely unusable (i.e., the down-facing port at 315°) or performed sufficiently (horizontal ports at 90° and 270° or the 180° port). Due to the grounding optimization for this detector, it was possible to use it on three out of seven ports. The achieved energy resolution of 2.4(1)% on the 90° port without damping is already close to the resolution off-trap. However, mounted on the 180° port it performed with a resolution of 2.0(1)%. A comparison of a spectrum taken with PHU-40 vibration damping and PHDM-NS damping material with a spectrum taken off-trap and on-trap without damping is presented in Fig. C.8. An energy resolution of 2.2(1)% on the 90° port is achieved with the PHDM-NS

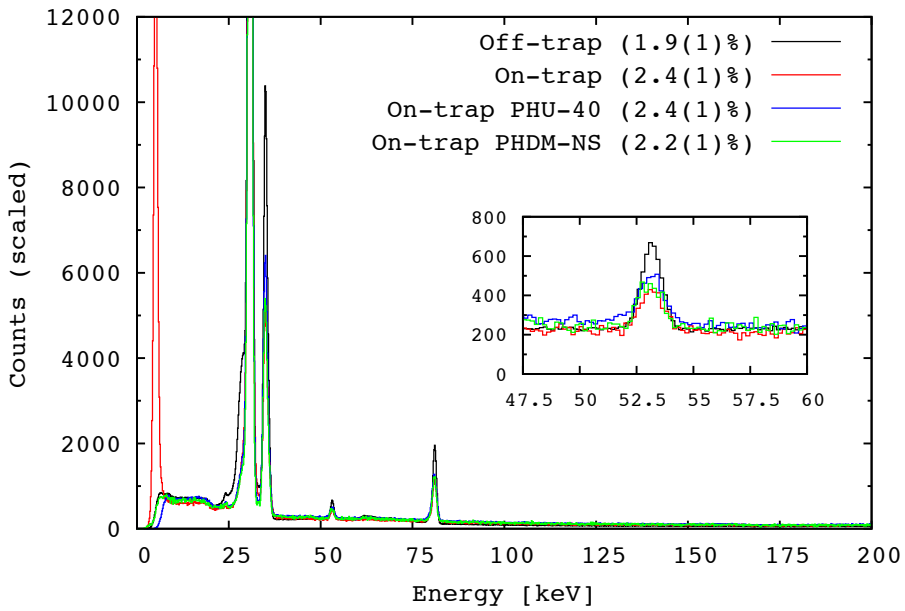

Figure C.8: Comparison of the ^{133}Ba spectra taken with different settings for Si(Li) #438. The black curve shows the spectrum taken off-trap, blue and green are on-trap spectra with two different types of damping material around the cryostat and the red curve presents an on-trap spectrum taken without vibration damping.

Setting	FWHM [Ch]	Peak center [Ch]	Resolution [%]
Off-trap	6.2(1)	321(2)	1.9(1)
On-trap	7.1(1)	297(2)	2.4(1)
On-trap PHU40	7.2(1)	295(2)	2.4(1)
On-trap PHDM-NS	6.4(1)	297(2)	2.2(1)

Table C.4: Si(Li) #438 fit values of the 53 keV γ-line.

material. Therefore, the detector can be used for an experiment on-trap, provided that sufficient vibration damping is applied. Tab. C.4 gives an overview of the achieved energy resolution depending on the detector location (on- and off-trap) and the applied damping.

C.5 Si(Li) #404 - Usable (with damping)

C.5.1 History

Si(Li) #404 is one of the three detectors that arrived at TRIUMF in October 2010 and has never been sent back, since it has performed according to its specifications. Even though the performance on-trap is slightly worse than off-trap (resolution of 1.9(1)% compared to 1.6(1)%), it has always been used in past experiments (for ^{116}In see Fig. 5.1). No

Setting	FWHM [Ch]	Peak center [Ch]	Resolution [%]
Off-trap	25.8(1)	1692(2)	1.6(1)
On-trap	32.7(1)	1744(2)	1.9(1)
On-trap - PHU-40	30.2(1)	1738(2)	1.7(1)
On-trap - PHDM-NS	N/A	N/A	N/A

Table C.5: Si(Li) #404 fit values of the 53 keV γ-line.

modifications had to be employed in order to reduce its vibration sensitivity or the low-energy noise contribution.

C.5.2 Current operation

In Fig. C.9 a comparison of the reset signal with and without compressor on is presented. For both cases, the reset signal appears to be clean from micophonia structures and the noise level is around 10 mV while the detector resets at a frequency of about 20 Hz. Fig. C.10 compares the spectra taken with Si(Li) #404 on-trap (with and without damping) and off-trap. With an energy resolution of 1.9(1)% at 53 keV on-trap without damping the detector is suitable for being used in an experiment even without vibration damping. By using damping material to isolate the detector cryostat from the EBIT frame the resolution can be improved to 1.7(1)%. An overview of the fit values at 53 keV for the different spectra is given in Tab. C.5.

C.6 Si(Li) #405 - Status: unusable

C.6.1 History

Si(Li) #405 was one of the detectors that came to Vancouver in 2010 and performed according to its specifications. It was used during the past experiments (^{116}In (Fig. 5.1) and ^{124}Cs) and was always located on the horizontal 270° port.

C.6.2 Current operation

Though performing sufficiently during the experiments, the detector got more vibration sensitive over time as shown in the bottom right panel of Fig. C.11. The wave pattern in the reset signal appeared only when the compressor was switched on, directly indicating the effect of the compressor vibrations on the detector signal. This observation was entirely

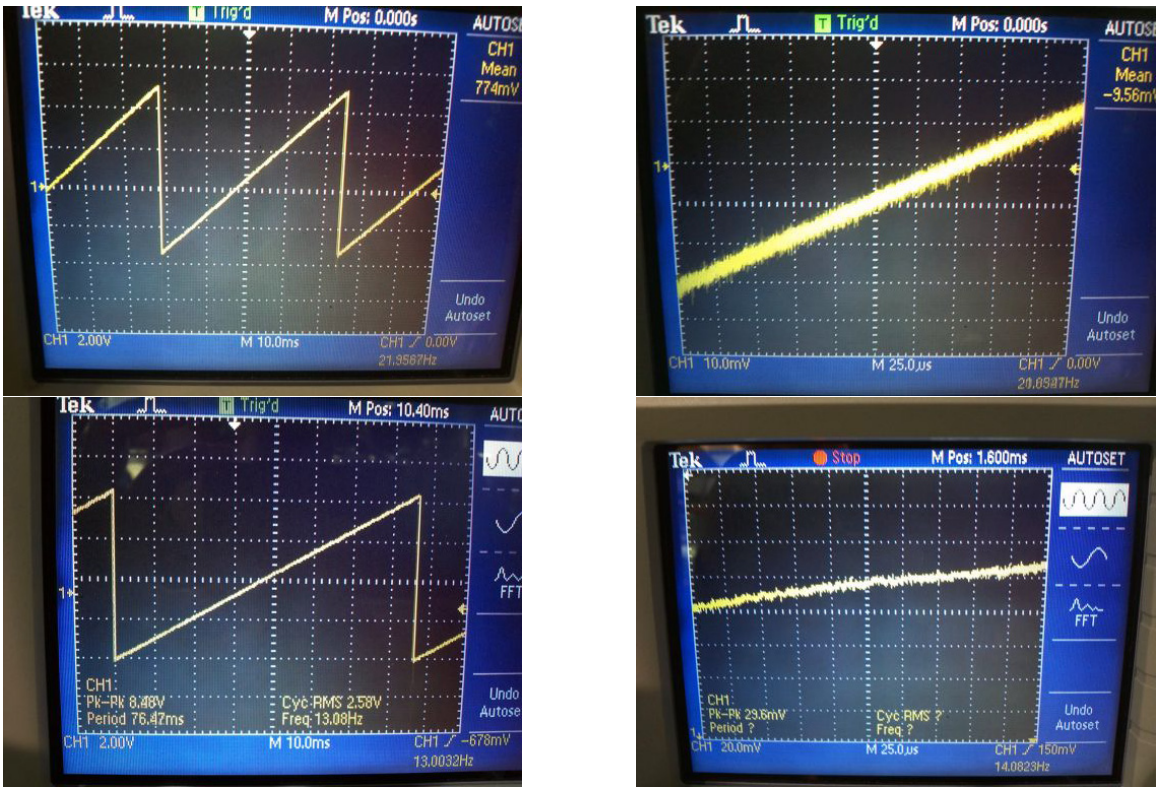

Figure C.9: Direct reset signals for Si(Li) #404. The upper two panels show the signal on two different scales with the detector on-trap while the He-compressor was off. The bottom two panels present the signal when the compressor was switched on.

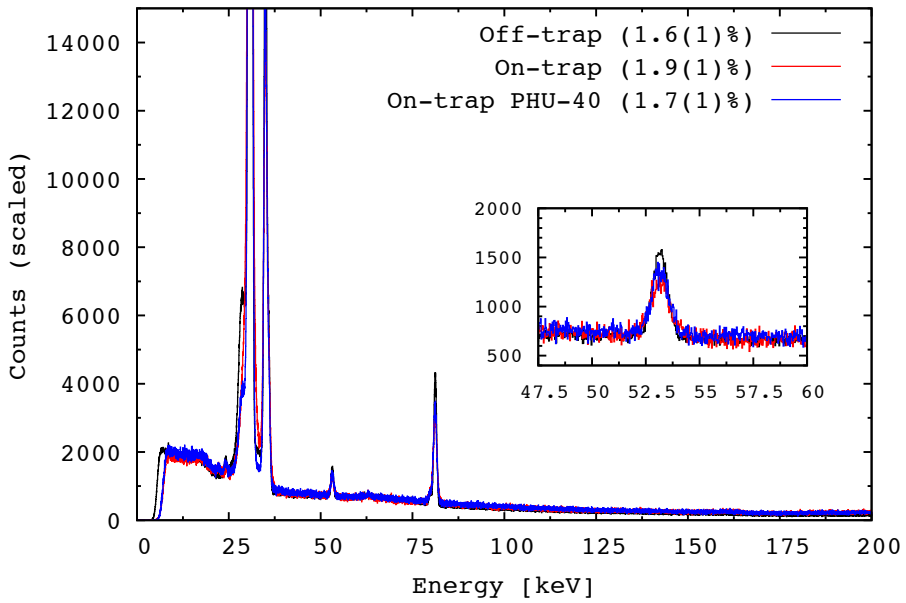

Figure C.10: Comparison of the ^{133}Ba spectra taken with different settings for Si(Li) #404. The black curve shows the spectrum taken off-trap and in blue the on-trap spectrum taken with the PHU-40 damping material around the cryostat is presented. The red curve presents an on-trap spectrum taken without vibration damping.

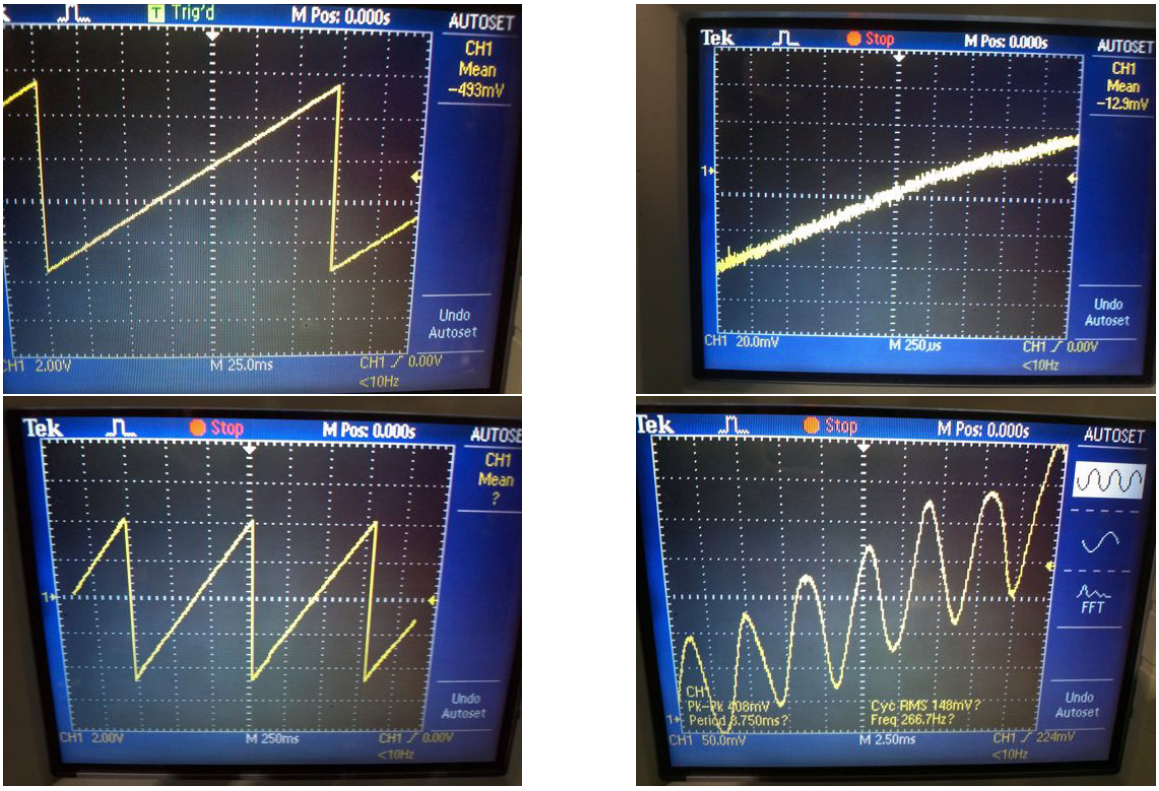

Figure C.11: Direct reset signals for Si(Li) #405. The upper two panels show the signal on two different scales with the detector on-trap while the He-compressor was off. The bottom two panels present the signal when the compressor was switched on.

new for this detector, which indicates the possibility of degrading electrical components in the preamplifier electronics or the high-voltage filter. The upper two panels of Fig. C.11 illustrate the reset signal while the compressor was switched off. The reset signal is stable at 10 Hz and also the noise level was minimal at around 10 mV.

C.6.3 Hardware changes/fixes

In order to minimize the vibration sensitivity the detector was modified in the detector lab. Next to the usual grounding optimization a capacitance in the high-voltage filter was changed (47 nF to 1 nF) in order to make it exactly the same as for the other detectors. Another modification was the replacement of a resistor in the HV-filter from 1 GΩ to 100 MΩ. Further, the high-voltage feed-through connection was poorly soldered and about to break, which explains the performance deterioration over time.

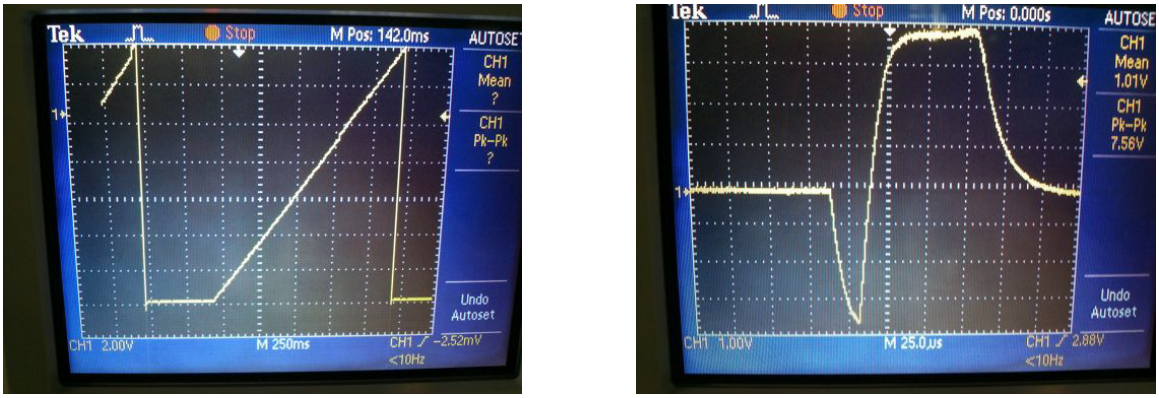

Figure C.12: Left: Direct reset signal from Si(Li) #405 taken off-trap after changing the HV-filter components. Right: Signal from Si(Li) #405 after passing the signal-processing amplifier. The signal was recorded, while the Si(Li) was located off-trap after the HV-filter components had been exchanged.

C.6.4 Current operation

This detector was ramped up carefully to make sure that the leakage current would not exceed 10 nA. The latter was not the case but instead the reset signal (Fig. C.12) showed an unusual feature. After each reset the signal would go into a plateau for 500 ms before starting to ramp up again. The length of that plateau became longer (order of seconds) after the high voltage was ramped up completely and the current went down. The signal after passing the signal-processing amplifier is presented in Fig. C.12. The time for the pulse width is less than 100 μs and does not correspond to the length of the plateau in the reset signal.

After changing the HV-filter components back to the way they were before, another off-trap test with a ^{133}Ba source was performed. The plateau in the reset signal was still present, however the length decreased from 500 ms and higher down to about 7 ms (compare Fig. C.13 left panel). A picture of the signal after being processed by the signal-processing amplifier is shown in Fig.C.13. A third inspection from the detector lab did not solve the problem. The reset signal still shows a plateau after each reset, whereby the length is increasing with time. At the present stage this detector is not usable for data taking anymore.

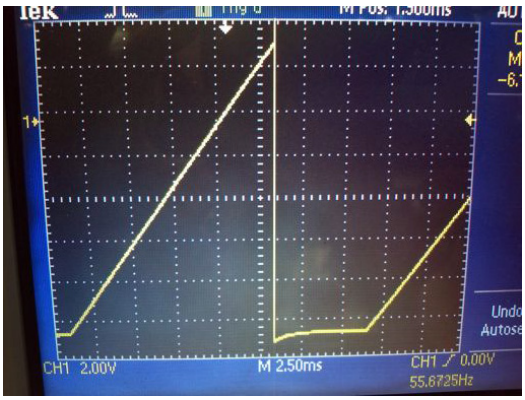

Figure C.13: Left: Direct reset signal from Si(Li) #405 taken off-trap after the HV filter has been changed back to the way it was built in by Canberra (capacitance: 47 nF and resistor: 1 GΩ). Right: Output signal from the signal-processing amplifier for Si(Li) #405 taken off-trap after changing the HV-filter components.

C.7 Si(Li) #406 - Status: unusable

C.7.1 History

Si(Li) #406 came to Vancouver in 2010 but was extremely vibration sensitive on-trap and was never used for an experiment before. The major problem was extremely high low-energy noise, which would cause the DAQ system to crash. The energy threshold had to be set so high, that the energy region of interest (20 keV to 35 keV) could not be monitored anymore. Off-trap tests revealed that moving the Al-housing of the preamp-electronics induced the noise problem. After contacting Canberra they suggested that a resistor between the test output and ground might be broken, i.e., not providing 51 Ω. Measuring the resistance revealed a value of 49.5 Ω, which differed enough from the specified value to induce noise. Exchanging the resistor with a new one provided by Canberra, however, did not result in a performance improvement. Another suggestion was to put ferrites around the signal and HV cables, which did not solve the problem either.

C.7.2 Hardware changes/fixes

This detector has been modified twice in the detector lab. The first time, the following changes were done:

- Improved grounding (connection between HV ground and post-amp ground)
- FET source (preamp ground) connected to post-amp ground

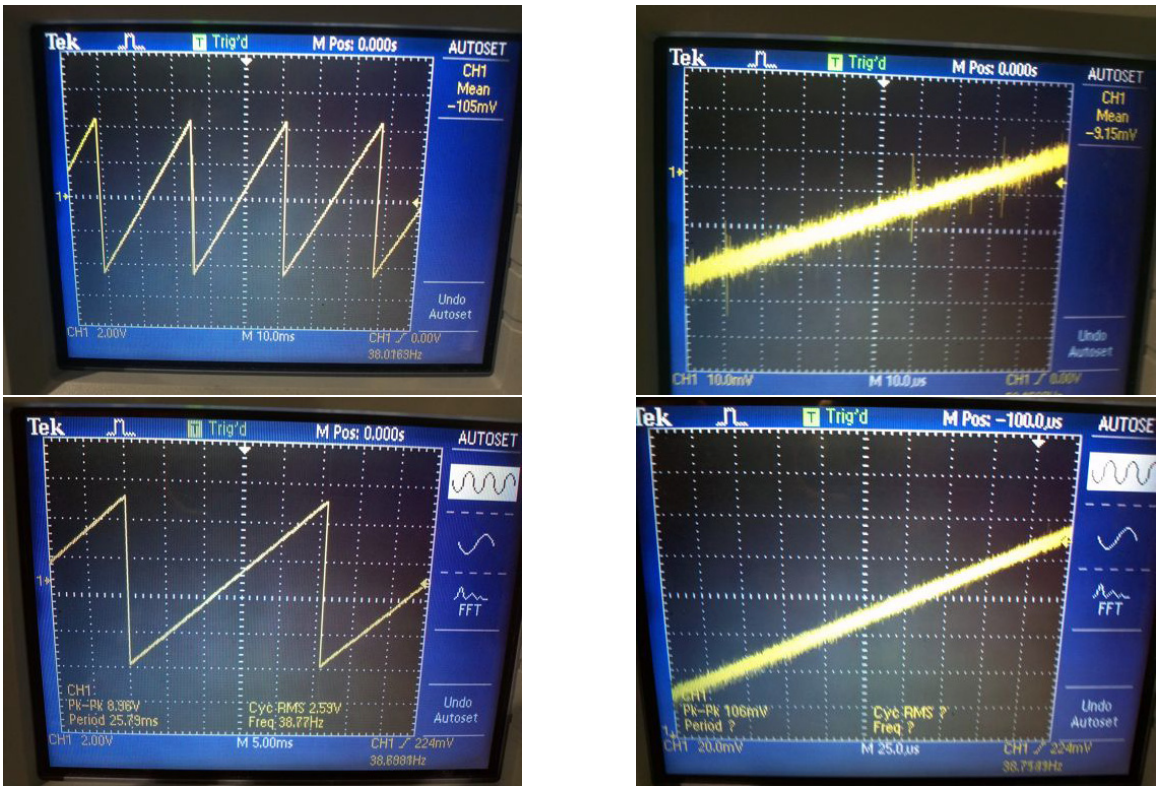

Figure C.14: Direct reset signals for Si(Li) #406. The upper two panels show the signal on two different scales with the detector on-trap while the He-compressor was off. The bottom two panels present the signal when the compressor was switched on.

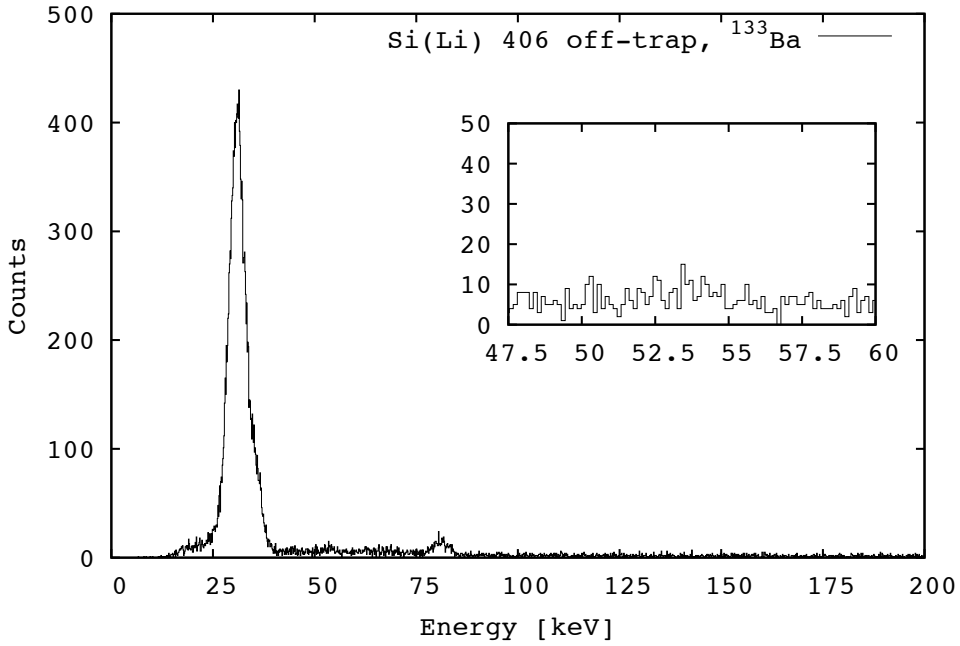

Figure C.15: ^{133}Ba spectrum taken with Si(Li) #406 off-trap. Shown is the energy region between 0 and 200 keV. The inset shows the energy region between 47.5 keV and 60 keV. A value for the energy resolution compared to the other Si(Li)s could not be extracted since it was not possible to identify a peak at 53 keV.

- Twisted pair
- Copper-tape around housing
- Support screws isolated to avoid contact to dirty ground
- Insulation paint scratched off

Further, the inspection revealed a missing HV filter for this detector, which might have caused the high-frequency pattern in the reset signal. In addition, this detector had noise problems, whenever the preamp-electronics housing was opened.

C.7.3 Current operation

The first modifications did not improve the detector performance enough to get it into a usable state. The low-energy noise was still high and the ^{133}Ba X-rays were not resolved but just a bulk in the spectrum. This was somewhat unexpected since the reset signal improved compared to before the modifications. The high-frequency pattern was less strong and also

Figure C.16: Output signal of the signal-processing amplifier for Si(Li) #406 taken off-trap.

the noise level decreased from up to 100 mV to about 10 mV.

During the second modification a high-voltage filter according to the detector specifications was implemented. An off-trap ^{133}Ba spectrum (Fig. C.15) was taken but the detector performance did not improve. Even though the reset signal has a low noise level, it is unstable and moves up and down. The output signal of the signal-processing amplifier, i.e., the signal after amplification and pulse shaping, which goes into the ADC, has an unusual feature after the actual pulse. An image of that signal is presented in Fig. C.16. After a detailed examination of the signals and several modifications, one has to conclude that the detector is not usable for data taking in its current state.

C.8 Conclusion

In summary, five (#404, #431, #432, #427, #438) out of seven detectors can currently be used for an online experiment. Si(Li) #404 is by far the most reliable detector, and the Si(Li)s #427 or #431 are not usable without applying vibration damping. The optimization by the detector lab improved the performance of Si(Li) #427, compared to the last

	Energy resolution [%]			
Det. #	Off-trap	No damping	PHU-40	PHDM-NS
427	2.0(1)	3.5(1)	2.4(1)	**2.1(1)**
438	1.9(1)	2.4(1)	2.4(1)	**2.2(1)**
404	1.6(1)	1.9(1)	1.7(1)	**1.6(1)**
432	2.1(1)	2.7(1)	2.2(1)	**2.0(1)**
431	2.0(1)	2.8(1)	2.7(1)	**2.0(1)**

Table C.6: Overview of the achieved energy resolution of five tested Si(Li) detectors depending on the environment and damping material. All values are given in %.

experiment, where it was not even possible to operate it off-trap anymore.

Si(Li) #431 yields good resolution (2.0(1)%) off-trap, which can be reproduced on-trap, as long as the detector is mounted in the new support structure with implemented vibration damping material. The detectors #405 and #406 are not usable in their current state. Several attempts to implement a new high-voltage filter or, respectively, exchange the high-voltage filter did not show the aimed at effect but even worsened the performance. Tab. C.6 gives an overview of the present performance status of the five usable detectors. It remains to be decided what should be done with the two non-operational detectors and whether sending them back to Canberra for repair is a possibility. However, five working detectors to occupy the three large acceptance ports and two detectors for the smaller acceptance ports are sufficient for data collection during an experiment.

Appendix D

FAC FILES

```
#Input file for 124Cs
#Calculation of the energy levels and radiative transition rates

from pfac import fac

SetAtom('Cs', 55, 124.0)

_____________________________________________________
#Closed('3d')
fac.Config('1s1 2s2 2p6 3s2 3p6', group = 'n2')
fac.Config('1s2 2s2 2p5 3s2 3p6', group = 'n3')
_____________________________________________________
# Self-consistent iteration for optimized central potential
fac.ConfigEnergy(0)
fac.OptimizeRadial(['n2'])
fac.ConfigEnergy(1)

#Generating structures
fac.Structure('Cs.lev.b', ['n2', 'n3'])
fac.MemENTable('Cs.lev.b)
fac.PrintTable('Cs.lev.b', 'Cs.lev', 1)

#Generate Transitions
fac.TransitionTable('Cs.tr.b', ['n2'], ['n3'], -1)
fac.PrintTable('Cs.tr.b', 'Cs.tr', 1)
```

Figure D.1: FAC input file for ^{124}Cs.

```
#(3 energy levels, 2 transitions, initial hole in 1s, final hole in 2p or 3p)
#NELE = Number of bound electrons

Closed('3d','4s','4p','4d','5s','5p','6s')
Config('1s1 2s2 2p6 3s2 3p6', group = 'n2')
Config('1s2 2s2 2p5 3s2 3p6', group = 'n3')
NELE       = 55 (=Neutral)
 ILEV  IBASE    ENERGY      P   VNL   2J
   0    -1  0.00000000E+00 1   600    3 1*2 2*7 3*18 4*18 5*8 6*2  2p5
2p+3(3)3
   1    -1  3.47687055E+02 1   600    1 1*2 2*7 3*18 4*18 5*8 6*2  2p5
2p-1(1)1
   2    -1  3.09638181E+04 0   600    1 1*1 2*8 3*18 4*18 5*8 6*2  1s1
1s+1(1)1
NELE       = 55
   2  1     0  3  3.096382E+04  4.424013E-01  9.202476E+15  3.415206E-02
   2  1     1  1  3.061613E+04  2.237253E-01  4.549829E+15 -2.442409E-02

Closed('3d','4s','4p','4d','5s','5p','6s')
Config('1s1 2s2 2p6 3s2 3p6', group = 'n2')
Config('1s2 2s2 2p6 3s2 3p5', group = 'n3')
NELE       = 55
 ILEV  IBASE    ENERGY      P   VNL   2J
   0    -1  0.00000000E+00 1   600    3 1*2 2*8 3*17 4*18 5*8 6*2  3p5
3p+3(3)3
   1    -1  6.83779305E+01 1   600    1 1*2 2*8 3*17 4*18 5*8 6*2  3p5
3p-1(1)1
   2    -1  3.49711888E+04 0   600    1 1*1 2*8 3*18 4*18 5*8 6*2  1s1
1s+1(1)1
NELE       = 55
   2  1     0  3  3.497119E+04  6.219491E-02  1.650270E+15  1.204920E-02
   2  1     1  1  3.490281E+04  2.900224E-02  7.665345E+14 -8.236100E-03

Closed('3d','4s','4p','4d')
Config('1s1 2s2 2p6 3s2 3p6', group = 'n2')
Config('1s2 2s2 2p5 3s2 3p6', group = 'n3')
NELE       = 45
 ILEV  IBASE    ENERGY      P   VNL   2J
   0    -1  0.00000000E+00 1   402    3 1*2 2*7 3*18 4*18    2p5
2p+3(3)3
   1    -1  3.47773008E+02 1   402    1 1*2 2*7 3*18 4*18    2p5
2p-1(1)1
   2    -1  3.09661714E+04 0   402    1 1*1 2*8 3*18 4*18    1s1
1s+1(1)1
NELE       = 45
   2  1     0  3  3.096617E+04  4.425109E-01  9.206157E+15  3.415500E-02
   2  1     1  1  3.061840E+04  2.237758E-01  4.551530E+15 -2.442594E-02
```

Figure D.2: FAC output file for ^{124}Cs (part1).

```
Closed('3d','4s','4p','4d')
Config('1s1 2s2 2p6 3s2 3p6', group = 'n2')
Config('1s2 2s2 2p6 3s2 3p5', group = 'n3')
NELE       = 45
 ILEV  IBASE    ENERGY      P   VNL   2J
    0    -1  0.00000000E+00 1   402    3 1*2 2*8 3*17 4*18    3p5
3p+3(3)3
    1    -1  6.84647843E+01 1   402    1 1*2 2*8 3*17 4*18    3p5
3p-1(1)1
    2    -1  3.49758583E+04 0   402    1 1*1 2*8 3*18 4*18    1s1
1s+1(1)1
NELE       = 45
    2  1     0  3  3.497586E+04  6.227675E-02  1.652883E+15  1.205632E-02
    2  1     1  1  3.490739E+04  2.903514E-02  7.676054E+14 -8.240229E-03

       Closed('3d','4s','4p')
Config('1s1 2s2 2p6 3s2 3p6', group = 'n2')
Config('1s2 2s2 2p5 3s2 3p6', group = 'n3')
NELE       = 35
NLEV       = 3
 ILEV  IBASE    ENERGY      P   VNL   2J
    0    -1  0.00000000E+00 1   401    3 1*2 2*7 3*18 4*8     2p5
2p+3(3)3
    1    -1  3.48133791E+02 1   401    1 1*2 2*7 3*18 4*8     2p5
2p-1(1)1
    2    -1  3.09654633E+04 0   401    1 1*1 2*8 3*18 4*8     1s1
1s+1(1)1
NELE       = 35
    2  1     0  3  3.096546E+04  4.426781E-01  9.209212E+15  3.416184E-02
    2  1     1  1  3.061733E+04  2.238190E-01  4.552090E+15 -2.442873E-02

Closed('3d','4s','4p')
Config('1s1 2s2 2p6 3s2 3p6', group = 'n2')
Config('1s2 2s2 2p6 3s2 3p5', group = 'n3')
NELE       = 35
 ILEV  IBASE    ENERGY      P   VNL   2J
    0    -1  0.00000000E+00 1   401    3 1*2 2*8 3*17 4*8     3p5
3p+3(3)3
    1    -1  6.97974957E+01 1   401    1 1*2 2*8 3*17 4*8     3p5
3p-1(1)1
    2    -1  3.49995900E+04 0   401    1 1*1 2*8 3*18 4*8     1s1
1s+1(1)1
NELE       = 35
    2  1     0  3  3.499959E+04  6.345792E-02  1.686518E+15  1.216599E-02
    2  1     1  1  3.492979E+04  2.955966E-02  7.824756E+14 -8.311660E-03
```

Figure D.3: FAC output file for ^{124}Cs (part2).

```
Closed('3d')
Config('1s1 2s2 2p6 3s2 3p6', group = 'n2')
Config('1s2 2s2 2p5 3s2 3p6', group = 'n3')
NELE       = 27
NLEV       = 3
  ILEV  IBASE    ENERGY      P   VNL   2J
    0    -1  0.00000000E+00 1   302    3 1*2 2*7 3*18        2p5
2p+3(3)3
    1    -1  3.49532190E+02 1   302    1 1*2 2*7 3*18        2p5
2p-1(1)1
    2    -1  3.09913445E+04 0   302    1 1*1 2*8 3*18        1s1
1s+1(1)1
NELE       = 27
NTRANS       = 2
MULTIP       = -1
GAUGE       = 2
MODE       = 1
    2  1     0  3  3.099134E+04  4.440971E-01  9.254183E+15  3.420226E-02
    2  1     1  1  3.064181E+04  2.244530E-01  4.572288E+15 -2.445353E-02
Closed('3d')
Config('1s1 2s2 2p6 3s2 3p6', group = 'n2')
Config('1s2 2s2 2p6 3s2 3p5', group = 'n3')
NELE       = 27
NLEV       = 3
  ILEV  IBASE    ENERGY      P   VNL   2J
    0    -1  0.00000000E+00 1   302    3 1*2 2*8 3*17        3p5
3p+3(3)3
    1    -1  7.15784053E+01 1   302    1 1*2 2*8 3*17        3p5
3p-1(1)1
    2    -1  3.50648625E+04 0   302    1 1*1 2*8 3*18        1s1
1s+1(1)1
NELE       = 27
NTRANS       = 2
MULTIP       = -1
GAUGE       = 2
MODE       = 1
    2  1     0  3  3.506486E+04  6.502040E-02  1.734496E+15  1.230339E-02
    2  1     1  1  3.499328E+04  3.019971E-02  8.023272E+14 -8.393538E-03
# Closed('3d')
Config('1s1 2s2 2p6 3s2 3p6', group = 'n2')
Config('1s2 2s2 2p5 3s2 3p6', group = 'n3')
NELE       = 17
  ILEV  IBASE    ENERGY      P   VNL   2J
    0    -1  0.00000000E+00 1   301    3 1*2 2*7 3*8         2p5
2p+3(3)3
    1    -1  3.54801245E+02 1   301    1 1*2 2*7 3*8         2p5
2p-1(1)1
    2    -1  3.10212606E+04 0   301    1 1*1 2*8 3*8         1s1
1s+1(1)1
NELE       = 17
    2  1     0  3  3.102126E+04  4.480370E-01  9.354318E+15  3.433707E-02
    2  1     1  1  3.066646E+04  2.259573E-01  4.610341E+15 -2.452548E-02
```

Figure D.4: FAC output file for ^{124}Cs (part3).

Eidesstattliche Erklärung der Studierenden

Hiermit versichere ich, dass die vorliegende Arbeit mit dem Titel

In-trap decay spectroscopy on highly-charged radioactive ions towards measurements on intermediate nuclei in $\beta\beta$ decay

selbständig verfasst worden ist, und dass keine anderen Quellen und Hilfsmittel als die angegebenen benutzt worden sind und dass die Stellen der Arbeit, die anderen Werken - auch elektronischen Medien - dem Wortlaut oder Sinn nach entnommen wurden, auf jeden Fall unter Angabe der Quelle als Entlehnung kenntlich gemacht worden sind.

.....	.....
Münster, Datum	Unterschrift

Ich erkläre mich mit einem Abgleich der Arbeit mit anderen Texten zwecks Auffindung von Übereinstimmungen sowie mit einer zu diesem Zweck vorzunehmenden Speicherung der Arbeit in eine Datenbank einverstanden.

.....	.....
Münster, Datum	Unterschrift

Bibliography

[1] J. Suhonen. *Nucl. Phys. A*, **752**:53c–66c, 2005.

[2] K. Grotz and H. V. Klapdor. *Die schwache Wechselwirkung in Kern-, Teilchen- und Astrophysik - Eine Einführung.* Teubner Studienbücher, 1989.

[3] F. Avignone III et al. *arXiv:0708.1033v2 [nucl-ex]*, 2007.

[4] A. S. Barabash. *Phys. Rev. C*, **81**:035501, 2010.

[5] M. Doi, T. Kotani and E. Takasugi. *Progr. Theor. Phys., Suppl.*, **83**:1–175, 1985.

[6] N. Ackerman, B. Aharmim, M. Auger et al. *Phys. Rev. Lett.*, **107**:212501, 2011.

[7] M. Agostini, M. Allardt, A. M. Bakalyarov et al. *arXiv:1501.02345v1 [nucl-ex]*, 2015.

[8] A. S. Barabash. *Nucl. Phys. A*, **935**:52–64, 2015.

[9] H. Primakoff and S. P. Rosen. *Rep. Prog. Phys.*, **22**:121, 1959.

[10] S. Stoica and M. Mirea. *Phys. Rev. C*, **88**:037303, 2013.

[11] K. Nakamura and others (Particle Data Group). *J. Phys. G: Nucl. Part. Phys.*, **37**: 075021, 2010.

[12] J. Kotila and F. Iachello. *Phys. Rev. C*, **85**:034316, 2012.

[13] J. Suhonen and O. Civitarese. *Phys. Rep.*, **300**(34):123 – 214, 1998.

[14] A. Barabash. *Phys. Atom. Nucl.*, **73**:162–178, 2010.

[15] J. Engel, P. Vogel and M. R. Zirnbauer. *Phys. Rev. C*, **37**:731, 1988.

[16] J. Suhonen, S. B. Khadkikar and A. Faessler. *Nucl. Phys. A*, **529**:727, 1991.

[17] J. Suhonen, S. B. Khadkikar and A. Faessler. *Phys. Lett.*, **B237**:8, 1990.

[18] J. D. Vergados. *Nucl. Phys. A*, **506**:482, 1990.

[19] S. Elliott and P. Vogel. *Annu. Rev. Nucl. Part. Sci.*, **52**:115, 2002.

[20] J. Schechter and J. W. F. Valle. *Phys. Rev. D*, **25**:2951, 1982.

[21] M. Duerr, M. Lindner and A. Merle. *arXiv:1105.0901*, 2011.

[22] W. Rodejohann. *Int. J. Mod. Phys. E*, **20**:1833–1930, 2011.

[23] C. Macolino and the GERDA collaboration. *Mod. Phys. Lett. A*, **29**:1430001, 2014.

[24] K.-H. Ackermann and the GERDA collaboration. *Eur. Phys. J. C*, **73**:2330, 2013.

[25] C. E. Aalseth. *Phys. Atom. Nucl.*, **67**:2002, 2004.

[26] H. Ejiri, J. Engel, K. Fushimi et al. *Nucl. Phys. B*, **110**:375, 2002.

[27] H. Ejiri, J. Engel, R. Hazama et al. *Phys. Rev. Lett.*, **85**:2917, 2000.

[28] H. Ejiri, J. Engel and N. Kudomi. *Phys. Lett. B*, **530**:27, 2002.

[29] R. Arnold, C. Augier, A. M. Bakalyarov et al. *Nucl. Instrum. Methods Phys. Res. A*, **536**:79, 2005.

[30] C. Arnaboldi, F. T. Avignone III, J. Beeman, M. Barucci and M. Balata. *Astropart. Phys. J.*, **20**:91, 2003.

[31] C. Arnaboldi, F. T. Avignone III, J. Beeman et al. *Nucl. Instrum. Methods Phys. Res. A*, **518**:775, 2004.

[32] K. Zuber. *Phys. Lett. B*, **519**:1, 2001.

[33] I. Ogawa, T. Kishimoto, S. Umehara et al. *J. Phys.: Conf. Ser.*, **203**:012073, 2010.

[34] N. I. Rukhadze, A. M. Bakalyarov, C. Briançon et al. *J. Phys.: Conf. Ser.*, **375**: 042020, 2012.

[35] M. Auger, D. J. Auty, P. S. Barbeau et al. *Phys. Rev. Lett.*, **109**:032505, 2012.

[36] A. Gando, Y. Gando, H. Hanakago et al. *Phys. Rev. Lett.*, **110**:062502, 2013.

[37] S. Fukuda, the Super-Kamiokande Collaboration et al. *Phys. Rev. Lett.*, **86**:5651, 2001.

[38] Q. R. Ahmad, R. C. Allen, T. C. Andersen et al. *Phys. Rev. Lett.*, **89**:011302, 2002.

[39] K. Eguchi and the KamLAND collaboration. *Phys. Rev. Lett.*, **90**:021802, 2003.

[40] M. Apolonio and the CHOOZ collaboration. *Phys Lett. B*, **466**:415, 1999.

[41] A. de Gouvêa. *arXiv:hep-ph/0411274v1*, 2004.

[42] R. N. Mohapatra, S. Antusch, K. S. Babu, G. Barenboim et al. *arXiv:hep-ph/0412099v2*, 2004.

[43] A. Abada and G. Bhattacharyya. *Phys. Rev. D*, **68(3)**:033004, 2003.

[44] N. Cabibbo. *Phys. Rev. Lett.*, **10**:531–533, 1963.

[45] M. Kobayashi and T. Maskawa. *Prog. Theor. Phys.*, **49**:652–657, 1973.

[46] R. N. Cahn, D. A. Dwyer, S. J. Freedman et al. *arXiv:1307.5487 [hep-ex]*, 2013.

[47] W. Hampel, G. Heusser, J. Kiko et al. *Phys. Lett. B*, **420**:114, 1998.

[48] C. M. Cattadori and the GNO collaboration. *Nucl. Phys. Proc. Suppl.*, **110**:311, 2002.

[49] J. N. Abdurashitov, V. N. Gavrin, S. V. Girin et al. *Phys. Rev. C*, **59**:2246, 1999.

[50] J. N. Abdurashitov, V. N. Gavrin, S. V. Girin et al. *Phys. Rev. C*, **80**:015807, 2009.

[51] Y. Fukuda et al. *Phys. Rev. Lett.*, **81**:1562–1567, 1998.

[52] F. P. An and the Daya Bay collaboration. *Phys. Rev. Lett.*, **108**:171803, 2012.

[53] M. Maltoni, T. Schwetz, M. Tortola and J. W. F. Valle. *New J. Phys.*, **6**:122, 2004.

[54] M. Maltoni, T. Schwetz and J. W. F. Valle. *Phys. Rev. D*, **67**:093003, 2003.

[55] A. Bandyopadhyay, S. Choubey, R. Gandhi, S. Goswami and D. P. Roy. *Phys. Lett., B*, **559**:121, 2003.

[56] N. Fornengo, M. Maltoni, R. T. Bayo and J. W. F. Valle. *Phys. Rev. D*, **65**:013010, 2002.

[57] F. Deppisch, H. Päs and J. Suhonen. *Phys. Rev. D*, **72**:033012, 2005.

[58] B. Pontecorvo. *Zh. Eksp. Teor. Fiz*, **34**:257, 1958.

[59] B. Pontecorvo. *Zh. Eksp. Teor. Fiz*, **33**:549, 1957.

[60] Z. Maki, M. Nakagawa and S. Sakata. *Prog. Theor. Phys.*, **28**:870, 1962.

[61] B. Aharmim, S. N. Ahmed, A. E. Anthony et al. *Phys. Rev. C*, **88**:025501, 2013.

[62] T. Schwetz. *Phys. Script*, **T127**:1, 2006.

[63] K. Abe, J. Adam, H. Aihara et al. *Phys. Rev. Lett*, **112**:181801, 2014.

[64] A. de Gouvêa, J. Jenkins and B. Kayser. *Phys. Rev. D*, **71**:113009, 2005.

[65] X. Qian and P. Vogel. *Prog. Part. Nucl. Phys.*, in press, 2015.

[66] K. P. Jackson, A. Celler, W. P. Alford et al. *Phys. Lett. B*, **201**:25, 1988.

[67] C. D. Goodman, C. A. Goulding, M. B. Greenfield et al. *Phys. Rev. Lett.*, **44**:1755 – 1759, 1980.

[68] J. H. Thies, P. Puppe, T. Adachi et al. *Phys. Rev. C*, **86**:054323, 2012.

[69] J. H. Thies, D. Frekers, T. Adachi et al. *Phys. Rev. C*, **86**:014304, 2012.

[70] J. H. Thies, T. Adachi, M. Dozono et al. *Phys. Rev. C*, **86**:044309, 2012.

[71] P. Puppe, A. Lennarz, T. Adachi et al. *Phys. Rev. C*, **86**:044603, 2012.

[72] P. Puppe, D. Frekers, T. Adachi et al. *Phys. Rev. C*, **84**:051305, 2011.

[73] S. Rakers, C. Bäumer, A. M. van den Berg et al. *Phys. Rev. C*, **71**:054313, 2005.

[74] M. Kortelainen and J. Suhonen. *Phys. Rev. C*, **76**:024315, 2007.

[75] D. Frekers, J. Dilling and I. Tanihata. *Can. J. Phys.*, **85**:57, 2007.

[76] B. A. Brown, M. Horoi and R. A. Senkov. *Phys. Rev. Lett*, **113**:262501, 2014.

[77] M. Kortelainen and J. Suhonen. *Europhys. Lett.*, **58**:666, 2002.

[78] S. Rahaman, V.-V. Elomaa, T. Eronen et al. *Phys. Lett. B*, **703**:412 – 416, 2011. ISSN 0370-2693.

[79] A. A. Kwiatkowski, T. Brunner, J. D. Holt et al. *Phys. Rev. C*, **89**:045502, 2014.

[80] K. Gulyuz, J. Ariche, G. Bollen et al. *Phys. Rev. C*, **91**:055501, 2015.

[81] P. Vogel. *J. Phys. G: Nucl. Part. Phys.*, **39**:124002, 2012.

[82] V. A. Rodin, A. Faessler, F. Šimkovic and P. Vogel. *Nucl. Phys. A*, **766**:107, 2006.

[83] V. A. Rodin, A. Faessler, F. Šimkovic and P. Vogel. *Nucl. Phys.*, **A793**:213, 2007.

[84] F. Šimkovic, A. Faessler, H. Müther, V. Rodin and M. Stauf. *Phys. Rev. C*, **79**: 055501, 2009.

[85] F. Šimkovic, A. Faessler, V. A. Rodin, P. Vogel and J. Engel. *Phys. Rev. C*, **77**: 045503, 2008.

[86] M. Kortelainen and J. Suhonen. *Phys. Rev. C*, **75**:051303, 2007.

[87] T. Tomoda, A. Faessler, K. W. Schmid and F. Grümmer. *Nucl. Phys.*, **A452**:591, 1986.

[88] W. C. Haxton and G. J. Stephenson Jr. *Prog. Part. Nucl. Phys.*, **12**:409, 1984.

[89] E. Caurier, J. Menéndez, F. Nowacki and A. Poves. *Phys. Rev. Lett.*, **100**:052503, 2008.

[90] E. Caurier, F. Nowacki and A. Poves. *Phys. Lett. B*, **711**:62, 2012.

[91] J. Engel and G. Hagen. *Phys. Rev. C*, **79**:064317, 2009.

[92] K. Chaturvedi, R. Chandra, P. K. Rath et al. *Phys. Rev. C*, **78**:054302, 2008.

[93] P. K. Rath, R. Chandra, K. Chaturvedi et al. *Phys. Rev. C*, **80**:044303, 2009.

[94] J. Barea and F. Iachello. *Phys. Rev. C*, **79**:044301, 2009.

[95] J. Suhonen. *Phys. Lett. B*, **607**:87, 2005.

[96] O. Civitarese and J. Suhonen. *Phys. Lett. B*, **626**:80, 2005.

[97] O. Civitarese and J. Suhonen. *Nucl. Phys. A*, **653**:321, 1999.

[98] J. Abad, A. Morales, R. Nunez-Lagos and A. Pacheco. *Ann. Fis. A*, **80**:9, 1984.

[99] D. H. Madison, E. Merzbacher, P. Richard et al. *Atomic inner shell processes*. 1975.

[100] W. Bambynek, H. Behrens, M. H. Chen et al. *Rev. Mod. Phys.*, **49**:961, 1977.

[101] H. Behrens and J. Jänecke. *Numerical tables for beta decay and electron capture*, volume I/4. Berlin-Heidelberg-New York: Springer, 1969.

[102] R. Jopson, H. Mark, C. Swift and J. Zenger. *Phys. Rev.*, **124**:1, 1961.

[103] J. H. Hubbell, P. N. Trehan, N. Singh et al. *J. Phys. Chem. Ref. Data*, **23**:339–364, 1994.

[104] R. Firestone and V. S. Shirley. *Table of Isotopes CD-rom, John Wiley & Sons*, 1996.

[105] M. O. Krause. *J. Phys. Chem. Ref. Data*, **8**:307, 1979.

[106] K. Słabkowska, E. Szymańska, M. Polasik et al. *Physics of Plasmas*, **21**:031216, 2014.

[107] D. Burch, L. Wilets and W. E. Meyerhof. *Phys. Rev. A*, **9**:1007, 1974.

[108] J. Bhattacharya, B. Talukdar and U. Laha. *Z. Phys. D - Atoms, Molecules and Clusters*, **14**:107–109, 1989.

[109] H. F. Beyer, H. J. Kluge and V. P. Shevelko. *X-ray radiation of highly charged ions*. Springer Series on Atoms and Plasmas, 1997.

[110] M. F. Gu. *Can. J. Phys.*, **86**:675, 2008.

[111] C. T. Chantler, A. C. L. Hayward and I. P. Grant. *Phys. Rev. Lett*, **103**:123002, 2009.

[112] P. Bricault, M. Dombsky, P. W. Schmor and G. Stanford. *Nucl. Instrum. Meth. Phys. Res. B*, **126**:231, 1997.

[113] M. Dombsky, D. Bishop, P. Bricault et al. *Rev. Sci. Instrum.*, **71**:978, 2000.

[114] P. Bricault et al. *Nucl. Instr. and Methods*, **B204**:31924, 2003.

[115] Y. Blumenfeld, T. Nilsson and P. Van Duppen. *Phys. Scr.*, **T152**:014023, 2013.

[116] U. Köster. *Eur. Phys. J.*, **15**:255, 2002.

[117] I. Bylinskii and M. K. Craddock. *Hyperfine Interactions*, **225**:9–16, 2013.

[118] P. G. Bricault, F. Ames, M. Dombsky, P. Kunz and J. Lassen. *Hyperfine Interactions*, **225**:25–49, 2014.

[119] M. Dombsky and P. Kunz. *Hyperfine Interactions*, **225**:17–23, 2013.

[120] J. Lassen, P. Bricault, M. Dombsky et al. *AIP Conf. Proc.*, **1099**:76973, 2009.

[121] S. Raeder, H. Heggen, J. Lassen et al. *Rev. Sci. Instrum.*, **85(3)**:033309, 2014.

[122] P. Bricault et al. *Rev. Sci. Instrum.*, **79**:02A908, 2008.

[123] R. K. J. Dilling and G. Ball. *Hyperfine Interactions*, **225**:1–8, 2014.

[124] J. Dilling, R. Krücken and L. Merminga. *ISAC and ARIEL: The TRIUMF Radioactive Beam Facilities and the Scientific Program*. Springer, 2014.

[125] J. Dilling, R. Baartman, P. Bricault et al. *Intern. J. Mass Spectrom.*, **251**:198, 2006.

[126] T. Brunner, M. Smith, M. Brodeur et al. *Nucl. Instrum. Methods Phys. Res. A*, **676**: 32 – 43, 2012.

[127] M. Brodeur, V. Ryjkov, T. Brunner et al. *Int. J. Mass Spectrom.*, **310**:20, 2012.

[128] A. Lapierre, M. Brodeur, T. Brunner et al. *Nucl. Instrum. Methods Phys. Res. A*, **624**:54 – 64, 2010.

[129] A. Lennarz, A. Grossheim, K. Leach et al. *Phys. Rev. Lett*, **113**:082502, 2014.

[130] K. G. Leach, A. Grossheim, A. Lennarz et al. *Nucl. Instrum. and Methods A*, **780**: 91–99, 2015.

[131] M. Smith, L. Blomeley, P. Delheij and J. Dilling. *Hyperfine Interactions*, **173(1-3)**: 171–180, 2006.

[132] A. T. Gallant, J. C. Bale, T. Brunner et al. *Phys. Rev. Lett.*, **109**:032506, 2012.

[133] T. Gallant, A. M. Brodeur, C. Andreoiu et al. *Phys. Rev. Lett.*, 113:082501, 2014.

[134] A. Chaudhuri, C. Andreoiu, T. Brunner et al. *Phys. Rev. C*, **88**:054317, 2013.

[135] M. Brodeur, T. Brunner, C. Champagne et al. *Phys. Rev. Lett.*, **108**:052504, 2012.

[136] E. Mané, A. Voss, J. A. Behr et al. *Phys. Rev. Lett.*, **107**:212502, 2011.

[137] D. Frekers, M. Simon, C. Andreoiu et al. *Phys. Lett. B*, **722**:233 – 237, 2013. ISSN 0370-2693.

[138] T. D. Macdonald, B. E. Schultz, J. C. Bale et al. *Phys. Rev. C*, **89**:044318, 2014.

[139] M. Smith, M. Brodeur, T. Brunner et al. *Phys. Rev. Lett.*, **101**:202501, 2008.

[140] G. Gräff, H. Kalinowsky and J. Traut. *Zeit. f. Physik*, **297(1)**:35, 1980.

[141] G. Bollen, S. G. Moore, R. B. and H. Stolzenberg. *J. Appl. Phys.*, **68**(9):4355, 1990.

[142] L. S. Brown and G. Gabrielse. *Phys. Rev. A*, **25**:2423, 1982.

[143] F. Major, V. Gheorghe and G. Werth. *Charged Particle Traps. Physics and Techniques of Charged Particle Field Confinement*. Springer, Berlin, 2004.

[144] P. K. Ghosh. *Ion Traps*. Oxford University Press, 1995.

[145] R. Klawitter, U. Chowdhury, A. Chaudhuri et al. EBIS Conference Proceedings. 2014.

[146] T. Brunner. PhD thesis, Technische Universität München, Physik Department E12, 2011.

[147] H. Stöcker. *Taschenbuch der Physik*. Verlag Harri Detsch, 2000.

[148] *COMSOL, Finite element simulation tool kit.*

[149] G. Sikler, J. R. C. López-Urrutia, J. Dilling et al. *Euro. Phys. J. A*, **25**:63, 2005.

[150] T. Brunner, A. Lapierre, C. Andreoiu et al. *Eur. Phys. J. A*, **49**:142, 2013.

[151] D. A. Dahl. *Int. Journ. Mass Spec.*, **200**:3, 2000.

[152] D. M. Asner, R. F. Bradley, L. de Viveiros et al. *arXiv:1408.5362[phys.ins-det]*, 2014.

[153] K. G. Leach, A. Lennarz, A. Grossheim et al. *EPJ Web of Conferences, arXiv:1411.0026 [physics.ins-det]*, 2014.

[154] B. M. Penetrante, J. N. Bardsley, D. DeWitt, M. Clark and D. Schneider. *Phys. Rev. A*, **43**:4861, 1991.

[155] T. Brunner. private communication.

[156] A. Grossheim. private communication.

[157] G. F. Knoll. *Radiation Detection and Measurement*. John Wiley and Sons, Inc., 1999.

[158] C. FRANCE. Technical report, 1 chemin de la Roseraie B. P. 311 Parc des Tanneries F-67380 LINGOLSHEIM, 2012.

[159] Kaiser aluminum - rod and bar alloy 2017 - technical data. URL `www.kaiseraluminum.com`.

[160] *ORTEC®- Preamplifier introduction.*

[161] *Silicon Drift Detectors Explained.* Oxford Instruments - The Business of Science.

[162] *Cooled Lithium-Drifted Silicon and Germanium Detectors User's Manual.* Canberra, 1, chemin de la Roseraie 67383 LINGOLSHEIM cedex.

[163] R. Keitel, D. Bishop, D. Dale et al. *ICALEPCS99*, **674**, 1999.

[164] *SIS3302-14xx Firmware-Gamma User Manual, SIS GmbH, Version sis3302-M-1407-1-V131-gamma.doc as of 11.09.2009.*

[165] T. Papp. *X-ray Spectrom.*, **32**:458–469, 2003.

[166] C. Visñovezky, A. Limandri, M. E. Canafoglia, R. Bonetto and J. Trincavelli. *Spectrochimica Acta, Part B*, **62**:492–498, 2007.

[167] A. S. Lorente and others (HyperGamma Collaboration). *Nucl. Instrum. and Meth. A*, **573**:410, 2007.

[168] M. Agnello, E. Botta, T. Bressani, M. Bruschi et al. *Nucl. Instrum. and Meth. Phys. Res. A*, **606**:560568, 2009.

[169] National Nuclear Data Center, Brookhaven National Laboratory. 2012. URL `http://www.nndc.bnl.gov`.

[170] K. Szymańska, P. Achenbach, M. Agnello et al. *Nucl. Instrum. and Meth. Phys. Res. A*, **592**:486492, 2008.

[171] Tinkerforge GmbH, Stukenbrock, Germany. URL `http://www.tinkerforge.com`.

[172] M. Good. private communication.

[173] *Polytech*®high-density polyurethane foam grade 40, *Technical Data Sheet*. Technical report, Polymer Technologies Inc., 2014.

[174] Polyform®high-density molded - non-skinned (phdm-ns) polyurethane foam, *Technical Data Sheet*. Technical report, Polymer Technologies Inc., 2014.

[175] S. Agostinelli et al. *Nucl. Instrum. and Meth. Phys. Res. A*, **506**:250–303, 2003.

[176] J. Blachot. *Nucl. Data Sheets*, **111**:717, 2010.

[177] M. Bhattacharya, A. García, M. M. Hindi et al. *Phys. Rev. C*, **58**:1247, 1998.

[178] C. Wrede, S. K. L. Sjue, A. García et al. *Phys. Rev. C*, **87**:031303(R), 2013.

[179] H. Akimune, H. Ejiri, M. Fujiwara et al. *Phys. Lett. B*, **394**:23, 1997.

[180] M. Sasano, H. Sakai, K. Yako et al. *Phys. Rev. C*, **85**:061301, 2012.

[181] K. Zuber. private communication.

[182] K. G. Leach, A. Lennarz, A. Grossheim et al. *JPS Conference Series, arXiv:1411.4083*, 2014.

[183] URL `https://www.triumf.info/wiki/DAQwiki/index.php/MIDAS`.

[184] I. Antcheva, M. Ballintijn, B. Bellenot et al. *Computer Physics Communications*, 180: 24992512, 2009.

[185] *International Atomic Energy Agency*. Live chart of nuclides. 2014. URL `https://www-nds.iaea.org/relnsd/vcharthtml/VChartHTML.html`.

[186] L. P. Ekström and R. B. Firestone. WWW Table of Radioactive Isotopes. *database version*, 1999. URL `http://ie.lbl.gov/toi/index.htm`.

[187] K. Levenberg. *The Quarterly of Applied Mathematics*, **2**:164–168, 1944.

[188] D. Marquardt. *Journal of the Society for Industrial and Applied Mathematics*, **11(2)**: 431–441, 1963.

[189] F. Salvat, J. Fernández-Vera and J. Sempau. Penelope-2008: A code system for Monte Carlo Simulation of electron and photon transport. *workshop proceedings, barcelona, spain*. 2008.

[190] D. C. Radford. *Notes on the use of the program gf3*. Physics Division Oak Ridge National Laboratory, 1.1 edition, May 2000.

[191] J. B. Kortright and A. C. Thompson. X-ray data booklet , center for x-ray optics and advanced light source. Lawrence Berkeley National Laboratory, 2001.

[192] L. J. Kieffer and G. H. Dunn. *Rev. Mod. Phys*, **38**:1, 1966.

[193] M. Rosenbusch, D. Atanasov, K. Blaum et al. *Applied Physics B: Lasers and Optics*, **114**:147–155, 2013.

[194] R. Klawitter. private communication.

[195] W. R. Plaß, T. Dickel and C. Scheidenberger. *Int. J. Mass Spec.*, **349**:134, 2013.

[196] E. K. Warburton, J. A. Becker and B. A. Brown. *Phys. Rev. C*, **41**:1147, 1990.

[197] Y. A. Litvinov and F. Bosch. *Rep. Prog. Phys.*, **74**:016301, 2011.

[198] K. Takahashi and K. Yokoi. *Nucl. Phys. A*, **404**:578 – 598, 1983. ISSN 0375-9474.

[199] N. Winckler, H. Geissel, Y. A. Litvinov et al. *Phys. Lett. B*, **679**:36, 2009.

[200] Y. Litvinov, F. Attallah, K. Beckert et al. *Phys. Lett B*, **573**:80 – 85, 2003. ISSN 0370-2693.

[201] Y. A. Litvinov, F. Bosch, H. Geissel et al. *Phys. Rev. Lett B*, **99**:262501, 2007.

[202] K. G. Leach, I. Dillmann, R. Klawitter, J. Dilling et al. Investigating electron-capture rates of highly-charged ions. *TRIUMF - Experimental proposal*, S1478, 2015.

[203] T. W. Burrows. *Nucl. Data Sheets*, **107**:1747, 2006.

[204] L. Frevert, R. Schöneberg and A. Flammersfeld. *Zeit. f. Physik*, **439**:182, 1965.

[205] A. García, Y.-D. Chan, M. T. F. da Cruz et al. *Phys. Rev. C*, **47**:2910, 1993.

[206] S. K. L. Sjue, D. Melconian, A. García et al. *Phys. Rev. C*, **78**:064317, 2008.

[207] C. E. Svensson, R. A. E. Austin, G. C. Ball et al. *Nucl. Instrum. Methods Phys. Res. B*, **204**:660, 2003.